

Experimentele en computationele studie
van vaattoegang voor hemodialyse

Experimental and Computational Study
of Vascular Access for Hemodialysis

Koen Van Canneyt

Promotoren: prof. dr. ir. P. Verdonck, prof. dr. ir. S. Eloit
Proefschrift ingediend tot het behalen van de graad van
Doctor in de Ingenieurswetenschappen: Biomedische Ingenieurstechnieken

Vakgroep Civiele Techniek
Voorzitter: prof. dr. ir. J. De Rouck
Faculteit Ingenieurswetenschappen en Architectuur
Academiejaar 2012 - 2013



ISBN 978-90-8578-537-8
NUR 954
Wettelijk depot: D/2012/10.500/63

Supervisors:

Prof.dr.ir. Pascal Verdonck
Prof.dr.ir. Sunny Eloot

Research lab:

Biofluid, Tissue and Solid Mechanics for Medical Applications (bioMMeda)
Institute Biomedical Technology (IBiTech)
Ghent University (UGent)
De Pintelaan 185 - Block B
9000 Gent
Belgium

Members of the exam committee:*Chairman:*

Prof.dr.ir. Hendrik Van Landeghem Faculty of Engineering and Architecture,
UGent

Secretary:

Prof.dr.ir. Patrick Segers Faculty of Engineering and Architecture,
UGent

Reading committee:

Prof.dr.ir. Cécile Legallais Faculty of Engineering, Université de
Technology de Compiègne, France

Dr. Nils Planken Department of Radiology, Academic
Medical Center Amsterdam, the Netherlands

Dr. Jan Tordoir Department of Surgery, Maastricht University
Medical Center, the Netherlands

Prof.dr.ir. Frans van de Vosse Department of Biomedical Engineering,
Technical University Eindhoven, the Netherlands

Prof.dr.ir. Jan Vierendeels Faculty of Engineering and Architecture,
UGent

Other members:

Prof.dr.ir. Pascal Verdonck Faculty of Engineering and Architecture,
UGent

Prof.dr.ir. Sunny Eloot Faculty of Medicine and Health Science,
UGent

This research was funded by Ghent University (appointment as assistant academic staff) and by the European Commission 7th framework program (FP7-2007-2013: ARCH, Project n.224390).

Samenvatting Summary

Samenvatting

DEEL 1: KLINISCHE ACHTERGROND, HULPMIDDELEN EN COMPLICATIES

Deel 1 biedt aan de lezer de nodige klinische achtergrond om de studies, die later aan bod komen, te kunnen kaderen. Na een korte beschrijving van het cardiovasculaire stelsel, de nieren en de bloedvaten in de bovenste ledematen, wordt dieper ingegaan op nierfalen, de nood voor een vaattoegang en tot slot de drie types vaattoegangen.

Van nierfalen tot de nood voor een vaattoegang

Wanneer een patiënt lijdt aan terminaal nierfalen, moeten de functies van de nieren overgenomen worden. Het ontvangen van een nier via transplantatie is de ideale vervangtherapie. Voor patiënten op de transplantatiewachlijst, of patiënten die niet geschikt zijn als orgaanontvanger, bestaan er twee opties: peritoneaaldialyse of hemodialyse.

Bij peritoneaaldialyse wordt een dialysaat (electrolyten oplossing) gravitair in de buikholte gebracht via een peritoneale katheter en werkt het sterk doorbloede buikvlies (peritoneum) als membraan om de afvalstoffen uit het bloed in het dialysaat te brengen. Na enkele uren laat men het ‘vuile’ dialysaat gravitair wegstromen uit de buik. Dit gebeurt meerdere keren per dag manueel of ’s nachts automatisch. Slechts 5-10% van de dialysepatiënten maakt gebruik van die techniek.

De meest voorkomende vervangtherapie is hemodialyse, met ongeveer een half miljoen patiënten alleen al in Europa. Bij hemodialyse stroomt het bloed van de patiënt extracorporeel door een kunstnier, een kunstmatig orgaan. In die kunstnier wordt het bloed gezuiverd (diffusie en convectie) en wordt het overtollig water uit de patiënt onttrokken (ultrafiltratie). Omdat de patiënten niet 24u/24u zouden moeten verbonden blijven aan het hemodialysetoestel, moet het filteren in de kunstnier efficiënt gebeuren. Het bloed van de patiënt moet daarom, tijdens de dialysesessie (meestal 3-4 u, 3x per week), met een relatief hoog debiet (300-400 ml/min) uit het lichaam

stromen, door de kunstnier en terug naar de patiënt. Er moet dus een vaattoegang gecreëerd worden die deze hoge debieten kan garanderen, die frequent bruikbaar is en die zo weinig mogelijk complicaties veroorzaakt. Hiervoor bestaan er drie mogelijkheden: een arterio-veneuze fistel, een arterio-veneuze greffe en een centraal veneuze katheter.

Arterio-veneuze fistel (AVF)

Een arterio-veneuze fistel (AVF) is een directe verbinding tussen een arterie (slagader) en een vene (ader). Hierbij naait een (vaat)chirurg het hoge-druk-arteriële-systeem aan het lage-druk-veneuze-systeem. Die fistel wordt meestal in de arm, bij voorkeur in de onderarm, aangelegd, door de vene op de zijkant van de arterie te naaien. De verbinding zelf noemt men de anastomose. De fistelcreatie zorgt dus voor een bypass van het haarvaten-systeem in de hand (een soort kortsluiting) en voor een hoog debiet door de arm. Waar in de arm normaalgezien debieten van maximaal 100 ml/min aanwezig zijn, kan dat postoperatief 10-20 keer hoger zijn.

Door de verhoging van druk en debiet in de vene, wordt die vene groter en verstevigt de wand. Dat proces noemt men maturatie en is noodzakelijk om ongeveer 6 weken na de operatie de vene te kunnen aanprikken met een arteriële (aanzuig) en een veneuze (terugvoer) dialysenaald. In 25-45% van de gevallen faalt dit maturatieproces echter. Eens de fistel gematureerd is, is de meest voorkomende complicatie het vernauwen van de bloedvaten. Die stenosevorming vermindert het bloeddebiet door de fistel, waardoor de efficiëntie van de hemodialysebehandeling sterk vermindert. Vooral deze complicatie zorgt ervoor dat ongeveer 50% van de fistels binnen het jaar een radiologische of chirurgische interventie nodig hebben om hun werking te garanderen.

Daarnaast is het ook mogelijk dat er een te groot debiet door de fistel anastomose stroomt en dat de drukval van arterie naar vene te laag is. Hierbij komt de doorbloeding van de distale delen (stroomafwaarts, meer specifiek, de hand) in het gedrang. Deze ischemie kan leiden tot necrose van het weefsel. Ook een *overload* van het hart, dat het verhoogde debiet door de arm, als surplus, moet aanleveren, is hierbij een ernstige complicatie.

Er is aangetoond dat een fistel de minste complicaties teweegbrengt, vergeleken met de andere vaattoegangen. Daarom hoort dit type vaattoegang de eerste keuze te zijn bij een hemodialysepatiënt.

Arterio-veneuze greffe (AVG)

De arterio-veneuze greffe (AVG) is een variant van de AVF. Bij een AVG wordt onderhuids een kunstmatig textiel buisje genaaid tussen de arterie

en de vene. Deze vaattoegang wordt meestal toegepast bij patiënten wiens venen van een mindere kwaliteit zijn. In het geval van een greffe, worden de dialysenaalden dan ook in de greffe zelf geprikt. De meest voorkomende complicatie hierbij is stenosevorming aan de veneuze anastomose en in de bloedafvoerende vene. Algemeen kan aangenomen worden dat er bij greffe meer interventies nodig zijn om de vaattoegang goed werkend te houden dan bij een fistel.

Centraal veneuze katheter (CVC)

Een centraal veneuze katheter (*'central venous catheter'*, CVC) bestaat uit één of twee lumens (buisjes) en wordt ingebracht in een vene die naar de vena cava superior of de rechter voorkamer van het hart loopt. Deze katheter wordt, meestal ter hoogte van het sleutelbeen, naar buiten geleid zodat hij verbonden kan worden met het dialysetoestel. Het gebruik van katheters als permanente vaattoegang wordt afgeraden door het veelvuldig voorkomen van complicaties zoals infectie en thrombose. De CVC wordt echter wel gebruikt bij hemodialyse tijdens het matureren van een fistel of wanneer geen enkele fistel of greffe meer kan aangelegd worden.

Er is een grote verscheidenheid aan beschikbare katheter designs. Van het 'shotgun'-ontwerp (terugvoer-lumen langer dan aanzuig-lumen), over symmetrische ontwerpen, tot ontwerpen waar beide lumens los van elkaar hangen ('split'-ontwerp). Elk van die designs heeft voor- en nadelen.

DEEL 2: INGENIEURSHULPMIDDELEN

Deel 2 behandelt enkele (ingenieur-)technische onderwerpen, ter verduidelijking van de gebruikte methodes in de uitgewerkte studies. Vooreerst wordt het Europees ARCH-project kort toegelicht. Enkele studies die beschreven worden in dit manuscript maken deel uit van dat Europees project. Enkele andere studies zijn gebaseerd op data uit het ARCH-onderzoek. Daarna wordt de basis van de vloeistofmechanica beschreven: de algemene vloeistofeigenschappen (dichtheid, viscositeit, ...), de behoudswetten en de specifieke karakteristieken van vloeistof in beweging. Om deze ingenieursachtergrond te vervolledigen worden de gebruikte technieken, zowel computationeel als experimenteel, ingeleid.

Computationale methodes

Vooreerst werd gebruik gemaakt van *computational fluid dynamics* (CFD, numerieke stromingsleer) berekeningen. Die techniek bestaat erin een volume eerst onder te verdelen in zeer kleine cellen ('meshen'). Daarna worden

de wetten van behoud van massa en momentum berekend in elke cel om zo met een iteratief proces de stroming in het volledige volume te begroten en visualiseren. Daarnaast laat deze techniek ook toe om schuifspanningen te berekenen.

Een tweede computationele methode die in dit werk gebruikt werd, is kinetische modellering. Deze techniek verdeelt het lichaam in virtuele compartimenten om het inwendige massatransport te kwantificeren.

Experimentele methodes

In het experimenteel (*in vitro*) gedeelte van dit onderzoek werd gebruik gemaakt van siliconemodellen van de bloedvaten in de arm. Die modellen werden aangesloten op gestuurde pompen en geconnecteerd met drukvaten, reservoirs en weerstanden stroomafwaarts. Nadat fysiologische druk- en stromingsrandvoorwaarden gecreëerd werden, konden zowel de distensie (diameter verandering ten gevolge van drukgolf) als de stromings- en drukprofielen nauwkeurig opgemeten worden. De bekomen data diende deels als input van de computermodellen, en deels om de output van de computermodellen te verifiëren.

Voor het experimenteel gedeelte werd ook gebruik gemaakt van *Particle Image Velocimetry* (PIV). Hierbij wordt op een perfect transparant model een laser vlak aangebracht. Door het model stroomt een vloeistof waarin kleine reflecterende deeltjes, partikels, zijn aangebracht. Een camera registreert de deeltjes die door het laser-verlichte gebied bewegen. Door vergelijking van opeenvolgende beelden kunnen dan lokale snelheden berekend worden.

DEEL 3: STUDIES OVER AVF'S

Computationele studie van stroming in een AVF anastomose

Tot op heden is er weinig interesse voor de geometrie van de anastomose zelf, hoewel dit een cruciaal onderdeel is van het stromingspad en er tot 95% van het bloed in de arm moet door stromen. In de studie beschreven in *hoofdstuk 10* gaan we dieper in op de stroming in de arterio-veneuze anastomose en beschrijven we de invloed van de grootte van die verbinding en van de hoek tussen arterie en vene op zowel het debiet als de drukverdeling. We creëerden 11 verschillende computermodellen van een arterie, waarop langs de zijkant een vene is geconnecteerd, en waarbij de anastomose grootte varieerde tussen de 12.6 en 23.6 mm² en de anastomose hoek tussen de 27° en 90°. Met CFD-berekeningen werd de stroming in deze eenvoudige AVF-modellen geanalyseerd.

In een eerste luik hebben we een uitstroom debietsverdeling vastgelegd en het instroom debiet gevarieerd tussen de 600-1200 ml/min. We konden aantonen dat de drukval over de anastomose (drukverschil tussen arteriële en veneuze druk, de 'weerstand') kwadratisch stijgt met een groter wordend debiet en dat de drukval kleiner wordt als de anastomose vergroot of als de hoek wijder wordt dan 43° .

In een tweede luik hebben we de drukken aan in- en uitlaat vastgezet en opnieuw de 11 verschillende modellen doorgerekend. Naar analogie met de bevindingen uit het eerste deel, merkten we nu dat het instroomdebiet steeg als de anastomose oppervlakte of hoek groter werden. Omdat de drukval over de anastomose zodanig daalde, werd er zelfs bloed vanuit het distale deel van de arterie (van de hand) aangezogen naar de vene. Dit laatste kan klinisch leiden tot distale hypoperfusie of zelfs ischemie.

Deze studie toonde duidelijk aan dat de grootte en de hoek van de anastomose zeer bepalend zijn voor de stroming in de fistel. Omdat een te kleine anastomose meestal maturatie verhindert, wordt snel overgeschakeld naar een (te) grote anastomose. Het gebrek aan interesse voor de geometrie van de anastomose lijkt echter onterecht. Een verandering van 2 mm lengte bijvoorbeeld kan leiden tot een verhoging van de drukval met 30%.

Experimentele validatie

Binnen het Europese project ARCH (*hoofdstuk 7*) werd een computerprogramma ontwikkeld dat aan de hand van patiënt-specifieke, preoperatieve, medische beelden en gegevens, de direct postoperatieve debieten en drukken in arteries en venen kan voorspellen. Hierbij kan reeds vóór de aanleg van de fistel, patiënt-specifiek, de optimale fistellocatie gekozen worden. Alvorens het computermodel in de klinische praktijk kan getest en geoptimaliseerd worden, was het aangeraden om de nauwkeurigheid van het model en de achterliggende fysica rigoureus te verifiëren. Deze verificatie was mogelijk aan de hand van experimentele validatiestudies (*hoofdstuk 11*). Hierbij werd een model gebouwd dat gebaseerd is op patiënt-specifieke data, werd dit experimentele model met de computer nagebouwd en werden resultaten van het experiment en het computermodel vergeleken.

De eerste experimentele setup, besproken in *sectie 11.1*, bestond uit een pomp (cfr. het hart) gekoppeld aan een siliconen model van zowel de aorta, de belangrijkste arteriën in de arm, een AVF ter hoogte van de pols, als enkele venen. De geometrie (lengtes en diameters) en de distensie werden opgemeten en overgezet naar het numerieke *pulse wave propagation* model (een 1D representatie van een vaatstructuur voor het berekenen van druk- en

debietsgolven). We maten druk- en debietsgolven op 11 plaatsen experimenteel op en vergeleken deze met de computationele resultaten. Het was duidelijk dat het computermodel de gemiddelde druk en het gemiddelde debiet accuraat kon simuleren. De golfvormen zelf waren echter minder gedempt dan in het experimentele model. Dit laatste wellicht door het ontbreken van visco-elasticiteit in het computermodel.

Verder voerden we een analyse uit rond de precisie van de outputwaarden, rekening houdend met de onnauwkeurigheden van de inputdata. Dit werd uitgevoerd aan de hand van Monte Carlo simulaties waarbij elke parameter, binnen een opgegeven nauwkeurigheid, 5000 keer werd veranderd. Hieruit bleek duidelijk dat de onzekerheid op de gemeten waarden (vb. diameter arterie $\pm 10\%$) sterk kon teruggevonden worden in een onzekerheid op de gesimuleerde output. Dus het reduceren van de onzekerheid op de inputdata, heeft een grote invloed op de onzekerheid van de computer resultaten. Deze kennis moet in rekening gebracht worden wanneer het model klinisch geïmplementeerd wordt.

Een tweede validatiestudie, besproken in *sectie 11.2*, maakte gebruik van een patiënt-specifiek model van een arterio-veneuze fistel. Hierbij werd de stroming gevisualiseerd ter hoogte van de anastomose door middel van PIV-metingen. Daarnaast hebben we de drukval over de anastomose (van arterie tot vene) experimenteel opgemeten voor meer dan 200 verschillende debieten. We vonden een goede overeenkomst tussen het stromingsbeeld gegenereerd door de PIV-metingen en dat gesimuleerd door het CFD-model. Daarnaast vonden we opnieuw een kwadratisch verband tussen debiet en drukval en kwam dit verband goed overeen met de resultaten van de computerberekeningen.

Er kan dus gesteld worden dat, rekening houdend met een vastgestelde onzekerheid, beide computermodellen betrouwbare resultaten geven en dus kunnen ingezet worden om patiënt-specifieke hemodynamica nauwkeurig te simuleren.

Diagnose methodes

In *hoofdstuk 12* werden twee methodes bestudeerd die de arts kan helpen bij de diagnostiek rond AV-fistels.

Ten eerste hebben we in *sectie 12.1* een methode uitgewerkt die in staat is stenoses te detecteren met een diameterreductie van 25-50%. De huidige methodes zijn meestal gebaseerd op drukvalverhoging of debietsvermindering en kunnen slechts vernauwingen detecteren van ongeveer 70% diameterreductie ($\approx 90\%$ doorstroomoppervlakte reductie). De hier bestudeerde methode maakt echter geen gebruik van de gemiddelde druk maar

van de pulsdruk (maximale min minimale druk tijdens een hartslag cyclus). We toonden aan, via een silicone experimenteel model, dat stenoses in een vroegtijdig stadium kunnen gedetecteerd worden aan de hand van drukgolven geregistreerd aan de dialysenaald. Deze pulsdruk analyse (*pulse pressure analysis (PPA)*) bleek onafhankelijk van debiet en hartslag. Klinische studies moeten deze experimentele resultaten natuurlijk bevestigen, maar deze lage-kostenmethode biedt goede perspectieven.

Een tweede diagnosemethode die onder de loep werd genomen is de *pulsed wave Doppler ultrasound* (PWD-US) debietsmeting (sectie 12.2). Bij PWD-US wordt de gemiddelde snelheid [m/s] in een doorsnede berekend en vermenigvuldigd met de oppervlakte van de doorsnede [m²] om zo het debiet [m³/s of ml/min] te bekomen. Deze methode kan bijvoorbeeld gebruikt worden om direct postoperatieve debietsmetingen uit te voeren. Deze metingen blijken namelijk een voorspellend karakter te hebben rond het slagen van de fistelmaturatie. Een efficiënte en betrouwbare methode om debieten te meten is dus nodig.

Het bleek dat men met PWD-US (echografie) de bloedsnelheid, in het centrum van een bloedvat, in de richting van de probe, nauwkeurig kan bepalen. Wanneer echter wordt overgegaan naar debietvoorspellingen, blijken er grote onnauwkeurigheden in de metingen te ontstaan. Een patiëntspecifiek CFD-model werd opgebouwd, en de ultrasone spectra werden computationeel gegenereerd. We analyseerden zowel een pre- als een postoperatief model, beiden ter hoogte van de elleboog en van de pols.

We toonden aan dat er, bij complexe stroming, reeds fouten worden geïntroduceerd wanneer de snelheid zoals opgepikt door de US-probe (in de richting van de probe) wordt omgezet naar de snelheid in de lengterichting van het bloedvat. Maar het werd vooral duidelijk dat de grootste onnauwkeurigheid wordt geïntroduceerd wanneer de snelheid in een punt (vb. centrum van het bloedvat, 0D) of op een lijn (over de volledige diameter van het bloedvat, 1D) wordt omgezet naar de gemiddelde snelheid in de doorstroomoppervlakte (2D). De vorm van het lokale snelheidsprofiel is namelijk volledig onbekend. We vergeleken aannames van parabolische profielen (*Poiseuille* stroming), vlakke profielen (*plug* stroming) en tijdsafhankelijke profielen (*Womersley* stroming).

Er kon geconcludeerd worden dat er geen enkele aanname werkt in elk van de situaties en dat er bij gebruik van PWD-US debietsdata rekening moet gehouden worden met zeer grote onnauwkeurigheden op de verkregen debietwaarden.

DEEL 4: STUDIES OVER AVG'S

Helicale greffe designs

Zoals vermeld is stenosevorming een veel voorkomende complicatie bij greffes. Deze vernauwingen worden veroorzaakt door neo-intimale hyperplasie. Dit ongecontroleerd groeien van cellen uit de intimalaag van de bloedvatwand wordt gedreven door abnormale lokale stromingspatronen. In de literatuur staat beschreven dat fenomenen als lage gemiddelde wandschuifspanning (lage *time-averaged wall shear stress*, TAWSS), sterk oscillerende wandschuifspanning (hoge *oscillatory shear index*, OSI) en hoge verblijfstijd (hoge *relative residence time*, RRT) deze neo-intimale hyperplasie induceren. Daarnaast is er beschreven dat stroming met veel wervels deze ongunstige hemodynamica reduceren.

In *hoofdstuk 13* hebben we de beschreven stromingsfenomenen bestudeerd in greffes met een spiraalvormig (helix) design, aan de hand van CFD-simulaties. Er werden vijf verschillende helicale designs, parametrisch, ontworpen (met torsielengtes van 1,75 tot 6 keer de greffe diameter) en vergeleken met een rechte, conventionele greffe. Uit de berekeningen, uitgevoerd met hoge nauwkeurigheid, kon worden afgeleid dat het introduceren van een spiraalvorm (*swirl*) in het design van een greffe leidt tot een meer complex stromingsbeeld en dat de zones met ongunstige hemodynamica gereduceerd worden. De graad van reductie bleek echter niet proportioneel met de ingebrachte heliceiteit en we kunnen aannemen dat de effectiviteit van deze greffes dan ook casus per casus moet bekeken worden.

DEEL 5: STUDIES OVER CVC'S

Computationale studie rond katheter met nieuw tipdesign

Bij het ontwerp van een katheter is het de bedoeling dat de recirculatie zo laag mogelijk is (eventueel zelfs bij omgekeerde connectie van de aansluitingen), dat het bloed niet stilstaat in de lumens (klontervorming) en dat het bloed zo weinig mogelijk wrijving ondervindt (beschadiging van rode bloedcellen, *hemolyse*).

In *hoofdstuk 14* werd het ontwerp van een nieuwe katheter, met een symmetrische tip, onder de loep genomen. Een uitgebreide CFD-analyse toonde aan dat er een verwaarloosbare recirculatie optrad in de nieuwe VectorFlow katheter. Dit werd zowel in een experimentele studie als in een studie op een varkensmodel bevestigd. Daarnaast was het in de computationele studie mogelijk de stromingspatronen rond de tip te bestuderen en parameters

rond klontervorming en hemolyse te analyseren en te vergelijken. De stromingsfenomenen en parameters bleken voor het nieuwe design vergelijkbaar met die bij reeds bestaande standaard ontwerpen. De studie toonde de grote potentie van de VectorFlow katheter, door het uitblijven van recirculatie, en opent de deur voor verdere (pre-)klinische studies.

Computationale studie naar suboptimaal werkende katheters

Wanneer het gewenste dialysedebiet niet meer kan verkregen worden bij gebruik van een katheter met twee lumens, wordt ofwel verder gedialyseerd met het verlaagde bloeddebet of worden de aanzuigzijde (arteriële lumen) en de terugvoerzijde (veneuze lumen) omgekeerd geconnecteerd. Omdat de meeste katheters ontworpen zijn om in gewone werking zo weinig mogelijk gezuiverd bloed (uit veneuze lumen) terug aan te zuigen (via arteriële lumen), recirculatie genaamd, zorgt een omkering van de connecties meestal wel voor een verhoogde recirculatie.

In *sectie 15.1* hebben we eerst bij een groep van 22 patiënten onderzocht hoe efficiënt de hemodialyse is als de connecties omgekeerd worden. Hieruit bleek dat de efficiëntie niet significant verschilde bij gewone versus omgekeerde connectie voor ureum, creatinine, beta-2-microglobulin (β_2M) en fosfaat. Daarnaast werd een eerste mathematische model opgebouwd door een 1-compartiment kinetisch model te koppelen aan een dialysemodel. De studie rond de klaring (afvoer) van ureum tijdens dialyse toonde aan dat er slechts een reductie van de efficiëntie, op basis van de hoeveelheid verwijderde stof, van 9.2% optrad bij een recirculatie van 10%.

Om de vertraagde distributie van stoffen in het lichaam beter te kunnen modelleren werd in *sectie 15.2* het meer volledige 2-compartimenten kinetisch model uitgewerkt. Hierbij werden vier verschillende opgeloste stoffen bestudeerd: ureum, methylguanidine, β_2M en fosfaat. Hiermee werd aangetoond dat in een standaard dialysesessie (4 uur), een katheter met één lumen zorgt voor een minder efficiënte dialyse vergeleken met een katheter met twee lumens. Daarnaast werd duidelijk dat het omkeren van de lijnen bij een suboptimaal werkende katheter beter is dan het blijven dialyseren in correcte connectie maar met verminderd debiet.

Vertrekkend van het 2-compartimenten kinetisch model, zijn we in *sectie 15.3* dieper ingegaan op een verlengde dialysesessie (8 uur), die vooral 's nachts, zowel in dialysecentrum als thuis, kan plaatsvinden. Daardoor hebben ze vaak een lagere impact op het leven van de patiënt. Vooreerst vonden we dat er in een 8 u dialyse, bij gelijke debieten, een verhoging van de dialyseefficiëntie plaatsvond ten opzichte van 4 u dialyse. De verwijdering van de opgeloste stoffen was, door het vertraagde transport in het lichaam, echter niet verdubbeld.

Om de nachtrust van de patiënten te bewaren (minder opstaan om concentraatzakken te verwisselen en minder alarms) en de kost van water onder controle te houden, zou dialyse met een gehalveerd debiet aangewezen kunnen zijn. Voor deze lange trage dialyse vonden we een efficiëntie vergelijkbaar met standaard 4 u dialyse. Ten slotte werd nog de optie bestudeerd waarbij de patiënt zichzelf met één naald aanprikt (in plaats van twee) in een arterio-veneuze fistel of waarbij er een katheter met enkel lumen gebruikt werd. Hierbij vonden we een verhoogde efficiëntie ten opzichte van de standaard 4 u dialyse.

DEEL 6: ALGEMENE CONCLUSIES

Door het uitvoeren van de verschillende computationele en experimentele studies, komen we tot volgende stellingen:

- Bij een AVF moet de grootste drukval over de anastomose liggen.
- Het gebruik van een helix vorm in het ontwerp van een AVG introduceert een complexer stromingsveld en reduceert de zones met ongunstige hemodynamica, maar doet deze echter niet verdwijnen.
- De VectorFlow CVC is een veelbelovende katheter door de verwaarloosbare recirculatie.
- Het *pulse wave propagation* model en het numerieke stromingsleerpakket voor hoge debieten, ontwikkeld in het ARCH-project, zijn experimenteel gevalideerd en kunnen gebruikt worden voor implementatie in de klinische praktijk.
- Experimenteel onderzoek vereist ervaren onderzoekers.
- Het uitvoeren van polsdruk analyse aan de arteriële dialysenaald kan leiden tot het vroegtijdig detecteren van stenoses.
- Standaard *pulsed wave Doppler ultrasound* metingen leveren geen betrouwbare waarde voor het bloeddebiet.
- Bij een slecht werkende dubbel lumen CVC tijdens standaard (4 u) dialyse moet het omkeren van de katheter connecties en behoud van voldoende debiet de voorkeur krijgen.
- Trage dialyse met een dubbel lumen CVC, of dialyse met een enkel lumen CVC of met één naald in de AVF, zijn goede alternatieven tijdens dialyse met verlengde duur (8 h).

Summary

PART 1: CLINICAL BACKGROUND, DEVICES AND COMPLICATIONS

The first part provides the reader with the necessary clinical background to understand the conducted studies in this work. After a brief description of the cardio-vascular system, the kidneys and the blood vessels in the upper extremities, kidney failure, the need for a vascular access and the three types of vascular access are discussed.

From a failing kidney to the need for a vascular access

If a patient suffers from an end-stage renal disease (total kidney failure), the functions of the kidneys must be reproduced. Receiving a kidney transplant is the best replacement therapy. For patients on the transplant waiting list or patients not suitable as organ recipient, there are however two options: peritoneal dialysis or hemodialysis.

During peritoneal dialysis, a dialysate (electrolyte solution) is brought, by gravity, in the abdominal cavity via a peritoneal catheter. The highly vascularized peritoneum acts as a membrane, bringing waste products from the blood into the dialysate. After a few hours, the spent dialysate is drained, by gravity, from the abdomen to a waste bag. This sequence is repeated several times a day manually or at night automatically. Only 5-10% of dialysis patients make use of this technique.

The most common renal replacement therapy is hemodialysis, with more than half-a-million patients in Europe. Within this therapy, the patient's blood flows extracorporeally through an artificial kidney, an artificial organ. In an artificial kidney, the blood is purified (convection and diffusion) and excess water is removed from the patient (ultrafiltration). To avoid that the patient should remain connected to the dialyzer 24/7, the treatment should happen as efficient as possible. The patient's blood should therefore, during the dialysis session (usually 3-4 h, 3/week), flow with a relative high flow rate (300-400 ml/min) through the artificial kidney. Therefore, there is the need to create a vascular access which can provide these high flow rates, which

is frequently usable and which has a low complication rate. There are three possibilities: an arterio-venous fistula, an arterio-venous graft and a central venous catheter.

Arterio-venous fistula (AVF)

An arterio-venous fistula (AVF) is a direct connection between an artery and a vein. A (vascular) surgeon sews the high-pressure arterial system to the low-pressure venous system. The fistula is mostly created in the arm, preferably in the lower arm, by connecting a vein to the side of an artery (end-to-side). The connection itself is called the anastomosis. The fistula creation causes a bypass of the capillary system (sort of short circuit) and an increase in blood flow through the arm. Normally, the flow in the arm is around 100 ml/min, but after fistula creation this can increase by a factor ten to twenty.

Due to the increase in pressure and flow, the vein enlarges and the vein wall reinforces. This process, called maturation, is required to puncture the vein, mostly starting 6-8 weeks after the surgery, with an arterial (suction) and venous (return) dialysis needle. However, failure to mature occurs in 25-45% of the cases.

Once the fistula matured, the narrowing of the vessels is the most common complication. This stenosis formation reduces the blood flow rate and inhibits an efficient dialysis treatment. This complication in particular, is responsible for the fact that up to 50% of fistulas need a surgical or radiological intervention within the first year.

In addition, a too high flow rate and/or too low pressure drop over the arterio-venous anastomosis often occur. Hereby, the blood circulation to the distal part (downstream, more specifically the hand) is inhibited. This distal hypoperfusion syndrome can lead to ischemia and even necrosis of the tissue. Furthermore, the heart has to deliver this elevated blood flow to the arm and a cardiac overload can occur.

It has been shown that the complication rate in fistulas is lower compared to the other vascular access options. Therefore, an AVF should be the first option as vascular access.

Arterio-venous graft (AVG)

An arterio-venous graft (AVG) is a variant on an AVF. With a graft, an artificial textile tube is sewn, subcutaneously, between an artery and a vein. This vascular access is usually used in patients with low quality veins. In the case of a graft, the dialysis needles are inserted in the graft itself. The most common complication is stenosis formation at the venous anastomosis and

in the draining vein. The number of vascular access interventions needed to maintain the graft's well functioning is higher compared to the necessary interventions associated with a fistula.

Central venous catheter (CVC)

A central venous catheter (CVC) consists of one or two lumens (tubes) and is inserted into a vein leading to the vena cava superior or the right atrium. The catheter is brought, usually at the height of the collar bone, to the outside to be able to be connected with the dialysis machine. The use of catheters as permanent vascular access is not recommended due to the frequent occurrence of complications such as infection and thrombosis. The CVC is nonetheless used for hemodialysis during the maturation of a fistula or if no more fistula or graft can be constructed.

There is a great variety in available catheter designs. From the 'shotgun' design (return lumen longer than suction lumen), over symmetrical designs to designs where both lumens are separated ('split' design), each with their own advantages and disadvantages.

PART 2: ENGINEERING TOOLS

In the second part, some engineering background is provided. This should make the methods, applied in the studies, more clear. First, the European ARCH-project is briefly explained. This is because some studies in this dissertation were, on the one hand, part of this research project or, on the other hand, rely on data from it. Next, the basic principles of fluid mechanics are described, starting from the overall liquid properties (density, viscosity, ...), over the conservation laws, to specific characteristics of the fluid in motion. To complete this engineering background part, the used techniques, both computational and experimental, are introduced.

Computational methods

Some computational studies were conducted based on computational fluid dynamics (CFD) calculations. In CFD, a volume has to be subdivided into a large number small volume cells ('meshing'). Then, in each cell, an iterative procedure is applied until the laws of conservation of mass and momentum result in negligible residuals. This allows us to visualize and analyze the flow in great detail. In addition, also shear stresses or blood residence times can be calculated.

The second computational method that was used in this work is kinetic modeling. This technique virtually divides the body into several compartments to quantify the internal mass transport phenomena.

Experimental methods

Silicone models of the blood vessels in the arm were used during the experimental (*in vitro*) part of the research. These were connected to (controlled) pumps, (pressure) reservoirs and downstream resistances. When physiological pressure and flow conditions were created, we could measure distension (change in diameter due to pressure changes) and flow and pressure profiles accurately. The obtained experimental data could partly serve as input for computer models and partly to verify the output generated by the computer models.

During the experimental studies, Particle Image Velocimetry (PIV) was used as well. A thin laser sheet is applied on a transparent model and a liquid, seeded with small tracer particles, flows through the model. A camera records the particles flowing through the illuminated region of interest. The locations of the particles over consecutive images are compared to achieve the local velocity field.

PART 3: STUDIES ON AVFs

Computational study on flow in a AVF anastomosis

Although the anastomosis is a crucial element in the blood flow path and 90-95% of the blood flow in the arm passes it, there is, in general, a significant absence of interest in the geometry of the anastomosis. In the study described in *chapter 10*, the flow in the anastomosis region was assessed in more detail and we described the impact of the size of the anastomosis, as well as of the angle between vein and artery, on flow rates and pressure distribution. Therefore, we created 11 different computational models of a vein connected to the side of an artery with a varying anastomosis size (12.6-23.6 mm²) and anastomosis angle (27-90°). The flow in these simplified AVF models was analyzed based on CFD-calculations.

First, an outflow distribution was fixed, while the inflow flow rate was changed between 600 and 1200 ml/min. We were able to show that the pressure drop over the anastomosis (arterial minus venous pressure) changes quadratically with the inflow rate and decreases when the anastomosis size increases or the angle gets wider then 43°.

Later, we fixed the inlet and outlet pressures and recalculated all 11 CFD models. In analogy with the conclusions from the first part, we found an increased flow rate when the anastomosis size or angle increased. Because the decrease in pressure drop over the anastomosis was very high, blood was 'stolen' by the vein from the distal artery (from the hand). This 'steal syndrome' can clinically lead to distal hypoperfusion or even ischemia.

The study clearly showed that the anastomosis size and angle have a great influence on the flow field in the fistula. Because a too small anastomosis can inhibit the maturation process, physicians switch too fast to a (too) large anastomosis. The lack of interest concerning the geometry of the anastomosis seems, however, unfair. A change of, for example, 2 mm in anastomosis length can lead to a pressure drop increase of 30%.

Experimental validation

Within the context of the European ARCH project (*chapter 7*), a computational modeling framework was developed to predict direct postoperative flow and pressure in both arteries and veins, based on patient-specific, preoperative, medical images and functional data. The goal is to predict, patient-specifically, the optimal AVF anastomosis location. Before the testing and optimization of the model framework in clinical practice, it was recommended to rigorously verify the numerical model and the underlying physics. This verification was performed using experimental validation (*chapter 11*). First, an *in vitro* model was built based on patient-specific data, second, the experimental model was reconstructed in the computer model and, finally, the experimental and computational results were compared.

The first experimental setup we used, discussed in *section 11.1*, consists of a pump (cf. the heart) coupled with a silicon model of the aorta, the most important arteries in the arm, an AVF at the wrist and a basic venous circuit. The geometry (lengths and diameters) and the distensibility were measured and converted to the numerical *pulse wave propagation* model (a 1D representation of the vessel topology for the calculation of pressure and flow waveforms). We obtained experimentally pressure and flow waveforms on 11 different locations throughout the silicon model and compared these with the computational results. It was clear that the computational model was able to accurately simulate the mean pressure and flow rates. The waveforms themselves were however less attenuated compared to the experimental results. The latter is probably caused by the absence of visco-elasticity in the computer model.

Furthermore, we studied the precision of the numerical output values, taking into account the uncertainties of the input data. This analysis was conducted using Monte-Carlo simulation in which every parameter was changed 5000 times, within its predefined uncertainty range. We showed that the uncertainties of the measured values (e.g. diameter artery $\pm 10\%$) are clearly notable when analyzing the uncertainty of the simulated output. Thus, reducing the uncertainty of the input data might significantly increase the accuracy of the computational results. This knowledge should be taken into account when applying the model in clinical practice.

A second validation study, discussed in *section 11.2*, used a patient-specific model of an arterio-venous fistula in which the flow field was firstly visualized, in the anastomosis region, by PIV measurements. Secondly, the pressure drop over the anastomosis (artery to vein) was acquired experimentally for more than 200 different flow rates. We found an excellent match between the flow field captured by the PIV measurements and the flow field simulated by the CFD model. Furthermore, we found a quadratic relation between flow rate and pressure drop and, once again, an excellent match between experimental and computational results.

We can state that, taking the defined uncertainties in consideration, both computational models are reliable tools and can be used to simulated patient-specific hemodynamics.

Diagnostic tools

In *chapter 12*, two methods were studied in order to help the physician with the diagnosis of an AV fistula's patency.

First, we elaborated on a stenosis detection method, able to detect stenoses with a 25-50% diameter reduction (*section 12.1*). The current methods are most often based on pressure drop increase or flow rate decrease and can only detect sections with at least 70% diameter reduction ($\approx 90\%$ area reduction). Our studied method does not make use of the mean pressure but of the pulse pressure (max minus min pressure over a cardiac cycle). We showed, based on an *in vitro* study, that early detection of stenoses is possible, based on the pressure data gathered at the arterial needle. We found that this pulse pressure analysis (PPA) method is independent of flow rate and heart rate. Of course, clinical investigations have to confirm the experimental results, but this low-cost method shows a great potential.

A second diagnostic method that was examined was pulsed wave Doppler ultrasound (PWD-US) flow rate acquisition (*section 12.2*). Within this PWD-US method, a cross-sectional averaged velocity [m/s] is estimated and multiplied with the area of the cross-section [m²], to end up with the flow rate [m³/s or ml/min]. This method can, for example, be used to measure direct-postoperative flow rates. The outcome of the maturation process seems to be predictive when looking at this flow rate data. The flow rate should therefore be measured with an efficient and reliable method.

We found that PWD-US can determine the flow velocity, in the center of the vessel lumen and in the direction of the US probe, accurately. However, when this velocity data are transferred to flow rate data, large uncertainties are introduced. We built a patient-specific CFD model and generated computationally the ultrasound spectra. Both a pre- and a postoperative model, both at the elbow and the wrist level, were studied.

We showed that, for complex flow fields, errors are already introduced when the velocity captured by the US probe (in the direction of the probe) is converted to the velocity in the longitudinal direction of the vessel. It was however clear that the major inaccuracies are introduced when the velocity in a point (e.g. in the center of the vessel, 0D) or on a line (e.g. over the full diameter of the vessel, 1D) are transferred to the cross-sectional averaged velocity (2D). This is caused by the fact that the shape of the local flow profile is totally unknown. We compared the assumption of a parabolic profile (Poiseuille flow), a flat profile (plug flow) and a time-dependent profile (Womersley flow).

We can conclude that, in all cases, one should take into account that, when using PWD-US flow rate data, a large uncertainty is present in the flow rate output.

PART 4: STUDY ON AVGs

Computational study of flow in helical AVGs

As mentioned, stenosis formation is a frequent occurring complication within grafts. This narrowing of the vessel is caused by neo-intimal hyperplasia. This uncontrolled growth of cells in the intimal layer of the vessel wall is triggered by the local flow field. In literature, we can find that phenomena like low time-averaged wall shear stress (TAWSS), high oscillatory wall shear stress (high oscillatory shear index (OSI)) and high relative residence time (RRT) induce neo-intimal hyperplasia. Furthermore, it is described that a flow field with strong vortices reduces the zones with unfavorable hemodynamical conditions.

In *chapter 13*, we studied the discussed flow phenomena in grafts with a helical design, using CFD simulations. Five different helical graft designs were, parametrically, constructed (pitch lengths from 17.5 to 6 times the diameter of the graft) and compared with a conventional straight graft. From the calculations, performed with great accuracy, we could conclude that introducing helicity ('swirl') in the design leads to a more complex flow field and reduces zones with unfavorable hemodynamical conditions. However, the rate of reduction seemed not fully proportional with the introduced helicity. We can presume that the effectiveness of such a graft has to be studied case-by-case.

PART 5: STUDIES ON CVCs

Computational study of flow in a novel CVC

When designing a catheter, one wants the catheter to have a low recirculation (eventually even in reversed connection mode), no standstill of blood in the lumens (clotting) and low levels of shear forces on the blood cells (damaging of red blood cells, hemolysis).

In *chapter 14*, we assessed a new catheter, with a symmetrical tip design. An extensive CFD analysis on the new VectorFlow catheter revealed that the recirculation was negligible. This finding was confirmed in both an experimental (*in vitro*) study and in a study on a pig. The computational model made it possible to study the flow field around the tip and to analyze parameters concerning clotting and hemolysis. The data representing the flow phenomena in the new design were comparable with the values from existing standard designs. Our study showed the potential of the VectorFlow catheter, due to the total absence of recirculation, and opens the way for future (pre)clinical studies.

Computational study on malfunctioning CVCs

When the required dialysis flow can no longer be achieved during a dialysis session with a double lumen catheter, either dialysis with the lowered flow rate can be performed, or the connections of the suction side (arterial lumen) and draining side (venous lumen) can be switched. Because most catheters are designed to minimize recirculation (suction of cleansed blood from venous lumen back in arterial lumen) when connected in the correct sense, a connection reverse mostly induces an increased recirculation.

In *section 15.1*, we investigated the hemodialysis efficiency, comparing normal to reversed catheter connection in 22 patients. We found, for urea, creatinine, beta-2-microglobulin (β_2M) and phosphorus, that there was no significant difference between the two types of connection. Next, we constructed a mathematical model by combining a 1-compartment kinetic model with a dialysis model. Our study of the clearance of urea showed that there was only a 9.2% decrease in dialysis efficiency, based on the the total solute removal, when a 10% recirculation is present.

To be able to simulate the retarded distribution of solutes in the body more accurately, a 2-compartment model was introduced in *section 15.2*. We studied four different solutes: urea, methylguanidine, β_2M and phosphorus. We showed that for a standard dialysis session (4 hours), dialysis with a single lumen catheter reflects in a less effective solute removal compared to dialysis with a double lumen CVC. Furthermore, reversing the lines in

suboptimal working catheters seemed a better option when compared to dialysis in normal connection but with a lowered flow rate.

Starting from the 2-compartment kinetic model, we investigated in *section 15.3* the use of an extended dialysis session (8 hours), mostly taking place during the night, in a dialysis center or at home. This can lower the impact of the renal replacement therapy on the patient's daily life. First, we found, for 8 h dialysis, an increase in efficiency compared to the standard 4 h dialysis. However, the total solute removal, for our studied solutes, was not doubled, due to the retarded transport in the body.

To preserve the night's rest of the patients (less frequent awakening to change reservoirs and less alarms) and to keep the water cost under control, halving the flow rates during dialysis can be an option. We found for this lowered-flow, extended (8 h), dialysis that the efficiency was comparable with the results of a standard 4 h dialysis session. Finally, we studied the option of a patient puncturing his own AVF with a single needle and the use of a single lumen catheter. An increased total solute removal was found in both cases compared to standard 4 h dialysis.

PART 6: GENERAL CONCLUSIONS

By conducting the different computational and experimental studies, we could conclude with the following statements:

- The main pressure drop in the AVF circuit should be over the anastomosis.
- Using a helical pattern in the design of an AVG introduces a more complex flow field and reduces, but does not delete, zones with unfavorable hemodynamic conditions.
- The VectorFlow CVC outperforms standard catheters due to the negligible recirculation.
- The pulse wave propagation model and the high flow CFD solver, developed in the ARCH-project, are experimentally validated and can be used for further clinical implementation.
- Experimental lab work needs experienced researchers.
- Pulse pressure analysis at the arterial needle can be used to detect stenoses in early stage.
- Standard pulsed wave Doppler ultrasound measurements cannot estimate reliable blood flow rates.
- Reversing connection lines is the best alternative for a dysfunctional double lumen CVC during standard (4 h) dialysis.
- Low-flow dialysis with double lumen CVC, or dialysis with single lumen CVC or single needle with an AVF, are considerable alternatives during extended (8 h) dialysis.

Contents

Samenvatting	v
Summary	xv
Contents	xxv
Introduction	xxxi
I Clinical background, devices and complications	1
1 Basic anatomy and physiology	3
1.1 Cardiovascular system	3
1.2 Kidney	5
1.3 Upper extremity	5
2 From a failing kidney to the need for a vascular access	9
2.1 Chronic Kidney Disease (CKD)	9
2.2 Renal Replacement Therapy (RRT)	10
2.3 Vascular Access (VA) for hemodialysis	13
3 Arterio-Venous Fistula (AVF)	17
3.1 General	17
3.2 Complications	18
3.3 Devices	25
4 Arterio-Venous Grafts (AVG)	27
4.1 General	27
4.2 Complications	29
4.3 Devices	29

5	Central Venous Catheter (CVC)	35
5.1	General	35
5.2	Complications	36
5.3	Devices	38
6	Comparison between vascular access options	43
6.1	Occurrence	43
6.2	Patency - Mortality	44
II	Engineering tools	47
7	Global approach (ARCH)	49
8	General fluid mechanics	51
8.1	Fluid characteristics	51
8.2	Fluid dynamics	55
8.3	Characteristics of fluid motion	61
9	Investigation methods	69
9.1	Experimental methods	69
9.2	Numerical methods	72
III	Studies on AVFs	79
10	Computational study of flow in AVF anastomoses	81
11	Experimental validation	93
11.1	Experimental validation of pulse wave propagation model . .	94
11.2	Experimental validation of high-flow CFD solver	113
12	Diagnostic tools	125
12.1	Pulse pressure analysis for stenosis detection	126
12.2	The accuracy of ultrasound volume flow measurements . . .	133
IV	Study on AVGs	149
13	Computational study of flow in helical AVGs	151

V	Studies on CVCs	167
14	Computational study of flow in a novel CVC	169
15	Computational study on malfunctioning CVCs	185
15.1	Reversing lines: <i>in vivo</i> and 1-compartment kinetic modeling	186
15.2	Single vs. double lumen CVC: 2-compartment kinetic modeling	195
15.3	Slow extended dialysis: 2-compartment kinetic modeling	209
VI	General conclusions	215
16	Conclusions	217
16.1	CFD analysis	217
16.2	Experimental assessment	219
16.3	Diagnostic tools	221
16.4	Kinetic modeling	222
	Bibliography	225
	Abbreviations and symbols	257
	List of figures	262
	List of tables	267

Introduction

Introduction

RATIONALE

This dissertation gathers the research performed over the last six years all relating to one of the three types of vascular access for hemodialysis: arterio-venous fistula (AVF), arterio-venous graft (AVG) and central venous catheter (CVC).

The rationale of this dissertation was to broaden the knowledge on (the design of) all three types of vascular access for hemodialysis, with the goal to optimize vascular access patency and, with it, hemodialysis efficiency.

To be more specific, we tried to answer following research questions:

- Creating a too small arterio-venous fistula anastomosis reduces the chance of proper fistula maturation. Should it not be preferable to create, in all cases, a large (cross-sectional area) anastomosis?
- The ultimate aim of the pulse wave propagation model coupled with results from the high flow computational fluid dynamics (CFD) solver, established in the ARCH-consortium, is to assist the surgical decision making in clinical practices. What can we learn from an *in vitro* validation?
- Can stenoses be detected by pulse pressure analysis and what are the advantages of this method?
- Can blood flow be adequately estimated based on standard pulsed wave Doppler ultrasound measurements?
- Does introducing a helical pattern in the design of an arterio-venous graft reduces unfavorable hemodynamics?
- What are the improvements of the VectorFlow catheter compared to standard designs?
- What are the alternatives for dysfunctional double lumen central venous catheters during standard (4 h) dialysis treatment?
- Which dialysis alternative(s) should be considered during extended (8 h) dialysis?

OVERVIEW

This manuscript consists of six main parts. Part 1 provides the reader with the necessary clinical background to understand the studies described in this work. Part 2 deals with some engineering-technical topics: a general description of fluid and fluid-mechanical principles and a discussion on the used experimental and computational methods.

Next, all experimental and computational studies are addressed, grouped by type of vascular access. Part 3, dealing with the arterio-venous fistula, starts with a computational study on the flow in AVF anastomoses, changing anastomosis size and angle. Next, two studies dealing with experimental (*in vitro*) validation of computer models are described. The final chapter of this part deals with two diagnostic tools: stenosis detection by pulse pressure analysis and flow rate estimation by pulsed wave Doppler ultrasound acquisition. In part 4, arterio-venous grafts with a helical design are studied. Part 5 gathers the studies on central venous catheters. First, the flow in a novel catheter design, with a symmetrical tip, is studied. And second, three studies, all based on the coupling of a kinetic model with a dialyzer model, highlight the differences in adequacy of different CVC dialysis treatments.

Finally, part 6 contains the general conclusions based on nine research statements.

PUBLICATIONS

(Joint) first author peer-reviewed papers

1. K. Van Canneyt, U. Morbiducci, S. Eloot, G. De Santis, P. Segers, P. Verdonck. *A Computational Exploration of Helical Arterio-Venous Graft Designs*. Revision submitted.
2. K. Van Canneyt¹, A. Swillens¹, L. Lovstakken, L. Antiga, P. Verdonck, P. Segers. *The accuracy of ultrasound volume flow measurements in the complex flow setting of a forearm vascular access*. Revision submitted.
3. L. Botti¹, K. Van Canneyt¹, R. Kaminsky, T. Claessens, R.N. Planken, P. Verdonck, A. Remuzzi, L. Antiga. *Validation of a high flow rate hemodynamics solver on a patient-specific model of vascular access for hemodialysis*. Submitted.
4. K. Van Canneyt, W. Van Biesen, R. Vanholder, P. Segers, P. Verdonck, S. Eloot. *Evaluation of alternatives for dysfunctional double lumen central venous catheters using a two compartmental mathematical model*

¹Both authors equally contributed.

- for different solutes. The International Journal of Artificial Organs. In press.
5. K. Van Canneyt¹, S. Eloot¹, R. Vanholder, P. Segers, P. Verdonck, W. Van Biesen. *Slow extended nocturnal home hemodialysis shows superior adequacy compared to in-center dialysis: a mathematical analysis*. Blood Purification. In press.
 6. W. Huberts¹, K. Van Canneyt¹, P. Segers, S. Eloot, J.H.M. Tordoir, P. Verdonck, F.N. Van de Vosse, E.M.H. Bosboom. *Experimental validation of a pulse wave propagation model for predicting hemodynamics after vascular access surgery*. Journal of Biomechanics. vol.45(9). 2012:1684-91.
 7. K. Van Canneyt, R.N. Planken, S. Eloot, P. Segers, P. Verdonck. *Experimental Study of a New Method for Early Detection of Vascular Access Stenoses: Pulse Pressure Analysis at Hemodialysis Needle*. Artificial Organs. vol.34. 2010:113-117.
 8. K. Van Canneyt, T. Pourchez, S. Eloot, C. Guillaume, A. Bonnet, P. Segers, P. Verdonck. *Hemodynamic impact of anastomosis size and angle in side-to-end arteriovenous fistulae: a computer analysis*. Journal of Vascular Access. vol.11. 2010:52-58.
 9. K. Van Canneyt¹, J. Kips¹, G. Mareels, E. Baert, D. Van Roost, P. Verdonck. *Experimental and numerical modelling of the ventriculosinus shunt (El-Shafei shunt)*. Proceedings of the Institution of Mechanical Engineers part h-Journal of Engineering in Medicine. vol.222. 2008:455-464.

Co-author peer reviewed papers.

1. T.W.I. Clark, K. Van Canneyt, P. Verdonck. *Computational flow dynamics and preclinical assessment of a novel hemodialysis catheter*. Seminars in Dialysis. 2012.
2. W. Van Biesen, J. Vanmassenhove, K. Van Canneyt, R. Vanholder, S. Eloot. *Influence of switching connection ports of double-lumen permanent tunnelled catheters on total solute removal during dialysis*. Journal of Nephrology. vol.24. 2011:338-344.
3. G. De Santis, M. De Beule, K. Van Canneyt, P. Segers, P. Verdonck, B. Verheghe. *Full-hexahedral structured meshing for image-based computational vascular modeling*. Medical Engineering & Physics. vol.33(10). 2011:1318-25.

4. F. Dewaele, A. Kalmar, K. Van Canneyt, H. Vereecke, A. Absalom, J. Caemaert, M. Struys, D. Van Roost. *Pressure monitoring during neuroendoscopy : new insights*. British Journal of Anaesthesia. vol.107. 2011:218-224.

Book chapters.

1. K. Van Canneyt, P. Verdonck. *Mechanics of biofluids in living body*. In: L. Zhou and A. Brahme (eds.) Comprehensive Biomedical Physics, Physical Medicine and Rehabilitation: Principles and Applications, Elsevier inc.. 2013.

Congress proceedings and abstracts

Over thirty congress proceedings and abstracts. A full list can be found on the Ghent University Bibliography Website²

²https://biblio.ugent.be/publication?f.type.term=conference&q._all.text=van+Canneyt+koen

One

Clinical background, devices
and complications

Basic anatomy and physiology

1.1 CARDIOVASCULAR SYSTEM

The cardiovascular system includes the heart and all blood vessels (Figure 1.1). The heart can be seen as a pulsatile pump, pumping the blood to the organs, tissues and cells and consisting of four chambers. The left part of the heart contains the oxygenated (arterial) blood, the right part the deoxygenated (venous) blood. The blood is collected from the systemic or pulmonary circulation in the atria and is pumped into the arteries by the ventricles. A schematic representation of the heart, with arrows indicating the blood flow path is shown in Figure 1.2.

The blood vessels can be split into five major types: arteries, arterioles, capillaries, venules and veins. The arteries can be seen as muscled vessels with a thick wall (≈ 1 mm) and with diameters from 2.5 cm (proximal aorta) to 1 cm (e.g. upper arm) or even to about 0.3 cm (e.g. lower arm). The mean arterial pressure is most often around 100 mmHg. The arterioles cover the vessels with a diameter ranging from 0.3 mm to 10 μm . The capillaries on the other hand are the

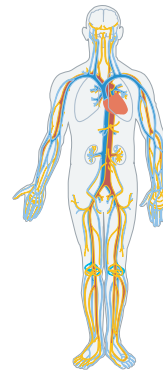


Figure 1.1: Cardiovascular system containing blood vessels and heart.

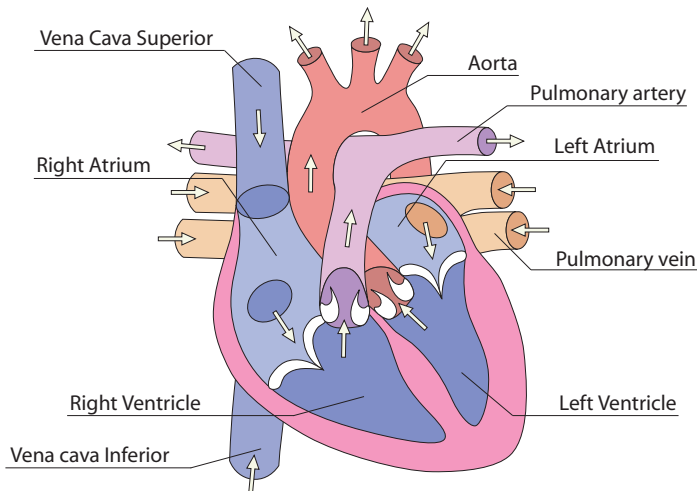


Figure 1.2: Schematic representation of the heart.

smallest vessels in the body. These have a diameter of around $8\text{--}10\text{ }\mu\text{m}$, the size of a red blood cell (Table 1.1). The capillaries can be seen as the driveways which provide direct access to nearly every cell in the body. Furthermore, they are ideally suited, because of their very thin wall ($0.5\text{ }\mu\text{m}$), for exchanging gases, nutrients, hormones, etc. from the blood to the interstitial fluid. Venules are the venous counterpart of the arterioles with a diameter between 8 and $100\text{ }\mu\text{m}$. When the venules join, they form veins. Veins are relatively thin walled (0.5 mm) with a transmural pressure around $5\text{--}10\text{ mmHg}$ and up to 65% of the total blood volume in the body [1].

Blood consists of mainly three different types of cells (see Table 1.1). It is generally well accepted that the red blood cells (RBC) are the only ones to be taken into account when explaining the macroscopic rheological properties of the blood. Nevertheless, in the capillary bed, white blood cells (leukocytes) and blood platelets (thrombocytes) may play an important role too.

Type of cell	Volume fraction	Dimension (μm)	Number/ mm^3
Erythrocytes (RBC)	0.45	8	4 to 6 (10^6)
Leukocytes	0.01	7 to 22	4 to 11 (10^3)
Platelets	0.01	2 to 4	2.5 to 5 (10^5)

Table 1.1: Parameters of cell types in blood.

A red blood cell can be considered as a bi-concave, very flexible disc, see Figure 1.3 (left). The RBC can be deformed to a high extent. This deformation occurs when the cell is exposed to a shear stress (definition in

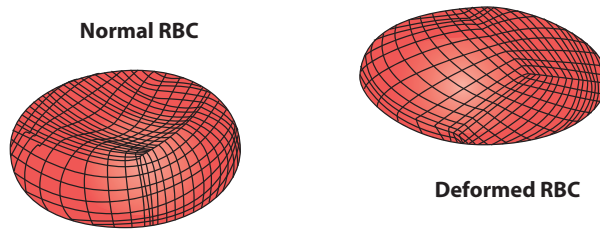


Figure 1.3: Deformation of red blood cells when exposed to an increasing shear force [2].

Chapter 8), as seen in Figure 1.3 (right). In the case of high shear stress with a low residence time or low shear stress with a high residence time, the rupturing of RBCs might take place. Which, in its turn, leads to the release of hemoglobin, also known as *hemolysis*.

1.2 KIDNEY

The two kidneys are located in the posterior part of the abdomen, below the peritoneum, on each side of the vertebral column. They account for about 22% of the total blood flow and are therefore, under physiological conditions, the organ with the highest blood supply [3]. Each adult kidney weighs about 150 g and has the size of a clenched fist.

The primary function of a kidney is removing toxic by-products of the metabolism and other molecules smaller than 69000Da^1 by filtration. They also regulate body fluid composition and volume, and control the electrolyte balance (K, Cl and Na). The kidneys also have an endocrine function. They produce hormones including renin and erythropoietin (EPO) and are thus contributing to the regulation of the blood pressure and the RBC production [4].

1.3 UPPER EXTREMITY

In the scope of this work on vascular accesses for hemodialysis, the vessels in the upper limbs (shoulder to arm) are the most important. An overview of the arterial and venous vessels involved in this research/clinical topic can be found in Figure 1.4 and Figure 1.5, respectively. At the heart side, the

¹One Dalton is defined as one twelfth of the rest mass of an unbound neutral atom of carbon-12 in its nuclear and electronic ground state ($1.66 \cdot 10^{-27}$ kg)

blood to the arm is delivered from the aorta to the subclavian artery over to the axillary artery. The arterial network in the arm can be simplified to the brachial artery in the upper arm and the radial (thumb side) and ulnar artery in the lower arm to the palmar arch in the hand. For the venous tract, the main vessels are the cephalic vein in both lower and upper arm and the median cubital, the basilic and axillary vein in the upper arm. The venous tract can be completed towards the heart by the subclavian, external jugular and internal jugular vein up to the superior vena cava.

It is estimated that under normal physiological conditions, around 2-3% of the total blood supply is distributed towards one arm. This is similar to the blood supply directly to the heart muscle, but is very low when comparing it to values for other direct branches of the aorta such as the brain or the kidneys with respectively around 14% and 22% of the blood supply [3].

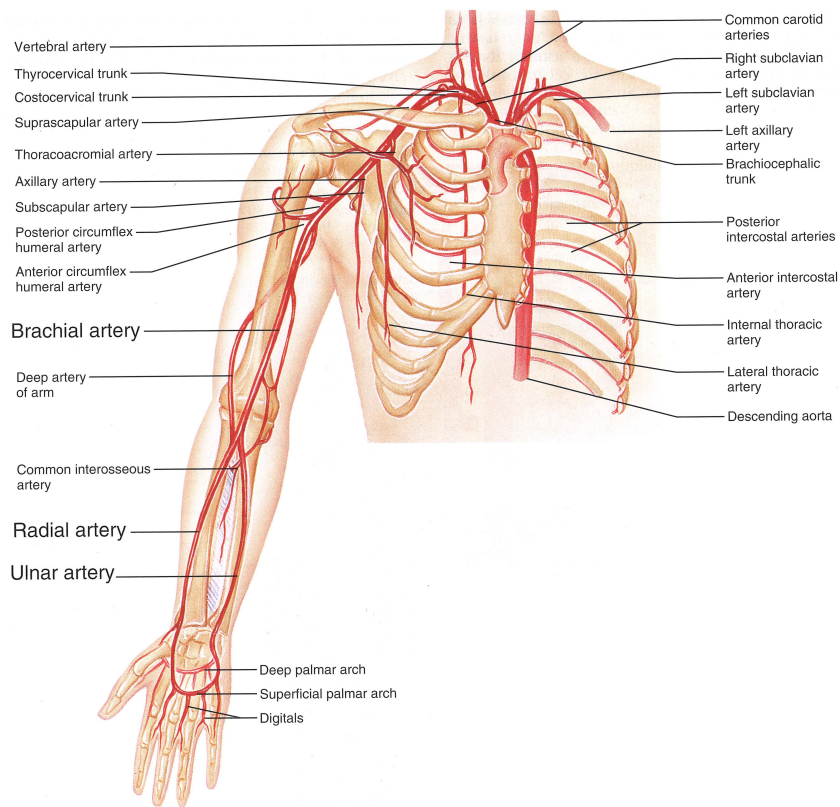


Figure 1.4: Arterial anatomy of the upper extremity [1].

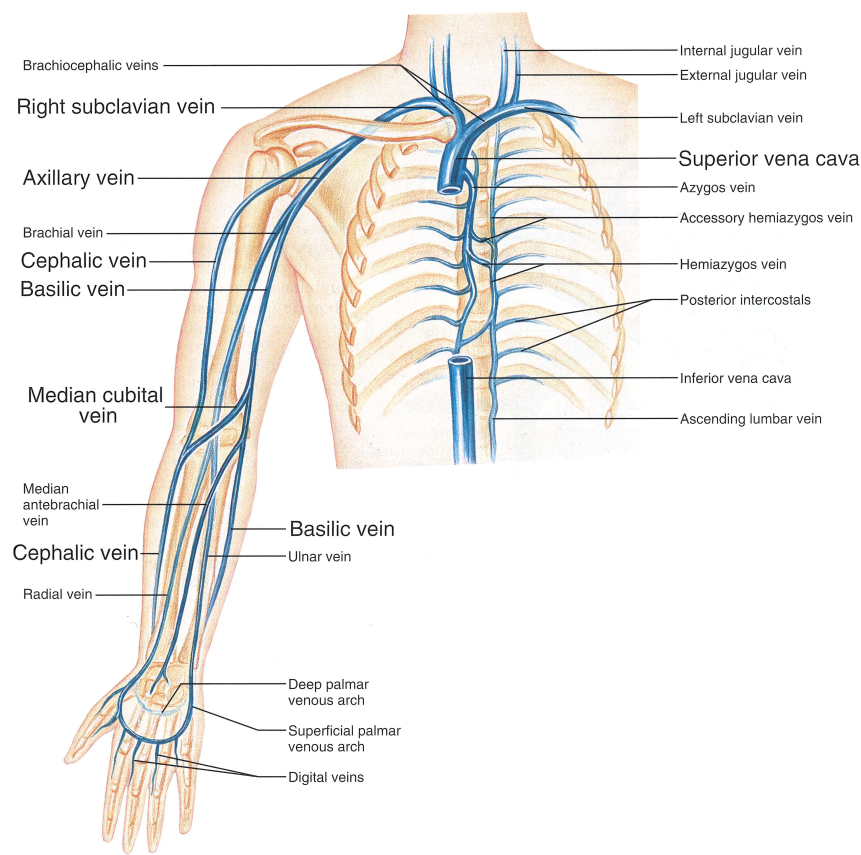


Figure 1.5: Venous anatomy of the upper extremity [1].

From a failing kidney to the need for a vascular access

2.1 CHRONIC KIDNEY DISEASE (CKD)

As stated by Levey et al., chronic kidney disease (CKD) is a world wide public health problem, with adverse outcomes of kidney failure, cardiovascular disease and premature death [5]. CKD can be classified into 5 stages from patients with damaged, but still normally functioning kidneys (CKD₁) up to patients with total kidney failure in the urgent need of a renal replacement therapy (CKD₅). The latter group, representing approximately 2% of all CDK patients [6], are often called end-stage renal disease (ESRD) patients [5, 7].

Severe loss of kidney function is a threat to life and requires removal of toxic waste products and restoration of both body fluid volume and composition. ESRD results from progressive chronic renal impairment (CKD₁₋₄) or unrecovered acute renal failure. Without renal replacement therapy (RRT), death from metabolic derangement follows rapidly.

The cost of ESRD patients for health care should not be underestimated. Approximately 6% of Medicare's (US) overall budget is required despite a prevalence of just 0.17% (year 2009) [8]. The incidence of patients with ESRD is expected to rise by 5-8% annually, with an average of 200 incidence patients per million population in Flanders and 122 in the Netherlands (January 2009) [9-12]. This rise in ESRD worldwide most probably reflects the

global epidemic of type 2 diabetes and the aging of the population in developed countries, so a higher incidence in elderly people [6]. At the end of 2009, 7 110 ESRD-patients were in Flanders on RRT (prevalence) [12]. The evolution of ESRD-patients on RRT in Flanders is visualized in Figure 2.1. It can be estimated that nowadays over 2 million patients worldwide are depending on RRT [10, 11].

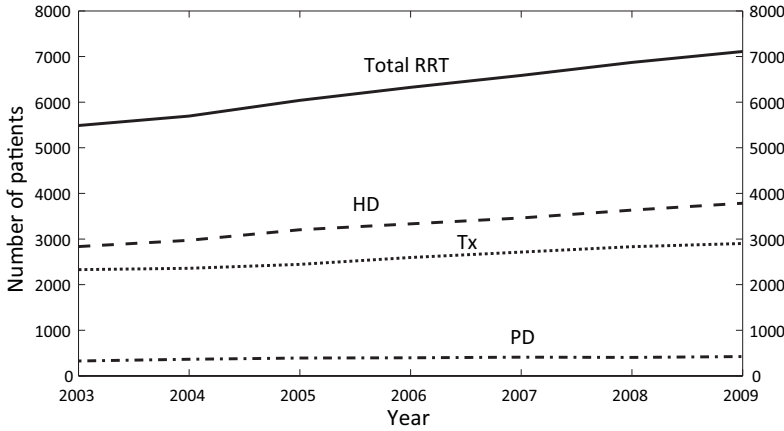


Figure 2.1: Prevalence of ESRD-patients in Flanders on a RRT (renal transplantation (Tx), peritoneal dialysis (PD) or hemodialysis (HD)), on the 31th of December. Note: Patients below the age of 20 were not reported in the ERA-EDTA Registry. (Data from ERA-EDTA annual reports 2004 to 2009, as referred in [12])

2.2 RENAL REPLACEMENT THERAPY (RRT)

Three commonly used techniques for renal replacement therapy are: renal transplantation (Tx), peritoneal dialysis (PD) and hemodialysis (HD). Tx can be seen as an acute RRT compared to the more chronic peritoneal dialysis and hemodialysis therapies.

2.2.1 Renal Transplantation (Tx)

The most optimal therapy for ESRD patients is receiving a transplant kidney from a deceased or living donor. Major complications are transplant rejection, infections and sepsis due to the immunosuppressant drugs that are required to decrease the risk of rejection. Donors sharing as many Human Leukocyte Antigens (HLA) as possible and, although non-ABO-compatible donation is possible, having the same ABO blood group with their recipient lead to an optimal transplant outcome. However, the biggest drawback for

transplantation is the fact that the number of donors cannot keep up with the number of transplant candidates.

The latest data (December 2010) of the Eurotransplant International Foundation¹ (EU) and of the National Institutes of Health (US) state, respectively, that there is a kidney waiting list of 10 800 and 50 000 active² patients [13, 14]. The European and United States organizations report 5 000 and 17 000 transplants each year and that 2 years after listing 53.4% and 51.3% of the patients are still waiting for a transplant. The evolution of the Eurotransplant active waiting list and transplant numbers are shown in Figure 2.2. In 2010, 3 705 patients received a kidney from a deceased donor and 1 262 received a kidney from a living donor (55% of them from a family related donor); for Belgium, these numbers are 404 and 49, respectively. The most recent numbers (2011) on kidney transplants from deceased donors show a 20% increase (up to 485) and a kidney waiting list of 837 patients for Belgium³.

In Figure 2.2, you can see clearly that the number of needed kidneys (patients on active waiting list) cannot be covered by the number of transplants. The graph shows that since 2000 the number waiting patients is decreasing and the number of kidney transplants (living and deceased donors) steadily

¹Including a selection of hospitals from Belgium, Germany, The Netherlands, Austria, Luxembourg, Slovenia and Croatia.

²Inactive candidates are considered to be temporarily unsuitable by their transplant center as transplant candidates (not transplantable).

³<http://www.eurotransplant.org/>

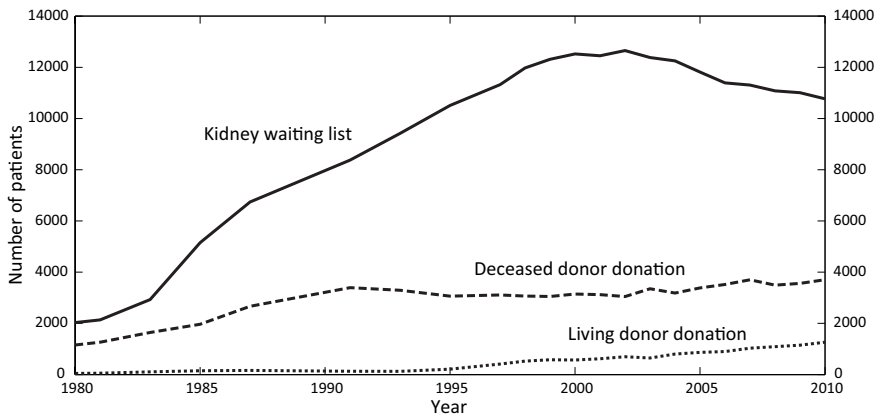


Figure 2.2: Patients on a kidney transplant waiting list compared to the number of kidney transplants from deceased and living donors as registered by Eurotransplant International Foundation from 1980 to 2010 [13].

increasing. Thus, the increase of the transplants is more than the increase of registrations on the waiting list. Note that one has to take into account that not all patients needing dialyzes are put on the waiting list and that this might have an influence on the decrease as well. The percentage of ESRD-patients in the different Eurotransplant countries not suitable for Tx is not known [personal communication].

Though transplantation is the best treatment, patients usually have to start with dialysis, due to a shortage of organs. Next to these patients on the waitinglist, a number of ESRD patients, not suitable for transplantation, are treated chronically with dialysis.

2.2.2 Peritoneal Dialysis (PD)

In peritoneal dialysis, a catheter is placed in the patient's abdomen through the skin. A bag of water-based electrolyte solution (containing i.a. sodium and glucose) is connected to the peritoneal catheter and drained into the peritoneal cavity by gravity. The process uses the patient's peritoneum in the abdomen as a membrane to exchange fluids and dissolved substances (electrolytes, urea and other small molecules) with the blood. When the dialysis is finished (4-6 hours), the fluid is drained back into a bag, which is then disconnected and discarded (Figure 2.3). This technique, which uses only gravity, is called continuous ambulatory peritoneal dialysis (CAPD). Around four fluid exchanges are used every day. Another method is called automatic PD (APD). Here, a machine refreshes fluid from the peritoneal cavity automatically for an 8-12 hours period. Patients use this system (APD) every night to avoid changing bags during the day (CAPD). APD has been considered to have several advantages over CAPD such as reduced incidence of peritonitis and mechanical complications [15]. However, the solute removal for CAPD seems larger than for APD [16].

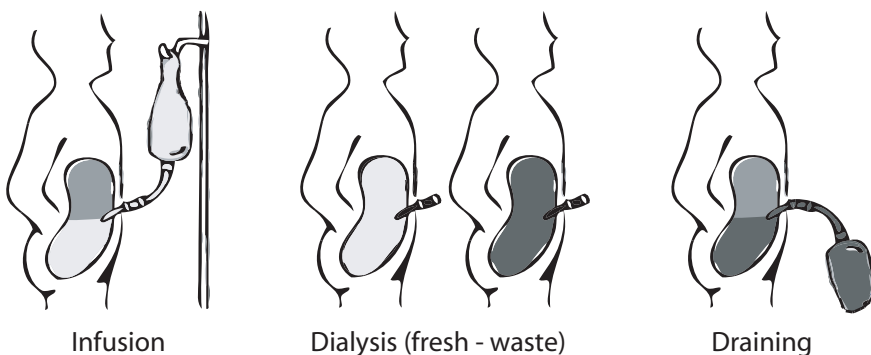


Figure 2.3: Schematic representation of peritoneal dialysis treatment.

In 2004, 11% of dialysis patients worldwide were receiving PD [10]. In Europe, in 2009, 6% of RRT patients had PD. The number of PD patients on APD was reported as 63% [12].

2.2.3 Hemodialysis (HD)

A third option as RRT is hemodialysis. In this chronic therapy, blood is taken from the patient using a vascular access (VA) and is sent through an extracorporeal circuit where waste products (e.g. urea) and water are removed from the blood in a hemodialyzer (artificial kidney). The purified blood flows on towards the VA of the patient. More details can be found in Figure 2.4. The hemodialyzer succeeds in purifying the blood and extracting the excess water due to basic transport phenomena, such as diffusion, ultra-filtration, and osmosis. For that reason the hemodialyzer can substitute most of the (failed) kidneys' function, but administering EPO to the patients on dialysis is needed. A general hemodialysis treatment takes about 9-15 hours a week, mostly spread over three (half day) sessions. An alternative is having several night sessions (e.g. 3 times 8 hours) a week. It can take place in a hospital, a low care unit or at home. Nowadays, thousands of people with irreversible renal failure are being treated for 15 to 20 years by hemodialysis.

Despite the widespread use of peritoneal dialysis, hemodialysis remains the main renal replacement therapy in most countries [10]. In western countries over 90% of all patients on a chronic RRT are depending on HD [12, 17]. At the end of 2009, 3 784 patients were receiving HD in Flanders (Figure 2.1) [12]. In Europe, it is estimated that, nowadays, more than half-a-million patients with end-stage renal disease are treated with hemodialysis [9–12].

Since dialysis cannot completely maintain the normal body fluid composition and cannot replace all the functions performed by the kidneys, the health of HD patients usually remains significantly impaired. Despite significant advances in the understanding of the biology of chronic kidney disease and the risk factors for poor outcome on HD, and improved dialysis technology, the annual mortality in HD patients remains as high as 15% to 25% worldwide [18].

2.3 VASCULAR ACCESS (VA) FOR HEMODIALYSIS

If hemodialysis is the chosen RRT, the most essential ingredient for long-term success is a reliable vascular access that can achieve a blood flow in excess of 600 ml/min [19]. Vascular access remains the lifeline for ESRD patients treated by chronic HD, and a major source of ESRD morbidity, mortality and hospitalization, with annual costs in the United States in excess of

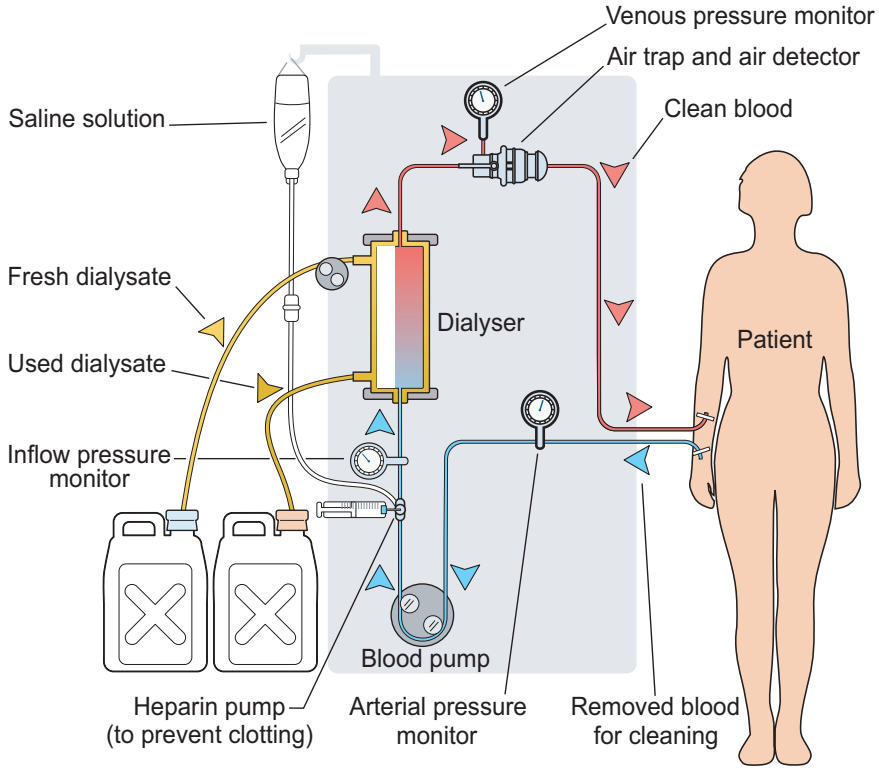


Figure 2.4: Schematic overview of hemodialysis treatment.

1.5 billion US dollar in 2007 [20]. VA procedures and complications account for over 20% of hospitalizations of dialysis patients [21].

The challenge to achieve successful vascular access grows as the dialysis population has an increasing proportion of diabetic, elderly and hypertensive patients, many with serious cardiovascular comorbidities. For example, in 2009, 44.5% of the patients on HD in the US were diabetic, 44.6% were older than 65 years and 28.8% were hypertensive [17].

According to the EBP⁴ (European) [22] and NKF-K/DOQI⁵ (American) [19] guidelines for vascular access, an adequate pre-operative assessment of the patient is essential, including patient history and physical examination, clinical evaluation by means of duplex ultrasonography of the upper-extremity arteries and veins, and central vein evaluation. Next to the importance of surgical planning, the timing of the referral of potential chronic HD patients to the nephrologist and/or surgeon is crucial. The optimal referral

⁴European Best Practice Guidelines

⁵National Kidney Foundation - Kidney Disease Outcomes Quality Initiative

timing for preparing a vascular access is when patients reach stage 4 of their CKD (CKD4) [19, 22].

As stated by Kjellstrand, as early as 1978, the vascular access remains the 'Achilles' heel' of chronic hemodialysis therapy [23, 24].

The three main options in vascular access for HD are the arterio-venous fistula (AVF), the arterio-venous graft (AVG) and the central venous catheter (CVC).

Arterio-Venous Fistula (AVF)

3.1 GENERAL

An Arterio-Venous Fistula (AVF) is an autologous direct connection, created by a surgeon, between an artery and a vein. This anastomosis connects the high pressure arterial circuit to the low pressure venous circuit. The normal high resistance pathway, the capillary bed, is bypassed. The increased flow and pressure in the venous segment initiates the maturation process. Both vessel remodeling (i.e. dilation) and flow increase are essential in order to use the fistula as vascular access. The dilation of the vein is needed to be cannulated by large needles (eg. 15G. needles). The flow increase is needed to perform an efficient hemodialysis treatment [19, 21, 25, 26]. Generally defined, a fistula is mature when it can be routinely cannulated by two needles and can deliver a minimum blood flow (typically 350-450 ml/min) for the total duration of dialysis, usually 3-5 h for high efficiency hemodialysis [27].

The first AVF reported in literature was one in 1966 created surgical side-to-side radial artery to cephalic vein fistula by surgeon Dr. Kenneth Appell of the team of Dr. James E. Cimino and Dr. Michael Brescia [28, 29] (Figure 3.1). This fistula is called the Cimino or Cimino-Brescia fistula and is still the basis of the currently created AVFs.

It should be possible to cannulate an AVF *reproducibly*. The access should deliver a *high* enough access *blood flow* (≥ 600 ml/min) to deliver an adequate dialysis dose [30, 31]. A preoperative ultrasound screening to determine adequate arteries and veins to create an AVF and postoperative flow

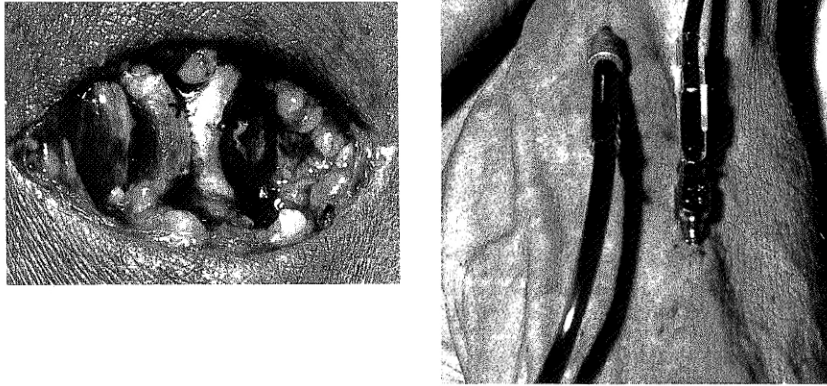


Figure 3.1: Cimino-Brescia shunt as described in the original paper (left: surgical connection; right: double needle puncturing) [28].

measurements to monitor maturation are a standard procedure [32, 33] and is advised by both the EBPg and NKF-K/DOQI guidelines [19, 22].

Most common locations to create an AVF are the lower and upper (non-dominant) arm, with the preference of choosing the position as distal as possible. This to preserve more proximal locations for future interventions. Although there exists a large number of variations in AVFs in the arm, three of the most common locations are shown in Figure 3.2.

An AVF can be seen as a 7 segment circuit, as schematically illustrated in Figure 3.3, consisting of the proximal artery (1), the distal artery (2), arterial collaterals (3), the proximal vein (4), the distal vein (5) and venous collaterals (6), added with the anastomosis itself (7).

3.2 COMPLICATIONS

The main complications leading to AVF failure are thrombosis (44%) and the overall failure to mature (23-46%) [36, 37]. An overview of the complications and their required treatment are listed below.

3.2.1 Infection

Wound complications, as infection, tend to occur early following the access creation. When not treated properly and effectively, it can lead to VA failure [38]. The infection of autologous fistulas (AVFs) is rare compared to the prosthetic grafts (AVGs, Chapter 4) [39].

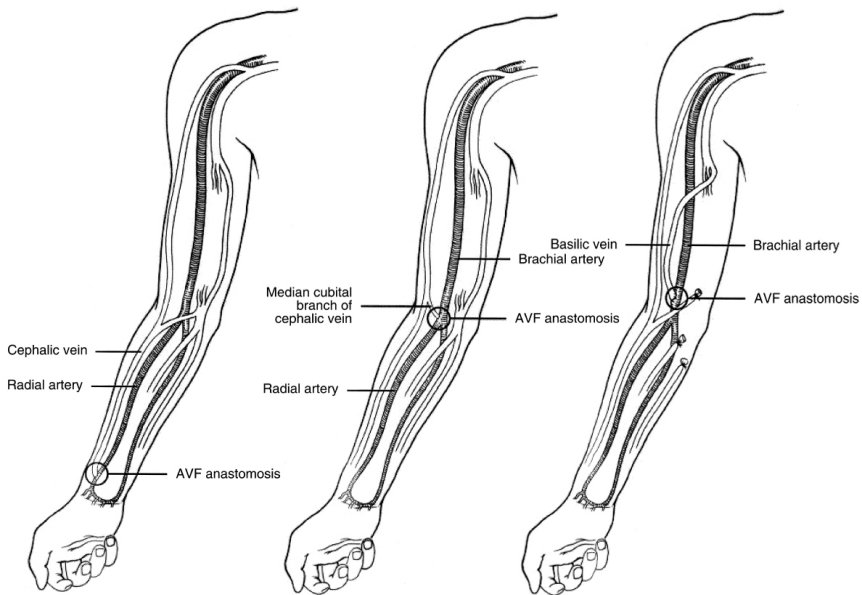


Figure 3.2: Three different AVF configurations: Radio-cephalic; Brachio-cephalic and Brachio-Basilic transposition [21].

3.2.2 Non-maturation

After the creation of an AVF, changes in hemodynamics and on anatomic, molecular and functional level occur. The most important factor in fistula maturation is the response of the feeding artery and the draining vein to the increase in shear stress (definition in Chapter 8) that occurs following the AVF creation [40]. At a physiological level, this increase generally results in a dilation of the vessel with a reduction of neo-intimal hyperplasia (beneficial remodeling) [41]. This shear-stress-mediated dilation decreases the level of peak shear stress back to the preoperative situation [42], while the mean shear stress increases significantly. Next to the shear stress, the vessel wall responds to the increased transmural pressure by vessel wall thickening. So this medial hypertrophy (growth of the media layer of the vessel) is a necessary step in the maturation process in contrast with the neo-intimal hyperplasia (growth of the intima layer of the vessel, stenosis formation) due to shear stress unfavorable conditions which hamper the maturation. Non-maturation can therefore occur due to different reasons:

1. An insufficient increase in flow directly postoperative: It is shown that AVFs with an initial, directly postoperative blood flow rate below 400 ml/min fail to mature in the majority of cases [26]. This in-

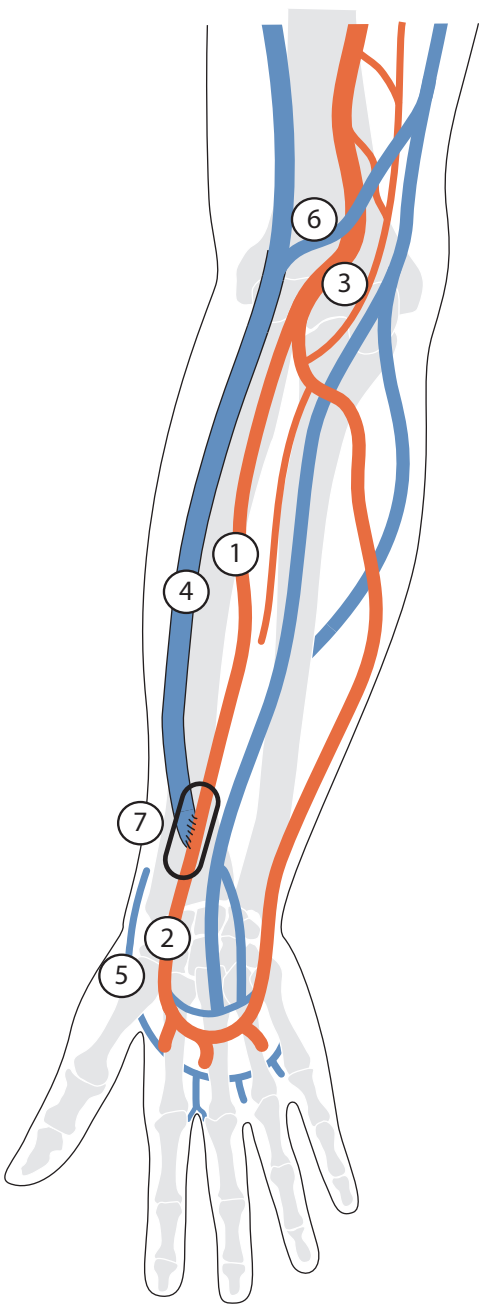


Figure 3.3: Seven segment AVF circuit: Proximal artery (1); distal artery (2); arterial collaterals (3); proximal vein (4); distal vein (5); venous collaterals (6) and arterio-venous anastomosis (7) [34, 35].

sufficient increase in flow can be due to a blockage of the arterial inflow path or the venous outflow path by a stenosis (see Section 3.2.4) or might even be linked to the skills of the surgeon (vessel handling, kinking, torsion, endothelial injuring) [41]. This can even lead to an early thrombosis (total blockage of the flow path). The increase in blood flow can also be hampered by an inadequate construction of the anastomosis itself (e.g. a too small anastomosis opening). To overcome these problems, percutaneous intervention is indicated for any stenosis and surgical intervention can be performed if necessary [22, 39].

2. A failure of arterial and venous dilation: The ‘quality’ of the vessels can be dominant, where non-compliant arteries and veins (preop) will probably lead to non-dilation after AVF creation. Increasing age (calcification of vessels), female gender, diabetics and presence of peripheral or coronary diseases are predictive to the non-maturation [41]. Also multiple venous puncturing before AVF creation can decrease the chances for non-maturation.

As shown in Figure 3.4, the fistula maturation is the most difficult hurdle to overcome when a fistula, ready to cannulate, is required. Radiological or surgical interventions to correct the underlying lesion, have been reported to convert an immature fistula to one that is usable for dialysis in 44 to 97% of cases [30].

3.2.3 Ischemia or hypoperfusion syndrome

When constructing an AVE, a ‘preferential’ flow path of low resistance is created. This can lead to a decrease in blood flow to the distal parts of the arm (towards the hand), which is called steal syndrome. For the majority of radio-cephalic fistula (lower arm), there is a 40% decrease in blood pressure in the thumb and in 70% of the cases the flow in the radial artery is retrograde [38]. Although ‘steal’ appears in a large number of cases, it does not always lead to complications as hypoperfusion or ischemia. Hypoperfusion is a general lack of oxygen supply, ischemia is the full obstruction of oxygen, thus blood, supply and can even result in finger gangrene (necrosis of the tissue). In Figure 3.5, you see an example of a hand suffering from ischemia (top-right), the same patient’s hand after the ligation of the fistula (bottom-right) and a CT-reconstruction of the patient’s vessel bed (left).

Upper arm AVFs are more likely to develop critical ischemia symptoms (10-25%) than lower arm fistulas (1-1.8%) [44]. Other risk factors are increasing age and diabetes [45]. Causes of ‘steal’ and ischemia are often a stenosis in the distal artery (see section 3.2.4) or a too low pressure drop over the

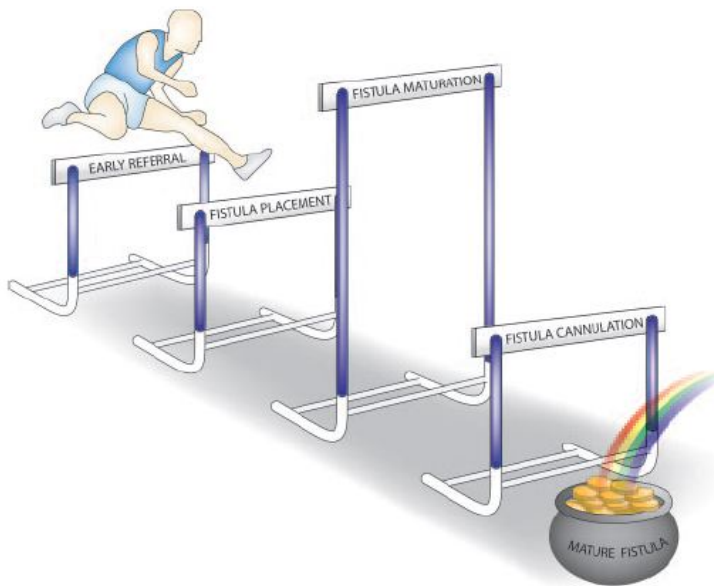


Figure 3.4: The 'fistula hurdle'. Several hurdles must be overcome successfully to ensure that a patient initiates dialysis with a mature fistula. These include early referral of patients with chronic kidney disease to a nephrologist, fistula placement well before reaching ESRD, adequate fistula maturation, and successful cannulation of the fistula by the dialysis staff [30]

anastomosis, resulting in a huge fistula flow. When a too large anastomosis is created, to avoid non-maturation due to low flow for example, the flow in an upper arm AVF can be up to 1 or 2 l/min.

There are multiple options to decrease this high flow condition: Distal Revascularization-Interval Ligation (DRIL) [46–48], Proximalization of the Arterial Inflow (PAI) [49], Revision Using Distal Inflow (RUDI) [50] all to create a longer flow pathway, narrowing of the initial draining vein at the anastomosis side (banding) [51–53], and even creating an artificial stenosis in the draining vein [54].

All these solutions aim to increase the AVF flow resistance. This increase reduces the access flow and/or increases the pressure in the distal arteries. More care for the patient's personal preoperative vasculature and taking more care to the anastomosis size during VA creation would, in my personal opinion, lead to fewer of these problems [34].

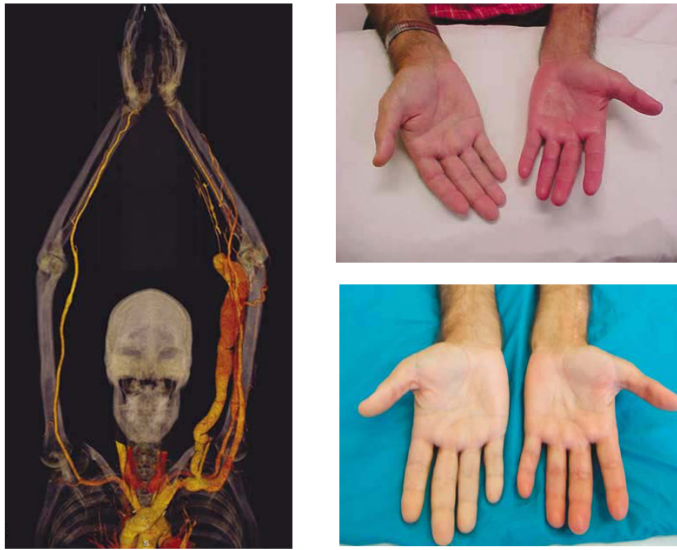


Figure 3.5: Left: Computed Tomography (CT) angiogram 3-D reconstructions revealing grossly dilated AVF, minimal arterial supply to the left hand, and venous dilation along the left brachial plexus; Top-right: Left hand ischemia; Bottom-right: Return of muscle mass, 3 months after ligation of the high-flow fistula [43].

3.2.4 Stenosis formation and thrombosis

As mentioned in the section on non-maturation, neo-intimal hyperplasia or growth of the intimal layer of the vessel is mostly due to a decrease in shear stress. In addition to the absolute magnitude of the shear stress, the specific pattern over time plays an important role as well. An oscillatory shear stress often results in a pro-inflammatory state with an increase in cellular proliferation [41, 55, 56]. Methods to quantify this will be discussed in Section 8.3.4.

The EBPG and NKF-K/DOQI guidelines define a stenosis if the growth of the vessel wall to the inside lumen is more than 50% of the vessel diameter (75% of the vessel area) [19, 22]. Next to these hemodynamic factors, surgical injury, the cannulation with dialysis needles, surgical stress and angioplasty initiate neo-intimal hyperplasia formation, might result in stenosis formation (Figure 3.6) [41].

The most common locations for stenosis formation in AVFs are shown in Figure 3.7. Obstruction of the vessel by a stenosis can be treated by Percutaneous Transluminal Angioplasty (PTA, balloon dilation), stent placement or by a surgical procedure.

3. ARTERIO-VENOUS FISTULA (AVF)

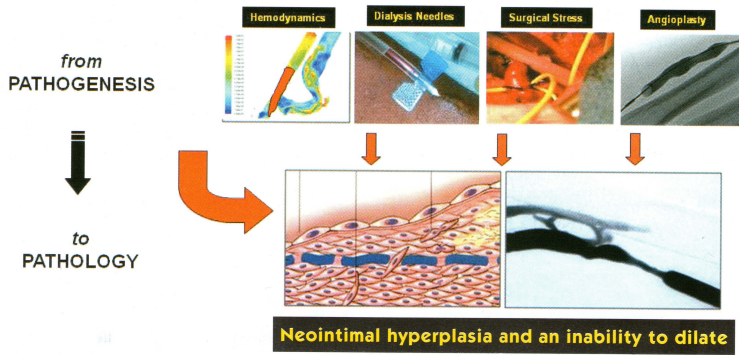


Figure 3.6: Stenosis formation: from pathogenesis to pathology (adapted from [41]).

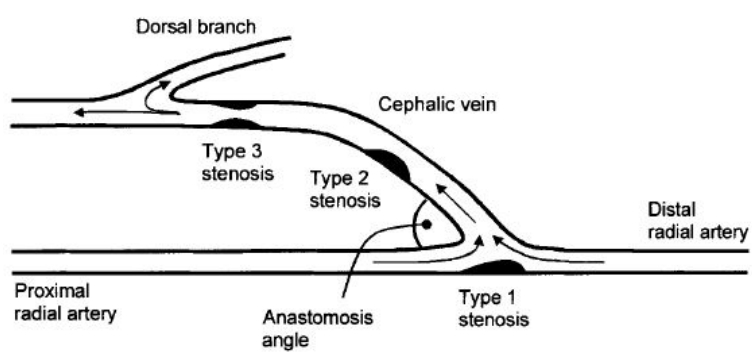


Figure 3.7: Stenosis locations [57].

3.2.5 Venous hypertension

When the major pressure drop is not over the anastomosis but over a proximal venous stenosis, venous hypertension may occur. The entire limb can get swollen or a large aneurysm may develop.

3.2.6 Cardiac failure

Cardiac failure is a condition in the structure or function of the heart that impairs its ability to supply sufficient blood flow to meet the body's needs. Although not a short term complication, heart failure is the most common cause of death in the dialysis population, being responsible for 45% of all fatalities.

High-output cardiac failure is a rare complication, which occurs in patients with a high-flow fistula. It has been estimated that cardiac failure occurs when 20-50% of the cardiac output flows through the anastomosis [38]. Treatment usually involves sacrificing the fistula, although banding might be an option [39].

3.3 DEVICES

In the field of autologous fistula creation, new product design seems a 'contradictio in terminis', however, one company found a device in the field of arterio-venous fistulas. The Optiflow was created by Bioconnect Systems, inc. (Ambler, PA, USA) and is shown in Figure 3.8. The device replaces the hand-sewn suturing for AVF creation. It is stated that the device introduces a 'laminar' flow path to 'optimize' hemodynamics and provides a mechanical scaffold to avoid peri-anastomotic stenoses. After pre-clinical test on porcine AVFs, a preliminary clinical study on 54 patients in four countries was performed. The outcome of the study showed a 82% unassisted primary patency¹ after 90 days, which is favorable when compared to published unassisted primary patency rates of 70% [37, 58]. The device is still under investigation and not yet for sale.

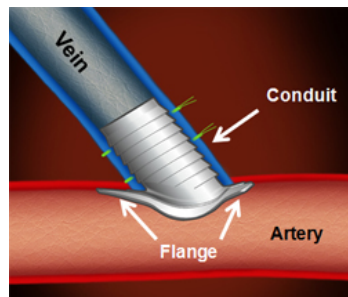


Figure 3.8: Optiflow by Bioconnect Systems, inc. (Ambler, PA, USA)

¹definition in Section 6.2

Arterio-Venous Grafts (AVG)

4.1 GENERAL

One of the first vascular access creation techniques was the Scribner-Quinton shunt in the 1960s [59]. This is a technique where one connected an artery to a vein, in the lower arm, by means of an external Teflon tube (Fig. 4.1). This first Arterio-Venous Graft (AVG) as vascular access opened the era of chronic hemodialysis treatment. The most common problems associated with this VA were clotting, systemic infections, necrosis at the Teflon tubing exit sites, dislodgement of the shunt resulting in severe blood loss and, last but not least, severe patient anxiety [29].

In the 1970s, after the introduction of the Cimino-Brescia AVF, the synthetic graft of PTFE (polytetrafluoroethylene) (Gore-Tex, W.L. Gore & Associates, Elkton, MD, USA), became popular, especially in the US. Popularity was growing fast because these AVGs were easier and faster to place and did not suffer from non-maturation complications as AVFs do.

Nowadays, an AVG is placed fully beneath the skin in loop configuration (Figure 4.2) and consists mostly out of expanded PTFE (ePTFE). The most common designs are the straight and the tapered version. However, no clinical or computational results were found showing a difference in performance or patency of the tapered versus the straight version [60, 61].

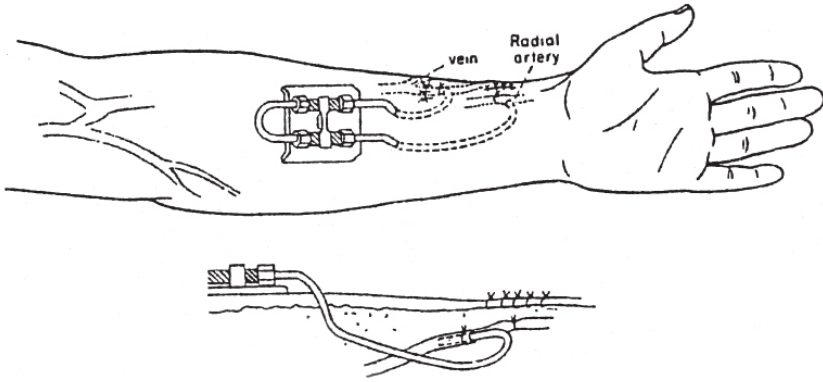


Figure 4.1: Scribner-Quinton (external) shunt [29].

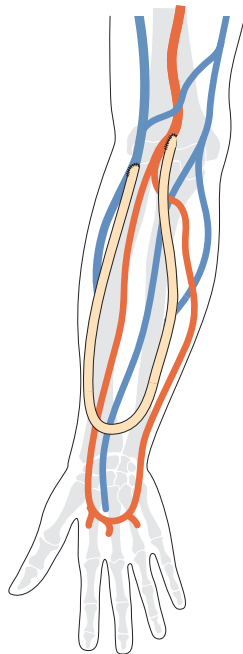


Figure 4.2: Brachial artery to cephalic vein loop graft (adapted from [35]).

4.2 COMPLICATIONS

AVGs suffer more from stenosis formation, clotting and infections compared to AVFs.

Although infections are more common in AVGs than in AVFs, it is the appearance of a thrombosis that accounts for approximately 70-80% of graft failures [30, 36]. Thrombosed grafts usually find their origin in an underlying stenosis, most often at the venous anastomosis or in the draining vein [30]. As for AVFs (Section 23), stenoses are most likely to occur on locations with low shear stress, or disturbed flow and shear patterns (oscillatory shear for example). Stenoses at the arterial anastomosis or in the graft itself, caused by chronic fibrin and cellular deposits, are more rare [62].

A lot of graft surveillance programs are ongoing in the dialysis centers, ranging from stenosis detection by physical examination (palpation) to documentation of the (increasing) intra-access pressure or the (decreasing) flow rate. Although the number of angioplasty interventions increased when introducing a surveillance program, the overall thrombosis-free survival did not differ [30]. One of the explanations might be that a stenosis after angioplasty develops faster (re-stenosis) compared to a *de novo* access stenosis. This is due to the vascular injury due to the angioplasty itself [63]. Even with stents, it is needed to repeat the interventions to prevent the re-occlusion of the access [64]. It seems that a pharmacological approach might prevent neointimal hyperplasia more effectively [30].

4.3 DEVICES

In the field of arterio-venous graft, in contrast to the autologous fistula, a lot more new technology is applied. The new devices on the market can be split in two groups: those related to the material of the graft and those related to the geometry of the graft or the anastomoses.

4.3.1 New materials

Firstly, a large number of companies are producing new materials based on PTFE, for example:

- Carbon-impregnated grafts by C.R. Bard, Inc. (Murray Hill, NJ, USA) for reduced platelet deposition and thrombosis formation.
- Centerflex design by C.R. Bard, Inc. to reduce kinking.
- Gel-impregnated vascular grafts by Atrium Europe B.V. (Manchester, UK) to lower the porosity making it more blood tight.

- Film lamination process by Atrium Europe B.V. to reduce kinking and compression resistance for improved surgical handling and minimal needle hole bleeding.
- No-profile radial support by Gore-Tex (W.L. Gore & Associates, Elkton, MD, USA) to reduce kinking.

Secondly, more ‘exotic’ new material designs (compared to the historically used silk, vinyon, Dacron, and later PTFE and expanded PTFE (ePTFE)) are investigated and produced [8], for example:

- Treated xenogeneic or allogenic conduits (e.g. artery from a pig).
- Cell-seeded biodegradable scaffolds [65].
- Tissue-based grafts grown *in vivo* using the recipient’s body as an autologous bioreactor (not (yet) in humans) [66].
- ‘Self-assembly approach’, where completely biological grafts are grown *in vitro* without the aid of any exogenous biomaterials or scaffolds, for example the LifeLine Vascular Graft (Cytograft Tissue Engineering, inc, Novato, CA, USA).

4.3.2 New geometry concepts

The devices, working on the geometry of the grafts or the anastomoses, all aim to create more favorable hemodynamics and thus reducing the intimal hyperplasia growth and inhibiting stenosis formation and thrombosis occurrence. Five designs are described hereafter in detail:

Hooded or cuffed graft

The Venafllo graft by C.R. Bard, Inc. (Figure 4.3) and the Flixene Trumpet vascular graft by Atrium Europe B.V. (Figure 4.4) are based on the same principle. The local hemodynamics at the venous anastomosis are changed to avoid regions with unfavorable wall shear stress patterns. This is examined earlier in a CFD study [67]. It is shown clinically that the patency rates increase [68] and the stenosis formation (intimal hyperplasia) is reduced [69].

Helical design

The SwirlGraft was created by Veryan Medical (Horsham, West Sussex, UK) and is based on the so called Small Amplitude Helical Technology (SMAHT). The graft was based on a ‘Helical grafts’ patent by Caro et al. [70] and is shown in Figure 4.5. It was expected that the helical design would lead to a swirling flow and in-plane mixing. As a result of this, a relative uniform wall shear stress was expected with inhibition of flow stagnation, separation and instabilities at the venous anastomosis to reduce stenosis formation.

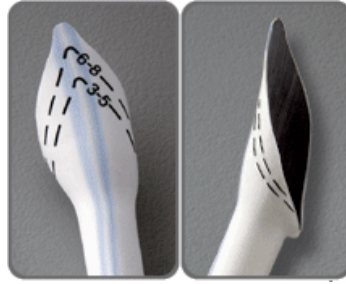


Figure 4.3: Venaflo graft by C.R. Bard, Inc. (Murray Hill, NJ, USA)



Figure 4.4: Flixene Trumpet Vascular Graft by Atrium Europe B.V. (Manchester, UK)

The groups of Caro and Sherwin previously studied to a great extent the influence of ‘out-of-plane’ geometries on the flow field [71, 72] and are since 2011 working on a helical stent design (BioMimics 3D Stent by Veryan Medical) [73].

The early idea on SMAHT was studied in a preliminary work introducing arterio-venous helical designed grafts in loop configuration in pigs. They showed a reduction in intimal hyperplasia occurrence [74]. Despite the addition of a small CFD and flow visualization (ink) analysis, no analysis of the flow in the anastomotic region was studied yet [75].

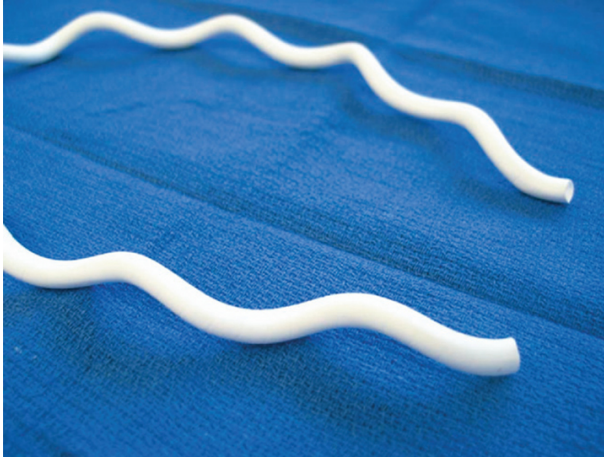


Figure 4.5: SwirlGraft by Veryan Medical (Horsham, West Sussex, UK)

A preliminary clinical trial on 20 patients showed a comparable primary patency¹ with numbers from literature and an improved secondary patency [76]. In some cases, the graft however was stretched under the skin and the helical geometry was reduced. Therefore these grafts were working as a conventional graft.

Finally, Glickman [77] reported in 2009 that a prospective randomized study of 180 patients had been conducted in the US. At that point a mean follow up of 6 months was conducted comparing the SwirlGraft with a standard ePTFE graft. An improved primary and secondary patency was found (Figure 4.6), but to this day, no full data report was published.

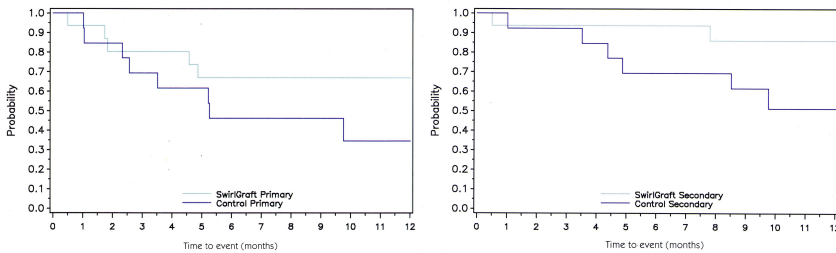


Figure 4.6: Primary (left) and secondary (right) patency of SwirlGraft compared to standard ePTFE graft after 6 months follow up in 180 patients [77].

¹definition in Section 6.2

Spiral flow

Tayside Flow Spiral by Tayside Flow Technologies Ltd (Dundee, UK) is based on the concept of Spiral Laminar Flow (SLF). In this design, the manufacturer claims that a ‘laminar’ flow is created at the venous anastomosis graft section and that ‘turbulent’ flow patterns are inhibited. They claim that these flow patterns trigger flow mediated signals that lead to vascular remodeling, such as intimal hyperplasia formation. Although their definition of ‘laminar’ and ‘turbulent’ is not in line with the general fluid dynamics definition (see Section 8.3.1), the concept of delivering an ‘undisturbed’ flow pattern to the venous anastomosis can be understood from their claim. The Tayside Flow Spiral wants to restore the ‘natural’ swirling flow (Figure 4.7) as remedy to stenosis formation. The design is in a way similar to the helical graft of Veryan Medical. To date, no clinical studies comparing the outcome of the Tayside graft have been reported, nor any technical nor scientific papers were published.

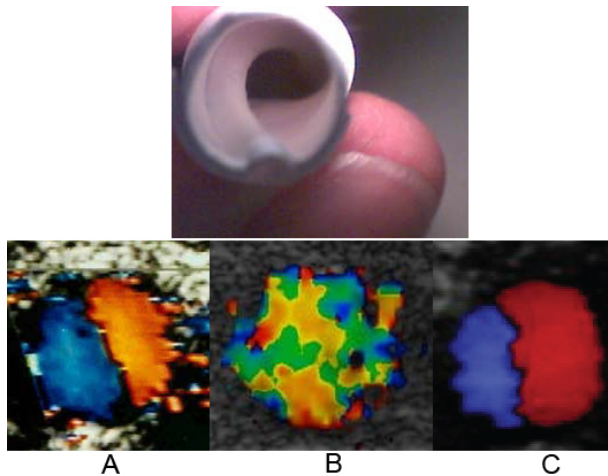


Figure 4.7: Tayside Flow Spiral by Tayside Flow Technologies Ltd (Dundee, UK): (A) Natural blood flow within a healthy artery; (B) Turbulent blood flow from a non SLF graft; (C) Blood flow from a SLF graft

Tapered arterial design

This is a graft design reported by Krueger et al [78]. This idea was proposed not to reduce the stenosis formation at the venous anastomosis, as in the previous examples, but to reduce the stenosis formation at the arterial anastomosis. The latter being comparable to the stenosis at the AV-fistula anastomosis, shown in Figure 3.7. The *in vitro* design is shown in Figure 4.8 and

they found that when applying a narrowed section at the graft entrance, the oscillating vortex at the arterial lumen wall disappeared, potentially reducing stenosis formation at the arterial anastomosis.

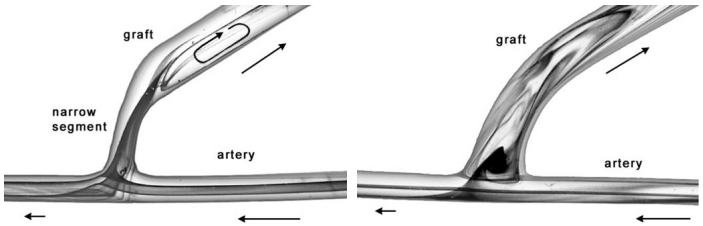


Figure 4.8: Flow visualization in a tapered graft inlet (left) versus a conventional graft inlet [78].

Complete venous anastomosis design

Flixene IFG by Atrium Europe B.V. is a graft in which the venous anastomosis and part of the proximal and distal vein are included. Therefore, a PTFE T-shape section, with stent support, is added at the venous end of the graft (see Figure 4.9). This compression resistant nitinol reinforced distal outflow section provides a faster implantation technique and smooth flow transition into the vein. No clinical or scientific study has (yet) been published on this concept.

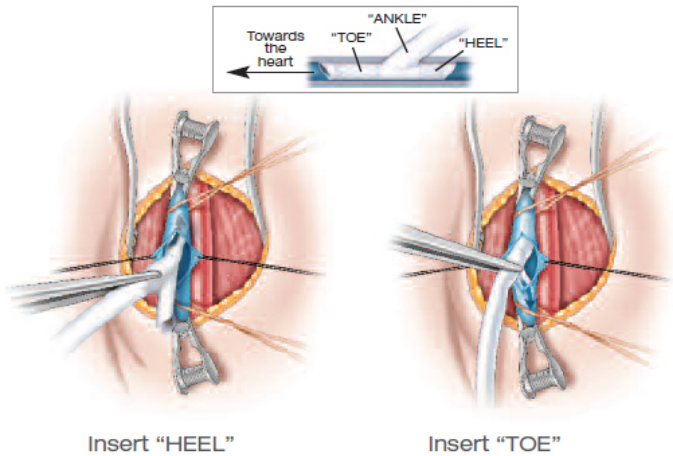


Figure 4.9: Flixene IFG by Atrium Europe B.V. (Manchester, UK)

Central Venous Catheter (CVC)

5.1 GENERAL

A Central Venous Catheter (CVC) is a tube with one or two lumens, to be inserted in a central vein leading directly to the right atrium. This VA option should only be applied when a temporary vascular access is needed ('acute'), for example during AVF maturation, or if no AVF nor AVG can be created in the patient ('chronic'). A short-term CVC is intended to be placed only for a short period and are easy to place, stiff and placed directly over a guidewire into the central vein. A long-term or permanent CVC however is softer and is placed by means of 'tunneling'. This to provide an access with a lower infection rate.

The first catheter was used as acute vascular access and introduced by Shaldon et al. in 1961 [79]. They introduced two separate single lumen catheters in the femoral artery and the femoral vein. Later, introducing a CVC in the vena cava superior was referred to as the 'Shaldon catheter' and is mostly used as short term solution [80, 81]. The first to introduce a CVC in the subclavian artery were Erben et al. in 1969 [82]. However nowadays, this method is more and more abandoned because the risk of occlusion of the subclavian artery by a stenosis at the cannulation site is over 40% compared to 10% in the internal jugular vein [83]. The introduction of a catheter in the internal jugular vein is however technically more difficult because the anatomical landmarks are less prominent [84]. The right internal jugular

vein is preferred because it is generally larger than the left side and a more direct course to the vena cava superior. Develter et al. showed that single lumen catheters in the right internal jugular vein resulted in significantly better survival compared to other insertion sites [85]. For immobilized patients, the femoral vein can be used as insertion location due to its easy puncture and low risk of injuring vital organs. This option should however be avoided due to infection risk [86]. At first, only single lumen catheters were used, but in the early 1980s, catheters with two lumens were introduced [84]. The suction lumen is called the 'arterial' lumen and the other one the 'venous' lumen.

Nowadays, as a long-term catheter, a tunneled central venous catheter in the right jugular vein leading its tip in the vena cava superior or right atrium, as shown in Figure 5.1, is the preferable option.

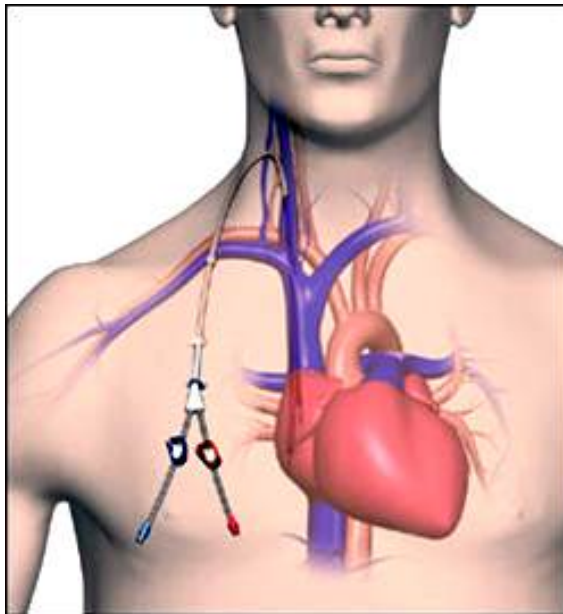


Figure 5.1: CVC in internal jugular vein leading to the right atrium over the vena cava superior [87].

5.2 COMPLICATIONS

The most common type of failure is due to inadequate dialysis blood flow (up to 51%) [36]. When catheter dysfunction occurs immediately after insertion,

the placement itself is more likely to be the problem. However, most patients initiate dialysis with a well functioning CVC, but after a while, the aspiration of the ‘fresh’ blood becomes more and more difficult. Most centers intervene if the maximal blood suction rate decreases below 200 ml/min [88]. The underlying problem might be an intraluminal or extraluminal thrombus (fibrin sleeve or sheath formation) (Figure 5.2) and/or the suction of the arterial lumen to the wall. The reduction of the dialysis blood flow is a more common problem with dual-lumen than with single lumen catheters [88], this might be due to the sequential arterial (suction of blood to the artificial kidney) and venous phase (returning the blood to the patient) of the same lumen in single lumen catheter dialysis.

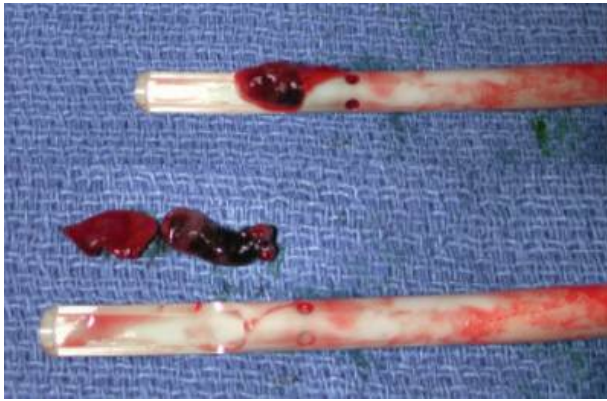


Figure 5.2: (a) Clot seen at the catheter tip of the Maxid catheter (Mahurkar type). The clot is anchored in the distal side holes and extends into the catheter. (b) The clot after extraction from the catheter. A cast of the side holes is seen on the distal clot [89].

Low catheter blood flows may be corrected by forceful aspiration and flushing with a small syringe, changing the patient's position or switching the arterial and venous lines [30]. This last option increases the recirculation of the catheter.

The standard procedure to reduce intraluminal clotting is injecting a volume of anticoagulant into the catheter for locking. Heparin and Citrate are commonly used anticoagulants: e.g. solutions of 5000 IU/mL to 2500 IU/mL heparin, 4% to 30% of citrate or even combinations as the Tau-roLock Hep500 (Tauro-Implant GmbH, Winsen, Germany) (anti-microbial Cyclo-Taurolidine, 4% citrate and for the Hep500 series added with 500 IU/mL heparine) are used. Locking solutions might leak into the patient's body and therefore, the amount of injected locking solution (i.e. equal

or larger than the catheter volume) as well as the speed of injection are still a matter of debate [90–92].

When the ‘mechanical’ measures to overcome the low flow in a catheter are unsuccessful, malfunctioning catheters can be treated acutely by use of a thrombolytic agent, mostly in an empirical way. If catheter malfunction persists despite repeated thrombolysis and the flow is insufficient to provide an adequate dialysis dose, then the catheter should be exchanged, preferably over a guidewire [30].

Catheters are also prone to frequent infection [30]. Where the infection rate per 1000 days is 0.2 for AVFs and 1 for AVGs, the infection rate increases to 2.4 for tunneled and even 6.5 for non-tunneled CVCs [86, 93]. It was calculated that a one episode catheter-related blood stream infection increases hospital cost between 11 000 and 54 000 US dollars [86].

5.3 DEVICES

5.3.1 Material design

The requirements for catheters are obvious but to some extent contradictory. The internal lumen should be as large as possible to reduce flow resistance while the overall size should be small. Although a thinner wall might be preferable, the catheter should be resistant to kinking, cracking or breaking. The catheter should be rigid enough during placement to slide easily over a guidewire, but be soft and flexible to be able to bend in the subcutaneous tunnel and avoid the tip to damage the lumen of the vein. Some catheter materials such as polyurethanes have thermoplastic qualities, so they are more rigid during placement, but once they reach body temperature they become softer. The most commonly used materials to manufacture permanent CVCs are polyethylene, teflon, silicone, polyurethane and carbothane [94].

5.3.2 Shaft designs

A single lumen catheter can be designed with or without sideholes. Sideholes should give the advantage of providing enough blood flow rate in case the catheter tip is blocked. However, more and more disadvantages are rising, such as an increasing risk of clot formation at the sideholes (as in Figure 5.2) upon the blocking the full lumen diameter [95].

Concerning dialysis over two lumens, the first option is using two single lumen catheters next to each other as with the Tesio (Medcomp, Harleysville, HA, USA) [96] or the Canaud [97] catheter. For double lumen catheters, three general shaft designs are present: the double-D design; the oval-shape design and the concentric design. Figure 5.3 shows an example of the three

designs with the same cross-sectional area. The double-D and the concentric design have a lower overall circumference compared to the oval-shape design. The volume to contact surface area is low for the concentric design compared to the other designs. This has a negative impact on the ‘shear rate’ acting on the blood and can cause additional shear stresses, pressure drop and blood damage. Therefore, the concentric design is not a reasonable option. This was also shown in a computational study by Mareels et al. [98]. The volume to contact surface area for the oval-shaped catheter is lower compared to the double-D design, but the larger outer perimeter is a drawback for the oval-shape.

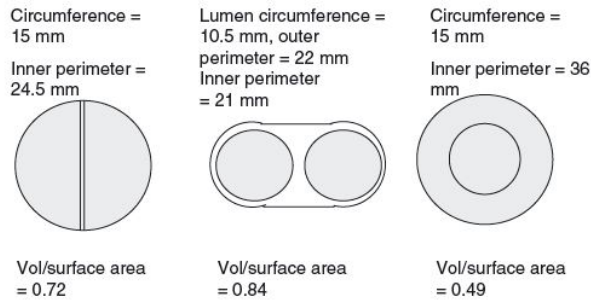


Figure 5.3: Three catheters (Double-D, Oval-shape and Concentric) with the same lumen total cross-sectional area [94].

5.3.3 Tip designs

Considering the tip design, a straight cut (both lumens have the same length), a shotgun (bayonet or step-tip design with the arterial lumen shorter than the venous lumen), a split design (both lumen tips separated from each other) or a variation are in use. Because the occurrence of flow recirculation from the venous to the arterial lumen is higher with the straight cut tip, the use of a more distal arterial (suction) lumen as in the shotgun design seems more appropriate.

Examples of shotgun tip designs can be found in Figure 5.4, with, for the double-D design, the Mahurkar catheter (left) and, for the oval design, the Quinton catheter (middle) as commercial example (Covidien, Dublin, Ireland). On the right side of Figure 5.4, a catheter tip starting with a round venous lumen evolving to a double-D design at the arterial inlet, commercially available as DuraFlow or DuraMax (AngioDynamics, Latham, NY, US), is shown.

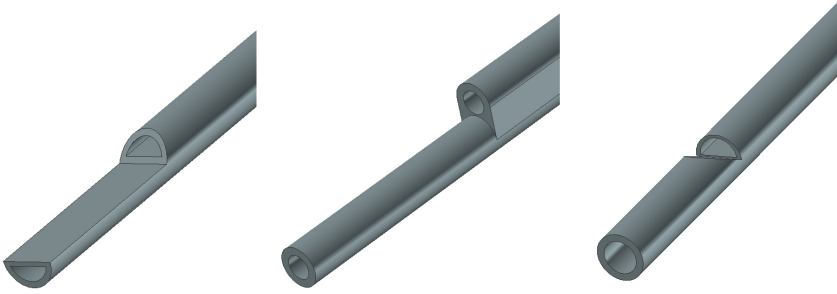


Figure 5.4: Examples of shotgun tip designs: (A) double-D as in Mahurkar catheter (Covidien, Dublin, Ireland); (B) oval-shape as in Quinton catheter (Covidien, Dublin, Ireland) and (C) round tip with double-D lumen as in the DuraFlow and DuraMax catheter (AngioDynamics, Latham, NY, US).

The Tal-Palindrome catheter (Covidien, Dublin, Ireland), reported by Tal in 2005 [99] and shown in Figure 5.5, is a design somewhere between the straight cut and the shotgun. The double-D catheter has two symmetrical lumens of the same length but orientated in opposite direction. This design has the advantages of the shotgun design added with the fact that, with switching the catheter ports (e.g. when one of the lumens get partially blocked), the recirculation does not increase. Tal showed that the overall recirculation is also significantly lower compared to other designs (even the split tip), no clinical data have confirmed this yet [99].

The split tip design, as shown for some commercial examples in Figure 5.6, combines the advantage of the double-D shaft, the simple placement of a single-body catheter and the multiple sideholes (similar to the Tesio-design) [94, 100]. Mareels et al. showed that a catheter with split tip (Ash

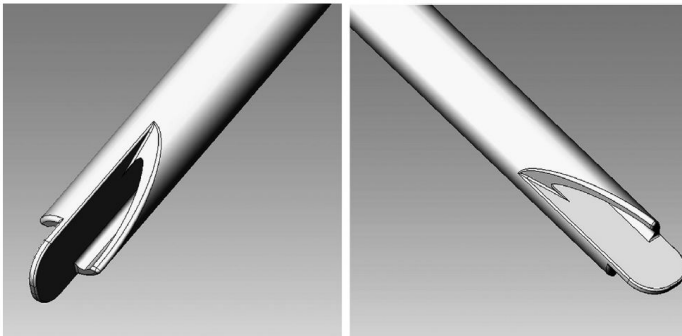


Figure 5.5: Drawing of the tip of the symmetric Palindrome catheter [99].

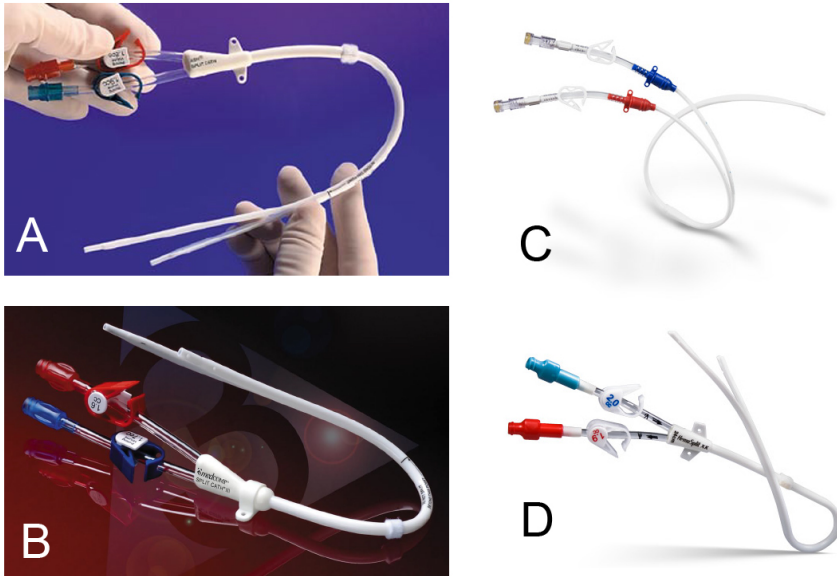


Figure 5.6: Examples of split tip designs: The Ash Split Cath (A) and Split Cath III (B) by Medical Components, Inc. (Medcomp, Harleysville, HA, USA) on the left and the Pourchez RetrO catheter (C) and HemoSplit XK (D) by C.R. Bard, Inc. (Murray Hill, NJ, USA) on the right.

split) had the lowest arterial tip volume with a shear stress above 10Pa, but the blood residence time at this location was higher [98]. The Ash Split Cath (Medcomp, Harleysville, HA, USA), launched in 1997, became the ‘gold standard’ catheter for hemodialysis by securing nearly 60% of the U.S. market.

To finalize this overview, the latest variation on the split tip design, the Centros (Ash Access Technology inc., Lafayette, IN, US) is shown in Figure 5.7. This self-centering catheter was designed to avoid complete sheathing of the catheter and therefore holding a portion of the catheter in the middle of the vena cava. The lumen tips bend inward from the contact points at the lumen wall. Side holes are not present because the lumen tips should not be in contact with the vena cava wall and should therefore not become occluded. A seven week study on nine patients showed an increased average flow for the Centros compared to standard catheters [101].



Figure 5.7: Centros catheter (Ash Access Technology inc., Lafayette, IN, US) [101].

5.3.4 Catheter-graft combination

There is a combination of a catheter and graft on the market under the name HeRO (Hemodialysis Reliable Outflow) (Hemosphere, Inc., Eden Prairie, MN, US) as shown in Figure 5.8. The device has a traditional arterial graft anastomosis and to avoid the venous anastomosis complications in AVGs (stenosis and thrombosis), the 6mm ePTFE graft is connected to a 5mm (16Fr.) silicone outflow catheter. The venous outflow component is placed in the central venous vasculature with the distal tip in the right atrium. A clinical study [102] showed that the infection rate per 1000 catheter days was reduced to 0.7, i.e. between the values for AVF and AVG. The device had also similar patency rates compared to AVGs.

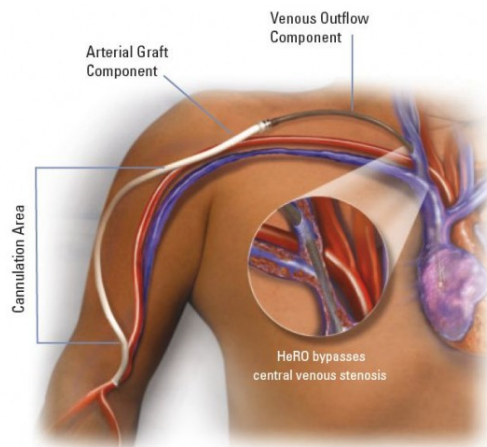


Figure 5.8: HeRO graft-catheter by Hemosphere, inc. (Eden Prairie, MN, US).

Comparison between vascular access options

6.1 OCCURRENCE

The Dialysis Outcomes and Practice Patterns Study (DOPPS) has shown large international variations in vascular access practices. The patients surveyed¹ used an arterio-venous fistula in 66% of the cases in Europe, as compared to 15% in the United States. A central venous catheter was used in 31% in Europe as compared to 60% in the US. Physicians used an arterio-venous graft in 2% of the cases in Europe as opposed to 24% in the US [103]. As mentioned before, elderly, diabetics and female patients tend to have lower quality native vessels, and therefore a lower patency of AVFs. This can be seen in the prevalence of AVFs created in the examples shown in Figure 6.1.

Allon et al. state, after reviewing the literature, that among patients who are referred for their initial vascular access surgery, placement of a forearm fistula is feasible in only 40 to 50%. However, placement of an upper arm fistula is possible in an additional 25 to 35% of patients. Thus, some type of fistula can be placed in at least 75% of patients, with the remainder requiring the creation of a graft [30]. So the numbers of fistulas created in Europe are in line with these findings, while the large number of AVGs created in the US should be decreased. After the results of the DOPPS study were published,

¹New access types from 1996 until 2000

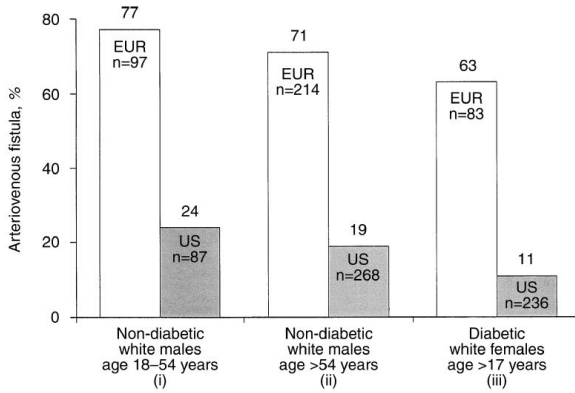


Figure 6.1: Arterio-venous fistula (AVF) use among patients in Europe (EUR) and the United States (US) for three different patient groups (n refers to the total number of patients in the particular subgroup) [103].

the Fistula First Breakthrough Initiative (FFBI) was started in July 2003. At the start of the DOPPS study, the prevalence rate of AVFs in the US was 24% (80% for Europe)[103] and is now increased to 59.5% (August 2011) [104].

However, in recent years, the chronic dialysis population has become substantially older, more likely to be female and diabetic, and has higher comorbidity. Many of these patients appear to have vessels of low quality for construction of native fistulas. Therefore, it is expected that in Europe the percentage of AVGs created will increase [21].

6.2 PATENCY - MORTALITY

Primary patency is the interval from the time of access placement until the first intervention to maintain or re-establish patency or until access thrombosis. Assisted primary patency is the interval from the time of access placement until access thrombosis, in this case including surgical or endovascular interventions to maintain the functionality of a patent access. Secondary (cumulative) patency is the interval from the time of access placement until access abandonment, including surgical or endovascular interventions and even after thrombosis. [105]. This is visualized in Figure 6.2.

The one year primary patency rates for AVFs and AVGs are similar (43% versus 41%), but when only the matured AVFs are taken into account, this one year primary patency rate increases to 54% [36, 107].

For CVC, patency rates are not frequently described in literature, mainly due to the short term or median-long term (6-9 months) use of this vascular

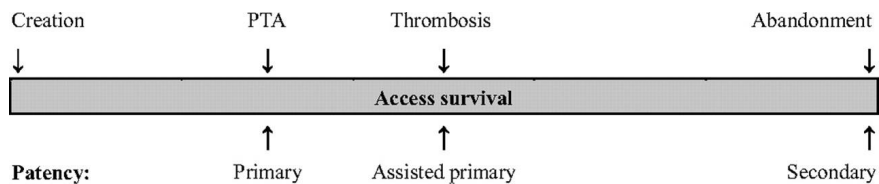


Figure 6.2: Visual explanation of patency rates. Primary patency is the intervention-free access survival. Assisted primary patency is the thrombosis-free access survival. Secondary patency ends when the access is abandoned.[106]

access option. Hodges et al. reported however a primary patency rate at one year of 9% [36].

When analyzing the secondary patency rates in multiple large studies, the ratio between one year secondary patency of grafts versus fistulas is fluctuating around 1, as shown in Figure 6.3.

Concluding from these secondary patency rates that AVGs are as good working as AVFs is too easy. When analyzing the revision rate to keep the access patent, the interventions required for AVGs is 3 to 4 times higher compared to AVFs (See Figure 6.4). So the costs to keep an AVG from total failure will be higher as well as the burden for the patients. For AVGs, it is

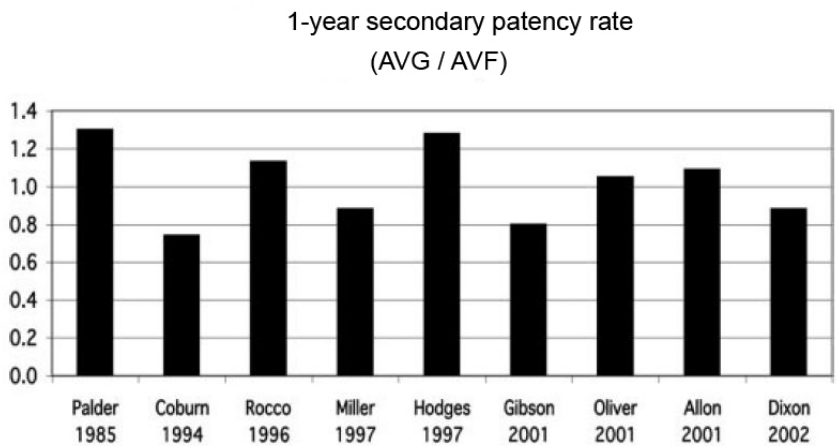


Figure 6.3: Secondary patency rate at 1 year for graft/fistula. Note that the ratio is approximately 1.0, indicating comparable secondary patency for grafts and fistulas.[30]

calculated that for every revision procedure performed, the ‘new’ primary patency rate is reduced (23-16-17% for revision 1, 2 and 3).

For CVCs, when the probability of maintaining the patient on a CVC (including use of new catheters) is included, the one-year survival is 81% compared to the one-year survival of one single catheter of only 48.7% reported by McLaughlin et al. [108]. While also other values of the cumulative one-year survival between 47% and 93% were reported in literature [88].

The mortality is two- to three-fold higher in patients who initiate dialysis with a catheter, as compared to those having a fistula [109]. In numbers, the mortality of 16.8% for patients with a non-tunneled CVC and 15.2% for those with a tunneled CVC compared to 9.3% and 7.1% for those with an AVG and AVF [110]. Moreover, mortality is reduced by approximately 50% in patients who switch from a catheter to a permanent access (fistula or graft), as compared with those who remain catheter dependent [111]. DOPPS data even showed that in incident hemodialysis patients, access failure for both AVG and AVF is greater in patients with prior CVC, even a relative risk of 1.81 for AVF failure after CVC use is reported [112, 113].

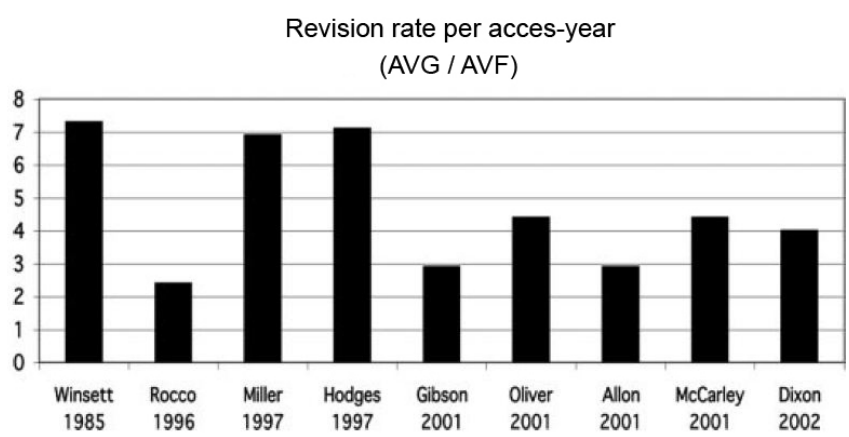


Figure 6.4: Revision rate per access-year for grafts/fistulas. Note that all of the ratios are > 1, indicating a much higher revision rate in grafts than in fistulas.[30]

Two

Engineering tools

Global approach (ARCH)

Despite the magnitude of the clinical problem related to AVF-creation, there has been an absence of novel therapeutic interventions in this field due to complex mechanisms responsible for AVF complications. Most complications are closely related to both the sudden and sustained hemodynamic changes involved in AVF creation.

With this knowledge, an international consortium submitted a project to the European Commission (EC) for the FP7-ICT-2007-2 call that got granted for 3.5 years starting June 2008 until November 2011. The project was called ARCH (Patient-specific image-based computational modeling for improvement of short- and long-term outcome of vascular access in patients on hemodialysis therapy ¹) and had a working budget of around 3.76 million euro. The consortium consisted out of 8 main partners with another 3 'third parties' as shown in Table 7.1.

The ARCH project aimed at the development of a service infrastructure for patient-specific assessment, surgical planning and follow-up of the vascular access (Figure 7.1). This infrastructure was based on a multi-scale computational modeling framework, coupling 1D network models of the systemic circulation to 3D computational fluid dynamics (CFD) or Fluid Structure Interaction (FSI) models of selected vascular tracts (stenosed vessel segments, branching, anastomosis or venous valves). The input data was

¹<http://www.vph-noe.eu/vph-projects>

Name	Country	Role
Istituto di Ricerche Farmacologiche 'Mario Negri' ^a	Italy	Engineering
Technische Universiteit Eindhoven ^b	The Netherlands	Engineering
Universiteit Gent	Belgium	Engineering
The University of Sheffield	UK	Engineering
Maastricht University Medical Center	The Netherlands	Clinical
Ghent University Hospital ^b	Belgium	Clinical
Ospedali Riuniti di Bergamo ^b	Italy	Clinical
University Medical Centre Ljubljana	Slovenia	Clinical
Philips Medical Systems Nederland b.v.	The Netherlands	Industry
Philips Electronics Nederland b.v.	The Netherlands	Industry
Esaote Europe b.v.	The Netherlands	Industry

^a Coordinator

^b Third party

Table 7.1: Members of the ARCH consortium.

drawn from medical imaging and functional evaluations through innovative image analysis and signal processing techniques. The development and the validation of the patient-specific image-based computational modeling tools were a main feature in the projects outline.

The general goal was to improve treatment quality and to decrease the costs of VA creation and management. A considerable part of the project was therefore directly aimed at tackling four major clinical issues in VA management: non-maturation, long-term patency, steal syndrome and heart failure. Pilot observational studies were performed on volunteers and on hemodialysis patients during model development for calibration and for verification of theoretical predictions. The consortium published the clinical study protocol for the ARCH project in 2011 [114].

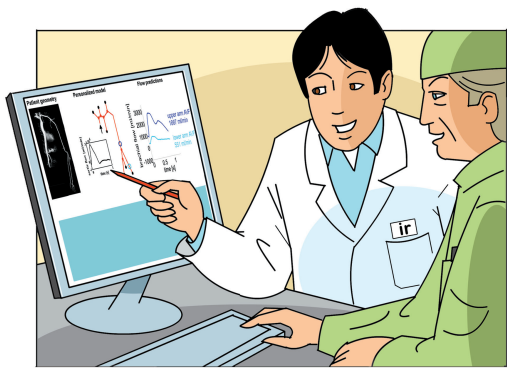


Figure 7.1: ARCH concept: Patient-specific modeling for AVF surgical planning based on medical images [115].

General fluid mechanics

8.1 FLUID CHARACTERISTICS

8.1.1 Density

The mass density or specific gravity, ρ , of a fluid is the mass per unit volume (kg/m^3). ρ is a function of temperature and pressure. For example, pure water will reach its maximal density at atmospheric pressure at a temperature of 4°C , namely 999.97 kg/m^3 . At 37°C and at atmospheric pressure, the density of blood is about 1050 kg/m^3 .

8.1.2 Viscosity

Dynamic and kinematic viscosity

If a force acts on a fluid, the fluid will exert a certain resistance to flow (internal friction). The rate of resistance is fluid specific and is called viscosity. For example, syrup will deform less easily than water which means that syrup has a higher viscosity than water. The dynamic viscosity, μ , sometimes simply called viscosity, has the dimension of kg/m.s or Pa.s . An old dimension of μ is poise which equals 0.1 Pa.s . When the dynamic viscosity is negligible ($\mu \approx 0$) the fluid is said to be ideal, which means that in this case no shear stress will appear.

The dynamic viscosity is only slightly dependent on the pressure while it is highly dependent on the temperature. For fluids, the viscosity will decrease with increasing temperature as the cohesion and the intramolecular forces will decrease.

The viscosity of water, μ_{water} , is 10^{-3} Pa.s at 20°C and the viscosity of plasma is around $1.3 \cdot 10^{-3}$ Pa.s at 37°C . The viscosity of blood is highly dependent on the hematocrit level (concentration of RBCs in blood) and will be discussed in the section on blood rheology (p.54).

Another viscosity parameter is the kinematic viscosity, ν . The relationship between dynamic and kinematic viscosity is:

$$\nu = \frac{\mu}{\rho} \quad (8.1)$$

in $[\text{m}^2/\text{s}] = [\text{kg}/(\text{m.s})] / [\text{kg}/\text{m}^3]$.

Newtonian fluid

Newtonian fluids are characterized by a linear relationship between shear stress, τ , and velocity gradient, du/dy , in the x-direction perpendicular to the flow direction, also known as Newton's Law of viscosity (Figure 8.1):

$$\tau = \mu \frac{du}{dy} \quad (8.2)$$

in $[\text{N}/\text{m}^2] = [\text{N.s}/\text{m}^2] \cdot [\text{1}/\text{s}]$

The velocity gradient, du/dy , is also often called the shear rate.

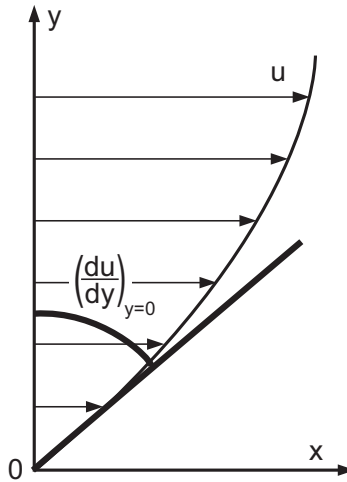


Figure 8.1: Shear stress.

Non-newtonian fluid

A non-Newtonian fluid can be characterized by a viscosity that varies with motion.

Most non-Newtonian fluids have a molecular chain structure. For some of these fluids, the molecules will tend to orient in planes of maximum tension resulting in a decreasing viscosity with increasing velocity gradient. These types of fluid are called pseudo-plastics or 'shear-thinning' fluids. On increasing shear rate, the fluid is 'thinning'. For others, the viscosity will increase with an increasing velocity gradient. The latter fluids are called dilatant or 'shear-thickening' fluids. Blood and polymer-solutions are shear-thinning, while suspensions (paints) are shear-thickening. For non-Newtonian fluids, the viscosity varies with the shear rate (Figure 8.2).

For all the fluids mentioned above, the shear stress will disappear at the moment the shear rate approaches zero. Some other fluids only will start to deform at the moment the shear stress exceeds a certain critical level. Those fluids are called plastic fluids (e.g. toothpaste). One needs to overcome a given shear force before the fluid flows. This critical value of the corresponding shear stress is called the yield-stress, τ_0 .

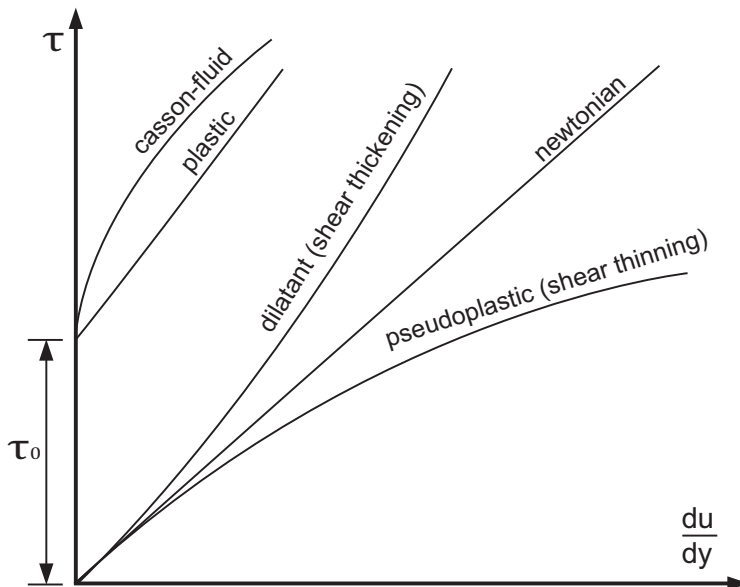


Figure 8.2: Rheological behavior of different fluids.

Blood rheology

The study of the rheological behavior of a fluid implies the hypothesis of a continuum medium. Therefore, one has to cautiously examine within which limits the continuous model is still applicable. It is difficult to obtain rheological data which is directly related to the whole rheological properties of blood. The blood is a complex living medium, which can be considered in a first approach as a concentrated dispersion of mainly red blood cells (RBC) (erythrocytes) in blood plasma.

If for simplicity a Newtonian model of the blood is used, one should take into account that the viscosity changes with hematocrit, H . In men the average hematocrit is around 45%, in women around 43%, but this value can vary enormously [116]. The Newtonian viscosity is often calculated by the equation derived by Mockros and Leonard for bovine blood[117]:

$$\mu = \mu_p e^{0.0235 H} \quad (8.3)$$

with H the hematocrit (in %) and μ_p the plasma viscosity. 3.5 mPa.s is commonly used as the Newtonian viscosity value for blood, corresponding to a hematocrit of 42% and a plasma viscosity of $1.3 \cdot 10^{-3}$ mPa.s.

An example of a shear thinning model of blood viscosity is the **Quemada model**, depending on the shear rate and hematocrit [118, 119]. The dynamic viscosity is defined as:

$$\mu = \frac{\mu_p}{(1 - 1/2 kH)^2} \quad (8.4)$$

with parameter k a function of the intrinsic viscosities.

$$k = \frac{k_o + k_\infty \sqrt{\gamma/\gamma_c}}{1 + \sqrt{\gamma/\gamma_c}} \quad (8.5)$$

$$\begin{aligned} \text{with } \ln k_o &= 3.874 - 10.410 H + 13.800 H^2 - 6.738 H^3 \\ \ln k_\infty &= 1.3435 - 2.803 H + 2.711 H^2 - 0.6479 H^3 \\ \ln \gamma_c &= -6.1508 + 27.923 H - 25.600 H^2 - 3.697 H^3 \end{aligned}$$

k_o characterizes the red blood cell aggregation at zero shear stress, k_∞ describes the orientation and deformation of red blood cells at a shear rate value far above the critical shear rate γ_c and γ characterizes the shear rate.

In Figure 8.3, the influence of the hematocrit and the shear rate on the viscosity can be noticed for an example with a plasma viscosity of 1.3 mPa.s. For the zones with low shear rate (e.g. bulk flow in the middle of an arterial lumen), the dynamic viscosity is high (See Figure 8.3, top), while for the zones at the wall (shear rate around 2000), the viscosity decreases to 3.2-4 mPa.s (Figure 8.3, bottom).

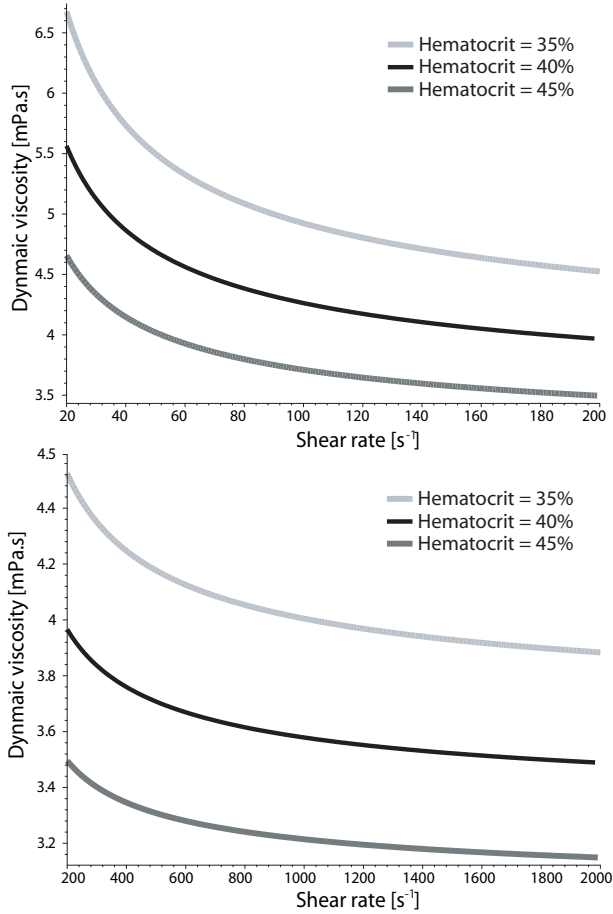


Figure 8.3: Dynamic viscosity for two ranges of shear rate and three different values of hematocrit calculated by the Quemada model.

8.2 FLUID DYNAMICS

Generally, a fluid flow is a rather complex three-dimensional, time-dependent phenomenon. However, in many (biological) situations it is possible to make simplified assumptions that allow a much easier understanding of the problem without sacrificing much needed accuracy. One of these simplifications involves simplifying a real 3D-flow to a one- or two-dimensional flow. In almost any flow situation, the velocity field actually contains all three velocity components (u, v, w) and each is a function of all three space coordinates (x, y, z):

$$\vec{v} = u\vec{e}_x + v\vec{e}_y + w\vec{e}_z \quad (8.6)$$

In a lot of situations the three-dimensional flow characteristics are important in terms of the physical effects they produce. For these situations it is necessary to analyze the flow in its complete three-dimensional character. Neglecting one or two of the velocity components in these cases would lead to considerable misrepresentation of the effects produced by the actual flow. Therefore, there are four unknowns, when considering an incompressible, 3-D, Newtonian fluid; the three velocity components, u , v and w and the pressure, p . Therefore, there is a need of four independent equations to calculate these parameters in every point of the flow field. These equations can be found in the foundational axioms of fluid dynamics also known as the the conservation laws. These conservation laws consist of the conservation of mass, the conservation of momentum and the conservation of energy. If only velocity and pressure are taken into account, the conservation of energy (or first law of thermodynamics) can be neglected. Therefore, only the conservation of mass and momentum equations are derived and described in the following sections.

8.2.1 Conservation of mass

If a differential element as presented in Figure 8.4 is considered, the mass flow in the x -direction is given by:

$$\left(\rho u + \frac{\delta(\rho u)}{\delta x} \frac{dx}{2} \right) dy dz - \left(\rho u - \frac{\delta(\rho u)}{\delta x} \frac{dx}{2} \right) dy dz \quad (8.7)$$

Resulting in a net rate of mass outflow equal to:

$$\frac{\delta(\rho u)}{\delta x} dx dy dz \quad (8.8)$$

An analysis similar to the one used for the flow in the x -direction gives the overall net rate of mass in y -direction and in z -direction, so the net rate of mass outflow is given by:

$$\left(\frac{\delta(\rho u)}{\delta x} + \frac{\delta(\rho v)}{\delta y} + \frac{\delta(\rho w)}{\delta z} \right) dx dy dz \quad (8.9)$$

The rate of mass change in an interval dt is:

$$\left(\rho + \frac{\delta \rho}{\delta t} dt \right) \frac{dx dy dz}{dt} - \rho \frac{dx dy dz}{dt} \Rightarrow \frac{\delta}{\delta t} (\rho dx dy dz) \quad (8.10)$$

The differential equation for conservation of mass is:

$$\boxed{\frac{\delta \rho}{\delta t} + \frac{\delta(\rho u)}{\delta x} + \frac{\delta(\rho v)}{\delta y} + \frac{\delta(\rho w)}{\delta z} = 0} \quad (8.11)$$

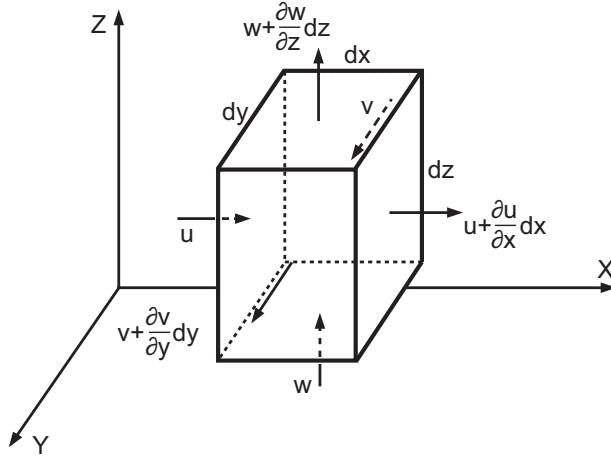


Figure 8.4: Schematic representation of the velocity in a 3D-differential element.

Equation 8.11 is also commonly referred to as the **continuity equation**. In vector notation, the full conservation of mass equation becomes:

$$\frac{\delta \rho}{\delta t} + \nabla \cdot \rho \vec{v} = 0 \quad (8.12)$$

For steady flow it reduces to:

$$\nabla \cdot \rho \vec{v} = 0 \quad (8.13)$$

For incompressible fluids, the fluid density, ρ , is constant throughout the flow field and equation 8.13 becomes:

$$\nabla \cdot \vec{v} = 0 \quad (8.14)$$

or

$$\frac{\delta u}{\delta x} + \frac{\delta v}{\delta y} + \frac{\delta w}{\delta z} = 0 \quad (8.15)$$

In a control-volume approach, the equation is transferred to:

$$\iint_{c.s.} \rho (\vec{v} \cdot \vec{n}) dA + \frac{\delta}{\delta t} \iiint_{c.v.} \rho dV = 0 \quad (8.16)$$

With c.s. being the control surface of the control volume, c.v., and \vec{n} the normal on the surface.

8.2.2 Conservation of momentum

Conservation of linear momentum is expressed by Newton's second law applied to a mass m :

$$\bar{F} = m \bar{a} \quad (8.17)$$

Where \bar{F} is the resulting force acting on the mass, m , and \bar{a} the corresponding acceleration. In general, two types of forces need to be considered:

1. Surface forces, which act on the surface as a result of the interaction with the surroundings of a fluid element. They consist of normal stress due to pressure and shear stresses due to viscosity.
2. Body forces, which are distributed throughout the fluid element.

In analogy with the method used to derive the conservation of mass equation, the resultant *surface forces* in the x -direction, for a differential element, can be seen as:

$$\left(\frac{\delta(\sigma_{xx})}{\delta x} + \frac{\delta(\tau_{yx})}{\delta y} + \frac{\delta(\tau_{zx})}{\delta z} \right) dx dy dz \quad (8.18)$$

Where σ_{xx} represents, as shown in Figure 8.5, the normal stress on a plane perpendicular to the x -direction. τ_{yx} and τ_{zx} represent the shear stresses in the x -direction on a plane perpendicular to, respectively, the y - and z -direction of the differential element.

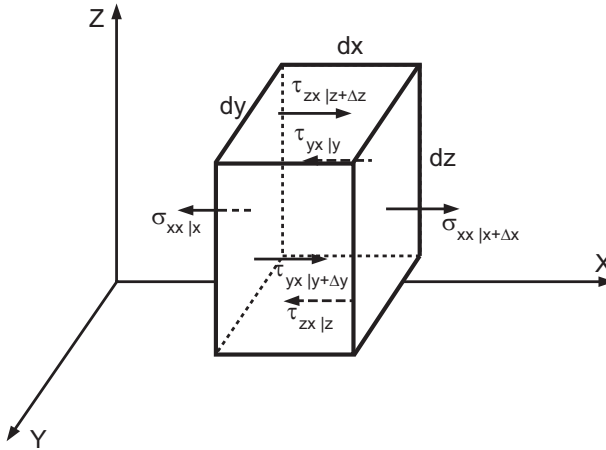


Figure 8.5: Schematic representation of surface forces in the x -direction in a 3D-differential element.

For most purposes, the only *body force* of interest is the weight of the differential element which can be expressed as:

$$F_x = \rho g_x \quad (8.19)$$

Where g_x is the component of the acceleration of gravity vector in the x direction. Other possible body forces are coriolis force or forces due to capillarity.

When the surface force of Equation 8.18 and the volume force of Equation 8.19 are inserted in the left hand side of Equation 8.17, one can derive the general differential equation of motion in fluid in the x -direction:

$$\rho g_x + \frac{\delta(\sigma_{xx})}{\delta x} + \frac{\delta(\tau_{yx})}{\delta y} + \frac{\delta(\tau_{zx})}{\delta z} = \rho \left(\frac{\delta u}{\delta t} + u \frac{\delta u}{\delta x} + v \frac{\delta u}{\delta y} + w \frac{\delta u}{\delta z} \right) \quad (8.20)$$

Hereby, the right hand side of Equation 8.17 is derived, similar to the method used in the section on conservation of momentum, by adding the net rate of momentum outflow with the time rate of change of momentum. The equation can then be simplified by the use of the substantial differential $\frac{D}{Dt}$, to

$$\boxed{\rho g_x + \frac{\delta(\sigma_{xx})}{\delta x} + \frac{\delta(\tau_{yx})}{\delta y} + \frac{\delta(\tau_{zx})}{\delta z} = \rho \frac{Du}{Dt}} \quad (8.21)$$

In contrast to the conservation of mass equation, the **conservation of momentum equations** should be written in all three dimensions, so three equations (x , y and z) make the complete set of equations to solve the conservation of momentum in a fluid. In a control volume approach, these equations become:

$$\sum \bar{F} = \iint_{c.s.} \rho \bar{v}(\bar{v} \cdot \bar{n}) dA + \frac{\delta}{\delta t} \iiint_{c.v.} \rho \bar{v} dV \quad (8.22)$$

The three conservation of momentum equations (in all three directions), in combination with the conservation of mass equation, form together the four necessary, independent equations to calculate in each point of the flow field (for an incompressible, laminar flow, with constant viscosity) the unknowns u , v , w and p .

8.2.3 Navier-Stokes equations

The **Navier-Stokes equations** are a specific representation of the conservation of momentum equations, with inclusion of body force, pressure force and viscous force.

$$\boxed{\rho \bar{F} - \bar{\nabla} p + \mu \bar{\nabla}^2 \bar{v} = \rho \frac{D\bar{u}}{Dt}} \quad (8.23)$$

8.2.4 Euler and Bernoulli equations

For the inviscid flow (ideal fluid) in which all shearing stresses are zero, the general equation of motion is reduced to (in vector notation):

$$\rho \bar{g} - \bar{\nabla} p = \rho \frac{D\bar{u}}{Dt} \quad (8.24)$$

These equations are commonly referred to as the **Euler equations of motion**. It can be seen as a simplified version of the Navier-Stokes equation (with only the gravity taken as body force, \bar{F} , and with no viscous force included).

If the only external force is the gravity in the z-direction and the equation is applied to a streamline (1D), the formula reduces to:

$$z + \frac{p}{\rho g} + \frac{v^2}{2g} = \text{constant} \quad (8.25)$$

This is the **Bernoulli equation**. Note that the equation can only be applied along a streamline and that the flow is assumed to be steady and inviscid. If one takes into account the (head) losses, h_{loss} [m], in a flow from point 1 to 2, the Bernoulli equation becomes:

$$z_1 + \frac{p_1}{\rho g} + \frac{v_1^2}{2g} = z_2 + \frac{p_2}{\rho g} + \frac{v_2^2}{2g} + h_{loss} \quad (8.26)$$

An application of this is for instance the blood flow through a narrowing in the coronary arteries (stenosis). When looking at the basic Bernoulli equation (no head losses) for an 'ideal' fluid, there will be no pressure gradient over the stenosis, only a transfer in energy (pressure energy pre-stenosis to kinetic energy inside the stenosis and pressure energy recovery post-stenosis). A viscous fluid flowing through a narrow stenosis however, introduces a significant energy loss. In the contraction segment, the head loss is low when shifting the potential energy to kinetic energy. On the contrary, in the expansion segment, a more 'energy expensive' transfer is present. Energy is lost by formation and maintenance of vortices (viscous drag) [120].

As experimentally shown by Berguer & Hwang (Figure 8.6), in the cases of a small radius reduction (below 50% of diameter or 75% of area reduction), the flow is not yet significantly disturbed and the energy recovery, distal to the narrowed section, is still high (no significant head loss) [120]. When the diameter reduction is above 50% (75% area reduction), the pressure drop has a quadratic relation with the flow rate. Here the decrease in blood flow will

become clinically relevant. If the patient suffers from a low blood perfusion, for example in his coronary artery due to a stenosis formation, the area reduction will already be around 75% of the lumen area so that an intervention (e.g. balloon dilation or stenting) becomes necessary.

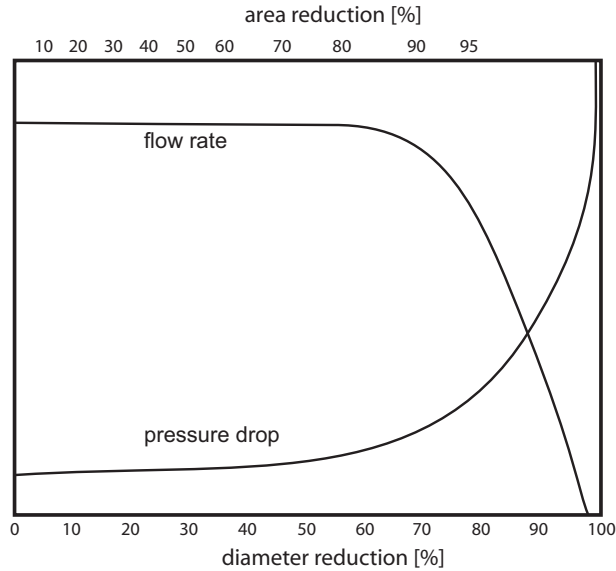


Figure 8.6: Qualitative plot of flow rate and pressure drop over a stenosis based on the work of Berguer & Hwang [120].

8.3 CHARACTERISTICS OF FLUID MOTION

8.3.1 Laminar and turbulent flow

There is a huge difference when a flow is laminar or turbulent. In laminar flow, fluid particles move along fixed streamlines with negligible particle mixing across the streamlines. The flow is called laminar because it looks like a series of thin sheets of fluid (lamine) sliding over one another. A turbulent flow is characterized by random fluctuations in fluid velocity and by intense mixing of the fluid on macroscopic level and large energy dissipation on microscopic level.

The **Reynolds number** is used to decide whether the flow is laminar or turbulent. The dimensionless Reynolds number is defined by :

$$Re = \frac{\rho UL}{\mu} \quad (8.27)$$

where ρ is the fluid density, U the average velocity, L a relevant characteristic length of the studied problem (e.g. the diameter of a vessel) and μ the dynamic viscosity of the fluid. The Reynolds number is a dimensionless parameter that gives a measure for the ratio of inertial to viscous forces. As a rule, one can use for stiff tubes (with L the diameter of the tube):

- $Re < 2000$ laminar flow
- $2000 < Re < 4000$ transient flow
- $Re > 4000$ turbulent flow

It should be emphasized, however, that this classical distinction of types of flow is only correctly defined for steady flow in rigid tubes. Furthermore, complex flow including the appearance of secondary vortices, does not mean that the present flow field is turbulent. By our ‘engineering’-definition above, these flow disturbances might be present in a laminar flow regime. It should be noted that in clinical environments, the term ‘turbulent flow’ is often used for flow regimes far below the turbulent threshold. Antiga and Steinman stated in their work ‘Rethinking turbulence in blood’ that blood flow is typically laminar; however, high frequency fluctuations suggesting turbulence have only been observed *in vivo* in the ascending aorta and arterio-venous grafts, and in flows past mechanical heart valves [121].

8.3.2 Poiseuille or plug flow

When starting from the equation of conservation of momentum, for a horizontal tube (no gravity forces), with a stationary, laminar flow (no derivative to time) and 1D flow (v and w are zero) with only a friction and a pressure force, all applied to a small cylindrical control volume (radius r and length L):

$$(p_2 - p_1) \pi r^2 = \mu \frac{\delta v}{\delta r} 2\pi r L \quad (8.28)$$

$$\frac{\delta v}{\delta r} = -\frac{r}{2\mu L} (p_1 - p_2) \quad (8.29)$$

$$v = -\frac{r^2}{4\mu L} (p_1 - p_2) + constant \quad (8.30)$$

For $r = R$ and $v = 0$ (‘no-slip’ at the wall)

$$v = \frac{(p_1 - p_2)}{4\mu L} (R^2 - r^2) \quad (8.31)$$

For $r = 0$, $v = v_{max}$ (in the center)

$$v_{max} = \frac{(p_1 - p_2)}{4\mu L} R^2 \quad (8.32)$$

$$v(r) = v_{max} \left(1 - \left(\frac{r}{R}\right)^2\right) \quad (8.33)$$

Note that $v_{avg} = v_{max}/2$ and that the velocity is in a quadratic relation to the radius, this is called a parabolic velocity profile. An example of the profile can be seen on the left panel of Figure 8.7 (Section 8.3.3). If we define the flow rate Q as $\int_0^R 2\pi v r dr$, the expression above becomes:

$$\Delta p = \frac{8\mu L}{\pi R^4} Q \quad (8.34)$$

This is the Poiseuille or **Hagen-Poiseuille equation**. This equation states that the pressure drop along the tube is directly proportional to the length of the tube, the rate of flow and the viscosity of the fluid, and inversely proportional to the fourth power of the internal radius, R .

This equation is applicable to a steady and laminar flow in a long and rigid cylindrical tube, with no slip at the wall and a homogeneous and Newtonian fluid. The term *Poiseuille flow* describes this parabolic flow profile.

If the flow profile is constant over the radius of the tube, $v(r) = v_{avg} = v_{max}$, it is called *plug flow*. When a Newtonian fluid enters a rigid tube with a plug flow profile, after a certain length, due to the viscous force, the profile will developed into a Poiseuille flow profile.

8.3.3 Oscillatory flow

To illustrate oscillatory flow, we start from the momentum and continuity equations for a homogeneous, incompressible and Newtonian fluid in a rigid cylindrical, horizontal tube (radius R) and assume a periodic motion. The velocity in the longitudinal direction (x) then becomes:

$$u = u_n(r) \frac{\delta p}{\delta x} e^{i\omega t} \quad (8.35)$$

With (in radial direction)

$$u_n(r) = \frac{i}{\rho\omega} \left[1 - \frac{J_0(\alpha \frac{r}{R} i^{3/2})}{J_0(\alpha i^{3/2})} \right] \quad (8.36)$$

With J_0 being a zero order Bessel function and α the Womersley number. This dimensionless parameter is the square root of a representation of the inertia force divided by the viscous force:

$$\alpha = R \sqrt{\frac{\omega}{\nu}} = R \sqrt{\frac{\rho \cdot 2\pi f}{\mu}} \quad (8.37)$$

With ω the angular frequency [rad/s] of the oscillations with frequency f [1/s], R the radius of the tube [m] as scale length and ν the kinematic viscosity [m²/s].

An example of the (scaled) flow profiles for different Womersley numbers can be found in Figure 8.7. If the Womersley number is small ($\alpha < 1$), a quasi-static Poiseuille profile can be found which is in-phase with the pressure gradient (as in the Poiseuille equation). The Womersley profiles for intermediate Womersley numbers are characterized by a phase-shift between the flow in the boundary layer (near the wall) and the flow in the central core of the tube. If the number is large ($\alpha \gg 1$), a plug flow is found which is 90 degrees out of phase with the pressure gradient.

In a blood vessel network, the frequency, the viscosity and the density can be assumed to be constant. Therefore the Womersley number is larger in larger vessels and small in smaller vessels. Typical values for a man are around 22 in the aorta and 4 in the brachial artery.

8.3.4 Shear stress calculations

The relationship between shear stress, τ , and shear rate, du/dy , as shown in Figure 8.1, is given by Equation 8.2 (Section 8.2). When applying this formula in the proximity of the wall, taking the local viscosity and the velocity gradient close to the wall, the Wall Shear Stress (WSS) can be calculated:

$$WSS = \mu \left. \frac{\delta u}{\delta y} \right|_{y=0} \quad (8.38)$$

This 1D formulation can be transferred to a 3D formulation by taking the derivative of the velocity to the normal, at the wall:

$$WSS_x = \mu \left. \frac{\delta u}{\delta n} \right|_{wall} \quad (8.39a)$$

$$WSS_y = \mu \left. \frac{\delta v}{\delta n} \right|_{wall} \quad (8.39b)$$

$$WSS_z = \mu \left. \frac{\delta w}{\delta n} \right|_{wall} \quad (8.39c)$$

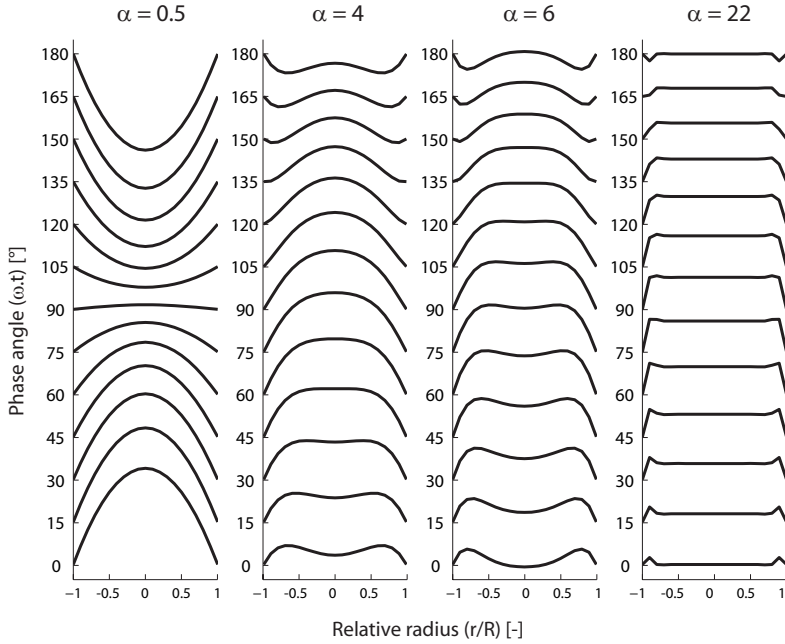


Figure 8.7: Womersley profiles for different Womersley parameters assuming a constant (real) pressure drop over the tube length. The velocity profile is visualized for different phase angles [2].

These three equations form the wall shear stress vector:

$$\overline{WSS} = [WSS_x, WSS_y, WSS_z] \quad (8.40)$$

Time-Averaged Wall Shear Stress (TAWSS)

For non-steady flow regimes, the WSS has a changing value in time. For a periodic flow, the Time-Averaged Wall Shear Stress (TAWSS) [Pa] can be calculated as the integral over time of the absolute value of the WSS-vector:

$$TAWSS = \frac{1}{T} \int_0^T |\overline{WSS}| dt \quad (8.41)$$

Malek et al. [122] indicate that in a normal artery the TAWSS should be between 1 and 7 Pa, in a normal vein between 0.1 and 0.6 Pa. The authors state that in arterial regions with TAWSS below 0.4 Pa, atherosclerosis (artery wall thickening due to the accumulation of fatty substances) will appear, while regions with a TAWSS above 7 Pa are only found in narrowed regions such as stenoses or heart valves.

Oscillatory Shear Index (OSI)

To investigate the oscillatory behavior of the WSS, the change in direction of the flow and therefore the velocity gradient during a cardiac cycle, the Oscillatory Shear Index (OSI) [-], originally introduced by Ku et al. [123], can be calculated.

$$OSI = \frac{1}{2} \left(1 - \frac{\left| \frac{1}{T} \int_0^T \overline{WSS} dt \right|}{\frac{1}{T} \int_0^T |\overline{WSS}| dt} \right) \quad (8.42)$$

with

$$\left| \int_0^T \overline{WSS} dt \right| = \sqrt{\left(\int_0^T WSS_x dt \right)^2 + \left(\int_0^T WSS_y dt \right)^2 + \left(\int_0^T WSS_z dt \right)^2} \quad (8.43)$$

For a flow field that highly oscillates, with the numerator $\left(\left| \int_0^T \overline{WSS} dt \right| \right)$ equal to zero, the OSI will become 0.5, its maximal value. For a unidirectional flow field, over the entire period, the numerator $\left(\left| \int_0^T \overline{WSS} dt \right| \right)$ is equal to the denominator $\left(\int_0^T |\overline{WSS}| dt \right)$ and the OSI becomes zero, its minimal value.

Regions in blood vessels with high OSI indicate a high oscillatory shear stress on the endothelial cells at the inner wall of the arterial lumen. This periodic change in direction of the shear stress on the cells, can causes cellular proliferation and intimal hyperplasia growth [41, 55].

Relative Residence Time (RRT)

A third wall shear stress parameter that is often used, is the Relative Residence Time (RRT) [Pa^{-1}], introduced by Himburg et al. [124] and defined as:

$$RRT = \frac{T}{\left| \int_0^T \overline{WSS} dt \right|} \quad (8.44)$$

This parameter can also be seen as a weighted combination of TAWSS and OSI:

$$RRT = \frac{1}{(1 - 2 \cdot OSI) \cdot TAWSS} \quad (8.45)$$

The parameter is called 'relative' residence time, because all particles are moving and have no absolute residence time on a single location.

More hemodynamic wall parameters and their relationship are listed in the work of Lee et al. [125].

8.3.5 Helicity

Next to parameters evaluating the flow field at the wall, it is possible to characterize the flow in the bulk as well. Belian et al. suggested the use of the density of the kinetic helicity per volume unit, H_k . This parameter seems to have a great influence on the evolution and stability of both turbulent and laminar flows [126]. H_k is defined as the scalar product of the velocity vector, \bar{v} and the vorticity vector, $\bar{\omega}$, of the flow field:

$$H_k = \bar{v} \cdot \bar{\omega} = \bar{v} \cdot (\bar{\nabla} \times \bar{v}) \quad (8.46)$$

The vorticity is the ‘curl’ of the flow field, around an axis (the direction of the vorticity vector). For a given total kinetic energy, the kinetic helicity is maximal when the velocity and the vorticity are in the same direction. The helicity is zero, when the direction of the velocity vector and the direction vorticity vector are perpendicular or, of course, when the vorticity or velocity are zero. Grigioni et al. transformed this equation to a Local Normalized Helicity (LNH) [127, 128]:

$$LNH = \frac{\bar{v} \cdot \bar{\omega}}{|\bar{v}| |\bar{\omega}|} \quad (8.47)$$

The LNH is a parameter between -1 and 1, depending on clockwise or counter-clockwise rotations of the flow field. Finally, the helicity, H , can be defined as the volume integral of H_k :

$$H = \frac{1}{V} \iiint H_k dV = \frac{1}{V} \iiint \bar{v} \cdot (\bar{\nabla} \times \bar{v}) dV \quad (8.48)$$

or of the volume integral of the absolute value of H_k :

$$H = \frac{1}{V} \iiint |\bar{v} \cdot (\bar{\nabla} \times \bar{v})| dV \quad (8.49)$$

The latter formula is used to avoid that clockwise rotations in the volume can be compensated by counter-clockwise rotation resulting in a zero volume-averaged helicity. It should be noted that the helicity is function of time, therefore, analysis of the flow field is often concluded by calculating the time-average over one cardiac cycle of the helicity.

Investigation methods

9.1 EXPERIMENTAL METHODS

9.1.1 Particle Image Velocimetry (PIV)

Particle Image Velocimetry (PIV) is a method to visualize the velocity distribution in fluids. As shown in Figure 9.1, a visual clear fluid flows through a visual clear model, and is seeded with small tracing particle (e.g. $100\ \mu\text{m}$ silver polyamide particles). The density of the particles should match the density of the used fluid. The region of interest (ROI) is illuminated with a laser sheet (2D) (e.g. Neodym-YAG (Nd:YAG) laser). A camera records the particles flowing through the illuminated region of interest (e.g. full frame interline CCD camera). The location of the particle over consecutive images are compared to achieve the flow velocity over a defined discrete timestep.

A 2D velocity field can be acquired by use of only one camera to achieve the velocity in two components (2D-2C standard PIV). If multiple laser planes, positioned perfectly next to each other, are taken into account, it is possible to calculate even the 3D-2C or even 3D-3C velocity. When stereo PIV is applied, two cameras in an angle of 90 degrees of each other (45 degrees of the laser sheet) are positioned. Hereby 3 component vectors can be calculated in the 2D plane (2D-3C).

Nowadays, the use of PIV for the validation of CFD computations is a common procedure. In the field of biomedical engineering and hemodynamics, many cases have already been published. Next to the more idealized

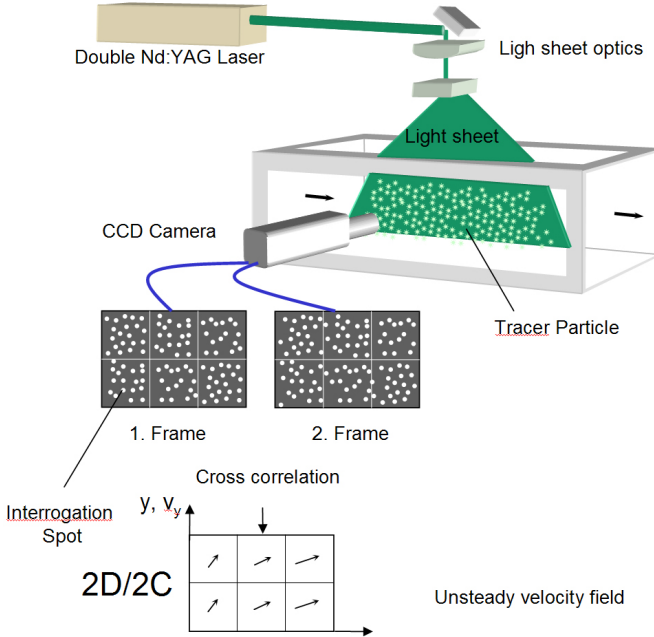


Figure 9.1: General PIV setup [129].

or generalized phantom models of for example an idealized arterial stenosis [130] or aneurysm [131], PIV validation is applied on a large scale in the field of medical devices as central venous catheters [98], blood pumps [132–135], stents [136] or artificial heart valves [137–139]. Even when shifting to anatomical realistic models, like in studies focusing on the validation of patient specific aneurysms [140] or stenosis regions [141], a good agreement between *in vitro* measurements and computational results was found.

Two studies were performed: (i) a large multi-center study, in which they compared different PIV algorithms on pre-defined models [142], and (ii) a FDA's 'Critical Path' Computational Fluid Dynamics (CFD) / Blood Damage Project, in which the use of PIV analysis in the CFD validation process is studied [143]. Both studies concluded that PIV is capable to measure accurately the mean (time-averaged) velocities, if the fluctuations in the flow conditions and the fluid properties are minimized.

9.1.2 Experimental assessments on silicon tube models

If a more general assessment of a hydraulic circuit is needed, a silicon model can be constructed. The silicon model does not need to be transparent, as for

PIV, because it will be used in a hydraulic bench test for pressure and flow evaluations. Once the silicon model is constructed, it can be coupled to a stationary or pulsatile pump, with or without adding some flow splits, windkessels or resistances (clamps) before or after the model ending. A setup is mostly ended with an open outflow or with constant height outflow reservoirs (Figure 9.2). The windkessel, when proximal, can be used to adjust the pulse pressure entering the model (damping) or when used distal from the model to mimic the peripheral compliance. The height of the outflow reservoirs can be set to achieve a constant pressure boundary condition. Outflow distribution can be changed by opening or closing the clamps.

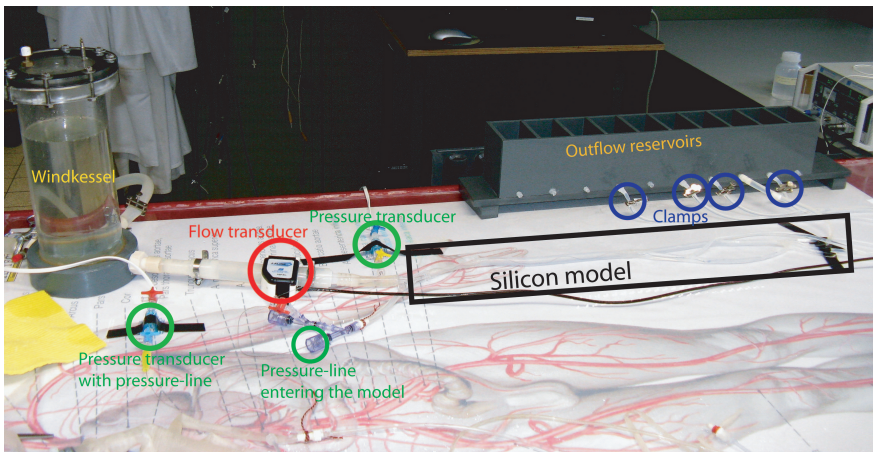


Figure 9.2: Example of experimental setup consisting of a pump (not shown), a windkessel, connecting tubes, the silicon model, clamps and outflow reservoirs. Pressure measured by a pressure transducer with pressure-lines and flow measured by a flow transducer.

To measure the pressure in a model, there are two options. Firstly, needles can be placed in the model, perpendicular to the silicon tube wall. Secondly, fluid-filled epidural catheters (pressure-lines)(Portex Epidural Catheter, Smiths Medical ASD inc., Keene, US) can be slid through the lumen of the model. With the pressure-lines, it is possible to measure the pressure on different locations without damaging the lumen. The needles or pressure-lines are connected to a calibrated fluid-filled pressure transducer (e.g. P10EZ-1 or DT-X PLUS (Becton Dickinson, Franklin Lakes, NJ, US)) which on its turn is connected to a DAQ-unit to process the pressure data.

Flow rates can be measured by volumetric measurements (collecting the fluid outflow for a period of time). Next to this very robust and reliable

method, it can be necessary to monitor and analyze the instantaneous flow rate over time. Therefore a flow transducer (e.g. Transonic flow meter Team 21 Compatible (Transonic Systems Inc., Ithaca, NY, US)) is clamped onto the circuit.

Next to the pressure and flow measurements, collecting geometrical data is important, especially when using the experiment to validate computational results. Most geometrical data can be collected with simple rulers. When for example the diameter at working pressure or the diameter change during a pressure change is needed, an ultrasound system (e.g. Picus ultrasound system, ESAOTE B.V., The Netherlands) can be used with, if necessary, some wall-tracking software (e.g. ArtLab, ESAOTE B.V.). For exact model reconstruction, high resolution X-ray Computed Tomography (micro-CT) can be used with a voxel size down to $210\text{ }\mu\text{m}$.

To have a full set of experimental data, one should determine the fluid characteristics. Viscosity can be measured with a capillary Ubbelohde viscometer (Schott, Germany). Hereby, a U-shaped glass tube is filled with a fluid and placed in a reservoir with controlled temperature. The time needed for the fluid to flow (by gravity) between 2 predefined markers on the capillary is taken. This time can then simply be multiplied by the calibration factor of the specific glass tube to obtain the kinematic viscosity. The density of the fluid on the other hand can be measured by filling a constant volume flask and comparing its weight with the weight of the flask filled with purified water.

Because fluid characteristics might change with temperature (Section 8.1), it is important to monitor the fluid working temperature during the experiments. When for example a mixture of water-glycerin is used, the viscosity can decrease from $8.1\text{ mPa}\cdot\text{s}$ to $6.9\text{ mPa}\cdot\text{s}$ if the temperature increases slightly from 18 to $22\text{ }^{\circ}\text{C}$ (51% glycerin-water mixture).

9.2 NUMERICAL METHODS

9.2.1 Computational Fluid Dynamics (CFD)

Computational Fluid Dynamics is a computational method to calculate all fluid dynamics (flow, pressure, heat,...) in a well defined domain, with well defined boundary conditions. A flowchart with the different steps in CFD analysis is shown in Figure 9.3.

The model is, in the field of biomedical engineering, mostly drawn in a CAD program (e.g. SolidWorks (Dassault Systèmes SolidWorks Corpora-

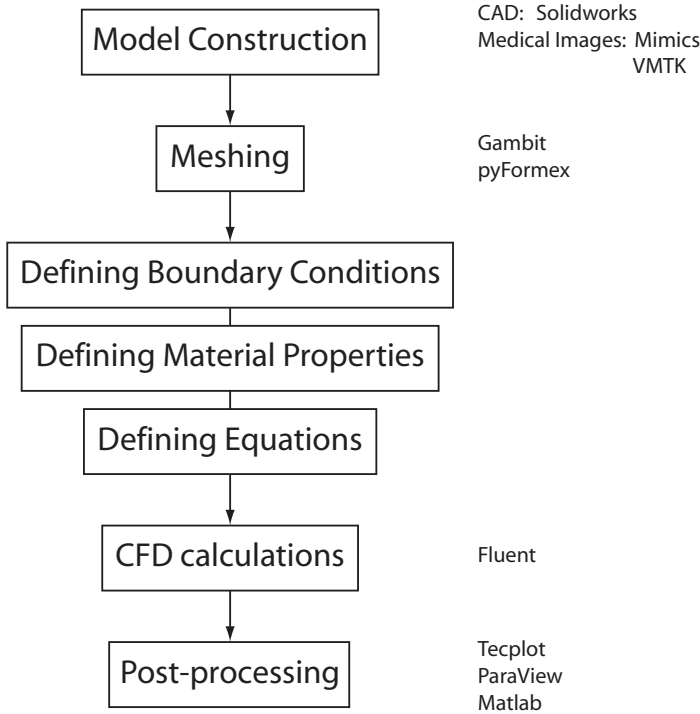


Figure 9.3: Flowchart of Computational Fluid Dynamics analysis with examples of the used programs in this work.

tion, Concord, MA, US)) or reconstructed from medical images (CT-scans) (e.g. Mimics (Materialise, Leuven, Belgium) or vmtk¹).

Before CFD calculations can start, the fluid domain is split into a discrete number of cells (meshing). These volume elements can be either large (coarse mesh) or small (fine mesh) according to the fluid domain. The cells can have different shapes as tetrahedrons, hexahedrons or prisms. The meshing process can be done in either commercially available packages as Gambit (Ansys Inc., Canonsburg, PA, US) or open-source programs as pyFormex².

Once the domain is meshed, the boundary conditions and material (fluid) properties should be defined. At the wall of the domain (e.g. the vessel wall), mostly, a no-slip condition is applied, assuming that the velocity at the wall is zero. At the entrance of the model, a constant or non-constant (e.g. periodic signal (heart rate) flow rate or velocity can be applied either

¹<http://www.vmtk.org>

²<http://pyFormex.org/>

as plug or Poiseuille profile (see Section 8.3.2). At the outflow tracts of the domain, a flow distribution can be applied or a pressure or velocity can be imposed. For the used fluid, viscosity and density should be defined.

Within all cells (finite volume method), the equations of conservation of mass and momentum are calculated in relation to the neighboring cells; most often, the Navier-Stokes equations (sometimes added with the conservation of energy) are used (Eq.8.23). For the CFD calculations reported in this work, the commercial program Fluent (Ansys Inc., Canonsburg, PA, US) was used.

If the iterative computations of these equations converge, with low residuals, the flow and pressure field can be analyzed (example in Figure 9.4). In this post-processing stage, derivatives of these results, e.g. wall shear stress (See Section 8.3.4) can be calculated. Analysis can either be done directly in Fluent, in the post-processing software ParaView (<http://www.paraview.org>) or Tecplot (Tecplot inc, Bellevue, WA, US) or even in general programs as Matlab (The Mathworks, Natick, MA, US).

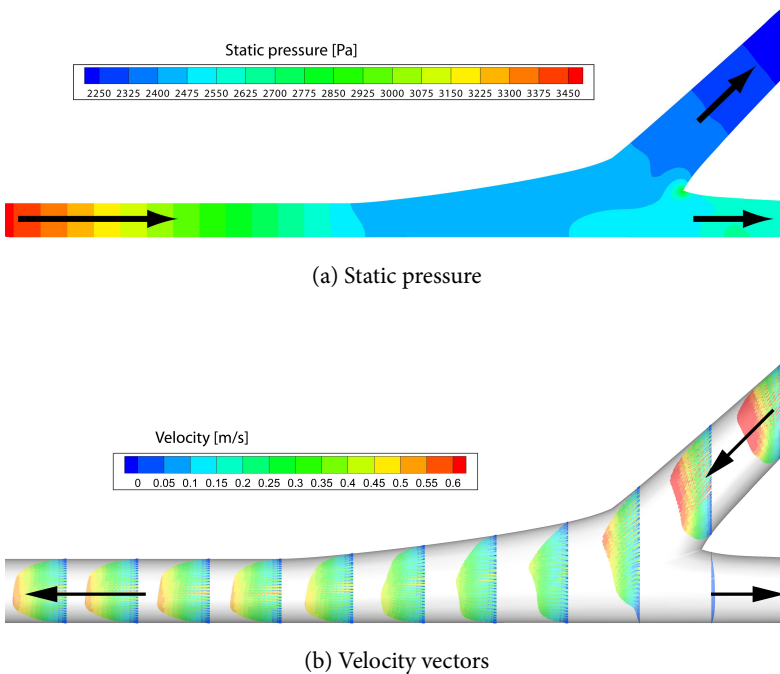


Figure 9.4: Arterial (top) and venous (bottom) anastomosis of an AVG configuration.

9.2.2 Kinetic modeling

In general, kinetic modeling describes the variation in time of a physical entity (e.g. mass, energy) which is exchanged among different systems, or between a system and the environment. This dynamic process is ruled by a driving force.

The human body can be considered as a biological system, consisting of different anatomical compartments, which are separated by semi-permeable membranes. Approximately 58% of the human body consists of water, which is divided over the extracellular (plasma water and interstitial water) and intracellular compartments. Transport between the different compartments can happen passively by free diffusion of non-loaded particles (e.g. water, oxygen, urea) or loaded particles (ions), and by forced diffusion via carriers or channels. Next to a passive, concentration driven process, transport can also occur as an active process where the energy is supplied by the ATP (Adenosine TriPhosphate), or as secondary active transport according to an electrochemical gradient.

To describe physiological processes in the human body mathematically, the body can be divided in different compartments which not necessarily correspond to an anatomical reality and in which a physical entity is considered uniformly distributed over the compartmental volume.

Such a kinetic model might consist of a large number of arbitrarily small compartmental entities, necessitating a statistical description. The resulting formula is then not based on fundamental physical principles, but is derived from (multiple) linear or non-linear regression analyses. However, an important limitation of these statistical models, is that predictions can only be safely made for the parameters that are clinically measured. Instead, in most cases, a mechanistic model with a limited number of compartments might be sufficient to describe solute kinetic behavior. The advantage of mechanistic models is that predictions beyond the scope of the examined parameters are more robust as these models are based on fundamental physical principles such as the conservation of mass and the conservation of energy.

So a pure mathematical non physiology-based model following the classic pharmacokinetic approach can be used. This model may consist of one, two or several compartments/pools (double pool example in Figure 9.5). Each compartment is characterized by a homogenous internal solute concentration (C_1, C_2, \dots) and a distribution volume (V_1, V_2, \dots), all changing in time caused by different transport processes: input (I) and output (O) (i.e. defined as an interaction in between compartments and/or the environment), and solute generation (G) and/or elimination (E) (i.e. defined as taking place inside the compartment). The mass input and output might be

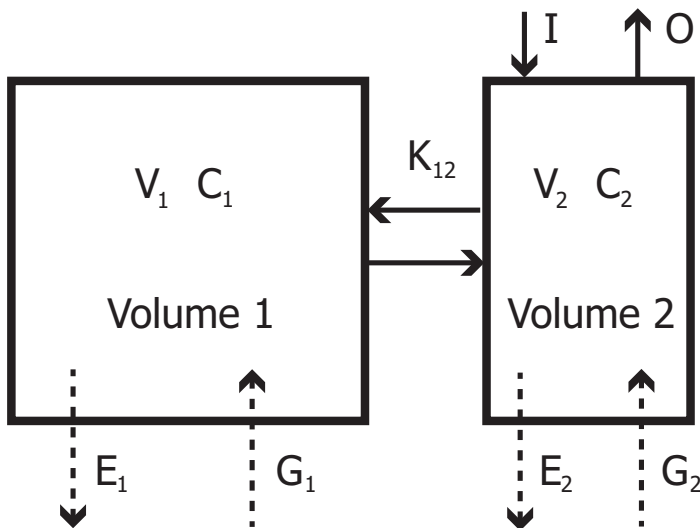


Figure 9.5: General representation of a double pool kinetic model. V: Volume; C: Concentration; G: Generation; E: Elimination; I: Input; O: Output and K_{12} : Inter-compartmental clearance.

proportional to the concentration itself (clearance K) or to the concentration difference (intercompartmental clearance K_{12}).

Finally, for each compartment separately, the mass balance is written as a differential equation. In case of more than one compartment, the differential equations should be solved simultaneously and treated as a coupled mathematical problem. From the representation in Figure 9.5, the basic equations can be defined as:

$$\frac{d(V_1 C_1)}{dt} = G_1 - E_1 + K_{12} \cdot (C_2 - C_1) \quad (9.1a)$$

$$\frac{d(V_2 C_2)}{dt} = G_2 - E_2 + I - O - K_{12} \cdot (C_2 - C_1) \quad (9.1b)$$

In the field of hemodialysis treatment, kinetic modeling can be applied in two different ways: identification of the unknown model parameters (i.e. calibration of the kinetic model), or simulation of intra and/or interdialytic parameters using an already calibrated kinetic model.

Identification is based on the determination of the unknown model parameters by fitting the solution of the (coupled) mass balance equation(s) to the clinically measured blood or plasma concentrations at different time

points during dialysis. Problems with identification might arise when too many parameters are unknown and the measured concentration data set is too small to yield enough accurate information. Calibration has been performed previously in the context of hemodialysis for β_2 -microglobulin (β_2M) by Stiller et al. [144], for phosphate by Spalding et al. [145] and for urea and guanidino compounds by Eloot et al. [146].

Once a calibrated kinetic model is available, simulations can be achieved, predicting the time course of solute concentration for future time points. Hence, simulations allow the comparison of solute removal and/or time-averaged concentrations when applying different dialysis strategies.

Three

Studies on AVFs

Computational study of flow in AVF anastomoses

K. Van Canneyt, T. Pourchez, S. Eloot, C. Guilleme, A. Bonnet, P. Segers
and P. Verdonck.

*Hemodynamic impact of anastomosis size and angle in side-to-end
arteriovenous fistulae: a computer analysis.*

Journal of vascular access. vol.11. 2010:52-58.

10.1 INTRODUCTION

The efficiency of hemodialysis treatment for end-stage renal disease patients is to a great extent dependent on the quality of the vascular access. In general, the most appropriate way of establishing a vascular access is by creating an arterio-venous fistula (AVF) as first described by Brescia et al. in 1966 [28] or a modification to this approach. However, as the construction of this autologous connection between the arterial and venous network is still the underlying cause of many clinical complications, optimization of the vascular access is the subject of many ongoing and finished studies as described by Cimino [29].

Nowadays, most clinicians start from the idea of an AVF as a 6 segment circuit consisting of the proximal artery (1), the distal artery (2), arterial collaterals (3), the proximal vein (4), the distal vein (5) and venous collaterals (6). However, to have a total hemodynamic description of the AVF, it is important to insert at least a seventh segment in the flow path, the anastomosis itself. The 7 segment approach is schematically illustrated in Figure 10.1.

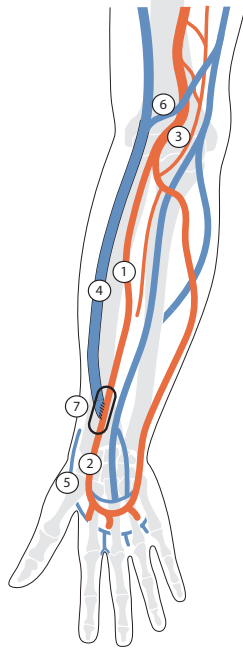


Figure 10.1: Seven segment AVF circuit: Proximal artery (1); distal artery (2); arterial collaterals (3); proximal vein (4); distal vein (5); venous collaterals (6) and arterio-venous anastomosis (7).

Given the virtually total absence of studies addressing the geometry of the anastomosis in the setting of an AVF, it can be stated that this is an aspect largely disregarded as a potentially determining factor of the access flow. Therefore, the present study was set up to study in detail the uncoupled effect of the anastomosis angle and anastomosis size in the setting of arterio-venous fistulas. With Computational Fluid Dynamics (CFD), the pressure drop and flow distribution curves were calculated and stream line patterns were studied [147, 148] in order to have an in depth insight in the access flow and the flow field at the anastomosis.

10.2 MATERIAL AND METHODS

A 3-D geometry of a matured side-artery-to-end-vein AVF was designed consisting of an artery with a diameter of 4 mm connected to a vein with a diameter of 6 mm (Figure 10.2). The connection was made by an anastomosis with given angle (A) and cross-sectional area (CSA), assuming an ellipsoidal cross-section with a given anastomosis length (L) and width (W). Steady flow in the geometry was assumed, following Sivanesan et al. [149].

All AVF models were constructed on an *in vivo* scale in the CAD package SolidWorks 2005 (SolidWorks Corporation, Concord, MA, U.S.A.) and exported into the grid generation software Gambit 2.2 (Ansys Inc., Canonsburg, PA, U.S.A.) via the IGES (Initial Graphics Exchange Specification) data format. The mass and momentum conservation equations are discretized and solved in the CFD package Fluent 6.3 (Ansys Inc., Canonsburg, PA, U.S.A.) after prescribing all boundary conditions. In the CFD-model, the blood flow is treated as 3-D, non-pulsatile, laminar, Newtonian (dynamic viscosity of 3.5 mPa.s representing a hematocrit around 40% [116]) and incompressible [150]. The post processing of the CFD results was executed using Tecplot 360 (Tecplot inc., Bellevue, WA, U.S.A.). Regression analysis, fitting a quadratic relation to the data, was used to assess the pressure drop results. Goodness of fit was expressed by the R^2 value. Analysis was done using SigmaPlot 10.0 (Systat Software Inc., San Jose, CA, U.S.A.). Our study addressed two issues: the impact on hemodynamics of the size and the impact on hemodynamics on the angle of the anastomosis.

10.2.1 Substudy 1: impact of anastomosis size on hemodynamics

The reference geometry for this first substudy, serving as point of comparison for all results, was an anastomosis characterized by $A = 30^\circ$, $L = 6$ mm and $W = 4$ mm ($CSA = 18.8$ mm²), with 900 ml/min inflow at the arterial inlet (Q_{ai}) and with a flow distribution of 8% and 92% towards the arterial outlet (Q_{ao}) and venous outlet (Q_{vo}), respectively (see also Figure 2).

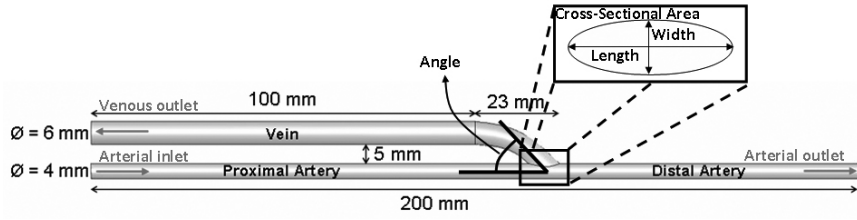


Figure 10.2: Reference arterio-venous fistula configuration.

The anastomosis size varied using geometries (LxW) of 8x2, 6x3, 8x3, 6x4 and 10x3 (L and W in mm), resulting in a cross-sectional area of 12.6 mm², 14.1 mm², 18.8 mm², 18.8 mm² and 23.6 mm², respectively.

We first calculated the flow field and pressure drop over the anastomosis for 5 different anastomosis geometries, imposing five different flow rates (600, 750, 900, 1050 and 1200 ml/min) but maintaining a fixed flow distribution of 8% arterial versus 92% venous outflow. The pressure drop over the anastomosis was calculated from the area-averaging static pressure at 25 mm from the anastomosis in the proximal artery and proximal vein.

Second, we ran an additional series of computer simulations to determine whether the anastomosis size also affects the flow distribution. To do so, the inlet and outlet pressures of the artery (P_{ai} , P_{ao}) and outlet pressure of the vein (P_{vo}) in the reference cases were considered as general conditions.

10.2.2 Substudy 2: impact of anastomosis angle on hemodynamics

Reference for this substudy is an anastomosis characterized by $A = 53^\circ$, $L = 6$ mm and $W = 4$ mm ($CSA = 18.8$ mm²), with 900 ml/min inflow at the arterial inlet (Q_{ai}) and with a flow distribution of 8% and 92% towards the arterial (Q_{ao}) and venous outlet (Q_{vo}), respectively. The anastomosis angle was varied over 27° , 34° , 45° , 53° , 63° , 76° and 90° , a clinically relevant range [149].

Again, simulations were first done imposing different flow rates (with a constant flow distribution) while studying the pressure drop over the anastomosis for the different angles, followed by simulations with fixed pressure boundary conditions and studying the effect of the angle on the flow distribution towards arterial and venous outlet.

10.3 RESULTS

10.3.1 Substudy 1: impact of anastomosis size

Figure 10.3a shows the pressure drop over the anastomosis for a fistula flow range of 600 to 1200 ml/min for different anastomosis sizes, but fixed anas-

tomosis angle of 30° . As anticipated, the pressure drop decreases with increasing anastomosis cross-sectional area. For the smallest anastomosis size ($L = 8$ mm, $W = 2$ mm, $CSA = 12.57$ mm²), the pressure drop varies from 8.1 mmHg (Q_{ai} 600 ml/min) to 30 mmHg (Q_{ai} 1200 ml/min), while for the case with the largest CSA, ($L = 10$ mm, $W = 3$ mm, $CSA = 23.6$ mm²) the pressured drop starts from 5 mmHg (Q_{ai} 600 ml/min) to rise up to 18.6 mmHg (Q_{ai} 1200 ml/min). The case of $L = 8$ mm and $W = 3$ mm is almost similar to the case of $L = 6$ mm and $W = 4$ mm. This is due to the fact that both cases have the same cross-sectional area ($CSA = 18.8$ mm²).

Figure 10.4a shows the effect of anastomosis size on the flow distribution for fixed pressure boundary conditions. For increasing anastomosis size, the arterial inflow increases to finally stabilize from a CSA of 20 mm² on. Furthermore, it is also clear from figure 4a that flow distribution is shifted towards the venous outflow when the anastomosis size increases. For a CSA of 12.6 mm², the flow distribution towards the arterial and venous outlet is 22% and 78%, respectively, while these numbers shift to 5% and 95% for $CSA = 23.6$ mm².

10.3.2 Substudy 2: impact of anastomosis angle

Figure 10.3b shows the pressure drop for different anastomosis angles for a fixed anastomosis size of 6 mm x 4 mm ($CSA = 18.9$ mm²). The pressure drop slightly increases for increasing anastomosis angle from 26° over 33° to stabilize at 45° . For anastomosis angle from 45° up to 90° , the pressure drop decreases significantly. The maximal difference in pressure drop among cases of different anastomosis angle at 1200 ml/min is 12.8 mmHg, which is in the same range as in the parameter study for the anastomosis size of Figure 10.3a (11.4 mmHg). Among the studied geometries, the maximal pressure drop is obtained for the 45° anastomosis (24.1 mmHg).

It can be seen in Figure 10.4b that venous outflow reaches a minimum around 43° anastomosis angle, while it is continually increasing for larger angles. Even for an anastomosis angle of 58° , the venous outflow exceeds the proximal arterial inflow, and with it, the flow in the distal artery changes direction.

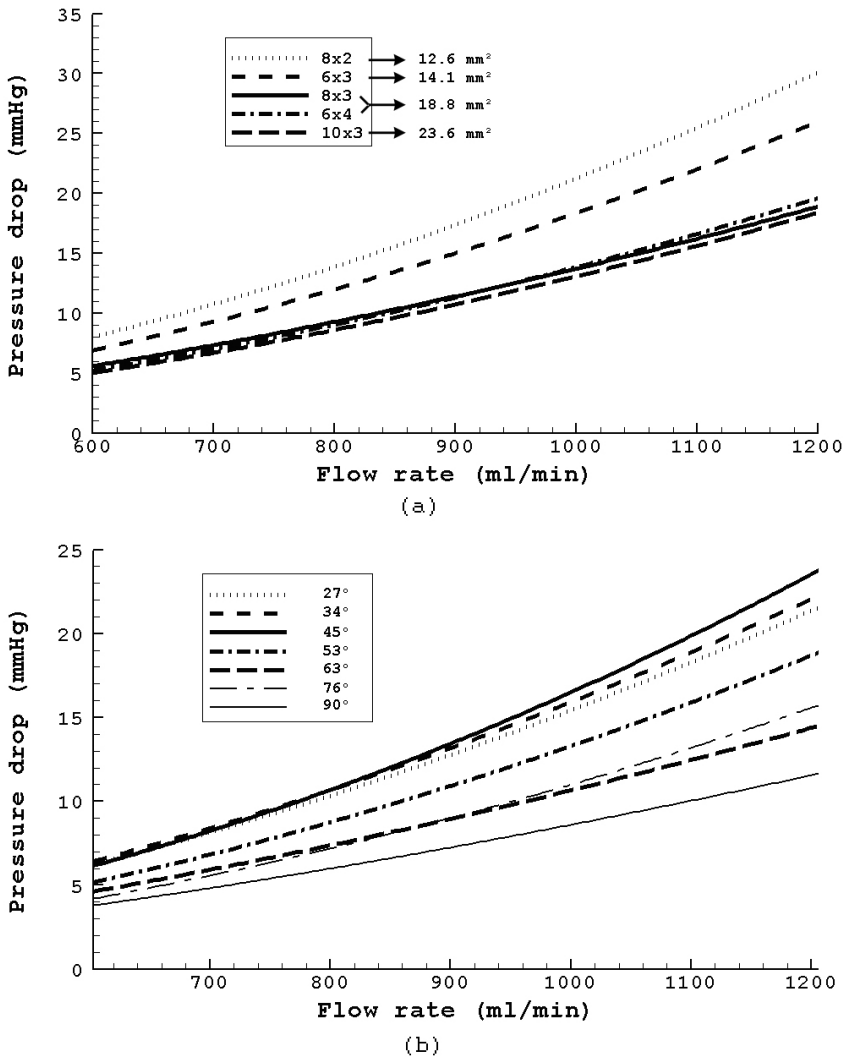
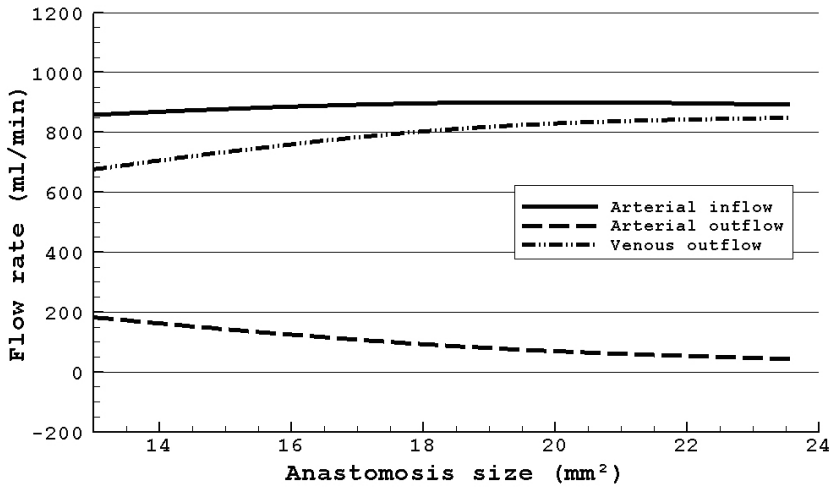
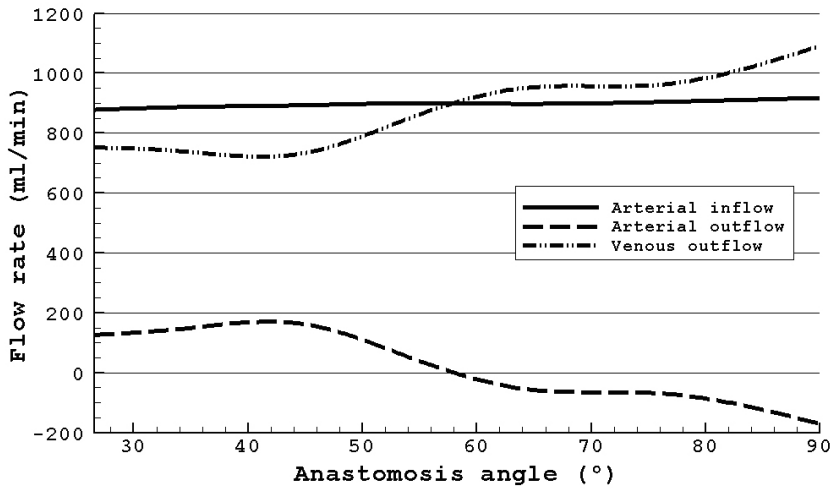


Figure 10.3: (a) Pressure drop over anastomosis versus blood flow rate for different anastomosis sizes (Length x Width, both in mm), anastomosis angle fixed at 30°. (b) Pressure drop over anastomosis versus blood flow rate for different anastomosis angles, anastomosis size fixed at 6x4 (CSA = 18.8 mm²).



(a)



(b)

Figure 10.4: (a) Flow rate at arterial inlet, outlet and venous outlet for different anastomosis sizes, starting from reference case $L = 6$ mm; $W = 4$ mm and $A = 30^\circ$. (b) Flow rate at arterial inlet, outlet and venous outlet for different anastomosis angles, starting from reference case $L = 6$ mm; $W = 4$ mm and $A = 53^\circ$.

10.4 DISCUSSION

Although several *in vitro* and computational studies [147, 148] already investigated the flow in AV-fistulas, none of them focused, according to our knowledge, on the hemodynamic impact of the geometry of the anastomosis. Therefore, the present study was set up to assess the importance of the AVF-anastomosis geometry by calculations of flow distribution and pressure drop at the anastomosis site.

The 6 segment approach (not taking into account the anastomosis) is reported in detail in literature overviews, describing AVF-complications and solutions [151, 152]. When, for example, an ischemic case is presented (where blood flow towards the hand is too low because of a too high AVF flow), suggested solutions are DRIL (distal revascularisation-interval ligation) [47, 48], PAI (proximalisation of the arterial inflow) [49] or RUDI (revision using distal inflow) [50] to create a longer flow pathway, besides banding (the narrowing of the initial draining vein) [51–53] and even creating an artificial stenosis in the draining vein [54]. Those are different solutions, aiming to increase the AVF flow resistance, and with it, to decrease access flow and/or increase pressure in the distal artery.

In this study, we focused on the 7th segment, the anastomosis itself, as a very important factor in the AVF hemodynamics. In this approach, there is a clear distinction between the pre- (6 element) and the postoperative (7 element) system. Before AVF creation, the main pressure drop between the high proximal artery pressure and the low proximal vein pressure is situated in the distal microcirculation and capillary bed. After creation of an AVF as vascular access, the high pressure in the proximal artery is maintained by the sympathetic reflex which increases the cardiac output and the enlargement of the feeding vessels. On the other hand, the low pressure in the proximal vein is maintained by the enlargement of the draining veins. However, the main pressure drop is now, in the ideal case, situated over the anastomosis. In this case, a high arterial pressure and a low venous pressure are maintained.

A chronically large anastomosis size causes a small anastomosis resistance. This small resistance will probably result in a high flow in the vascular access and the 'main' pressure drop will now be divided over the anastomosis and a narrowing of the vascular system. This high flow can trigger ischemia. The model of Barnes et al. enlightened that ischemia is avoided when the ratio of the resistances of the anastomosis versus proximal artery is smaller than the ratio of the resistances of the distal bed versus the arterial collaterals [153]. In the opposite situation, the possibility of flow reversal and ischemia is significant. Some authors suggest, as ideal solution for these

high flow cases, the closure of the large anastomosis and the creation of an anastomosis with a more appropriate size [153, 154]. But, on the contrary, in *in vivo* studies where analogous boundary conditions are meant to be created, anastomosis length (length of surgical incision) variations of 25% are permitted [155] and the hemodynamic impact of the anastomosis size seems neglected. This study shows that this change in anastomosis size has a large and underestimated impact on blood flow and local pressures.

Beside the size of the anastomosis, a second parameter determining anastomosis resistance is the angle of the anastomosis, as it will highly determine the local velocity field and hemodynamics, and hence the energy dissipation (pressure drop) over the anastomosis. In literature, the impact of the angle of an anastomosis has been studied in numerical, *in vitro* and *in vivo* studies in the domain of distal leg artery bypasses [156], human aorta bypasses [157] and pig aorta bypasses [158], but not in the context of AVF. Although the study of Chua et al. is using the configuration similar to the side-to-end AVF, the applied geometry has a very small graft-to-artery diameter ratio of 0.3 [157].

Because of the lack of studies dealing with the anastomosis resistance, the present study focused on the anastomosis size and anastomosis angle. It can be observed from our results that the pressure drop rises quadratically with increasing flow rate (all curves with R^2 -values above 0.99) and that, as expected, the pressure drop decreases with increasing anastomosis size. The quadratic term superimposed on the linear term (as observed in Hagen-Poiseuille flow) in the pressure drop curves is due to the secondary flow at the anastomosis site. This secondary flow can be seen in Figure 10.5(a-c). In the case of 90° , it is clear from Figure 10.5c that at the inner wall, a low flow zone appears. This can also be seen as a low wall shear stress (WSS) zone in Figure 10.5f, which may lead to a region with increasing intimal hyperplasia and stenosis formation. Figure 10.5c and 10.5d show a WSS distribution with higher peak values and less significant low value zone.

In the cases exceeding 58° of anastomosis angle, reverse flow in the distal artery is present. It should be noted that this 'steal' can lead to the distal hypoperfusion syndrome [159, 160] and results in ischemia [44, 161].

As limitation of the present study, it can be brought up that the used geometries and boundary conditions are a simplification of the complex cardio-vascular human anatomy and physiology. For example, the study of the cardiac adaptation (with the heart as the eight component of the circuit) was neglected. The model represents an ideal anastomosis without taking in consideration parameters as athero- and arterio-sclerosis and intimal hyperplasia formation, loss of wall distensibility, elasticity of the venous wall, endothelial dysfunction, AVF maturation and repeated cannulation,... But on

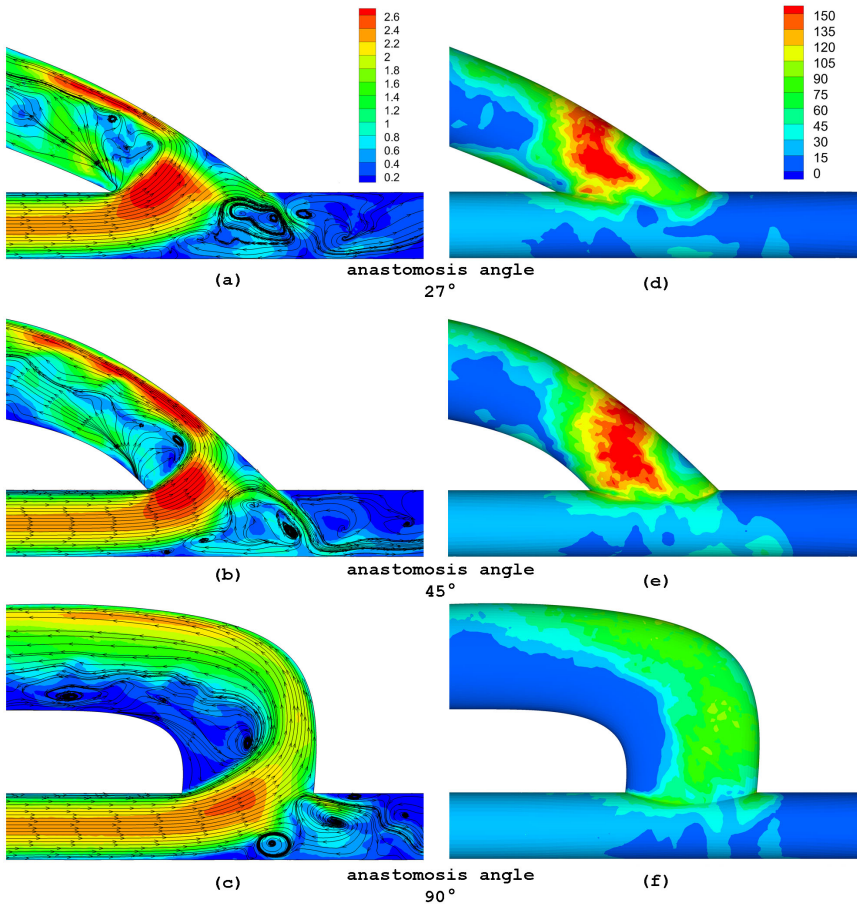


Figure 10.5: Left: Velocity magnitude [m/s] and in-plane streamlines (sagittal plane); Right: Wall shear stress [Pa] on the wall surface at the anastomosis side. All figures for inflow rate of 1200 ml/min: (a, d) 27°anastomosis angle; (b, e) 45°anastomosis angle and (c, f) 90°anastomosis angle.

the other hand, the idealized model allowed us to study the separated local hemodynamic impact of the anastomosis angle and size, hereby uncoupling anastomosis size and angle from each other and from other anatomic and physiologic factors. This is, obviously, different from clinical reality where the anastomosis angle and size are not totally independent, but a compromise of what is achievable in a given patient with a given arterial and venous territory.

The used non-parametric models and relative basic CFD calculations can be seen as a limitation, but do however not change the overall message

and conclusion of this study. Numerical values shown in Figures 10.3 and 10.3 cannot be seen as absolute values but more as indicative values to show the global trend of pressure drop and flow distribution variation in changing anastomosis dimensions. CFD is a well-established technique and it can be noted that the *in vitro* validation of CFD modeling has already been done in many other cases, among others in the field of vascular accesses (as in Section 11.2). Furthermore, it can be remarked that the anastomoses were oval shaped, due to minimize computational geometric and calculation errors. The side-artery-to-end-vein configuration was chosen in this study in favor of the side-to-side alternative, because the choice of anastomosis size and angle is more pertinent in the creation of this AVF [162].

Finding an optimal anastomotic length for a fistula, usable for all patients, is unrealistic due to the varying, patient-specific anatomic and physiologic conditions. As general idea should it always be kept in mind that the main pressure drop in the arterio-venous circuit should be over the anastomosis to avoid high pressure in the venous system and distal ischemia problems. A too small anastomosis on the other hand will have a tendency to non-maturation or poor flow during dialysis session.

From our clinical practice, the best anastomosis length at the wrist or forearm is probably 7 mm for small vessels. Evolving towards an elliptic shape after maturation and therefore taking 3 to 4 mm of width, an anastomosis size of 16.5 to 22 mm² can be found. These sizes are comparable with the results of lower pressure drop and higher venous outflow as seen in Figure 3a and 4a. The angle is, in most cases, easy to make with 30 to 45°, depending on the anatomy. The aim of making an angle of about 135° is demanding more vein length and was therefore also taken out of the computational study. For vessels already dilated, and especially for arteries, with a diameter more than 5 mm, the length is best about 5 to 6 mm. These lengths give an anastomosis size between 11.8 to 18.5 mm² (for 3 or 4 mm of width), resulting in the higher pressure drop values in Figure 3a. A longer anastomosis will cause too much flow in these cases, from our clinical experience. At the elbow, the reasoning mentioned for dilated, large, arteries can be used. So anastomosis lengths from 5 or 6 mm are the most appropriate choice. The angle to choose is depending on the anatomy, and should vary from 25 to 90°. For very big vessels at the elbow, the length ought to be 4 mm to avoid distal ischemia and the evolution toward a very high flow fistula. Finally, one should keep in mind that the initial size of the anastomosis and the vessels might change during maturation.

10.5 CONCLUSION

While the hemodynamic impact of the anastomosis size and angle of an AVF is in many studies and daily practice largely underestimated, we have shown in this computer analysis that the flow distribution and pressure drop change significantly with anastomosis size and angle. The results prove that the AV-anastomosis should be considered as an important and full component of the total AVF flow circuit. In particular, it is shown e.g. that a change of 2 mm in anastomosis length can increase the pressure drop by more than 30%. Therefore, in the surgical creation of an AVF as vascular access, the anastomosis geometry should be chosen with care while keeping in mind the impact of the geometry on pressure drop and flow distribution, both during creation of a fistula as during complication solving interventions.

Experimental validation

W. Huberts¹, K. Van Canneyt¹, P. Segers, S. Eloot, J.H.M. Tordoir,
P. Verdonck, F.N. Van de Vosse and E.M.H. Bosboom.

*Experimental validation of a pulse wave propagation model for predicting
hemodynamics after vascular access surgery.*
Journal of Biomechanics. vol.45(9). 2012:1684-1691.

L. Botti¹, K. Van Canneyt¹, R. Kaminsky, T. Claessens, R.N. Planken,
P. Verdonck, A. Remuzzi and L. Antiga.

*Validation of a high flow rate hemodynamics solver on a patient-specific
model of vascular access for hemodialysis.*
Submitted.

¹Both authors equally contributed.

11.1 EXPERIMENTAL VALIDATION OF PULSE WAVE PROPAGATION MODEL

11.1.1 Introduction

Hemodialysis is a common treatment for end-stage renal disease (ESRD) patients [9, 10]. To facilitate hemodialysis, a well-functioning vascular access is needed. The vascular access should be able to provide a high blood flow and should be easily accessible for repeated cannulation over time [21, 25]. The preferred vascular access is an arterio-venous fistula (AVF) in the arm, which is a surgically created connection between artery and vein (anastomosis), resulting in a significant flow increase (up to thirtyfold) and vessel remodeling [19, 21, 25, 26].

The AVF is usually created three months prior to initiation of hemodialysis either at wrist level (lower arm AVF) or at elbow level (upper arm AVF) [44, 163–165]. In current clinical practice, the selection is based on the patient's medical history and the caliber of the involved vessels, i.e. when the caliber of the radial artery and the distal cephalic vein assessed by duplex ultrasound exceed 2 mm a lower arm AVF is created, otherwise an upper arm AVF. Despite the preoperative diagnostics, complications after AVF creation occur frequently. Lower arm AVFs are hampered by non-maturation in up to 50% of all cases which implies that six weeks after surgery, either the AVF is not dilated sufficiently, the blood flow is too low, and/or the AVF is located too deep [19, 21, 25, 26, 44, 166]. Upper arm AVFs are hampered by long-term complications like distal ischemia and/or cardiac failure in 20% of all cases [21, 25, 44, 166].

To reduce the number of complications, tools to optimize the location for an individual patient are therefore of interest. Since a too low brachial flow directly after surgery is associated with non-maturation [26, 167] and since an immediate postoperative flow larger than 30% of the cardiac output is associated with distal ischemia and cardiac failure [44, 163–165], it might be beneficial for surgical decision-making to have a tool that is able to provide, preoperatively, a quantitative patient-specific estimate for the immediate postoperative flow.

Previously, a (distributed lumped parameter) pulse wave propagation model was developed that is able to simulate pressure and flow waveforms after both upper and lower arm AVF surgery [168]. This computational model, that is fed by patient-specific data was used to predict immediate postoperative mean flows in ten ESRD patients. It was shown that the model selected the same AVF location as an experienced surgeon in nine out of ten patients. However, the postoperative flow measured by Doppler ultrasound was only adequately predicted in six out of ten patients. Differences between model

predictions and measurements might have several reasons. First, the accuracy of the measured flows, input data and boundary conditions might limit the correspondence between the simulated and measured flows. Second, the model neglects vascular adaptation and autoregulation of the peripheral bed which might result in differences between measured and predicted flows. Another reason might be that the physical description of the pulse wave propagation of the pressures and flows is incomplete.

The only way to determine if the physical description is complete, is by validating the pulse wave propagation model with an experimental setup which mimics the surgical AVF procedure and gives the possibility to determine a larger number and more accurate mechanical, geometrical and hemodynamic (pressure and flow waveforms) data than would be possible in an *in vivo* situation [169, 170]. In addition, vascular adaptation and regulation of the peripheral beds are excluded and do not influence the comparison of experimental and simulation results. Furthermore, the experimental setup can be used to validate the simulated pressure and flow waveforms which are needed when adaptation laws will be included in future work.

For arteries, *in vivo* and experimental validation studies for pulse wave propagation models [169–173] have been performed. However, these study mainly focused on the systemic arterial tree with arterial flows much smaller than the flow after AVF creation. No validation study is reported that validates a pulse wave propagation model simulating the extreme flow increase after AVF surgery. Moreover, the propagation of measurement uncertainty in the model input to uncertainty in the model output (i.e. precision) was not analyzed previously. However, a quantitative estimate of the precision is required for a proper comparison as well as when inferences based on model predictions will be made. The output uncertainty can be assessed by using a method based on generalized chaos expansion [174] or by means of Monte Carlo simulations [175]. The advantage of the method of Xiu et al. is that less model runs are needed than for Monte Carlo simulations. However, the implementation is less straightforward since the model equations are made stochastic and the most suitable polynomials for expansion of the stochastic function need to be selected.

The aim of this study is to validate the previously developed distributed lumped parameter pulse wave propagation model for the prediction of pressure and flow before and after AVF creation. In this way it is determined if the physical description of the pulse wave propagation is correctly captured by the model. The uncertainty in pressure and flow waveforms, resulting from uncertainties in the model input parameters, is accounted for by using Monte Carlo simulations.

The manuscript is outlined as follows. First, the experimental setup is described and how mechanical, geometrical and hemodynamic properties are determined. This is followed by a brief description of the distributed lumped parameter pulse wave propagation model. Next, it is discussed how the model was adapted to the experimental conditions and how the model was validated with the experimental setup. In this context, the uncertainty analysis is described in detail.

11.1.2 Material and methods

In vitro experimental setup

Previous studies that used an experimental setup consisting of silicone tubes to validate a pulse wave propagation model mainly focused on the systemic arterial tree [170, 173] or single arterial tubes [172]. In addition, the simulated arterial flows were much smaller than the flows in the arm after AVF creation. In this study, a pulse wave propagation model is validated that simulates the flow increase after AVF surgery. Furthermore, the hemodynamical complex anastomosis is incorporated in this experimental study, whereas this was not addressed earlier in a silicone tube network.

The experimental silicone tube model, mimicking the anatomy and physiology of the human vasculature in the arm, was built based on patient-specific data obtained in a previous study [168]. The arterial geometrical data, obtained from magnetic resonance (MR) and ultrasound (US) examinations, were used to generate a three-dimensional (3D) CAD-model which was used as benchmark for manufacturing the 3D silicone tube model. For the construction of the silicone arterial model, Rapid Prototype models and dip-coating techniques were used (in-house techniques and knowledge). The venous silicone model, representing the venous outflow tract, was based on geometrical data obtained from US measurements of an ESRD patient and was constructed by painting silicone, layer by layer, on a steel rod [176]. This technique was chosen over dip-coating techniques as it was expected to result in lower wall thicknesses and thus lower stiffness. To mimic the AVF, the arterial and venous silicone models were connected by an anastomosis with an aperture of approximately 15 mm² and an in-plane angle of 30° [34]. The resulting silicone network model consisted of the brachial, radial, ulnar and interosseus artery (arterial tract) and of the cephalic, basilic, axillary and subclavian vein (venous tract).

This network model was built in a mock loop [177, 178] including a silicone aorta and subclavian artery constructed by Hemolab B.V. (Eindhoven, The Netherlands)(Figure 11.1, top). The arterial and venous silicone network was placed in a water tank to allow for ultrasound measurements.

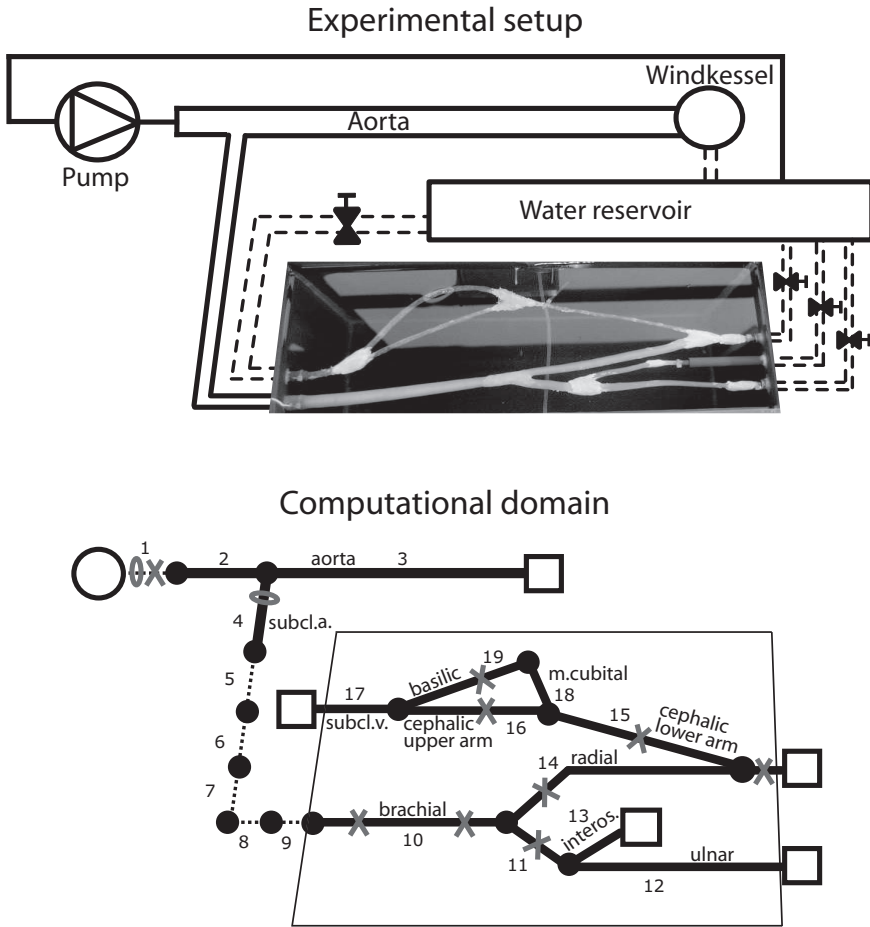


Figure 11.1: Network model mock loop scheme (top) and computational domain (bottom). The numbers refer to the edges given in Table 11.2. Pressure (x) and flow (o) waveform acquisition locations are shown.

The complete circulation circuit was filled with water and the water was pumped through the mock loop by a step pump (Parker Hannifin GmbH, Offenburg, Germany) that was regulated by a normalized modified sinus-squared ISO5840 function (Figure 11.2) in LabView (National Instruments Inc., Austin, Texas, USA). This resulted in a pump flow rate of approximately 5 l/min which is comparable to a physiological cardiac output [179]. The fluid entered the proximal aorta via a flexible valve (Hemolab B.V) and could thereafter flow in two directions: to the distal aorta which was closed by a windkessel, and to the subclavian artery which was the inflow artery of the

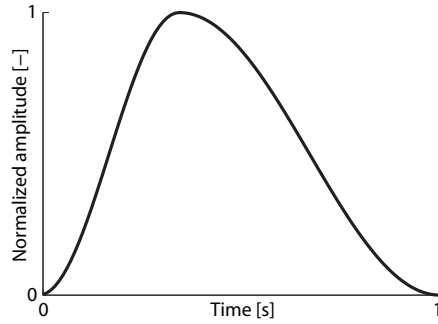


Figure 11.2: Pump input step function (modified sinus-squared ISO5840).

silicone network model. This silicone network model had three outflows in the arterial part (at radial, ulnar and interosseus artery) and one in the venous part (at the subclavian vein). For mimicking the preoperative situation, the venous outflow was closed with a clamp, whereas for the postoperative situation the clamp was released to mimic the presence of a lower arm AVF. The lower arm AVF was chosen because it involves the largest arterial and venous network and thus the most complex topology was studied.

Experimental measurement techniques

Geometrical measurements. The lengths of all arteries, connecting tubes and veins were measured using a ruler. In addition, the ruler was used to determine the location of the anastomosis with respect to the brachial bifurcation. The proximal and distal arterial and venous diameters were measured at working pressure with ultrasound (Picus ultrasound system, ESAOTE B.V., The Netherlands). The diameters of connecting tubes were determined with a micrometer.

Flow measurements. Flow waveforms were measured, at the proximal aorta and the proximal subclavian artery (Figure 11.1) with a Transonic flow meter acquisition system (Team 21 Compatible, Transonic Systems Inc., Ithaca, NY, USA). The signal was sampled at 500 Hz using a data-acquisition (DAQ) unit (BMC-2090, National Instruments Inc.). The acquisition software was programmed in LabView (National Instruments Inc., version 7.1, Austin, Texas, USA). For all outflow tracts, the time-averaged outflows were measured volumetrically.

Pressure measurements. Pressure waveforms were measured, using pressure transducers (P10EZ-1, Becton Dickinson Critical Care Systems, Singapore) connected to a multi channel compact amplifier system (PICAS, Peekel Instruments, Rotterdam, The Netherlands). The measurements were performed at predefined locations along the experimental model (Figure 11.1) by sliding a fluid-filled epidural catheter (Portex Epidural Catheter, Smiths Medical ASD inc., Keene, USA) through the experimental model. The pressure transducers were also connected to the DAQ-unit.

Mechanical properties of the silicone vessels. The diameter change (distension) of the arteries and veins was measured by using wall-tracking software (Artlab) that is incorporated in the Picus ultrasound system (ESAOTE B.V., The Netherlands). Since pressures were measured simultaneously, the distension, Δd , and the pulse pressure, Δp , were used to determine the local distensibility, D :

$$D = \frac{1}{A_o} \frac{\partial A}{\partial p} \approx \frac{1}{A_o} \frac{\Delta A}{\Delta p} = \frac{2d_{dia}\Delta d + (\Delta d)^2}{d_o^2 \Delta p} \quad (11.1)$$

in which A_o and d_o are the cross-sectional area and the diameter at mean pressure, and d_{dia} the diastolic diameter. The distensibility of the subclavian artery was estimated by using its wall-thickness-to-radius ratio of 0.1 and by assuming the Young's modulus equal to the one of the experimental aorta, as the subclavian artery was made from the same material. The distensibilities of the connecting tubes were assessed from static volumetric compliance measurements or set to 10^{-7} Pa^{-1} otherwise.

Pressure drop over the anastomosis. The extra pressure drop over the anastomosis was captured via a minor loss coefficient, defined as $K_{loss} = \frac{\Delta p}{\frac{1}{2}\rho v^2}$, in which Δp is the pressure drop from the inflow artery to the outflow vein, ρ is the density, and v is the mean blood velocity in the inflow artery. K_{loss} was determined by measuring the pressure drop as function of the Reynolds numbers from $Re=200$ to 3500 (Figure 11.3A).

Mathematical model

The pulse wave propagation model used here was previously developed by Huberts et al. [168], and will only be described in short. The computational domain for the simulations consisted of a truncated part of the aorta, the subclavian, brachial, radial, ulnar and interosseus arteries, the anastomosis, the cephalic, median cubital, basilic, axillary and subclavian veins, and, in

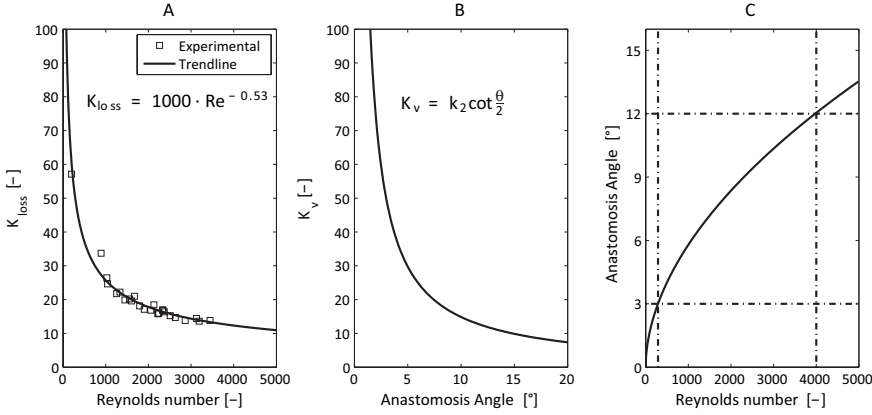


Figure 11.3: The experimentally derived minor loss coefficient as function of the Reynolds number (A) and the reduced minor loss equation (Equation (11.4)) implemented in the wave propagation model developed by Huberts et al. [168] as function of anastomosis angle (B). In panel C, the comparison between the experimentally derived loss coefficient (Reynolds number) and the loss coefficient implemented in the wave propagation model (anastomosis angle) is shown.

addition, all connecting tubes (Figure 11.1, bottom). The vessels were divided in segments with a maximum length of 5 cm. In each segment the local relation between pressure and flow is described. For the scope of modeling the effect of vascular access creation on blood pressure and flow distribution, segments are needed that represent arteries, veins and the anastomosis. All arterial and venous segments were modeled with a lumped parameter model derived from local mass and momentum equations. The anastomosis segment was modeled with a nonlinear resistance based on two semi-empirical loss coefficients, K_v and K_d , that describe the loss from the proximal artery to, respectively, the proximal vein and the distal artery and have been defined by Gardel [180, 181]:

$$K_v = k_1(1 - q^*)^2 + q^{*2} \left[k_2 \cot \frac{\theta}{2} - k_3 + \frac{k_4 - k_5 A^*}{A^{*2}} \right] + k_6 q^* (1 - q^*) \left(1 + \frac{1}{A^*} \right) \cot \frac{\theta}{2} \quad (11.2)$$

$$K_d = k_7(1 - q^*)^2 + k_8 q^{*2} - k_9 q^* (1 - q^*) \quad (11.3)$$

in which q^* is the ratio between flow through the vein and flow through the proximal artery, A^* is the ratio between cross-sectional area of the vein and cross-sectional area of the proximal artery and θ is the angle between proximal artery and proximal vein. Empirically determined values for the constants k_1 to k_9 are given in Table 11.1.

k_1	k_2	k_3	k_4	k_5	k_6	k_7	k_8	k_9
0.95	1.3	0.3	0.4	0.1	0.4	0.03	0.35	0.2

Table 11.1: Semi-empirical determined dimensionless constants k_1 to k_9 for equation (11.2) and (11.3).

Parts of the cardiovascular system, for which no detailed information on pressure and flow was required, were truncated and terminated with three-element windkessel models. Assembling all lumped segments resulted in a system of differential equations that describes the pulse wave propagation of the pressure and flow waveforms. This system was solved by numerical integration applying the trapezium rule for implicit time integration. On the first node, a measured (aortic) flow was prescribed, whereas the venous outflow was closed with a fixed intravenous pressure.

In this study, pressure and flow waveforms of the pulse wave propagation model were validated with experimentally derived pressure and flow waveforms. The input parameters of the pulse wave propagation model were adapted to the experimental setup. For this, geometrical (vessel length, vessel diameters) and mechanical characteristics of the vessels (vascular compliance) were mandatory. Furthermore, information on anastomosis configuration (location, angle), windkessel parameters, fluid properties (density and dynamic viscosity), intravenous pressure and an input (aortic) flow waveform were required. How these input parameters were obtained will be discussed in the next section.

Experimental validation: Model parameters for the pulse wave propagation model

The input parameters for the pulse wave propagation model were derived from the measurements and are given in Table 11.2. In addition, uncertainty domains of these input parameters were estimated as they are input for the uncertainty analysis.

Geometrical parameters. The measured lengths were directly used in the pulse wave propagation model and the uncertainty domain was set to $\pm 5\%$, which equals to a measurement error of 1 mm in the shortest vessel. Also the position of the anastomosis was varied within $\pm 5\%$. The uncertainty domain for the diameters was set to $\pm 10\%$. For the arterial and venous diameters, linear tapering within a vessel was assumed. The influence of tapering was investigated by changing the smallest diameter of a vessel while changing

the largest diameter in the opposite direction. The uncertainty domain for these changes were based on 10% of the smallest diameter.

Mechanical parameters. For the pulse wave propagation model, the local vessel wall compliance per segment length was needed. This was derived by multiplying the distensibility in Table 11.2 by the local cross-sectional area, thus assuming a constant distensibility within each vessel. For the distensibilities obtained with ultrasound, the measurement uncertainty domain was $\pm 15\%$, whereas for the distensibilities derived by volume compliance measurements, the measurement uncertainty domain was $\pm 20\%$.

Pressure drop over the anastomosis. To match the minor loss coefficients in the pulse wave propagation model with the measured loss coefficient, we assumed that the majority of the proximal artery flow flows through the proximal vein ($q^* \approx 1$) and that the arterial and venous cross-sectional areas were almost similar ($A^* \approx 1$). Equation 11.2 and Equation 11.3 then reduce to

$$K_v = k_2 \cot \frac{\theta}{2} - k_3 + k_4 - k_5 = 1.3 \cot \frac{\theta}{2} \quad \text{and} \quad K_d = 0.35 \quad (11.4)$$

This relationship for K_v is shown in Figure 11.3B. For an anastomosis angle, θ , between 3 and 12 degrees, the loss coefficient, K_v , matches the experimentally determined loss coefficient, K_{loss} , in the range of Reynolds numbers 250-4000 (Figure 11.3C). Finally, the loss coefficient, K_v , was modeled by the original Equation 11.2, while the anastomosis angle was varied between 3 and 12 degrees. Because the flow through the distal artery was small compared to the flow through the proximal vein, loss coefficient, K_d , was neglected.

Constants. The fluid used in the experiment was water which has, at room temperature (20°C), a density of 10^3 kg/m^3 and a dynamic viscosity of 10^{-3} Pa.s . These model parameters would hardly vary during the experiment and therefore the uncertainty domains were set to $\pm 1\%$ and $\pm 5\%$, respectively.

Boundary conditions. The peripheral resistance, R_p , of each windkessel was determined as the ratio of local mean pressure and local mean flow. The local mean flow was assessed by the volumetric measurements, while the mean pressure was assessed by time-averaging the measured local pressure waveforms. The characteristic impedance, Z_o , was assessed by using $\sqrt{\frac{\rho}{DA_o^2}}$ in which ρ is the blood density, D the local distensibility and A_o the cross-sectional area [182].

Finally, the compliance, C , for each windkessel was determined by dividing the time constant, by the difference between the peripheral resistance and the characteristic impedance ($R_p - Z_o$). For the aorta, the time constant was assessed from the local pressure waveform via the ‘area method’ [183]. The time constant in the radial artery was assessed from multiplying the local peripheral resistance with the compliance of the outflow tube. For the ulnar and interosseus arteries, the radial artery time constant was assumed. As a result, the time constant was 5.4 s in the aorta and 0.4 s in the other outflow arteries. In the uncertainty analysis, the time constants were varied by $\pm 20\%$.

For the inflow boundary at the aorta (i.e. the ascending aorta flow), we used the pre- and postoperative aortic flow measurements, with an estimated uncertainty domain of $\pm 5\%$. As outflow condition at the subclavian vein, we used the measured mean pressure with an uncertainty domain of $\pm 10\%$.

Uncertainty analysis

Simulations with the pulse wave propagation model were performed for both the pre- and postoperative configuration. To examine the propagation of input uncertainty to the output, Monte Carlo simulations were performed. Varying all input parameters independently within their uncertainty domain might result in non-physiological combinations of input parameters and thus non-physiological output (e.g. a small artery continuing in a larger artery). Therefore, the input parameters of adjacent vessels were changed simultaneously (Table 11.2). This resulted in 44 independent input parameters for the preoperative configuration and 58 parameters for the postoperative configuration. Input samples were generated by Latin Hypercube sampling, i.e.: For each input variable, its previously defined uncertainty domain is divided into equiprobable intervals and within each interval a value is randomly selected. Consequently, an input value is used only once for each interval and a full coverage of the parameter input space is obtained [184]. One sample is thus a point in the input parameter space. The total number of samples generated was 5000 times the total number of input parameters in analogy with previous studies of Huberts et al. [185].

For the preoperative configuration, the simulated pressure waveforms in the aorta, the proximal and distal brachial artery, the proximal and distal radial artery and the proximal ulnar artery were compared to the measured pressure waveforms (Figure 11.1, bottom). This was extended by the distal and proximal cephalic vein, and the basilic vein for the postoperative configuration. The flow waveforms were compared at proximal aorta and subclavian artery. For the comparisons, the median of the simulated pressure

Edge name	Edge number	Length [mm]	Diameter [mm]		Distensibility [Pa ⁻¹]	Mean flow [ml/min]		Mean pressure [mmHg]		Time constant [s]
			begin	end		pre	post	pre	post	
rigid connecting element	1	50 (5%)	28.9 (10%)	28.9 (10%)	$10^{-7} \text{ }^a(-)$					
proximal aorta	2	150 (5%)	28.9 (10%)	28.9 (10%)	$2.1 \cdot 10^{-5} \text{ (15\%)}$					
distal aorta	3	310 (5%)	28.9 (10%)	28.9 (10%)	$2.1 \cdot 10^{-5} \text{ (15\%)}$	4650 (10%)	4375 (10%)	98 (10%)	90 (10%)	5.4 (20%)
subclavian artery	4	100 (5%)	8.0 (10%)	8.0 (10%)	$7.7 \cdot 10^{-6} \text{ }^b(20\%)$					
rigid (tapered) connecting tube	5	60 (5%)	8.0 (10%)	10 (10%)	$10^{-7} \text{ }^a(-)$					
compliant connecting tube	6	130 (5%)	10 (10%)	10 (10%)	$1.1 \cdot 10^{-6} \text{ }^b(20\%)$					
rigid connecting tube	7	80 (5%)	10 (10%)	10 (10%)	$10^{-7} \text{ }^a(-)$					
compliant (tapered) connecting tube	8	20 (5%)	10 (10%)	6.0 (10%)	$1.1 \cdot 10^{-6} \text{ }^b(20\%)$					
rigid connecting tube	9	55 (5%)	6.0 (10%)	6.0 (10%)	$10^{-7} \text{ }^a(-)$					
brachial artery	10	215 (5%)	6.0 (10%)	4.5 (10%)	$1.7 \cdot 10^{-5} \text{ (15\%)}$					
proximal ulnar artery	11	67 (5%)	3.6 (10%)	3.6 (10%)	$1.1 \cdot 10^{-5} \text{ (15\%)}$					
distal ulnar artery	12	173 (5%)	2.7 (10%)	1.9 (10%)	$1.7 \cdot 10^{-5} \text{ (15\%)}$	46 (10%)	42 (10%)	96 (10%)	88 (10%)	0.4 (20%)
interosseus artery	13	110 (5%)	1.3 (10%)	1.3 (10%)	$1.1 \cdot 10^{-5} \text{ (15\%)}$	5 (10%)	5 (10%)	98 (10%)	88 (10%)	0.4 (20%)
radial artery	14	240 (5%)	3.4 (10%)	3.2 (10%)	$1.5 \cdot 10^{-5} \text{ (15\%)}$	50 (10%)	46 (10%)	96 (10%)	84 (10%)	0.4 (20%)
cephalic vein lower arm	15	210 (5%)	2.9 (10%)	3.0 (10%)	$1.4 \cdot 10^{-5} \text{ (15\%)}$					
cephalic vein upper arm	16	180 (5%)	4.3 (10%)	4.3 (10%)	$2.4 \cdot 10^{-5} \text{ (15\%)}$					
subclavian vein	17	32 (5%)	5.6 (10%)	5.6 (10%)	$8.4 \cdot 10^{-6} \text{ (15\%)}$			5.7 (10%)	5.7 (10%)	
median cubital vein	18	30 (5%)	4.5 (10%)	4.5 (10%)	$8.4 \cdot 10^{-6} \text{ (15\%)}$					
basilic vein	19	180 (5%)	4.5 (10%)	4.6 (10%)	$8.4 \cdot 10^{-6} \text{ (15\%)}$					

^a Assumed value for the rigid tubes.

^b Estimated from static volume compliance measurements.

Table 11.2: All input data for the wave propagation model that are derived from measurements on the experimental setup. The mean pressure, mean flow and time constant are only given for the edges that are closed by a windkessel segment. In brackets the estimated measurement uncertainty is given in percentages. The vessels that are changed simultaneously during the uncertainty analysis are grouped in one cell.

and flow waveforms of all Monte Carlo simulations was used as well as a confidence interval, formed by the 25th and 75th percentile interval.

11.1.3 Results

Preoperative results

Table 11.3 shows that the simulated mean flows correspond to the measured mean flows in the aorta, subclavian artery, the radial artery and the ulnar artery. The shapes of the simulated aorta and subclavian artery flow waveforms correspond to the measured flow waveforms, though the simulated subclavian artery flow appears less attenuated (Figure 11.4).

For all arteries, simulated and measured mean pressures are similar (Table 11.3). The shapes of the simulated pressure waveforms (Figure 11.4) correspond to the measured pressure waveforms, although the simulated pressures are less attenuated resulting in a more pronounced second peak, which is clearer in distal pressure waveforms. For the aortic pressure waveform, a phase difference of approximately 50 ms is observed. Presumably, the timing of the measured aortic pressure waveform is inaccurate as the systolic pressure peak arrives before the flow peak.

	Mean pressure [mmHg]		Mean flow [ml/min]	
	measured ^a	simulated ^b	measured ^a	simulated ^b
proximal aorta	95	93 (88,99)	4750	4747 (4682,4813)
subclavian artery			101	98 (36,161)
proximal brachial artery	98	93 (88,99)		
distal brachial artery	98	93 (87,99)		
proximal ulnar artery	98	93 (87,99)	46	44 (35,53)
proximal radial artery	98	93 (87,99)	50	48 (34,63)
distal radial artery	98	92 (86,99)		

^a Measured value without uncertainty interval.

^b Median value with 25th and 75th percentiles.

Table 11.3: Measured preoperative mean pressures and flows and their simulated values.

Postoperative results

During the analysis of the postoperative results it was observed that, in first instance, the resistance in the distal cephalic vein was not properly determined. After excising the distal cephalic vein from the setup, a non-smooth vessel lumen that was twisted over the full length was found resulting in a large pressure drop of 24 mmHg from the distal cephalic vein to the proximal cephalic vein (Table 11.4). This pressure drop was approximately ten times larger than the expected pressure drop as calculated from Poiseuille's law. As this additional pressure drop was not captured by the model, all Monte

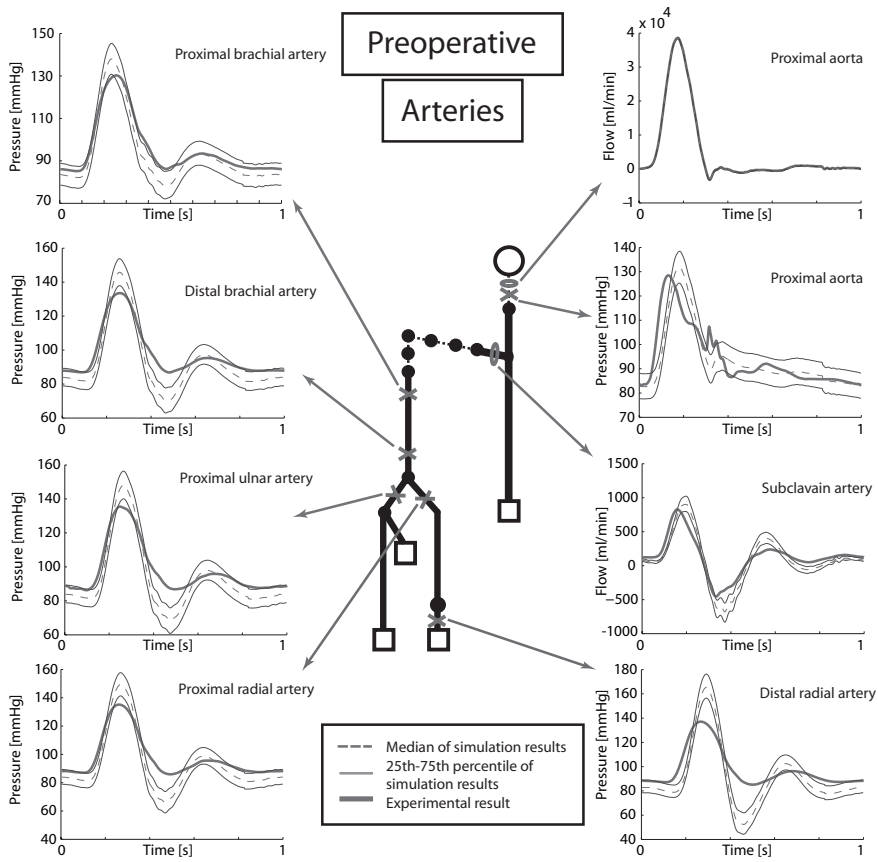


Figure 11.4: The preoperative pressure and flow waveforms on several arterial locations.

Carlo simulations were performed once more with a tenfold increased resistance in the distal cephalic vein with an uncertainty of $\pm 10\%$. Since vessel abnormalities could also be present in human vasculature and the resulting additional pressure drop has significant effect, the results of both analyses, with and without the extra resistance, are presented in Table 11.4.

When considering the additional resistance of the distal cephalic vein, the simulated mean flow of the subclavian artery and the distal cephalic vein in Table 11.4 now correspond to the measured mean flow. Beside a better agreement between measured and simulated flows, this is also the case for the pressures. In Table 11.4, it can be observed that the previous observed underestimation of the measured mean arterial flows and pressures are reduced, while measurements and simulations now coincide. This especially

holds for the distal cephalic vein pressure. As in the preoperative simulations, the simulated arterial pressure waveforms (Figure 11.5) are less attenuated than the experimentally measured ones. In addition, a similar phase difference in the aorta is observed. The shape of the measured and simulated venous pressure waveforms (Figure 11.6) are similar, although the differences are larger than for the arterial site, i.e. a phase difference of approximately 50 ms in the proximal cephalic and basilic vein.

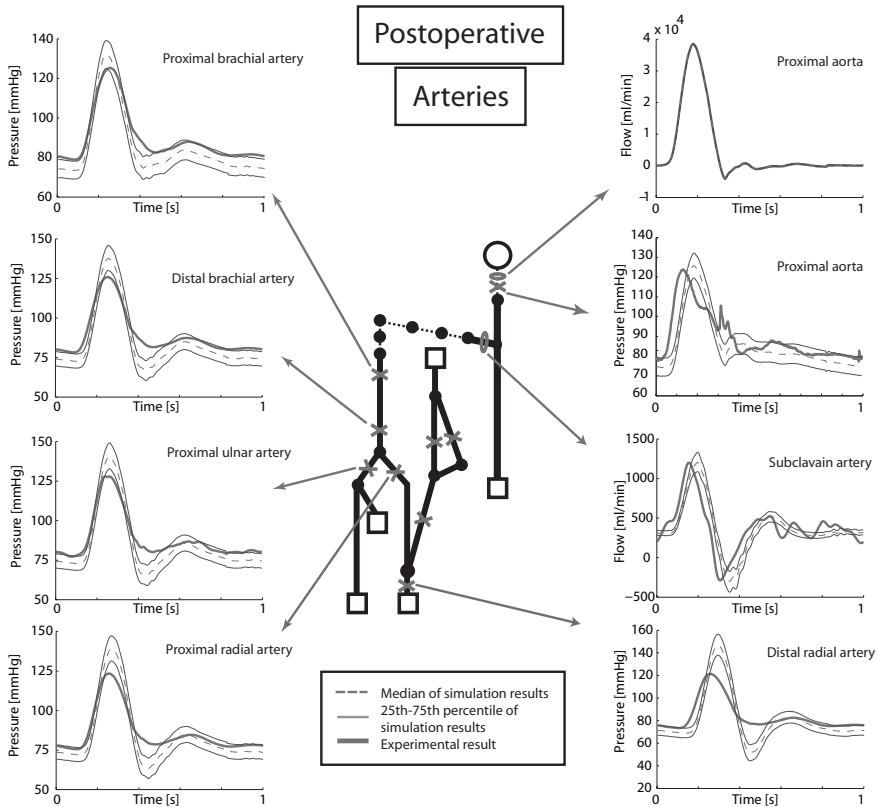


Figure 11.5: The postoperative pressure and flow waveforms on several arterial locations for simulations with additional resistance.

11.1.4 Discussion

In this study, we aimed to experimentally validate a previously developed pulse wave propagation model for the prediction of pressure and flow before and after AVF creation. In this way, it was determined if the physical

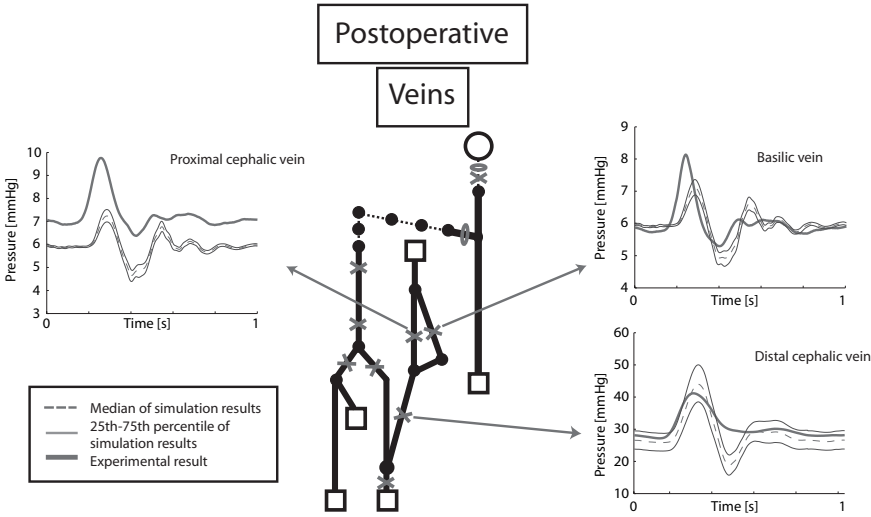


Figure 11.6: The postoperative pressure and flow waveforms on several venous locations for simulations with additional resistance.

description of the pulse wave propagation in both cases was captured correctly by the model. It was found that the pulse wave propagation model was able to accurately simulate the pre- and postoperative mean pressures and flows in the experimental setup but that the simulated pressure and flow waveforms were less attenuated than the measured waveforms. This most likely results from viscoelastic behavior of the experimental tubes [172, 186].

Experimental setups have previously been used to validate pulse wave propagation models, but not in the situation after AVF surgery when flows are significantly increased compared to normal and the anastomosis is included. Bessems et al. [172] have validated their pulse wave propagation model with both a straight and tapered viscoelastic silicone tube. Swillens et al. [173] used a silicone setup to validate their pulse wave propagation model in an aneurysm case study. An experimental setup that included a more detailed representation of the arterial tree and thus also physiological wave reflections resulting from bifurcations, was used by Matthys et al. [170]. Next to these experimental validations, Reymond et al. performed, recently, an *in vivo* validation of a patient-specific pulse wave propagation model of the systemic arterial tree [169, 171]. However, although geometry, flow and pressure measurements were all performed on one individual patient, it was impossible to measure all input parameters patient-specifically (e.g. local vessel distensibility and peripheral resistance and compliance). Thereby, pressure and

flow measurements are only possible on a limited number of positions over the systemic tree [169–171]. In addition, clinical measurements are usually hampered by large measurement uncertainties, which were not considered in any of the studies.

In this work, in contrast to these studies, the uncertainty of the model input was taken into account, yielding an estimation of the precision on the pressure and flow waveforms. The 25th-to-75th percentile interval captured a decrease or increase ranging, dependent on location, from 2 to 14% of the median value for the mean pressures, while for the mean flows larger uncertainties were observed. Preoperatively, the uncertainties of the mean flows in the subclavian artery, the radial artery and the ulnar artery were respectively 60%, 20% and 30%, while postoperatively the uncertainties of these vessels were about 17%, 20% and 25%. The uncertainty in mean flow in the distal cephalic vein was approximately 13%. The large uncertainties in mean flows can be explained by the fact that the flow waveform oscillates around zero which means that a small deviation in the waveform will result in a significant change in mean flow. Clinically, an uncertainty of approximately 20% in the mean flow in the subclavian/brachial artery is acceptable because the surgeon aims at an inflow of 400–500 ml/min while 300 ml/min is sufficient for proper hemodialysis treatment. When considering specific time points, the width of the 25th-to-75th percentile interval for the flows is maximum 300 ml/min and for the pressure maximum 20 mmHg. Thus, considering the precision is advised for validation studies.

When simulating the postoperative situation, at first instance, it was observed that the subclavian artery flow waveforms had similar shapes but that the mean flow significantly differed between measurement and simulation. Furthermore, the simulated mean pressure in the distal cephalic vein was significantly smaller than the measured mean pressure. Upon closer examination, a large pressure drop from the distal cephalic vein to the proximal cephalic vein was found in the experimental setup and all simulations were repeated with a larger resistance over the distal cephalic vein. As a result, the correspondence between simulated and measured pressure and flow waveforms significantly improved. Thus, when incorporating the additional pressure drops resulting from structures such as twisting or kinking in the computational model, the model is able to simulate the postoperative situation more adequately. For this, a clear picture of the vascular topology is required. Clinically, this can be obtained by using MR or ultrasound.

The experimental setup constructed for this study allowed for model validation, since we were able to mimic flow enhancement after AVF creation and since all measured pressure and flow waveforms were comparable

to physiological ones [187, 188]. The mean pressures and flows, both arterial and venous, simulated by the pulse wave propagation model, were adequately predicted and the overall shape of the pressure and flow waveforms were similar.

However, the simulated waveforms were less attenuated than the measured ones, indicating that introduction of viscoelasticity might improve the computational model's capability to describe the physical phenomena. Previous studies [170, 171, 173] already showed that a pulse wave propagation model is able to simulate pressure and flow waveforms in elastic arteries and that the introduction of viscoelasticity improves the simulations [169, 172, 189, 190]. Since viscoelasticity is observed in human arteries [191, 192], including viscoelasticity in the model for patient-specific modeling is required when the waveforms are of interest.

But, even after incorporating viscoelasticity into the pulse wave propagation model, which should result in a better description of the physical phenomena, clinical implementation might still be challenging. The reason for this is that the model needs to be adapted to patient-specific conditions which requires patient-specific model input parameters. Clinically, it is difficult to determine these parameters accurately due to limitations in measurement modalities or because the burden on the patient should be minimized. Fortunately, a sensitivity analysis can be applied to the model to determine which model input parameters are most important to assessed. Consequently, the number of required patient-specific measurements can significantly be reduced [185]. Another challenge is including vascular adaptation (e.g. flow-mediated dilatation, maturation) and regulation (e.g. autoregulation of the peripheral bed) in the model. This physiological mechanisms should be introduced, especially, when the (long-term) adaptation of a vascular access is of interest. The current model is only able to predict mean flows directly after surgery.

11.1.5 Conclusion

The pulse wave propagation model was successfully validated with an experimental setup, mimicking pressure and flow changes following an AVF creation. Mean pressures and flows were adequately predicted and the overall shape of the pressure and flow waveforms were similar for the experiment and measurement. However, the experimental waveforms were more attenuated most likely resulting from neglecting viscoelasticity in the model. Furthermore, it was found that the uncertainties in model input parameters significantly influence the output and should thus be taken into consideration in the analysis.

	Mean pressure [mmHg]			Mean flow [ml/min]		
	measured ^a	simulated ^b	simulated with extra R^b	measured ^a	simulated ^b	simulated with extra R^b
proximal aorta	90	83 (79,88)	86 (81,91)	4750	4748 (4676,4821)	4740 (4667,4812)
subclavian artery				378	508 (422,594)	362 (302,424)
proximal brachial artery	90	83 (78,87)	85 (80,91)			
distal brachial artery	90	81 (76,87)	85 (79,90)			
proximal ulnar artery	88	81 (76,87)	84 (79,90)	42	38 (31,46)	40 (32,47)
proximal radial artery	86	80 (75,86)	84 (78,89)	-	-	-
distal radial artery	84	76 (71,82)	81 (76,86)	46	42 (30,53)	44 (34,55)
distal cephalic vein	31	8.3 (7.5,9.2)	28 (25,32)	285 ^c	420 (352,490)	270 (239,305)
proximal cephalic vein	7.0	6.0 (5.8,6.2)	5.9 (5.8,6.0)			
basilic vein	6.0	6.0 (5.8,6.2)	5.9 (5.8,6.0)			
subclavian vein	5.7 ^d	5.7 ^d	5.7 ^d			

^a Measured value without uncertainty interval.

^b Median value with 25th and 75th percentiles.

^c Flow split percentages through proximal cephalic and basilic vein unknown.

^d Prescribed intravenous pressure.

Table 11.4: Measured postoperative mean pressures and flows and their simulated values.

11.2 EXPERIMENTAL VALIDATION OF HIGH-FLOW CFD SOLVER

11.2.1 Introduction

Patient-specific computational hemodynamics have proven to be a reliable tool for estimating flow, pressure fields and wall shear stress distributions *in vivo*. Here we consider the possibility to numerically simulate the blood flow behavior in the specific case of arterio-venous fistula (AVF) for patients on hemodialysis therapy. In this context, the prediction of vascular access short-term (maturation) and long-term (patency) functionality is of primary importance to improve the outcome of fistula creation and avoid surgical revisions, as currently investigated by computational tools for AVF surgery planning [115]. However, the non-physiological conditions occurring after anastomosis creation, such as high blood flow rates and flow instabilities, pose a potential challenge to numerical solution strategies.

Recently, Botti and Di Pietro [193] proposed an INS-solver² implementation aimed at simulating high-Reynolds number flows and tested it against published benchmarks to demonstrate optimal convergence rates in both space and time. Their strategy offers a very favorable trade-off between computational cost and robustness with respect to convection-dominated flows in complex 3D geometries, making the approach particularly suitable for hemodynamic applications in the context of patient-specific simulation in population studies.

The aim of the present study was the experimental validation of the solver on a patient-specific case of vascular access for hemodialysis. On the basis of a geometry reconstructed from medical images we consider a wide range of flow rates, up to the range of those required to perform hemodialysis treatment. To compare against experiments, we focus on the flow patterns within the anastomosis experimentally acquired by means of Particle Image Velocimetry (PIV) and the pressure drop across the anastomosis for varying flow rates. In particular, this latter aspect is significant to develop reliable computational tools for vascular network modeling [115].

The use of PIV for the validation of Computational Fluid Dynamics (CFD) solvers in the field of biomedical engineering and hemodynamics has been reported in literature for different cases but mainly under physiological, low or moderate flow, conditions. Next to the more idealized or generalized phantom models of, for example, an idealized arterial stenoses [130] or aneurysm [131], PIV validation is applied in a larger scale in the field of medical devices as central venous catheters [98], blood pumps [132–135], stents

²Solver based on the incompressible Navier-Stokes equations

[136] or artificial heart valves [137–139]. Even when shifting to anatomical realistic models, like in studies focusing on the validation of patient specific aneurysms [140], stenoses [141] or AVFs [194], a good agreement between *in vitro* measurements and computational results is found. In the context of unstable or turbulent flows both the results of the PIV-challenge [142] and the FDA's 'Critical Path' Computational Fluid Dynamics / Blood Damage Project study on the validation of a benchmark nozzle model [143] agreed that PIV is capable to satisfactorily measure the mean (time-averaged) velocities. However, in order to increase the accuracy and reproducibility the fluctuations in the flow conditions and in the fluid properties need to be taken under control [143]. Apart from PIV studies, in the context of transitional flow conditions, the work by Loth et al. satisfactorily compared numerical simulations and experimental velocity solutions acquired by means of laser Doppler anemometry in a porcine arterio-venous graft [195].

The numerical solutions were computed considering accurate time integration and, due to the unstable nature of the flow, the solutions were averaged to obtain the physical quantities of interest. The averaged velocity and pressure solution were compared with the experimental data.

11.2.2 Material and methods

3D computational and experimental model generation

For the experimental evaluation, a numerical model of a patient-specific anastomosis was reconstructed from high-resolution MR angiography images, acquired on a patient with a working AVF. The anastomosis geometry was segmented from MR images using the open-source software *vmrk*³. The three main vessels, proximal and distal artery and proximal vein, composing the end-to-side anastomosis, were segmented. Cylindrical flow extensions were added to all inflow and outflow sections of the computational domain, in order to impose fully developed steady-state Dirichlet boundary condition by means of a Poiseuille velocity profile.

The experimental anastomosis model was built at Vascular Access Models (Seaside, CA, USA) using a silicon block of 270x70x35 mm with a refractive index of 1.406 (Figure 11.7). The model was scaled by a factor 4:1 in order to simplify the production process and ensure a low surface roughness. Once the *in vitro* model was obtained, an additional high-resolution X-ray Computed Tomography (voxel size 210 μm) was performed and the images segmented and adopted as the final computational domain. This workflow ensures a perfect match between the *in vitro* and the computational model geometry.

³<http://www.vmrk.org>

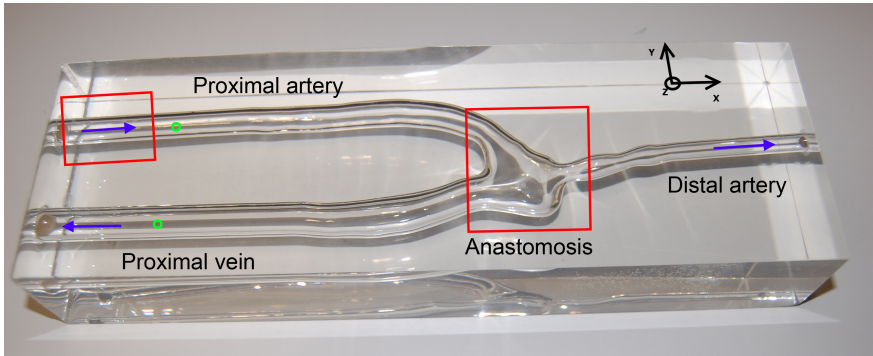


Figure 11.7: *In vitro* anastomosis model: PIV regions of interest (ROI) (red); Pressure measurement points (green); Flow directions are indicated in blue.

The discretized computational mesh was obtained following the procedure described in Antiga et al. [196]. Mesh size was specified on the basis of local vessel size, so that the number of elements at the cross section is kept constant irrespective of the local diameter of vessels. The hybrid mesh consisted of 975,710 tetrahedral and 104,168 prismatic cells.

Assumptions on flow conditions

In order to simplify the experimental setup, validation was performed under steady inflow conditions. This assumption is not in contrast with physiologic flow conditions since, due to small venous resistance and the high flow rates involved, the role of pulsatility is limited and the arterio-venous fistula is dominated by flow instabilities associated to the convection-dominated nature of the flow.

Furthermore, distal artery outflow was occluded. All the flow entering from the proximal artery inflow was forced through the venous outflow. Since the peripheral resistance of the distal artery is much higher than the venous resistance, the flow is largely directed to the venous outflow under *in vivo* conditions, to the point that reverse distal artery flow (steal syndrome) is commonly observed in clinical practice [197, 198]. Since we were interested in validating the CFD methodology in a wide range of flow regimes, the imposition of a prescribed flow split would have required to clip the outflow section with a trial-and-error approach in order to match the flow distribution at each flow rate here considered. Due to the instabilities arising at the highest flow rates, such a procedure would have been cumbersome and would have potentially increased measurements errors.

Since the imposition of a sealed distal artery and steady inflow boundary conditions does not introduce any fundamental simplification in the numer-

ical simulation task, we concluded that the described setup would not affect the significance of the validation process.

CFD computations

In the numerical model, a fully developed Dirichlet boundary condition was imposed at the inflow of the proximal artery section, while a homogeneous Dirichlet boundary condition was imposed at outflow of the distal artery in order to guarantee that the whole flow actually goes through the anastomosis toe towards the vein outflow. The structure was considered as rigid and the fluid was modeled as Newtonian and homogeneous. We considered a wide range of Reynolds numbers, namely Re equal to 100, 200, 550, 1000, 1500 and 2000, the latter being equivalent to a blood flow rate of 800 ml/min. The dimensionless Reynolds number was calculated based on the average velocity at the proximal artery (V), the proximal artery diameter (D) and the the kinematic viscosity (ν) with $Re = \frac{V \cdot D}{\nu}$. Starting from a homogeneous velocity-pressure field, simulations were advanced with a fixed time step, determined according to the Reynolds number. For Re equal to 100 and 200, a steady state solution was reached using a pseudo-time integration with time step equal to 0.01 s. For Re equal to 550 and 1000, with a time step equal to 0.001 s and for Re equal to 1500 and 2000, with a time step equal to 0.0005 s, a steady state solution could not be reached, and the simulations were halted after a total integration time of 2 s.

At the highest Reynolds numbers, the solution was highly unsteady with a steady inflow, due to the combination of high Reynolds numbers and a complex 3D geometry. In order to compare with experimental data, velocity and pressure fields were averaged taking into account all the time steps during the last second of integration time. The first second was ignored to minimize the effect of transients from the resting state to fully developed flow.

Particle image velocimetry

The velocity field was acquired over a 2D-plane located at the anastomosis by means of Particle Image Velocimetry (PIV) measurements. The mock loop for the PIV measurements was constituted by a reservoir, a stationary pump, a one meter long stiff inflow tube, the model and two outflow pathways. The PIV equipment consisted of a CCD camera with maximum spatial resolution of 1376x1040 pixels (PCO, Kelheim, Germany), a double cavity Nd:YAG laser, a synchronizer and acquisition and postprocessing software applications (ILA GmbH, Juelich, Germany).

The water-glycerin mixture, with the same refractive index as the silicon model, was seeded with 100 μm silver coated polyamid particles. The mixture had a density of 1122 kg/m^3 and a dynamic viscosity of 4.57 $\text{mPa} \cdot \text{s}$ at 30°C. The flow rate was measured volumetrically before and after each PIV acquisition and a set of PIV results was used for the validation process only when pre and post flow rates were within 2%.

The 32x32 mm Region Of Interest (ROI) (Figure 11.7) was deliberately positioned where the flow is expected to be more complex in order to challenge the numerical strategy. Based on this ROI location, the flow conditions were assessed at Reynolds 550 and Reynolds 1000, representing 220 and 400 ml/min blood flow in the 1:1 patient-specific case. A second ROI was defined at the inlet (Figure 11.7) of the model to assess the flow pattern entering the model. The acquired velocity, at a Reynolds number of 565, has been used to confirm the assumption of parabolic inlet flow.

Pressure drop measurements

Since one of the main candidate contributors to the overall resistance of an AVF is the concentrated resistance at the anastomosis, one of the most important points to be tackled by the validation process is the ability of the INS-solver to accurately reproduce the pressure drops across the anastomosis. At the highest flow regimes, in fact, the overall pressure drop is tightly linked to the non-linear losses induced by instabilities at the anastomosis and can be considered as surrogate global indicator of the capabilities of the solver of capturing the overall flow dynamics.

For the pressure drop measurement experimental setup, the model was built in the same mock loop as for the PIV measurements. The pressure drop was measured at the upper wall (positive Z-axis), at 108 mm from the proximal side of the anastomosis (Figure 11.7), using two different 4 Fr. needles connected to a single disposable pressure transducer (DT-X Plus; Becton Dickinson, USA).

To minimize the uncertainties on the experimental results, more than 200 measurements of flow rate versus pressure drops were acquired. In order to cover the full range of flow conditions with the same experimental setup, different water-glycerin mixtures were used, from the highest viscosity fluid (17.5 $\text{mPa} \cdot \text{s}$) required to achieve a measurable pressure drop (150 Pa for $\text{Re}=50$), up to the lowest viscosity mixture (4.2 $\text{mPa} \cdot \text{s}$) allowing the stationary pump to achieve the flow rate required for the highest Reynolds number (4600 ml/min for $\text{Re}=2200$).

11.2.3 Results

Overview of CFD results

The CFD velocity solutions at the anastomosis toe for Re equal to 100, 200, 1000 and 2000 are shown in Figure 11.8. For the case of Re 100, the region of high velocity magnitude fills the proximal artery, while this region shifts more and more to the outer wall when increasing the inflow rate. Next it is clear that the complexity of the present flow field at the anastomosis region and in the distal artery increases significantly comparing the Re 100 and Re 200 with the Re 1000 and Re 2000 case.

The increase in flow complexity at the highest Reynolds numbers can be appreciated in Figure 11.9 where the velocity magnitude contours are represented. Right after the first change in direction at the anastomosis, the bulk

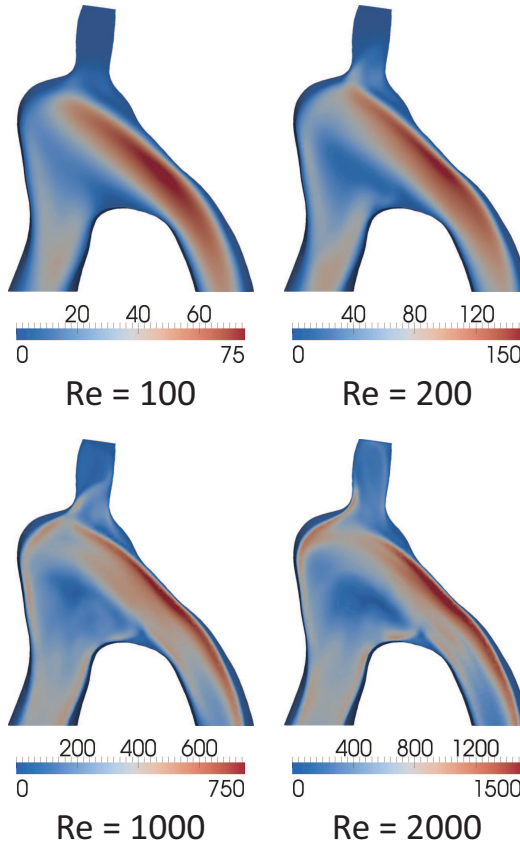


Figure 11.8: Contours of velocity magnitude (mm/s) for Reynolds numbers 100, 200, 1000 and 2000.

flow becomes more and more adherent to the outer wall of the vein as inertial forces start to dominate over viscous forces. The intensity of the recirculating vortex at the anastomosis toe increases and the iso-surface widens, reflecting a strong mixing near the vein centerline.

Experimental versus computed velocity field

The PIV and CFD velocity contours over the two-dimensional region of interest at the anastomosis (Figure 11.7) are compared considering two values of the Reynolds number, $Re=550$ and $Re=1000$, as shown in Figure 11.10.

Since we deal with unstable flows, we compare time-averaged CFD solutions against PIV data, which is inherently time-averaged (4 Hz acquisition for 100 seconds) in our setup. Overall, a good agreement is observed between *in vitro* PIV data and CFD results. Relevant flow features, such as the high-velocity jet at the upper wall and the wake zone at the distal (closed) artery, can be observed in both sets of data. Of note, the location of the recirculating vortex close to the proximal part of the anastomosis is accurately captured at both flow regimes here considered.

In general, PIV data appear more diffusive than CFD results. This is not surprising given the fact that in unstable flows at high-Reynolds numbers, the spatial and temporal resolution required to track swirling particles and sharp jets is considerably high, and the effect of averaging unstable flows

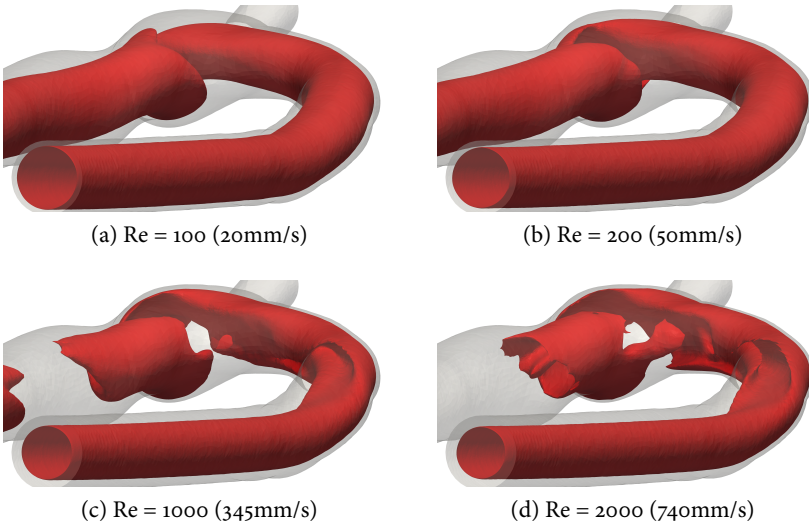


Figure 11.9: Iso-surfaces of the velocity magnitude.

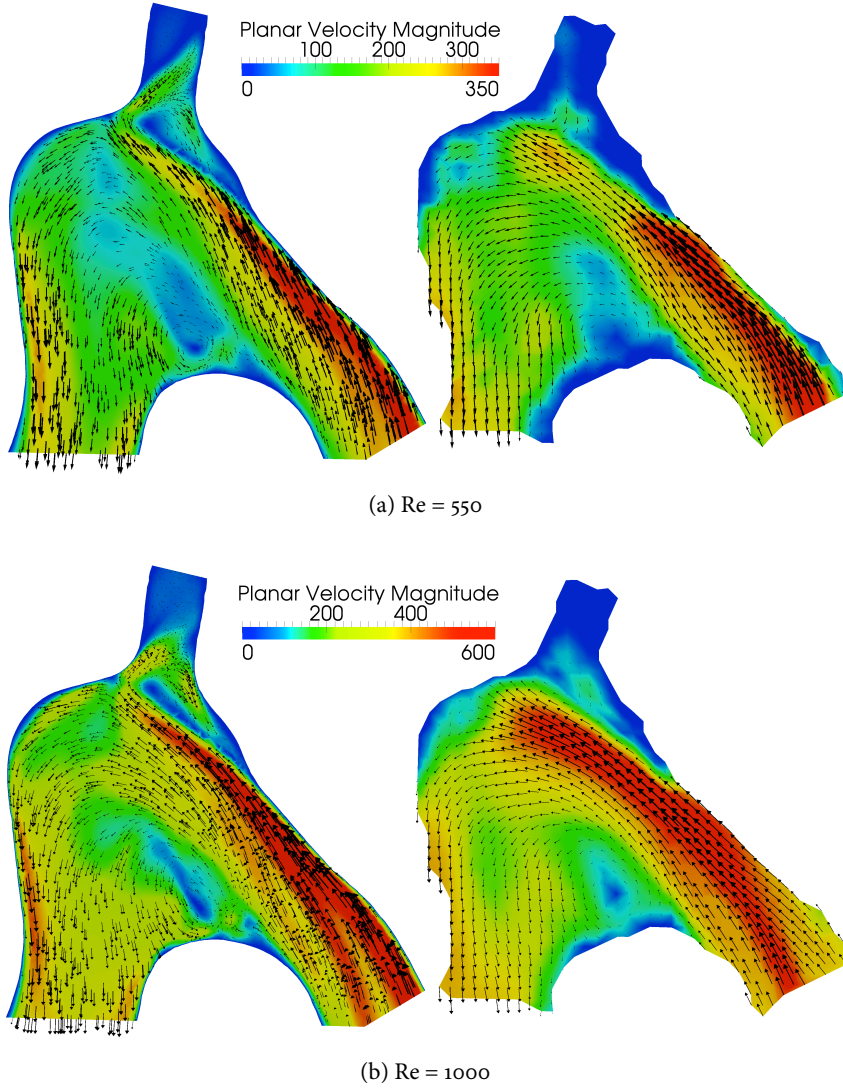


Figure 11.10: CFD (left) versus PIV (right) results for low speed (Re 550) (top) and high speed (Re 1000) (bottom) flow regimes at the arterio-venous anastomosis. Images are color-coded by means of planar velocity magnitude (mm/s), arrows show planar velocity vectors.

over long acquisition times results in a low-pass filtering effect. A lack of PIV data is observed at the bottom of the proximal vein. This was due to an insufficient penetration of the laser light sheet in the model up to this region (laser light from right to left in Figure 11.10), probably due to a complex interplay between the geometry of the model and the optical properties of the liquid and the model.

Experimental versus computed pressure drops

Charts representing Euler number ($\Delta p/\rho v^2$) versus Reynolds number and pressure drop (Δp) versus flow rate are presented in Figure 11.11. The pressure drop versus flow results were calculated from the Eu versus Re solutions taking the original 1:1 scaled geometry and assuming a blood viscosity and density of 3.5 mPa s and 1050 kg/m³.

The agreement between the experimental and numerical pressure drops across the anastomosis is remarkable. We found that all the experimental values were within the standard deviation range of the numerical pressure drops, meaning that all the experimental values would have potentially been observed in the numerical simulation.

As visual in Figure 11.11 (bottom), the averaged numerical values allow to conclude that the anastomosis exhibits a quadratic relation between pressure drop and flow rate. The quadratic relation was also observed in the (qualitative) computational results in Chapter 10. This confirms the need to model the anastomosis in patient-specific studies geometrically accurate in order to capture the effects of the instabilities and properly estimate the non-linear pressure drops involved when adopting modeling approaches to clinical predictions.

11.2.4 Discussion and conclusion

In this work, the solution strategy for incompressible Navier-Stokes equations proposed by Botti and Di Pietro [193] and previously tested against analytical solutions of model problems has been validated in a patient-specific case of an arterio-venous fistula for hemodialysis at high flow rate regimes. Although the *in vivo* configuration was simplified by sealing the distal artery and adopting steady inlet flow conditions, all the challenges involved in the simulation of convection-dominated flows in complex 3D geometries were retained. As a result, both numerical pressure drops and velocity solutions at the anastomosis were in excellent agreement with the experimental data. It is worth to point out that these results have been obtained without the adoption of the model or solver for turbulence or transition to turbulence.

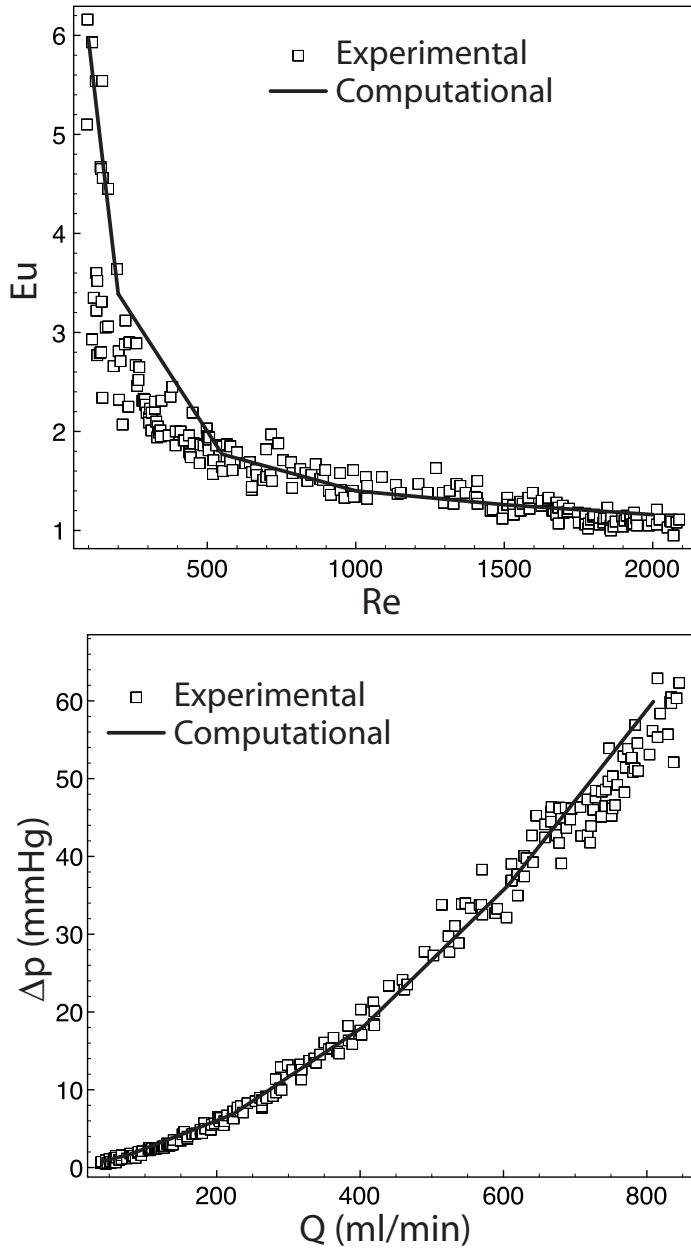


Figure 11.11: Reynolds number versus Euler number (top) and equivalent blood pressure drop versus flow rate (bottom).

After successful validation of the proposed solution strategy for simulations in realistic geometries at high flow regimes, the solver can now be employed to reliably predict flow patterns and pressure drops in patient-specific models of vascular access in patients on hemodialysis. More in general, the solver, here validated, may be useful for the numerical analysis of other vascular beds that are characterized by high-flow and blood velocities associated with alteration of vascular geometry such as atherosclerotic plaques, bifurcations and branching as well.

Diagnostic tools

K. Van Canneyt, R.N. Planken, S. Eloot, P. Segers and P. Verdonck.
*Experimental study of a new method for early detection of vascular access
stenoses: Pulse pressure analysis at hemodialysis needle.*
Artificial organs. vol.34. 2010:113-117.

K. Van Canneyt¹, A. Swillens¹, L. Lovstakken, L. Antiga, P. Verdonck and
P. Segers.
*The accuracy of ultrasound volume flow measurements in the complex flow
setting of a forearm vascular access.*
Revision submitted.

¹Both authors equally contributed.

12.1 PULSE PRESSURE ANALYSIS FOR STENOSIS DETECTION

12.1.1 Introduction

Complications of the vascular access (VA) for hemodialysis are a major cause of morbidity and mortality in end-stage renal disease (ESRD) patients [19, 199], with thrombosis due to flow limiting stenosis being the main origin of VA-failure [31, 200, 201]. The Kidney Disease Outcomes Quality Initiative (K/DOQI) clinical practice guidelines define a stenosis as relevant when it shows at least a 50% diameter reduction, accompanied by a hemodynamic or clinical abnormality [19, 199]. However, significant flow decline and increase in pressure drop appear only when the diameter is reduced to above 70%, and these criteria are therefore a late sign of stenosis development (Example in Figure 8.6 (p.61)). The current vascular access surveillance techniques (flow measurements and static-access pressure measurement) are thus unable to detect relevant stenoses (<50% diameter reduction) in an early stage, and these methods cannot further reduce the incidence of vascular access failure due to thrombosis [120, 202–206].

Up to date, monthly measurement of access flow is considered the best available surveillance tool for identification of patients at risk of access thrombosis [19, 199]. However, access flow shows variation between and within hemodialysis sessions [207]. Measurement of mean intra-access pressures is more straightforward and can be performed using pressure transducers within the dialysis machine [202, 208]. Intra-access pressures reflect vessel resistance and can be measured at the site of cannulation in the arterial and venous needle. However, current pressure measurements techniques and protocols are tedious, time consuming, and not ‘user friendly’. Staff frequently bypasses crucial steps (calibration, appropriate flushing, etc.), leading to poor quality data being collected and recorded [19, 199]. Therefore, monitoring techniques should be cheap, accurate, precise and easy to perform. The high thrombosis rates of arterio-venous fistulas and grafts in particular, require a sensitive and specific test that can unequivocally predict the likelihood of thrombosis over a specific time. A combination of mean intra-access pressure and flow measurements results in better prediction of access thrombosis. However, the sensitivity of a combined surveillance protocol for prediction of access thrombosis is only 73.3% and 68.8% in AVF and AVG, respectively [204].

To overcome the inability to predict early stage stenoses (<50 diameter reduction) and the low sensitivity of currently used tests, a non-invasive and inexpensive method based on the analysis of the pressure waveform profile and amplitude (PPA; pulse pressure analysis) is here extensively tested. The

method was assessed using a dedicated *in vitro* model of a radio-cephalic arterio-venous fistula (AVF).

12.1.2 Material and Methods

The vascular access model was integrated in a closed circuit (Figure 12.1). A blood mimicking fluid is pumped from a reservoir into a windkessel by a pulsatile pump (Harvard Apparatus, Bloodpump 4021, Model 55-3339, Holliston, USA). This creates a system where the pump represents the left ventricle and the windkessel the large central systemic arteries. From the windkessel, the fluid is distributed over the model and over a draining tube with a resistance representing the blood flow towards the body (except to the arm).

A water-glycerin mixture at 25°C was used to mimic blood, with a kinematic viscosity of $3.2 \cdot 10^{-6} \text{ m}^2/\text{s}$ as measured with a capillary Ubbelohde viscometer (Schott, Germany) and a density of 1090 kg/m^3 . This resulted in a fluid with a dynamic viscosity of $3.49 \text{ mPa}\cdot\text{s}$, corresponding to blood with a hematocrit of 42% [117].

In the vascular access model, the artery was connected to the draining vein (angle 60°). The internal diameters of the artery and vein were 4 mm and 7 mm, respectively. The arterial compliance was $8.2 \cdot 10^{-7} \text{ ml/Pa/cm}$ [209, 210], while the venous compliance was $46.0 \cdot 10^{-7} \text{ ml/Pa/cm}$ (Unpublished data). These different compliance values were achieved by constructing the different vessels with an appropriate number of silicon layers to obtain compliances in the physiological range.

To mimic the hemodialysis setting, two 15 Gauge needles (Bionic Medizintechnik GmbH, Frankfurt, Germany) were introduced. The arterial needle was inserted against the direction of flow 5 cm downstream the anastomosis and the venous needle was inserted along the flow and 5 cm more distal (Figure 12.1). Both needles were punctured and entered the silicon model for 1 cm by an angle of approximately 30 degrees. The introduced stenoses were made of rigid tubes with a length of 1 cm. Stenosis of 25% and 50% diameter reduction were placed on three different locations: (I) 10 cm proximal to the anastomosis ('proximal artery (PA) stenosis'); (II) in between the two needles ('distal vein (DV) stenosis'); (III) 3 cm distal to the needles ('proximal vein (PV) stenosis'). So the DV-stenosis was located 3.5 cm downstream the arterial needle tip whereas the PV-stenosis was located 9 cm downstream the needle tip. See also Figure 12.1, which indicates the position of the stenoses.

For each case, the initial boundary conditions were set before introducing any stenosis in the following manner. The flow towards the vascular access model was established using both the adjustable resistance towards the arm and the rest of the body (Figure 12.1). The flow in the artery was divided

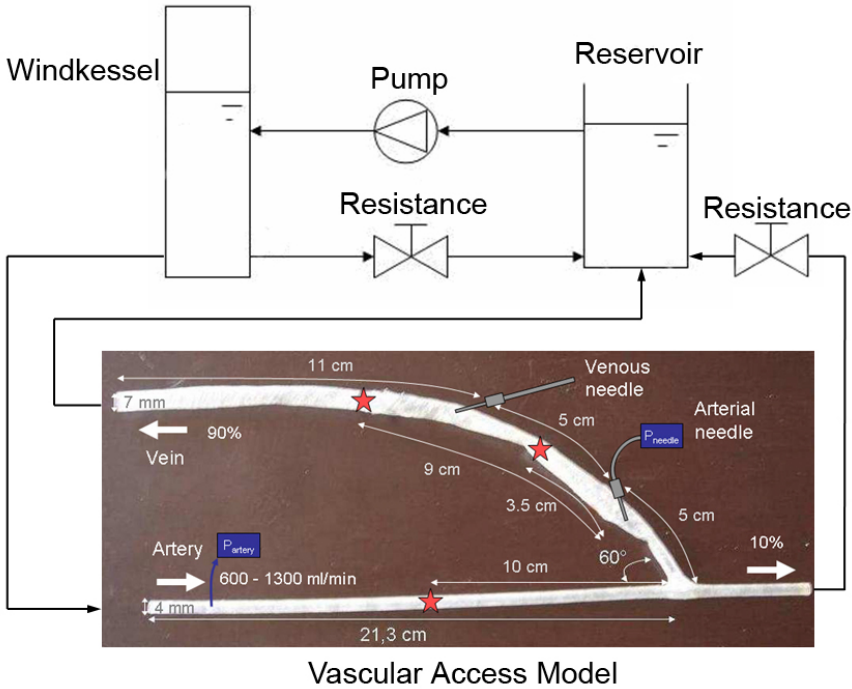


Figure 12.1: Vascular access model integrated in mock loop (* : stenosis locations)

into 90% towards the vein and 10% towards the distal artery, adjusting the outlet resistance of the vascular access model. The inlet pressure profile was measured in the proximal part of the artery and the air level in the windkessel was regulated such as to establish a profile with a pulse pressure (PP; systolic minus diastolic pressure) of about 40 mmHg.

Starting from the reference situation described above (no stenoses, 90% venous flow and 10% distal artery flow), the two different stenoses were successively introduced at the three positions, and for each case arterial blood flow (500-1300 ml/min) and heart rate (60; 75 and 90 beats/min) were varied.

The pulse pressure at the proximal part of the artery (PP_{PA}) and at the arterial needle (PP_{AN}) was measured using fluid filled pressure transducers (type DT-X PLUS, Becton Dickinson, New Jersey, USA). The signal was acquired at a sampling rate of 200Hz and displayed on screen using dedicated data acquisition hard- and software (National Instruments, Austin, USA). The values of PP used for analysis were the average of at least 6 cycles. A

dimensionless factor, '%-Pulse Pressure' (%PP), was defined as:

$$\%PP = 100 \cdot \frac{PP_{AN}}{PP_{PA}} \quad (12.1)$$

The pulse pressure analysis, PPA, consists of a comparison of the %PP measured in the different cases.

Statistical analysis

Data are generally given as mean \pm standard deviation, with data averaged per case (a given stenosis percentage at one given location) over the measured range of heart rate and blood flow. Analysis of variance (ANOVA) was performed to obtain a statistical ground to evaluate the PPA-method on detecting the presence of a stenosis, and discriminating between the locations of the stenosis. Post-hoc (Bonferroni) tests were used to assess details on which cases are different from each other in terms of %PP. Linear regression analysis was used to assess the relation between %PP and hemodynamic variables.

12.1.3 Results

Arterial blood flow rate versus %PP for the 50% stenosis is shown in Figure 12.2a. The %PP decreases with increasing blood flow and increases with increasing heart rate. In the control model (no stenosis), %PP was 20.26 ± 4.55 . A stenosis in the proximal artery significantly decreased %PP to 7.69 ± 2.08 ($P < 0.0001$), while presence of a stenosis in the venous part of the model increased %PP, with values of 36.20 ± 2.12 for the DV-stenosis and 32.38 ± 2.17 for the PV-stenosis (all $P < 0.0001$ compared to control). When applying the analytical formulation of the regression curves for an arterial blood flow of 800 ml/min (the mean value of blood flow in the experiments), the control case gives a %PP of 22.11. When we compare this to the PA-case, this value decreases to 6.80. For the stenoses distal to the needle, the %PP increases to 33.51 for the PV-stenosis and 36.92 for the DV-stenosis. The post-hoc analysis shows that the %PP is significantly different for the 50% stenosis upstream versus downstream of the needle ($P < 0.0001$). It is even possible to distinguish between the distal and the proximal vein stenosis ($P < 0.0001$).

Figure 12.2b shows the results for the 25% stenosis case, where %PP decreases from 20.26 ± 4.55 (control) to 15.45 ± 2.13 ($p = 0.0022$) for the PA-stenosis, while it increases after introduction of the DV-stenosis to 26.71 ± 3.01 ($p = 0.0003$) and to 26.53 ± 2.67 for the PV-stenosis ($p = 0.0004$). The post-hoc analysis shows that %PP for the 25% stenosis discriminates between the upstream and downstream location ($P < 0.0001$), but it is not possible to distinguish the distal from the proximal vein 25% stenosis.

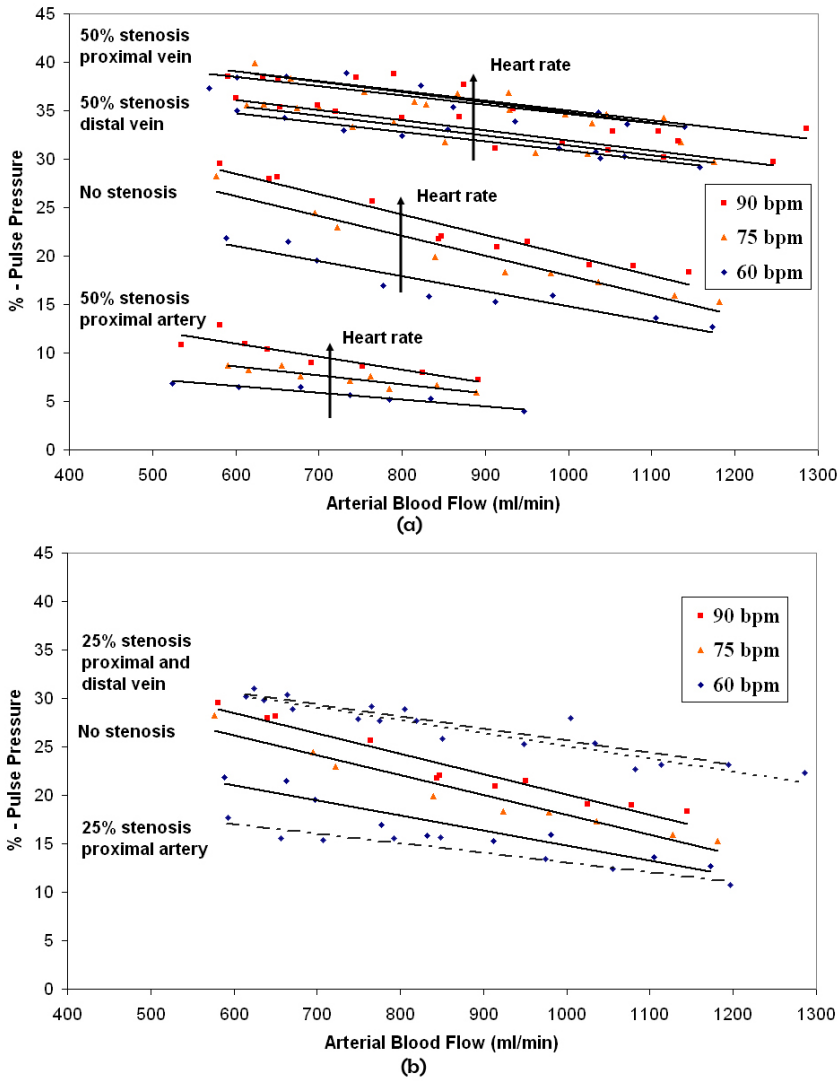


Figure 12.2: % - PP for varying arterial blood flow rates: (a) 50% stenosis cases for different heart rates versus the no-stenosis case; (b) 25% stenosis cases (--- proximal artery, - proximal vein and ··· distal vein stenosis) with heart rate of 60 bpm versus the no-stenosis case.

12.1.4 Discussion

There is an urgent need for a method that detects stenoses in early-stage in hemodialysis patients to prevent stenosis-related vascular access complications. In this work, we have presented a method, based on analyzing the PP at the hemodialysis line, and tested the method in an experimental hydraulic bench model setting. Hans-Dietrich Polaschegg stated in his patent [211, 212] that pulse pressure might be a method to detect stenosis, however no investigations or in-depth analysis on the method was performed. Although the basic principle of using pulse pressure is the same, the studied method in this work is unique.

Our experimental results for a 25% and 50% stenosis confirm what has earlier been described by Stergiopoulos et al. using a computer model of the arterial tree to study the effect of arterial stenoses [209]. When the PP is measured proximal to the stenosis and compared with the PP in the case without stenosis, it increases, while the PP decreases when it is measured distal from the stenosis. This trend is confirmed for all positions of the stenosis.

For the reference and 50% stenosis case, a clear effect of the heart rate and the arterial blood flow rate can be observed on the values of %PP (see Figure 12.2, panels a and b). We have tested the method over an anticipated range of heart rates and blood flow, and treated the measured data as independent samples, without accounting for the covariance effect of flow and heart rate. As such, the statistical test we applied is more conservative than an analysis of covariance, which would also account for the relationship between %PP and heart rate and blood flow. We feel that this approach is closer to the clinical reality, where at least the flow level is not known either. Despite this conservative approach, %PP was found to discriminate between the three locations for the 50% stenosis, and between upstream and downstream stenosis of the PA needle for the 25% stenosis. As such, we feel that the fact that heart rate and arterial blood flow rate may vary in a clinical setting, this does not jeopardize the power of the PPA for detection of stenoses in the different stenosis cases.

In experimental modeling, it is necessary to establish a ‘reference’ situation and report ‘normalized’ results, with changes from this reference position. From a clinical point of view, the *in vitro* nature of the study is the main limitation. The value of the proposed method of PPA will increase if it can be clinically proven that only the measurement of the PP at the needle (PP_{AN}) makes the stenosis detection method accurate and sensitive. The arterial pulse pressure could, for instance, be obtained from the brachial sphygmomanometer cuff or using techniques of applanation tonometry. Anyhow, an

inexpensive and ‘user friendly’ surveillance technique will only be obtained if the PP at the needle can be calculated directly within the dialysis machine, as for intra-access static pressure measurements. Beside these remarks, another limitation of the experimental model is the fact that it is a simplification of the human vascular system. Human vessels react on blood flow and pressure changes by vasodilation or vasoconstriction in an acute setting and structural remodeling in the longer term. When the method is used in daily clinical practice, these changes in the cardio-vascular system may interfere with the pressure profile analysis. Therefore a clinical trial should be performed to validate this detection method.

12.1.5 Conclusion

We have extensively *in vitro* tested a method, based on analysis of the pulse pressure, enabling detection of the presence and location of a 50% stenosis independent of heart rate and arterial blood flow rate. Nevertheless, a clinical study will have to confirm these experimental results and the potential of this low-cost method.

12.2 THE ACCURACY OF ULTRASOUND VOLUME FLOW MEASUREMENTS

12.2.1 Introduction

In Europe, more than half-a-million patients with end-stage renal disease (ESRD) are treated with hemodialysis and this population still increases annually by approximately 5-8% [9–12]. To make hemodialysis possible, a well-functioning vascular access is needed to facilitate high blood flow and to allow repeated cannulation over time [21, 25]. The preferred vascular access is created by surgically connecting an artery and a vein in the arm (an arteriovenous fistula; AVF). Ideally, the AVF matures, resulting in the required flow increase and vascular remodeling to allow for dialysis [21, 25, 26]. Despite the extensive preoperative examinations, non-maturation occurs in 23 to 46% of the cases [36, 37].

Direct postoperative flow measurements can be linked, in an early-stage, with the non-maturation in case of a too low fistula flow and with distal ischemia and cardiac failure in case of a too high fistula flow [26, 32, 44, 164, 167]. The ideal method to measure the flow rates should be non-invasive, workable in daily clinical practice and reproducible. Nowadays, one of the most widely available methods is based on pulsed wave Doppler (PWD) ultrasound (US), where PWD provides velocity information that is multiplied with an estimate of the cross-sectional area of the vessel to obtain volumetric flow.

Although PWD is a well-established method to measure flow velocities, it has some intrinsic limitations. The most important one is the 1D-nature of the measurement, since PWD only captures the velocity component in the direction of the US-beam. The translation of this 1D velocity measurement to the full cross-sectional velocity profile, in order to estimate the flow rate, requires a great number of assumptions. These uncertainties involved in the flow rate calculation are expected to increase significantly when a disturbed and complex flow field is introduced, as one may expect post AVF-creation. So, despite the fact that the PWD flow estimation is non-invasive and used on large scale in daily routine, the reproducibility, intra- and inter-observer variability, and the accuracy remain unclear [213–217].

In this study, we want to assess the accuracy of the flow rate as measured by US compared to the actual flow rate present in the setting of AVF. To ensure that we have gold standard information on the true velocity field measured by pulsed wave Doppler, we will follow an approach based on multiphysics simulations, integrating computational fluid dynamics with an ultrasound simulator. As we demonstrated before, this modeling technique allows to simulate synthetic but realistic ultrasound images, based on a known

but complex 3D-flow situation [218, 219]. As such, we will produce synthetic PWD spectra to derive flow rates, which can then be compared to the ground truth values known from CFD. For this analysis, two patient-specific geometries of one AVF patient, based on pre- and postoperative MR-images of the arm vasculature, will be used.

12.2.2 Material and methods

Multiphysics simulations to generate synthetic pulsed wave Doppler data

(A) FLOW SIMULATIONS IN A PATIENT-SPECIFIC MODEL OF AVF USING COMPUTATIONAL FLUID DYNAMICS (CFD)

Two sets of high-resolution MR angiography images were acquired from the same patient (51 year old, male, BMI 20.5), one set preoperatively and one 15 weeks after AVF creation. From these MR data sets, both a preoperative and a postoperative 3D-model were reconstructed. The preoperative model consists of the brachial artery, which bifurcates into the ulnar and the radial artery (Figure 12.3, top). The postoperative model additionally includes the arterio-venous anastomosis and the distal cephalic vein (Figure 12.3, bottom). The inflow segment was artificially prolonged for both pre- and postoperative models to ensure fully developed flow conditions (independent of the boundary conditions) at sites of flow investigation. To avoid disturbance of the distal high flow vortices in the postoperative model, straight outflow segments were added as well.

The two geometries were segmented from the MR images, using the open-source software `vmtk`². The model was meshed using `pyFormex`³, according to the methods described by De Santis et al. [220, 221]. A conformal and structured hexahedral mesh was applied on the models, resulting in 1.4 million cells for the preoperative case and 2.2 million cells for the postoperative case. A mesh-sensitivity analysis was performed to ensure that velocity fields were obtained independent of the mesh density.

A parabolic velocity profile was implemented as inlet boundary condition at the proximal brachial artery. The profile was determined based on the pre- and postoperative MRI Q-flow acquisition from the selected patient, but was rescaled such that a mean flow rate of 100 ml/min preoperative and 1000 ml/min postoperative were obtained. The ulnar artery received 40 ml/min in both the pre- and postoperative case, and the distal radial artery 60 ml/min. For the postoperative case, this results in a flow of

²<http://www.vmtk.org>

³<http://pyformex.org>

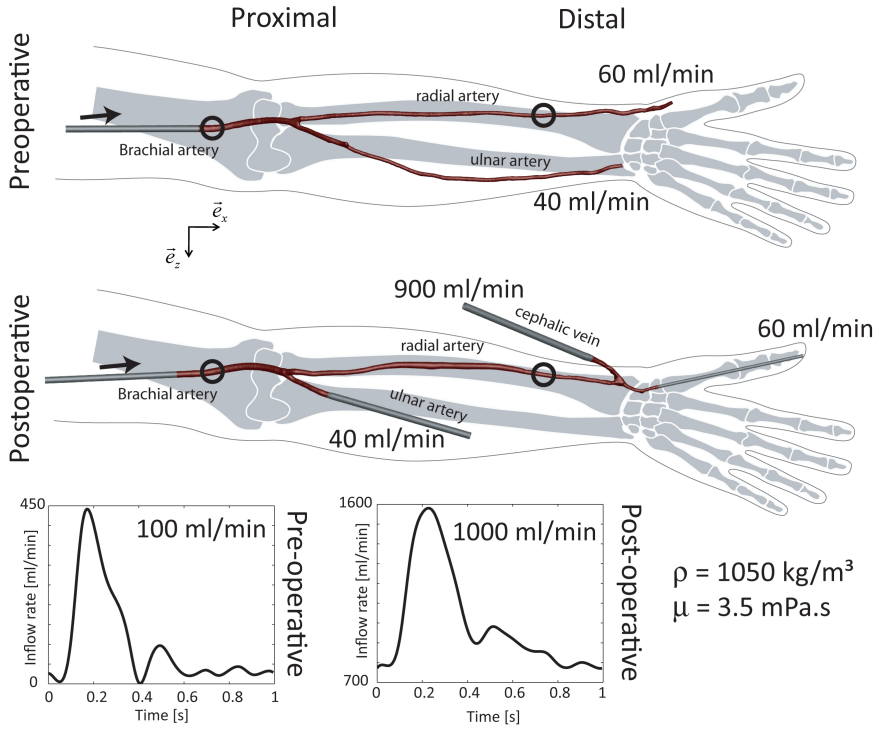


Figure 12.3: Pre- and postoperative model with indication of the assessed locations, boundary conditions and fluid properties.

900 ml/min going through the vascular access, which is in range with clinical practice and the European and American guidelines for vascular access [19, 22].

Blood was modelled as an incompressible Newtonian fluid with a density of 1050 kg/m^3 and a viscosity of 3.5 mPa.s . Rigid walls and no-slip conditions were set. Womersley numbers, α , defined as:

$$\alpha = R\sqrt{2\pi f\rho/\mu} \quad (12.2)$$

(with R the radius of the vessel, ρ the density of blood, μ the viscosity of blood and f the cardiac frequency), ranged from 1.8 to 3.3. For both geometries, two cardiac cycles were calculated to avoid transient effects, with a 5 ms time step. Ansys Fluent 12 (ANSYS inc., Canonsburg, PA, USA) was used to solve the Navier-Stokes equations with a finite volume method. Standard pressure discretization and second-order upwind momentum discretization schemes were applied.

(B) ULTRASOUND SIMULATIONS

We used the Field II software [222, 223] to simulate the radiofrequent (RF) signals originating from the AVF blood flow fields. This simulator is based on the spatial impulse response estimation approach as proposed by Tupholme [224] and Stepanishen [225], and allows to model arbitrary transducers and scanning sequences with great flexibility. Field II represents blood as an ensemble of random point scatterers on which the ultrasound waves reflect. As such, realistic Doppler spectra were obtained by moving the point scatterers during the simulated scanning procedure according to the AVF flow fields obtained from CFD. We implemented a realistic linear array transducer for peripheral vascular applications, and RF-signals were obtained by firing 8000 and 22000 sinusoidal pressure pulses during the cardiac cycle, for the preoperative and postoperative case, respectively (pulse repetition frequency (PRF) = 8/22 kHz, $f_0 = 5$ MHz, pulse length = 2.5 pulse periods). This higher pulse repetition frequency postoperatively was necessary to avoid aliasing for the higher flow velocities present in this setup. RF-data were simulated at 2 locations (cfr. o in Figure 12.3): (i) the brachial artery, 5 cm proximal to the radial-ulnar bifurcation (proximal location), and (ii) the radial artery, 5 cm proximal to the (location of the) anastomosis (distal location). Finally, the Doppler sonograms were produced by choosing an appropriate depth and size of the sample volume, and applying Fourier-analysis to the simulated RF-signals. For more background on the ultrasound simulator and the applied multiphysics simulation approach, we refer to Swillens et al. [218, 219].

Volume flow calculation based on pulsed wave Doppler spectra

The instantaneous volume flow, $Q(t)$, through a well-defined cross-section, A , can be calculated as the integration of the spatial velocity profile over the area:

$$Q(t) = \iint (\vec{v}(t) \cdot \vec{n}) dA = \iint v_n(t) dA \quad (12.3)$$

with $\vec{v}(t)$, the 3D-velocity vector in a certain point of the cross-section and \vec{n} the direction of the normal of the cross-section A . The projection of the velocity vector $\vec{v}(t)$ on the normal \vec{n} is denoted as $v_n(t)$. However, evaluation of this surface integral is highly cumbersome using conventional PWD, since it typically entails a range of assumptions, which are potentially erroneous for complex flow conditions. The different steps and according challenges in correctly assessing Equation 12.3 are described below.

(A) INTEGRATING OVER THE CROSS-SECTIONAL AREA A

Equation 12.3 shows that a correct measurement of the flow, Q , requires

knowledge of the spatial velocity distribution in the considered cross-section. As such, the most straightforward flow assessment requires a direct measurement of this spatial velocity profile. However, conventional PWD systems do not allow to simultaneously scan and process different sampling locations. Hence, directly assessing the spatial velocity profile is typically circumvented, and we investigated two commonly applied strategies in this matter:

(i) Equation 1 is simplified to:

$$Q(t) = v_{n,mean}(t) \cdot A \quad (12.4)$$

with $v_{n,mean}(t)$ the mean velocity in the considered cross-section, obtained by stretching the Doppler sample volume (SV) over the complete cross-section [226]. This method is further denoted as the *large sample volume* acquisition.

(ii) The velocity is measured at a specific location of the cross-section (typically the center point), and is further used to derive the spatial velocity profile by assuming the actual flow conditions. The flow Q is then obtained as:

$$Q(t) = \beta \cdot v_{n,max}(t) \cdot A \quad (12.5)$$

with β a correction factor that accounts for the shape of the velocity profile; $v_{n,max}(t)$ the velocity in the center of the vessel cross-section and assumed to be the maximal velocity (as is the case for fully symmetrical flow). A flat ($\beta=1$) or parabolic ($\beta=0.5$) profile are often assumed, but more complex flow profiles can be derived using Womersley theory. The β -factor for Womersley theory will be further indicated as β_α . This method was simulated by positioning a small sample volume (SV = 0.39 mm) in the center of the cross-sectional area. This approach is further denoted as the *small sample volume* acquisition.

Another potential error when estimating Q is the assessment of the cross-sectional area A , which is typically obtained from a simple measurement of the diastolic diameter ($\pi D^2/4$), hence assuming a circular shape of the cross-section. As such, we also assessed the diameter at the assessed locations, but directly from the 3D reconstructed vascular geometry, since rigid walls were assumed in the CFD-simulations.

(B) ASSESSMENT OF $v_n(t)$: ANGLE CORRECTION

Using a mean frequency estimator, the velocity in the US-beam direction, v_{PWD} , was derived from the Doppler spectra [226]. To reduce the variance of the spectrum estimates, the final velocity curve was obtained by averaging power spectra from several individual range samples within the sample volume.

Although this mean frequency estimator theoretically results in unbiased velocity estimates v_{PWD} [226], we also derived v_{PWD} by tracking the outer contour (envelope) of the spectrum based on image intensity (cfr. Figure 12.4). This is a common approach in clinical practice because it is less sensitive to shifts in measurement location compared to the mean frequency estimation [168, 227]. In the remainder of this paper, we will refer to $v_{PWD}(t)$ as obtained from respectively *mean-tracking* or *max-tracking* to indicate the difference.

Finally, the Doppler velocity v_{PWD} was converted to the angle-corrected velocity $v_n(t)$ as:

$$v_n(t) = \frac{v_{PWD}(t)}{\cos(\theta)} \quad (12.6)$$

With θ the angle between the ultrasound beam and the assumed flow direction. In this study, θ was set to 70° .

12.2.3 Results

Simulated Doppler spectra

Figure 12.4 shows the PWD-spectra when the small sample volume is positioned in the center of the cross-section (top-middle) and when a large sample volume covering the full cross-section was chosen, with both mean-tracking (solid white line) and max-tracking (dashed white line) visualized. For the postoperative case, the complex flow conditions with high velocity magnitudes result in increased spectral broadening and less smooth velocity curves, with a larger difference between mean- and max-tracking curves than for the preoperative case. For the large sample volume, the lower velocities near the vessel wall are also picked up, as can be observed for the spectra in the lower panels of Figure 12.4.

Velocity from PWD versus CFD

We focus on two cases when comparing the results from the synthetic PWD spectra to the true flow velocities (CFD):

1. *preoperative proximal* (brachial artery in preoperative conditions), because the flow field in this region seems the least disturbed as it is close to the straight inflow section and demonstrates low flow.
2. *postoperative distal* (radial artery in postoperative conditions) since the most complex flow field was expected for this case

Figure 12.5 (top) compares the velocity as picked up by pulsed wave Doppler, v_{PWD} , (in the direction of the ultrasonic beam), with the projection of the CFD velocity vector on this beam, v_n . Results are demonstrated for a small

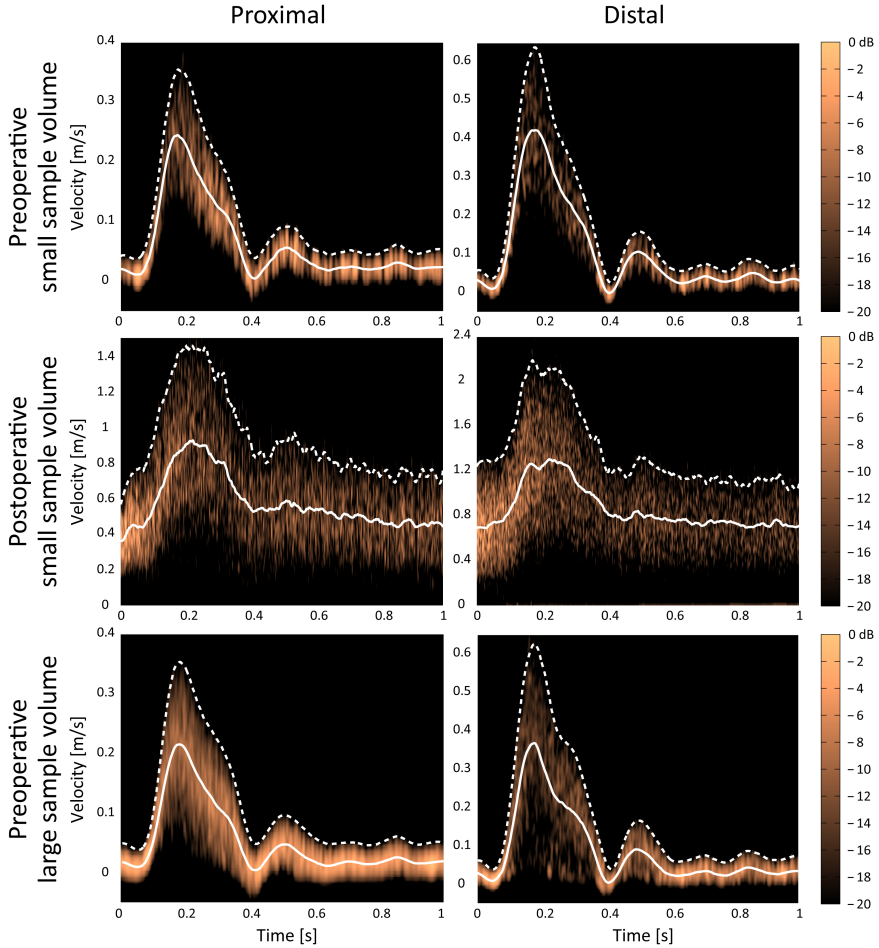


Figure 12.4: PWD-spectra as obtained from the small sample volume acquisition (top-middle) for all four case and PWD-spectra obtained for large sample volume acquisition (bottom) for the two preoperative cases. Mean-tracking (solid white line) and max-tracking (dashed white line) are indicated.

sample volume in the center of the cross-section. Comparison with the ground truth shows that max-tracking of the Doppler spectrum results in an overestimation of the velocity (mean bias of +65.5% for the preoperative and +46.4% for the postoperative case). The mean-tracking, on the other hand, shows a good agreement with the reference value obtained from CFD, with a slight underestimation of PWD (mean bias of -3.3% preoperative and -8.1% postoperative).

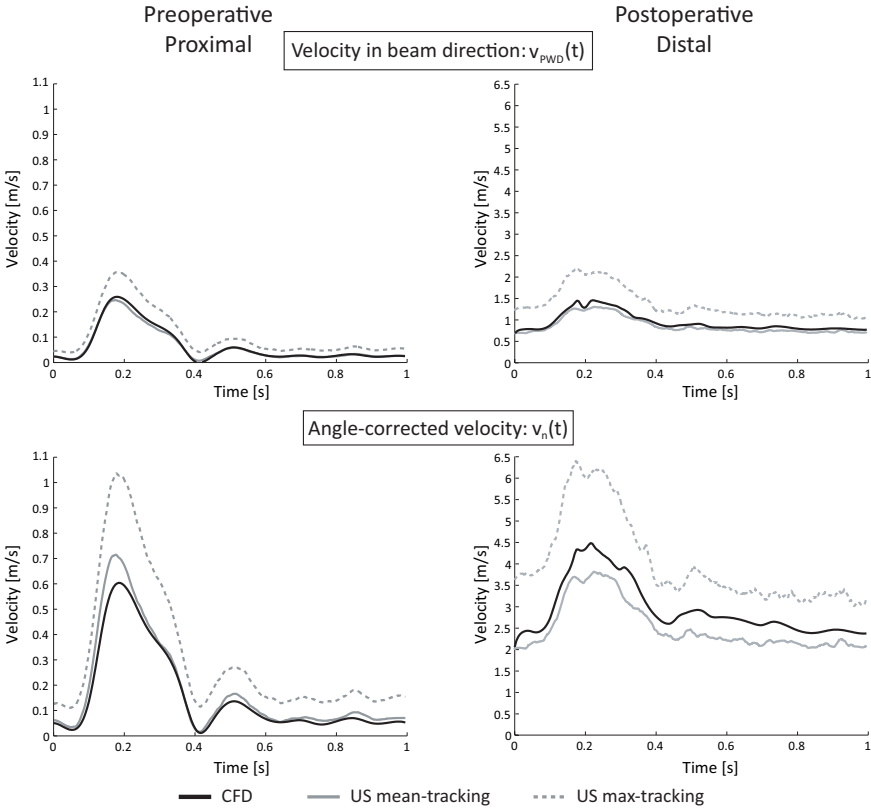


Figure 12.5: The upper panels show the velocity as picked up by PWD (in the US beam direction), with the mean-tracking in solid gray and the max-tracking in dashed gray. The CFD ground truth is displayed in solid black. The lower panels show the velocity after angle correction, with the same color coding as the upper panels. This comparison is illustrated for a small sample volume acquisition, in the preoperative proximal (left) and the postoperative distal region (right).

Figure 12.5 (bottom) compares the corresponding angle-corrected velocity v_n , with the projection of the CFD velocity vector on the normal of the cross-section. The angle correction further enforces the overestimation by the max-tracking (mean bias of +65.6% for v_{PWD} and +99.1% for v_n in the preoperative case). Angle correcting the mean tracking results in an overestimation preoperatively (bias=+16.3%) and an underestimation (bias=-14.2%) postoperatively.

Flow from PWD versus CFD

Figure 12.6 shows the volume flows obtained from the PWD spectra, for a small sample volume acquisition (solid gray for mean-tracking, dotted gray

for max-tracking), assuming a Womersley flow profile. The applied correction factors β_α , according to Equation 12.5, where 0.658, 0.626, 0.658 and 0.627 for preoperative proximal, preoperative distal, postoperative proximal and postoperative distal, respectively. While the proximal measurements (in the brachial artery) show a clear overestimation by ultrasound, both for the mean- and max-tracking, results are less univocal for the distal site (radial artery).

The deviation between the simulated volume flow measurements and the ground truth is further quantified in Table 12.1, providing an overview of the bias on the ultrasound data for the small sample volume acquisition. Both mean- and max-tracking of the Doppler spectra are reported, as well as different assumptions on the velocity profile (parabolic flow, Womersley

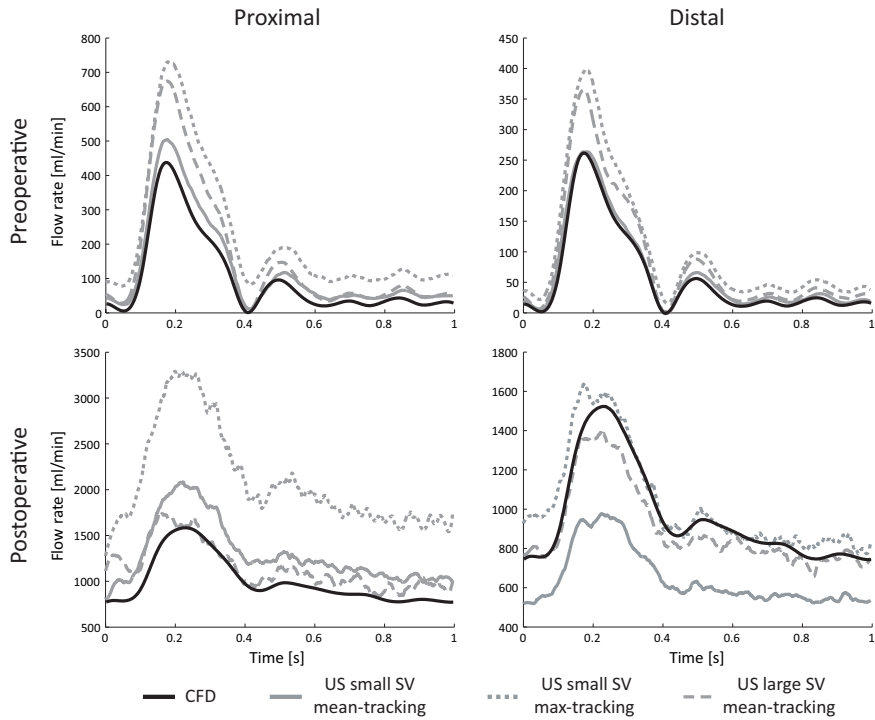


Figure 12.6: Volume flows (solid gray = mean-tracking, dotted gray = max-tracking), for a small sample volume (SV) acquisition, calculated with the β -value from Womersley theory (Equation 12.5) are shown together with the volume flows (dashed gray) for large sample volume (SV) acquisition (Equation 12.4), using mean-tracking, are compared to the CFD flow rate (solid black). Top: Preoperative cases; Bottom: Postoperative cases; Left: Proximal cases; Right: Distal cases.

flow, plug flow). Tracking the outer contour of the spectrum dramatically overestimates volume flow, except for the postoperative distal case (radial artery), where assuming a parabolic profile leads to an underestimation of -14.8%. Volume flow obtained from mean tracking is also systematically overestimated when assuming a plug flow profile or a Womersley profile (except the postoperative distal case), but is underestimated when assuming parabolic flow.

Small sample volume		Mean PWD-tracking			Max PWD-tracking		
% bias		Parabolic	Womersley	Plug	Parabolic	Womersley	Plug
preoperative	Proximal	-1.2	+30.1	+97.7	+69.2	+122.7	+238.4
	Distal	-10.8	+11.7	+78.5	+40.8	+76.3	+181.6
postoperative	Proximal	-1.4	+29.8	+97.3	+59.2	+109.5	+218.3
	Distal	-46.5	-33.0	+6.9	-14.8	+6.8	+70.4

Table 12.1: The bias for the time-averaged flow rate, in case of the small sample volume acquisition. Flows were calculated based on mean- and max-tracking of the Doppler spectrum, and different assumptions on the spatial velocity profile were investigated. β -values for a fully parabolic ($\beta = 0.5$), Womersley and plug ($\beta = 1$) flow were applied.

Large sample volume

To complete the analysis, the volume flows for a large sample volume (dashed gray) with mean-tracking, calculated according to Equation 12.4 are shown in Figure 12.6. These were based on PWD-spectra as shown in the lower panels of Figure 12.4. The bias of the simulated ultrasound data compared to the CFD values (comparing time-averaged flows), is listed in Table 12.2. From Figure 12.6 and Table 12.2, it is clear that the flow rates are overestimated by the US-algorithms, again, except for the postoperative distal case.

Large sample volume		% bias
preoperative	Proximal	+67.6
	Distal	+46.6
postoperative	Proximal	+14.2
	Distal	-6.3

Table 12.2: The bias for time-average flow rate, in case of large sample volume acquisition.

12.2.4 Discussion

In this paper, we studied PWD-based flow measurements in the brachial and radial artery in patients with an arterio-venous fistula, both in the pre- and postoperative case. We demonstrated that these PWD-based flow estimates are subject to a high degree of inaccuracy. This inaccuracy is not directly related to the inability of PWD to accurately capture the velocity component in the direction of the ultrasound beam, but is induced via two factors:

1. the angle-correction, which does not correctly estimate the velocity component along the assumed flow direction
2. the lack of knowledge on the flow profile

The inaccuracy induced by angle correction in volume flow estimation is demonstrated in Figure 12.7. It illustrates the process of angle-correcting the PWD velocity, both for the case of uni-directional laminar flow (= velocity vectors aligned with the axis of the vessel) and complex flow (= velocity vectors no longer aligned with the axis of the vessel). In both cases, the velocity measured by PWD, v_{PWD} (green), is the projection of the true 3D-velocity vector \vec{v} (black), on the direction of the ultrasound beam (\vec{e}_{us}). For uni-directional flow (Figure 12.7, top), v_{PWD} is the projection of the longitudinal velocity, v_x (blue), which in this case equals the velocity vector \vec{v} . However, when a complex flow field is present, v_{PWD} not only consists of a contribution from the longitudinal component v_x (blue), but also from the radial v_y component (red). As such, the angle-corrected Doppler velocity v_n does not only reflect the longitudinal velocity component v_x but also the radial velocity component v_y . Therefore, depending on the flow field and the orientation of the velocity vectors, angle-correction of v_{PWD} can either over- (Figure 12.5 (left), preoperative, proximal) or underestimate (Figure 12.5 (right), postoperative, distal) the velocity in the assumed flow direction ($v_n(t)$).

To illustrate that the orientation of the flow vectors indeed plays a role in the cases considered here, we display the flow fields and the in-plane velocity vectors for the four studied cases in detail in Figure 12.8. It is clear that in all cases the in-plane velocity vectors have a non-zero component in the radial y -direction, which is also picked up by the Doppler measurement as shown in Figure 12.7. For the preoperative proximal case, the velocity vectors point upwards, resulting in a positive velocity v_y , while for the postoperative distal case, the velocity vectors in the sample volume (indicated in white) point downwards, resulting in a negative velocity v_y . Note also the highly asymmetric, skewed nature of the flow profiles in the postoperative case.

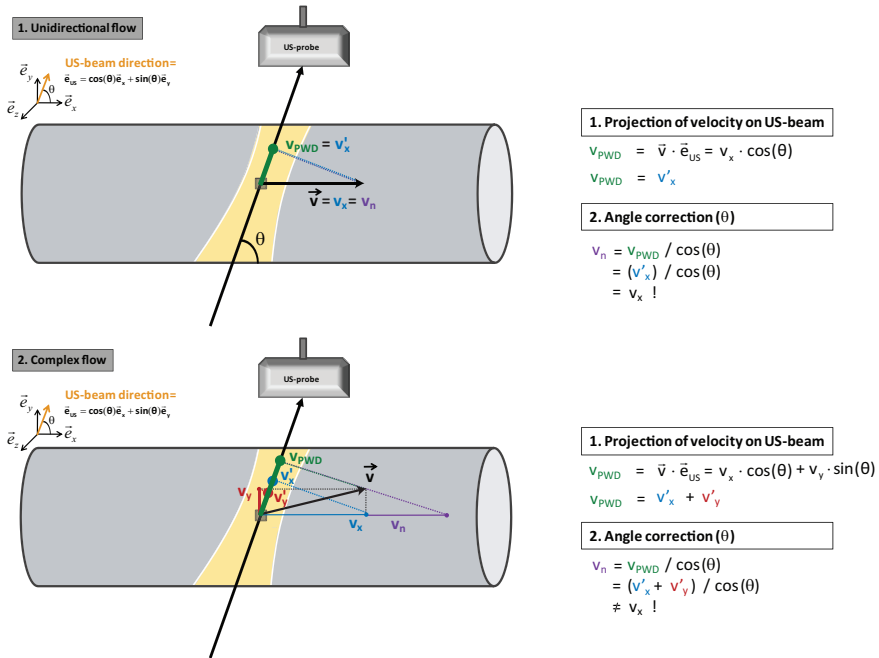


Figure 12.7: Illustration on why angle correction of the Doppler velocity works for unidirectional flow (upper case 1) but fails for complex flow (lower case 2).

Beside the angle-correction itself, the method applied to derive the velocity curve from the Doppler spectrum can introduce considerable errors in the flow estimation. The maximum frequency detector is seriously biased, as noticeable in Figure 12.4, since the maximum frequency cannot be univocally determined because of intrinsic spectral broadening processes [226]. Therefore, although it is a common approach in clinical practice [168, 227], due to the lower sensitivity to shifts in measurement location, the max-tracking leads to significant overestimation of the actual flow velocities and flows. Further, it should be noted that while max-tracking is usually performed by analyzing pixel intensity, mean-tracking requires direct access to the spectral estimates and thus registration of the RF-data during the measurement.

Further, the lack of knowledge on the spatial velocity profile contributes to the inaccuracy of the flow estimation. When assessing the velocity in a sample volume positioned in the center of the cross-section, a correction factor β needs to be assumed, which relates to the shape of the velocity profile. Our data seem to indicate that, for the investigated cases, there is no single

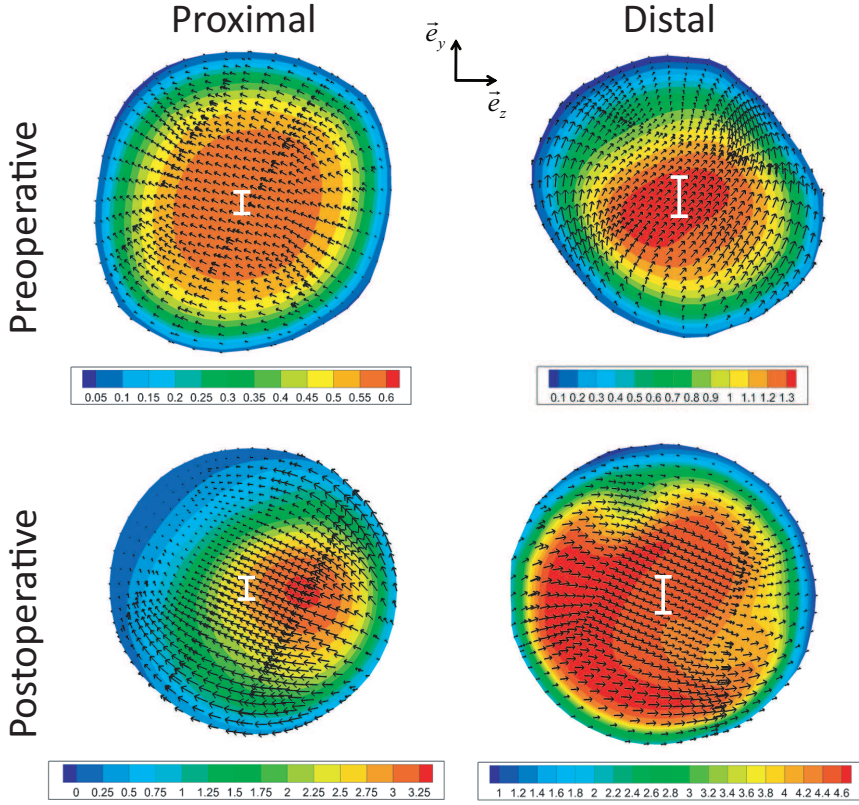


Figure 12.8: Velocity magnitude [m/s] in the four selected region of interest with the in-plane velocity vectors at the time point of peak velocity. The small sample volume (0.39 mm) is shown in white.

optimal choice for β . The β -values that one should use to match the PWD-derived velocity data, analyzed by mean-tracking, to the true mean velocity known from CFD are 0.506, 0.560, 0.507 and 0.935 for preoperative proximal, preoperative distal, postoperative proximal and postoperative distal, respectively. In the proximal locations, the assumption of a parabolic flow profile for a small centered sample volume ($\beta = 0.5$) seems reasonable. For the distal location in the small sample volume acquisition, the theoretical value ranges from 0.560 to 0.935 when changing from the pre- to the postoperative model. It is clear that the increase in overall flow rate induces a more complex flow pattern, see Figure 12.8, with a β value closer to the solution for plug flow. As stated before, the max-tracking significantly overestimates the flows. This results in ideal β -values of about 0.6 for the postoperative distal case and about 0.33 ($1/3^{th}$) for the other three cases.

In the assumption of fully symmetrical flow profiles, one expects that the use of the larger sample volume, using mean-tracking (Equation 12.4), should provide the most accurate estimate of the volume flow. Interestingly, our data indicate that this was not systematically the case. First of all, this method is challenged since the velocities in the vessel wall region are difficult to measure, even in straight vessel segments [228–232]. Furthermore, this method only assesses the mean velocity of the 1D velocity profile, instead of assessing the mean velocity for the complete 2D cross-section.

The cross-sectional area used for the PWD flow estimate was calculated based on the diameter measured perpendicular to the vessel assuming a circular cross-section. These estimated areas only differed 2.2%, 2.0%, 6.0% and 2.4%, for preoperative proximal, preoperative distal, postoperative proximal and postoperative distal respectively, with the 2D-cross-sectional areas calculated from the CFD solution. Therefore, the cross-sectional area calculation is, when comparing to the overall flow estimation bias in Table 12.1–12.2, no major source of error in our evaluation.

As described by Swillens et al., the use of multiphysics ultrasound simulations bears some inherent limitations, the most important being the assumption of linear ultrasound wave propagation, the use of rigid walls and the absence of surrounding tissue, the latter typically affecting the accuracy of blood velocity estimation [219]. The result of a velocity measurement with ultrasound is also dependent on the probe settings. The simulations were performed for a typical linear array probe used for vascular examinations, with PRF-settings that were tuned to allow capturing the maximum velocities as one would do in clinical practice. We believe that our specific choice has only a minor influence on the overall message and conclusion of this study. However, an in-depth analysis of probe settings and imaging parameters, coupled with different flow regimes, could provide more inside in the complex nature of PWD acquisitions. This could be included in a future large parameter study.

It is clear that, based on our study, it is difficult to provide strict guidelines to estimate blood flow rate by PWD-acquisition. Overall, for the investigated cases, measurements based on the small sample volume positioned in the center of the vessel, analysis based on mean-tracking and with the assumption of a parabolic flow profile showed greatest accuracy, except for the distal measurement in the postoperative case where the method underestimates flow by about 50%.

From a clinical perspective, it might be safer to apply a method which leads to more conservative (underestimated) values of flow rather than methods leading to overestimation, although the better method performs well

under all circumstances. More robust techniques are available when recording flow during hemodialysis therapy, based on connecting the patient to the extra-corporal circuit (e.g. ultrasound flow dilution (Transonic)). When assessing preoperative or direct postoperative flow, replacing PWD derived flow measurements can be more cumbersome. However, it should be noted that more advanced ultrasonic flow estimators are being developed, but are still in a preclinical phase. A potential solution for the demonstrated limitations regarding PWD volume flow measurements, is the use of 2D flow estimators (e.g. speckle tracking, vector Doppler) [233–243], avoiding the need to angle correct a 1D velocity, but their clinical applicability is to be demonstrated. In parallel, researchers have focused on the development of multi-gate Doppler acquisitions, allowing to directly assess the velocity profile, through simultaneous processing of several sample volumes along the US beam [244].

12.2.5 Conclusion

We conclude that, in the setting of a forearm vascular access, flow estimates based on pulsed wave Doppler are hampered by the complex flow patterns, especially in the postoperative setting. Flow estimation based on centerline measurement, analysed by mean-tracking of the spectral estimates and under the assumption of a parabolic flow profile seem to provide reasonable values for most cases.

Four

Study on AVGs

Computational study of flow in helical AVGs

K. Van Canneyt, U. Morbiducci, S. Eloot, G. De Santis, P. Segers and
P. Verdonck.

A Computational Exploration of Helical Arterio-Venous Graft Designs.

Revision submitted.

13.1 INTRODUCTION

Nowadays, over 20 million patients worldwide are in need of renal replacement therapy [10, 11]. In western countries, over 90 % of the patients waiting for a kidney transplant depend on hemodialysis [12, 17], and need a long-term vascular access. Although an arterio-venous fistula (AVF) is the first choice in most patients, in specific cases (e.g. low quality vessels in elderly or diabetics) an arterio-venous graft (AVG) is the second best option [245]. Hereby an artery and a vein, mostly in the (lower) arm are connected by a synthetic graft.

AVGs, however, deal with complications such as thrombosis and stenosis formation. As clinically observed, the stenosis formation with AVGs is mainly located at the venous anastomosis or in the draining vein [30, 75, 246]. These adverse events, due to maladapted intimal hyperplasia (IH) [30, 36], are driven by abnormal hemodynamics. It is known from literature that, after vascular access creation, the flow field may play a modulating role, with IH mainly located in regions of low wall shear stress, high oscillatory shear stress and high residence time [75, 124, 125, 246–250]. Furthermore, certain flow patterns in the bulk, induced by out-of-plane geometries, can be linked to disturbed shear distributions at the luminal surface [71–73, 251]. More specifically, helical flow tends to reduce these unfavorable hemodynamic conditions [128, 252–255].

With this in mind, a helical shape was introduced in AVG designs by Caro et al. [70, 74]. Up to now, the research on helical AVGs as vascular access consists of an animal model study [74], a preliminary clinical study on 20 patients [76], and a clinical trial on 180 patients, as suggested in the work by Glickman et al. [77]. In other studies, computational fluid dynamics (CFD) was applied to analyze the hemodynamic performances of helical grafts in a stand-alone [256, 257] and in a bypass configuration [258], not only to minimize disturbed shear but also to improve near wall and central flow mixing. Sun et al. compared the helical graft design from Caro et al. [74] with a new helical design, using steady-state flow conditions [256]. Cookson et al. investigated the in-plane flow structures and central flow mixing in helical conduits in steady-state flow conditions [259]. Coppola and Caro investigated the impact of arterial three-dimensionality on both wall shear stress and oxygen transport/transfer [73]. Zheng et al. simulated steady flows in helical grafts and carried out a parametric analysis with respect to the Dean Number and helical pipe geometric features, i.e., helical pitch and amplitude [257]. Recently, Zheng et al. simulated the physiological pulsatile flow in helical grafts and observed that helical geometry creates amplified WSS magnitudes near the wall, that oscillatory shear never exceeds

non-physiologically significant values, and that the strong secondary flows improve flow mixing between low-momentum fluid near the surface and high-momentum fluid near the central flow [260]. Only Wen et al. studied the graft in a coronary bypass setup (low flow, small diameter, no loop) and one helical design was compared to the straight conventional design [258]. So, while different computational studies have been performed in low flow (coronary) bypass configurations or in stand-alone configurations without (arterial or venous) anastomosis, up till now, the clinically relevant, high flow, helically-designed loop AVG configuration has not been studied in detail [75].

Therefore, the aim of this study was to investigate, using CFD, the impact of the introduction of helical design in an AVG loop as a vascular access for hemodialysis on the occurrence of (un)favorable hemodynamic conditions at the venous anastomosis [30, 75, 246].

13.2 MATERIAL AND METHODS

Six different parametric models of a graft connecting an artery and a vein were created in `pyFormex`¹. All models consist of a 4 mm (diameter) artery, a 6 mm graft section and a 6 mm vein, as shown in Figure 13.1. The graft section has a length of 300 mm in a loop configuration with both anastomosis angles set at 45 degrees. As a reference model, a straight conventional graft (SCG) was constructed. As shown in Figure 13.2, five helical design grafts (HDG-1 to HDG-5) were created to analyze the influence of a helical design on hemodynamics. The amplitude of the helix of the graft was 3 mm (half the graft's diameter) and one helix turn (pitch) was 105 mm; 87.5 mm; 70 mm; 52.5 mm or 35 mm long, respectively. HDG-3 is based on the design of the SwirlGraft (Veryan Medical Limited, UK).

The models were discretised with a fully conformal and structured hexahedral mesh [220, 221, 261]. Because of the high flow rates and the expected transitional flow patterns [262], an extensive mesh density and time step analysis was performed. 200Hz sampling and consecutive mesh refinement up to 4.3 million cells (4.5 million nodes) resulted in WSS values at the venous anastomosis region within 2 % of the results obtained with a 6.4 million cell model. With the used hexahedral meshed meshes, about 140 hours, on 24 nodes of an in-house cluster, were required to calculate two consecutive cardiac cycles, for one model.

¹<http://pyformex.org>

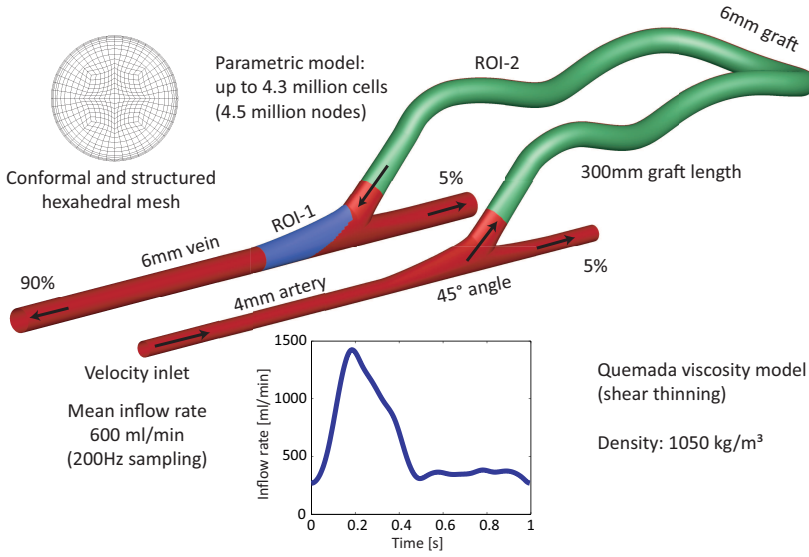


Figure 13.1: Summary of model, mesh, material properties and boundary conditions (example of HDG-3). Region of interest at venous anastomosis site (ROI-1) and region of interest in graft section (ROI-2) are highlighted.

The finite volume method was applied to solve the laminar governing equations of the fluid motion, by use of the general purpose CFD code Ansys Fluent 12 (ANSYS inc., Canonsburg, PA, USA).

A post-operative flow waveform from a vascular access patient was acquired by use of magnetic resonance imaging as described by Huberts et al. [168]. A patient-specific flow waveform was set, in terms of parabolic velocity profile, as inlet boundary condition at the proximal artery (Figure 13.1). The profile was scaled to achieve a time-averaged flow rate of 600 ml/min, which is in line with the European and American guidelines on vascular access [19, 22]. The inflow was redistributed such that 95% was sent to the graft (with a further downstream division of 90% of to the proximal vein and 5% to the distal vein), and 5% to the distal artery.

To mimic blood, a shear thinning fluid, defined by the Quemada viscosity model [118] (1.3 mPa.s plasma viscosity and 40% hematocrit) with a density of 1050 kg/m³, was implemented, as suggested Loth et al. [75].

As for the computational setting, standard pressure discretisation and second-order upwind momentum discretisation schemes were applied. After a time step sensitivity analysis, a 5 ms time step was chosen and two cardiac cycles were calculated. In all cases, the analysis and post-processing was

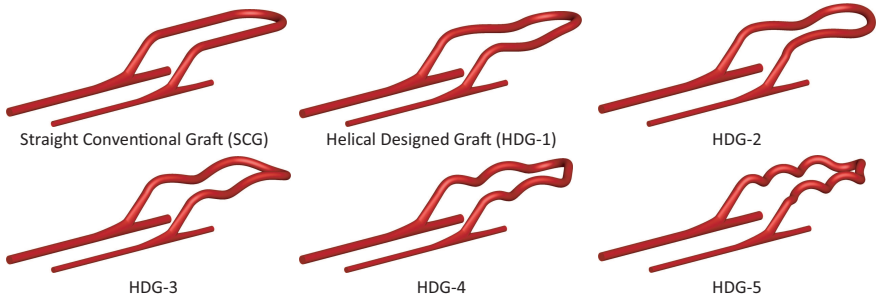


Figure 13.2: Overview of the studied designs.

performed on the second time step using Matlab (The Mathworks, Natick, MA, US) and Tecplot (Tecplot inc, Bellevue, WA, US) .

Three wall shear stress-based descriptors of the flow field were calculated in the region of interest (ROI) at the venous anastomosis (ROI-1, Figure 13.1). The time-averaged wall shear stress (TAWSS) was calculated as the integral over time of the absolute value of the WSS-vector, with T representing one cardiac cycle:

$$TAWSS = \frac{1}{T} \int_0^T |\overline{WSS}| dt \quad (13.1)$$

To assess the change in direction of the flow and, with it, the velocity gradient during a cardiac cycle, the oscillatory shear index (OSI), originally introduced by Ku et al. [123], was calculated:

$$OSI = \frac{1}{2} \left(1 - \frac{\left| \frac{1}{T} \int_0^T \overline{WSS} dt \right|}{\frac{1}{T} \int_0^T |\overline{WSS}| dt} \right) \quad (13.2)$$

The relative residence time (RRT), introduced by Himburg et al. [124] was qualified as:

$$RRT = \frac{T}{\left| \int_0^T \overline{WSS} dt \right|} \quad (13.3)$$

To compare all six cases, two different methods were used. First, the luminal surface area in ROI-1 subjected to low TAWSS and high OSI and RRT values was quantified. Second, a patching-method, based on areas of low TAWSS and high OSI or RRT, was explored. For the three parameters, the geometrical distributed areas of all six cases were unified to achieve one global patch per single parameter, as in Morbiducci et al. [263]. With

this method, three non-operator dependent or non-biased ROIs were determined (TAWSS-patch, OSI-patch and RRT-patch) and used to compute the average TAWSS, OSI and RRT. In both the area- and the patch-method, cut-off values of 1Pa for TAWSS, 0.1 for OSI and 1Pa⁻¹ for RRT were used.

Next to these wall shear parameters, bulk flow features were assessed by using a helicity-based descriptor. In the graft section (ROI-2; Figure 13.1), bulk flow features were characterised using the helicity-based descriptor H , expressed as the volume-average of the absolute kinetic helicity:

$$H = \frac{1}{V} \iiint |H_k| dV = \frac{1}{V} \iiint |\vec{v} \cdot (\nabla \times \vec{v})| dV \quad (13.4)$$

Note that the kinetic helicity intensity, H_k , is a measure of the alignment of the velocity vector \vec{v} , and the vorticity vector, $\text{curl } \vec{v}$. Both instantaneous and time-averaged H were calculated over the graft section (ROI-2; Figure 13.1). To achieve a more global quantity, the kinetic helicity intensity, H_k , can be normalized with the velocity and vorticity magnitude resulting in a Local Normalized Helicity (LNH) between -1 (counterclockwise helix when looking along with the flow direction) and 1 (clockwise) [264]. Descriptor LNH is a non-dimensional quantity and a measure of the alignment/misalignment of the local velocity and vorticity vectors and its sign is a useful indicator of the direction of rotation of helical structures [253, 255, 263].

Finally, the instantaneous and time-averaged static pressure drop were calculated over the graft section. All results were compared with the reference case, i.e. the straight conventional graft (SCG).

13.3 RESULTS

Figure 13.3 summarizes our findings with regards to the area in ROI-1 exposed to TAWSS below 1 Pa, OSI above 0.1 or RRT below 1 Pa⁻¹. It is clear that the results are not trivial to interpret, and the impact of the helical design is different for each investigated parameter. The area exposed to low TAWSS is only lower for designs HDG-4 and HDG-5, while the area exposed to high OSI values is reduced for designs HDG-3 and HDG-5. The only parameter that shows a more or less consistent relation with increasing helical pitch is the area exposed to high values of RRT, which first slightly increases but decreases for designs HDG-3 to HDG-5.

The parameter specific patches as well as the results for the average values in these patches are shown in Figure 13.4. Because for TAWSS a patch was created unifying the six zones (one for each case) with values below 1 Pa, the

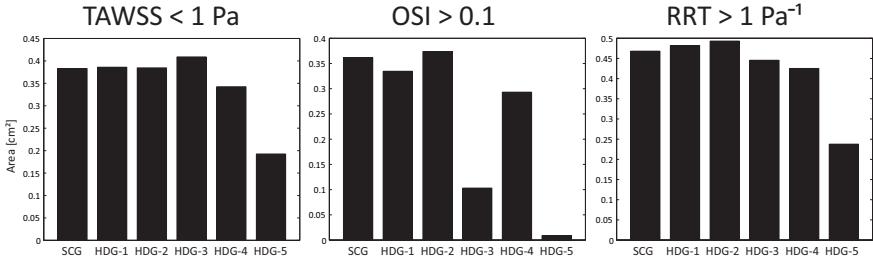


Figure 13.3: Area with unfavorable shear stress-related parameters for the six studied designs : TAWSS < 1 Pa (left), OSI > 0.1 (middle) and RRT > 1 Pa⁻¹ (right) in ROI-1.

higher the value of average TAWSS is, the more favorable the hemodynamics. For OSI and RRT, values above 0.1 and 1 Pa⁻¹, respectively, were chosen to create the patch. Therefore, low average value of these parameters indicate more favorable conditions. In general the patching method highlight the same trends as observed in the area-method. However, the values for TAWSS in cases HDG-1 to HDG-4 show less favorable wall shear stress values compared to the reference case. As for OSI, it is still evident that models HDG-3 and HDG-5 exhibit more athero-protective conditions. The other cases show a more distinct reduction in unfavorable OSI values compared

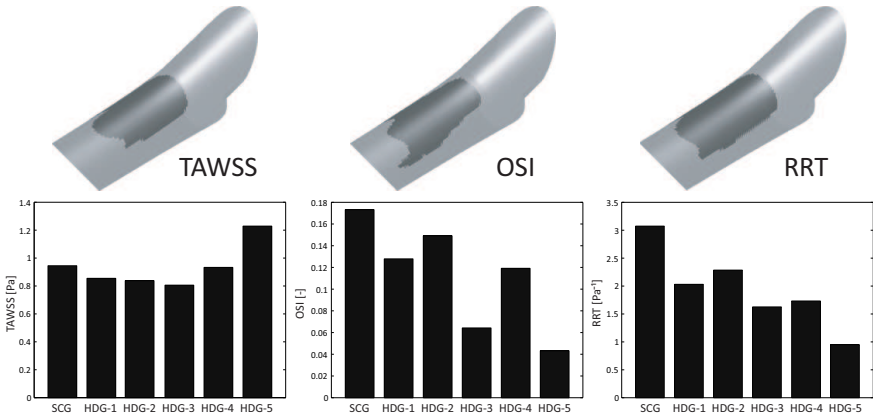


Figure 13.4: Top: The three patches (triangulated) created by unifying zones in ROI-1 with TAWSS < 1 Pa, OSI > 0.1 and RRT > 1 Pa⁻¹ respectively; Bottom: Area-weighted average of TAWSS, OSI and RRT in these patches for the six studied designs. Favorable values are high TAWSS and low OSI and RRT.

to the results from the area-method. The same overall reduction as for OSI can be found when analyzing the RRT results.

When calculating the area with TAWSS below 0.4 Pa, a well-accepted threshold for unfavorable WSS conditions [122], we find an area of 0.11 cm² for the SCG. This area increases by 20.7 %, 29.1 %, 41.5 % and 5.4 % when analyzing design HDG-1 to HDG-4. For the HDG-5 model, a 100 % low-TAWSS area reduction is found. The minimum value of TAWSS in ROI-1 for the HDG-5 low pitch design is 0.57 Pa.

Interestingly, the absolute kinetic helicity values averaged over the volume of ROI-2 (Figure 13.5; top) clearly indicate that the helicity in the bulk flow of the graft increases with the number of helix turns. In particular, a 2.6-fold increase in the time-averaged H is obtained in HDG-5, when compared to the reference case.

The pressure drop over the graft section (ROI-2) is shown in Figure 13.5 (bottom). An increasing number of helix turns in the graft design leads to a moderate increase in the pressure drop, which is most pronounced for HDG-5 (5.8 mmHg), compared to the 3.6 mmHg in the SCG.

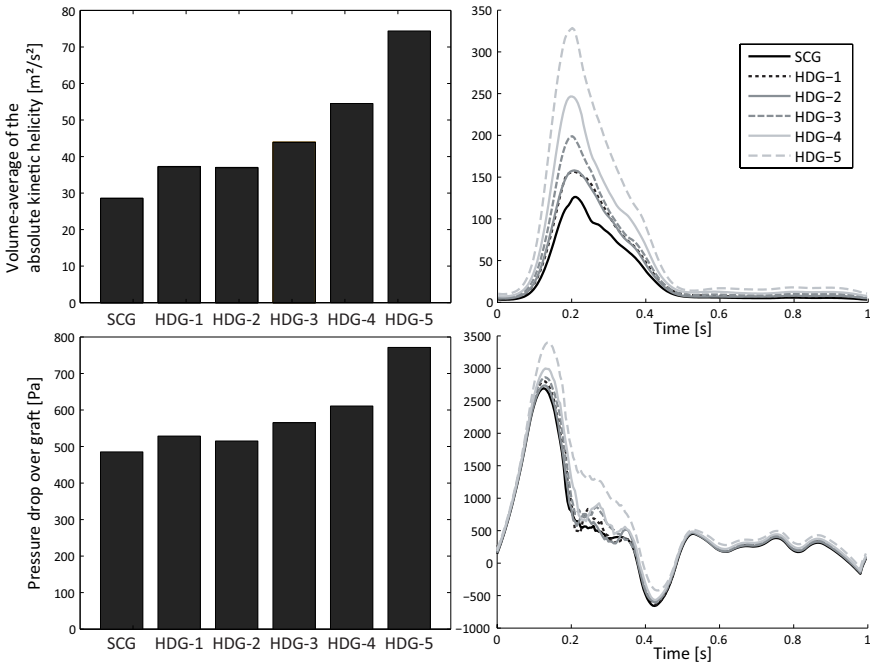


Figure 13.5: Volume-average of absolute kinetic helicity in the graft section (top) and pressure drop over the graft section (bottom) for the six parametric models: Time-averaged (left); One cardiac cycle (right).

The impact of the closed-loop AVG design on the bulk flow in the graft, is visualized in Figure 13.6 by the use of LNH iso-surfaces. When adopting high threshold values of LNH (± 0.7) for the visualization of markedly aligned/opposed velocity and vorticity vector fields, different topological features can be observed, depending on graft geometry. More in detail, Figure 13.6 highlights that, at peak systole, counter-rotating fluid structures (positive and negative LNH values indicate counter-rotating helical structures) characterize the flow into the grafts in such a way that is markedly dependent on the number of pitches of the helical conduits. In particular, focusing the attention on the outflow tract of the graft (i.e. the region of the venous anastomosis), it can be noticed from Figure 13.6 that: (1) no intertwined fluid structures with marked LNH magnitude appear in the distal part of SCG model; (2) the presence of high magnitude, counter-rotating (red and blue LNH iso-surfaces), intertwined fluid structures is a common feature of the bulk flow in helical grafts, independent of the number of pitches; and (3) the higher the number of pitches in the graft, the more counter-rotating fluid structures are intertwined.

In Figures 13.7 to 13.9, the velocity magnitude and in-plane streamlines are displayed at three different time points along the cardiac cycle. Two different venous cross-sections are considered for observation: (1) at the venous anastomosis, where the flow starts to bend from the graft section towards the horizontal vein (section A); and (2) at a venous cross-section located 10 mm (about 1.7 vein diameters, section B) downstream the venous anastomosis. It can be observed from Figures 13.7 to 13.9 how the helical graft geometry plays a primary role in the primary and secondary velocity patterns at the venous anastomosis region.

At early systole, Figure 13.7 shows that all AVG designs show a flow field that is characterized by two counter-rotating vortices. As the number of helix turns in the graft increases, the high axial velocity region shifts in a clock-wise direction. Moving from section A to section B, the high axial velocity is shifted to the opposite side with respect to the vein region and an action of axial flow stretching is exerted in section A. At this point, the AVG design seems to have a mild impact on the fluid patterns establishing into the region of the venous segment (i.e., ROI-1, Figure 13.1): Figure 13.7 clearly shows that no marked differences in terms of low velocity or recirculating flow patterns are present very close to the ROI-1 of all the AVG models.

At peak inlet flow rate, Figure 13.8 shows marked differences among the different AVG designs in the composition of translational and rotational flow: (1) at the venous anastomosis (section A), where an increase in the number of pitches imparts a marked clock-wise rotation of the location of

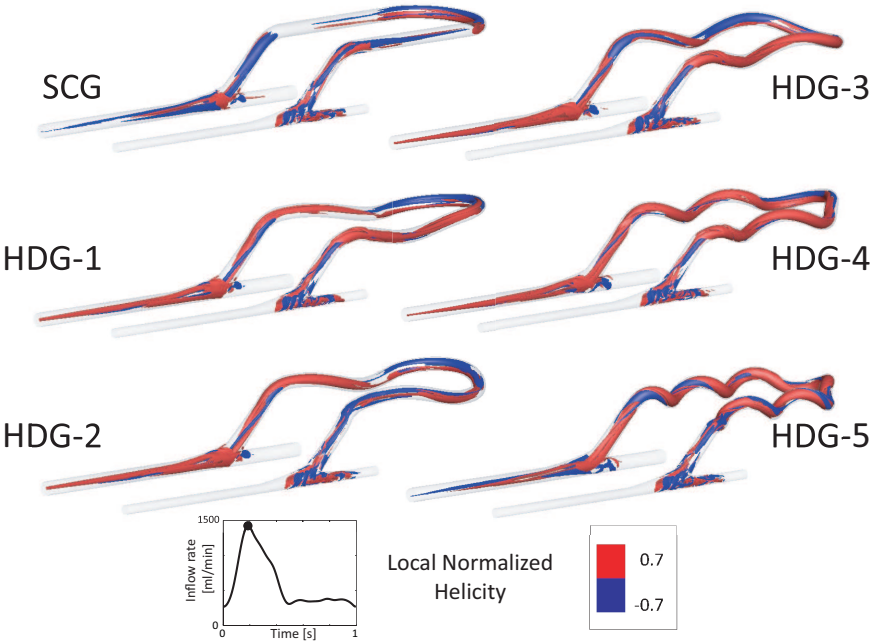


Figure 13.6: Iso-surface of Local Normalized Helicity (LNH) in the six studied designs, at peak systole (0.185 sec), highlighting counter-rotating fluid structures (positive and negative LNH values indicate counter-rotating helical structures) induced by the grafts.

high axial velocities and secondary flows stretching/folding; and (2) downstream of the venous anastomosis (section B), where ROI-1 experiences, for an increase of the number of pitches, a marked reduction in low velocity and recirculating regions close to the wall; this as a consequence of the multiple-vortex and the differently stretched secondary flow patterns.

At late systole, Figure 13.9 shows that increasing the number of pitches in helical grafts, and with it, helicity intensity, leads to a marked washout of the venous region ROI-1. Herewith, in model HDG-5, the extension of low velocity and recirculating regions very close to the wall are markedly reduced. This is particularly true at section B, due to the onset of a centralized, stabilizing vortex, opposed to more complex secondary flows characterizing the other models.

13.4 DISCUSSION

To study the influence of a helical design of an AVG as vascular access on the hemodynamics (in particular on shear-stress related parameters), six differ-

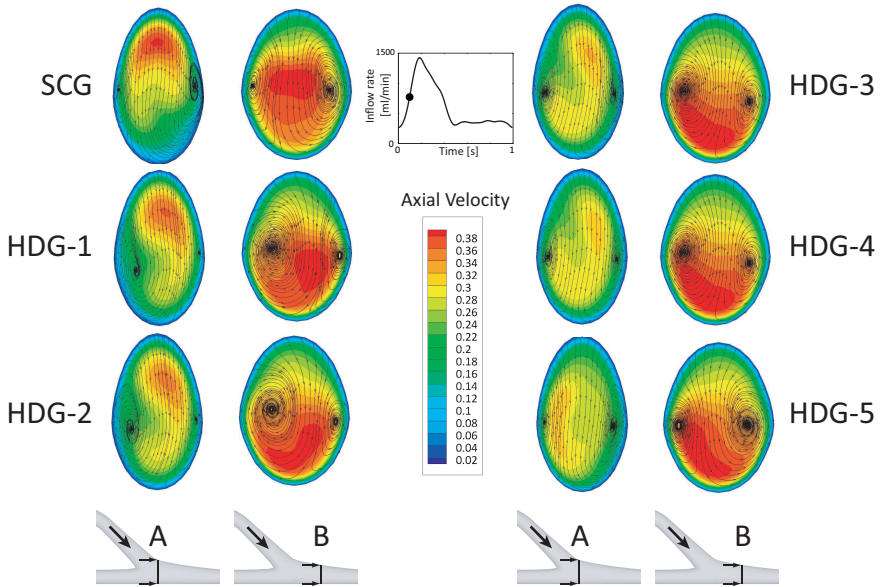


Figure 13.7: Axial velocity contours [m/s] and in-plane streamlines at early systole (0.09 sec). Two different venous cross-sections are considered as planes of observation: (A) at the venous anastomosis, where the flow starts to bend from the graft section towards the horizontal vein; (B) at a venous cross-section located 10 mm (about 1.7 vein diameters) downstream of the venous anastomosis.

ent computational models were created. All models were constructed parametrically, only changing the helical pitch in the graft. A straight conventional graft was introduced and flow patterns were compared to those in five different helical designed grafts (Figure 13.2).

There is no trivial relationship between the number of helix turns in the graft design and the investigated parameters. The design with the highest number of helix turns, HDG-5, scores best when comparing TAWSS, OSI and RRT. For the other designs, HDG-3 seems to score better than HDG-1, HDG-2 and HDG-4 in terms of OSI, but scores worse than HDG-4 for TAWSS and RRT. Hence, there is no one-on-one relation between the number of pitches in the graft and the investigated parameters quantifying disturbed flow and shear stress in the region of the anastomosis.

We tested two different methods to quantify the WSS-based descriptors TAWSS, OSI and RRT. Overall, both the area- and the patch-method result in the same overall conclusions. However, a case-wise analysis reveals some differences in the obtained results. Where the area-method indicates that HDG-1 and HDG-2 score comparable with the reference design SCG for all

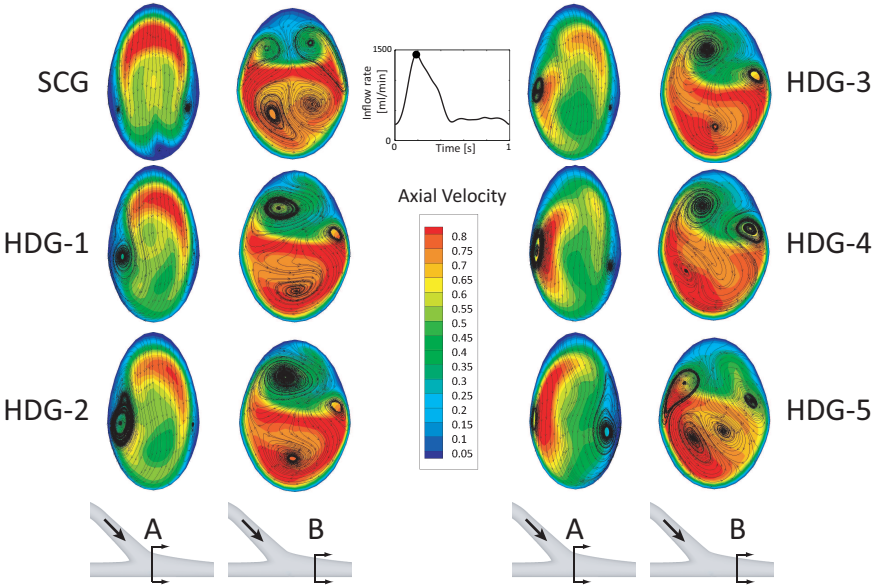


Figure 13.8: Axial velocity contours [m/s] and in-plane streamlines at peak systole (0.185 sec). Two different venous cross-sections are considered as planes of observation: (A) at the venous anastomosis, where the flow starts to bend from the graft section towards the horizontal vein; (B) at a venous cross-section located 10 mm (about 1.7 vein diameters) downstream of the venous anastomosis.

three parameters, the patch-method results in a worse outcome for TAWSS and a better outcome for OSI and RRT. When looking at HDG-3 (based on the design of an existing graft), low TAWSS area is higher than in SCG, while the high RRT area is comparable. The average value in the patch of TAWSS is somewhat smaller than in the reference case, but for the OSI a strong reduction of the area exposed to high values is found. Hence, the oscillating shear seems to be reduced in HDG-3. For the somewhat more helical design HDG-4, a reduced area is exposed to low TAWSS and high RRT, but again there is an increased area characterized by high OSI. Finally, the most helical design HDG-5 (with a pitch of 35 mm) revealed to be instrumental in reducing disturbed shear (Figures 13.3 and 13.4): in it, a relevant decrease in areas interested by low TAWSS and high RRT was observed. This is even more pronounced when observing the elimination of the region with a TAWSS below 0.4 Pa for HDG-5 case. Furthermore, HDG-5 even almost eliminates the area with OSI above 0.1.

To get more insight into the reason that makes a helical design of the graft instrumental in suppressing disturbed shear, a quantitative analysis of

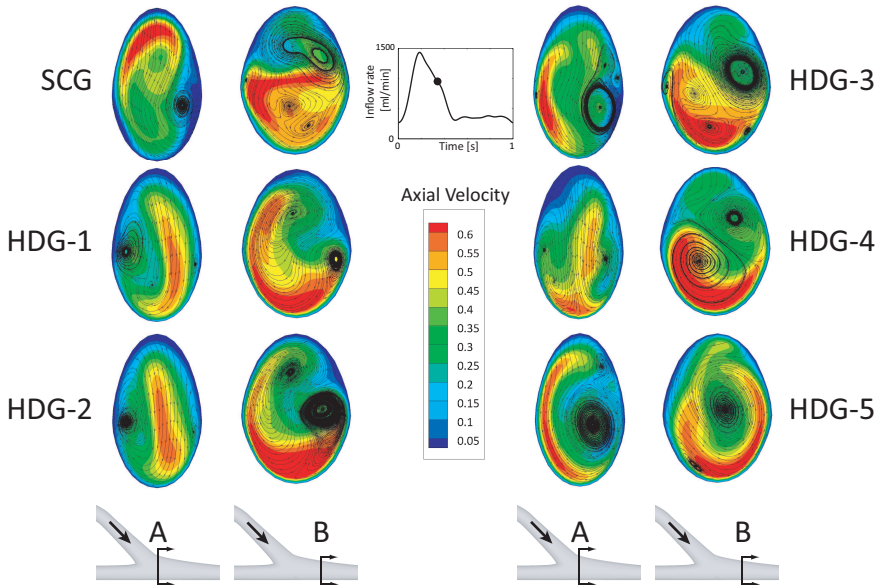


Figure 13.9: Axial velocity contours [m/s] and in-plane streamlines at late systole (0.34 sec). Two different venous cross-sections are considered as planes of observation: (A) at the venous anastomosis, where the flow starts to bend from the graft section towards the horizontal vein; (B) at a venous cross-section located 10 mm (about 1.7 vein diameters) downstream of the venous anastomosis.

the bulk flow, in terms of its helical content, was performed. Therefore the volume-integrated value of the absolute kinetic helicity into the graft was calculated. The absolute value of the kinetic helicity was considered because a clockwise helical pattern can otherwise compensate a counter-clockwise pattern when volume averages are calculated. Here we observed that an overall increase in the helical flow patterns within the graft is associated with the number of helix turns. This is due to the fact that in loosely coiled helix pipes both torsion and bending mutually contribute to the onset of helical flow. It should be noted that the flow is not only subject to the helical design of the graft, but to the flow split at the arterial and venous anastomosis, to the bending from the anastomosis to the horizontal position and to the bending of the loop graft as well.

Overall, the pressure drop over the graft (Figure 13.5; bottom) increases with increasing helicity. The pressure drop rises from 480.2 Pa to 771.3 Pa when comparing HDG-5 to SCG (i.e. increase of 60.6 %, but only 2 mmHg). So, in absolute values, both pressure drops seem negligible in the blood flow path from a clinical point of view (i.e. from about 100 mmHg at the left

ventricle to about 5 mmHg at the right atrium). When analyzing the pressure drop as a function of time (Figure 13.5; bottom-right), it is noticed that a negative pressure drop occurs between 0.39 and 0.48 seconds. This negative pressure difference over the graft is due to the fact that the flow gets inertia dominated because of the high-flow condition and the strong decreasing velocity.

The fluid patterns observed in Figures 13.7, 13.8 and 13.9 might be a consequence of the counter-rotating, intertwined fluid structures characterizing the bulk flow in helical grafts, as shown in Figure 13.6. We speculate that the more these helical flow structures are intertwined, the more they contribute to the flow stabilization in the downstream venous segment, thus the mitigation of the transitional effects and, ultimately, the disorganization of the flow field downstream of the anastomosis. This is in line with the well documented role played by helicity in reducing energy transport from the inertial to the dissipation scale, thus avoiding the onset of turbulence and, ultimately, promoting flow stabilization [265]. The fluid structures observed in the case of model HDG-5 during the deceleration phase (Figures 13.9) support the plausibility of our conviction: the presence of a centralized, predominating one-vortex secondary flow stabilizes the flow field, hence avoiding the breakdown of the flow in multiple vortex patterns.

As observed in Figure 13.6 to 13.9, for all HDGs, a swirl pattern present in the graft section generates a complex flow field in the anastomosis region. It should be remarked that the length of the straight graft section, proximal to the venous anastomosis, might influence the position of the swirl at the anastomosis site and, with it, the value of the local WSS-based descriptors. Although the connection of the venous end of the graft with the anastomosis was created equal for all designs, the initial choice of anastomosis inflow length and geometry might influence the fluid structures developing into the graft and downstream of the venous anastomosis. In the future, this can be object of further investigation.

In our study we focus our attention on the impact of the design of the graft, in terms of disturbed shear, at the venous anastomosis and not to disturbed shear into the graft. This driven-by-clinical-observation focus to the venous anastomosis makes it complicated to furnish an interpretation of disturbed shear at the anastomosis in terms of the physical nature of the flow structures into the AVG design. A description of the physical nature of the flow in terms of the paradigms of the fluid mechanics in helical conduits (Dean [266], Germano [267] and LM [268] numbers) can only loosely be adopted, because of the influence of the anastomosis (45 degree angle and non-circular cross-section at the venous anastomosis) and the applied unsteady flow conditions. For the sake of completeness, the mean Reynolds

number at the inlet was 909 and in the graft 576. The mean Dean numbers were 102, 121, 150, 195 and 273; the mean Germano numbers 100, 119, 145, 183 and 240; and the mean LM numbers 0.11, 0.10, 0.09, 0.08 and 0.06; in cases HDG-1 to HDG-5 respectively. Whether the use of mean Reynolds, Dean, Germano and LM numbers (mean data, along the axis of the graft) are a helpful design tool for AVGs in a clinical relevant setup (loop graft and unsteady flow conditions) should be investigated more in depth with a parametric approach.

It should be noted that despite the fact that HDG-5 gives the best results concerning the reduction of the unfavorable hemodynamics, the practical use of this design could be questioned. In clinical practice, the AVG is implanted in the arm under the skin. If the graft is fabricated from expanded polytetra-fluoroethylene (ePTFE), as most grafts nowadays are, the number of helix turns will, most probably, be reduced because of the tension of the skin. In the preclinical study of Huijbregts et al. on a design similar to HDG-3, angiographic examination showed already, in a number of cases, a reduction of the helical geometry [76]. They suggest that this might be due to overstretching the graft during implantation, or by elongation under arterial pressure. But even when a material which can resist this stretching would be used, the graft will still require a large space under the skin.

Although numerous authors stated that low TAWSS, high OSI and high RRT can be linked to IH and therefore stenosis formation [75, 124, 125, 246–250], no clear threshold values for IH formation, e.g. at the venous anastomosis of an AVG, for these wall shear stress descriptors can be found. We analyzed the results of all our studied cases using threshold values of 1 Pa for TAWSS, 0.1 for OSI and 1 Pa^{-1} for RRT. To somehow limit the impact of this arbitrary choice on the interpretation of our data, we also used, the patch-method, defining patches by those threshold values, and analyzing area-averaged parameters.

Our study contributes to a better understanding and quantitative analysis of the impact of novel graft designs on hemodynamics. Although helical designs have been introduced in bypass grafts, stents and vascular access grafts [74, 258, 269, 270], this study is the first in-depth (computational) analysis performed on helical designed vascular access grafts in a clinically relevant (i.e. closed-loop) configuration. Caro et al. added their pre-clinical animal study with some basic CFD work on a single helical graft. Without stating the used methods, they only showed a numerical helical graft in a straight configuration, focusing on the non-symmetric flow field in the graft itself. The paper also reported a small experimental in-vitro study showing the helical flow patterns in a 90° anastomosis, by the use of ink dilution [74].

Further numerical research in the field of helical designed grafts was only performed in a coronary bypass configuration [256–258].

The present study has to be seen as an addition to the research area of helical designs in grafts. In our in-depth CFD analysis, it was possible to calculate different WSS-descriptors, based on different methodologies, as well as bulk flow parameters. Because the loop configuration and the artery and vein anastomoses were included, clinically relevant flow patterns could be visualized. The strength of this study is that it does not only compare hemodynamics in non-helical and helical designed grafts, but also unravels the influence of changing the helical pitch on the flow field and wall shear parameters.

13.5 CONCLUSION

Introducing helix turns in the design of an AVG influences the hemodynamics in both graft, venous anastomosis and draining vein. The generation of helical flow leads to a more complex flow field which, with appropriate design parameters, may effectively reduce the area of zones exposed to unfavorable wall shear stress conditions that are associated with an increased risk of intimal hyperplasia. However, the value of the pitch in the graft design is not (fully) proportional to the distal hemodynamics conditions. It was demonstrated that the general mechanical approaches for helical conduits are not sufficient to describe the disturbed shear observed in the venous anastomosis region. We showed, by introducing more realistic conditions (unsteady flow and closed-loop configuration), that the optimal pitch length and optimal number of helix turns in an arterio-venous graft to reduce regions with unfavorable hemodynamics cannot be derived without studying case by case.

Five

Studies on CVCs

Computational study of flow in a novel CVC

T.W.I. Clark, K. Van Canneyt and P. Verdonck
*Computational flow dynamics and preclinical assessment of a novel
hemodialysis catheter.*
Seminars in Dialysis. 2012.

14.1 INTRODUCTION

Over 420 000 Americans with end-stage renal disease receive hemodialysis [17]. Native arterio-venous fistulas are the optimal form of vascular access, however synthetic grafts and dialysis catheters remain additional important access alternatives. Dialysis catheters are placed for acute hemodialysis and to serve as a bridge to a permanent form of vascular access. Catheters are also used as an access of last resort when patients have exhausted their vascular anatomy for placement of a fistula or graft [19].

Manufacturers of dialysis catheter design have typically emphasized higher flow rates, and since a higher flow rate through the dialyzer can theoretically result in a shorter treatment time, catheters have often been designed to function at the highest possible flow rate [271]. However, an increase in flow rate is offset by a higher pressure gradient over the catheter which in turn will induce elevated shear rates [98]. Moreover, there is no linear relation between blood flow rate and solute clearance, and it is adequate solute clearance which is the goal of maintenance hemodialysis rather than shorter treatment times [272].

Optimal dialysis catheter flow therefore requires a balance. Flow that is too high can produce high shear rates which has the potential to cause platelet activation and mechanical hemolysis. Flow that is too low can increase blood cell residence time within the catheter lumen and promote thrombus formation [98].

A critical parameter of dialysis catheter performance for optimal solute clearance is the access recirculation. It is important to have the smallest proportion of cleansed blood returning back to the dialyzer since higher percentages of recirculation can require a longer duration of hemodialysis for target solute clearance. In most dialysis catheter designs, increased flow rates and/or reversal of lines will increase catheter recirculation [273, 274].

In this study, we describe a novel hemodialysis catheter designated as the VectorFlow catheter. This catheter has helically contoured arterial and venous apertures to produce a spiral, three-dimensional transition in blood cell vectors as blood enters and leaves the catheter. These vectors are opposed so that the admixture of dialyzed and nondialyzed blood is reduced, thereby minimizing recirculation. Most current catheter designs have lumen apertures at the catheter tips which are perpendicular to the direction of blood flow in the superior vena cava or right atrium. Blood entering the arterial lumen in particular is subject to a rapid change in the net vector of blood flow, as the direction of blood flow must assume a sudden reversal in direction. The helically curved shape of the lumen apertures of the VectorFlow

catheter also serves to minimize blood cell residence time in the catheter tip and reduces blood cell shear stress by providing a more gradual transition in flow velocity to blood entering and leaving the catheter.

The performance characteristics of this catheter were studied in three settings: a simulated model using computational flow dynamics (CFD) (to measure shear stress, blood cell residence time, Platelet Lysis Index and catheter recirculation), a bench model of hemodialysis (to measure recirculation at varying rates of flow), and an animal model (to measure recirculation at varying rates of flow). The performance characteristics of this catheter are compared to several other current dialysis catheter designs.

We will focus mainly on the CFD study and only mention shortly the methods and results of the other two investigations (more details can be found in Clark et al. [275]).

14.2 MATERIAL AND METHODS

14.2.1 Computational Fluid Dynamics

Simulated 14 Fr. VectorFlow symmetrical tip and Tal Palindrome catheters (Figure 14.1) were rendered using SolidWorks software (Dassault Systèmes SolidWorks, Concord, MA) and exported into Gambit software (Ansys Inc., Canonsburg, PA, US). Since it is not feasible to evaluate catheter performance within a simulated right atrial model (due to complexity of assumptions regarding atrial size, proportion of flow from the inferior vena cava, and tricuspid function) these virtual catheters were placed within an 18 mm diameter and 120 mm long cylinder representing the superior vena cava (SVC) using Fluent flow simulation software (ANSYS inc., Canonsburg, PA, US). The computational flow dynamics model of dialysis catheter performance previously described and validated using Particle Image Velocimetry (PIV) by Mareels et al. was used for analysis [98, 276]. Each catheter and the SVC were meshed to obtain over 3,300,000 tetrahedral volume cells. The tetrahedral mesh was locally refined around the catheter tip to obtain optimal resolution for assessment of shear stress and to achieve grid independence. Fluent was used to iteratively solve the continuity and momentum equations with a finite volume method to result in a steady-state solution.

All boundaries were rigid, impermeable and with no slip at the vessel-wall surfaces. The SVC inlet flow was established at 3 l/min, and the SVC outlet was set to a reference pressure outlet of 0 Pa. This corresponded to an SVC velocity of 19.6 cm/sec, in accordance with prior clinical measurements of Cohen et al. [277]. The blood flow through the catheter was set to

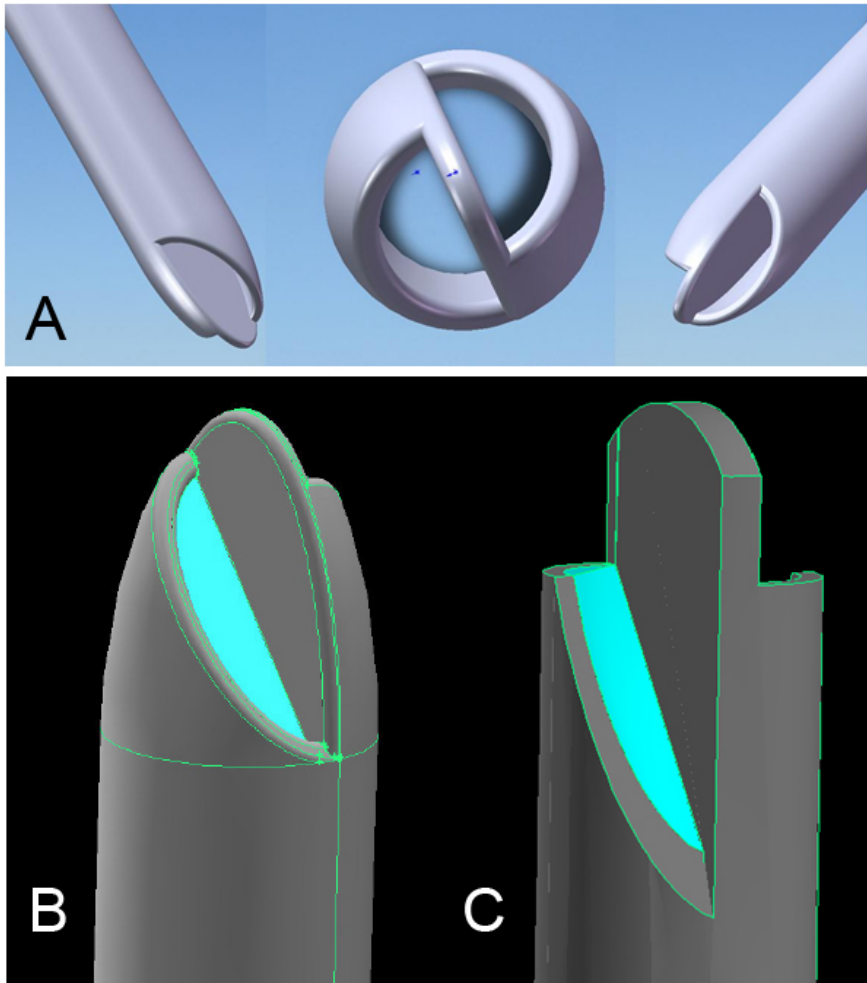


Figure 14.1: VectorFlow symmetrical tip catheter in multiple projections (A). Note the helical shape to the catheter tip at the arterial and venous lumens, which are symmetrical and opposed on each side of the catheter. Representations of VectorFlow (B) and Palindrome (C) catheter tips within Gambit software (ANSYS inc., Canonsburg, PA, USA) in preparation for computational flow dynamics. The arterial inlets are shaded.

400 ml/min. Blood was modeled as a non-Newtonian fluid, using the Quemada blood viscosity model [119]. Hematocrit was set to 40%, the plasma viscosity to 1.3 mPa.s and the blood density to 1060 kg/m³.

Shear stress and Platelet Lysis Index

Shear stress levels were calculated as the multiplication of dynamic viscosity and strain rate. To assess platelet activation and thrombosis formation, the Platelet Lysis Index (PLI) was calculated in the manner of Goubergrits and Affeld [278], based on the work of Giersiepen et al. [279]. The formula was initially derived from *in vitro* measurements of lactic dehydrogenase (LDH) release from lysed human platelets and is based on the combination of the magnitude of shear stress, τ , and exposure time to the vascular device, t :

$$PLI = 3.66 \cdot 10^{-6} \cdot t^{0.77} \cdot \tau^{3.075} \quad (14.1)$$

This index allows linking high shear stress to subsequent low flow zones via pathlines. The PLI can be used as a comparative tool in the quantitative assessment of the arterial catheter tip design rather than as a predictive tool of actual platelet activation. In the inlet of a catheter a minimum of 1000 pathlines were computed. Each pathline took 3000 steps of 10 micrometers to allow the pathline to extend past the disturbed flow in the catheter tip zone and into the region of Poiseuillian flow further downstream the arterial catheter lumen. At every point along each pathline, shear stress and velocity magnitude values were exported. The time value was computed as the distance between two subsequent points along a pathline divided by the average velocity over the segment. PLI values of every step along a pathline were summed. Subsequently, a weighted average of all pathline PLI values was computed using the entrance velocity of a pathline as weighing factor. As such, each pathline contributed to the PLI according to the amount of catheter inflow it represented.

Blood Residence Time

Blood cell residence time (RT) was calculated in the tip volume, 0.075 ml, by solving a specific form of the continuity equation as previously described by Mareels et al [98]. This RT value indicates the time blood remained in the arterial inlet volume before being drained to the arterial outlet, ie. the ‘washout time’ of blood in the arterial inlet and a proxy of the risk of catheter tip thrombosis. It was calculated by Mareels et al. [98] that for his reference catheter design, here described as the ‘step tip’ catheter, the average time needed for the blood particle to pass through the tip volume was 0.015 s.

Therefore, volume percentage with RT above 0.030 seconds (twice the average in the reference case) was calculated as possible threshold for higher risk of catheter thrombosis.

Access recirculation

Access recirculation was assessed by labeling all venous (dialyzed) blood flow particles and calculating the particle density in the arterial lumen outflow versus the distal vena cava superior outflow. From this, the percentage of recirculation was calculated as the percentage of blood particles returning through the arterial lumen compared to the blood particles brought in the system by the venous lumen inflow.

14.2.2 Bench model

An *in vitro* model was used to simulate caval hemodynamics for catheter measurements. A flow circuit was created with a hollowed dialyzer to simulate the SVC (internal diameter 35 mm) using 5% saline circulating through Gambro dialysis tubing at maximal flow rate of 2000 ml/min. The use of a 35 mm SVC with 2 l/min flow gives an average velocity of 3.5 cm/s. Since the fluid used in the experiment is 5% saline, with almost 3 times lower viscosity than blood, the applied Reynolds number (dimensionless factor used to compare flow fields with different geometry, velocity and viscosity) of the *in vitro* bench model is equal to the Reynolds number of the CFD calculations.

Within the center of this simulated SVC, the following catheters for recirculation measurements were introduced (more details and figures in Section 5.3): Duraflow (AngioDynamics, Latham, NY, US), Ash split-tip catheter (Medcomp, Harleysville, PA, US), DuraMax (AngioDynamics), Centros (AngioDynamics), Tal-Palindrome (Covidien, Mansfield, MA, US) and the VectorFlow symmetrical tip study catheter.

A second pump was used to provide constant flow through each dialysis catheter. Recirculation was measured of each catheter at flow rates of 400, 500 and 600 ml/min using an ultrasound-dilution technique. For asymmetrical tip catheters (i.e. step tip and split tip designs) lines were reversed and measurements obtained at each flow rate to assess the maximal recirculation of each catheter. For the VectorFlow and Tal-Palindrome catheters, the symmetrical tip design of these catheters is such that 'arterial' and 'venous' lumen designation is arbitrary and so line reversal would not result in a change in recirculation. Therefore, these measurements were obtained in these two catheters without designating the lines as 'reversed' or 'forward'.

14.2.3 *In vivo* model

A single domestic swine was utilized for *in vivo* assessment of catheters. The jugular vein was accessed percutaneously. The study catheters were advanced in random sequence. The following catheters were evaluated: VectorFlow (symmetrical tip) catheter, VectorFlow-Split Tip catheter (which was constructed during the course of this study but not available at the time of the bench model experiments) and Tal-Palindrome. To simulate a dialysis circuit, a pump was used with flow settings of 300, 400 and 500 ml/min. At each flow setting, catheter recirculation was measured in triplicate for the VectorFlow, VectorFlow-Split Tip and Tal Palindrome catheters. To serve as additional comparisons, Ash split tip and DuraMax catheters were run in reversed line positions (to produce maximal recirculation) at 500 ml/min and recirculation measured in triplicate.

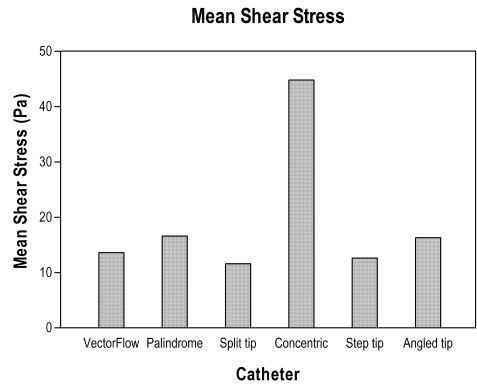
14.3 RESULTS

14.3.1 Computational Fluid Dynamics

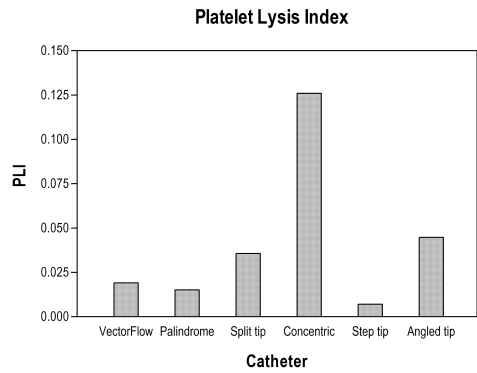
The results of CFD analysis of the VectorFlow and Palindrome catheters are summarized in (Figure 14.2 and 14.3). For comparison purposes, these results are graphed with the conventional catheter tip designs previously simulated under identical conditions by Mareels et al. [98]. Both the VectorFlow and Palindrome catheters were associated with levels of mean shear stress similar to split tip and step tip catheter designs (Figure 14.2a). The VectorFlow catheter was associated with an 18% lower mean shear stress compared to that of the Palindrome catheter, at 13.6 and 16.6 Pa, respectively.

The Platelet Lysis Index (PLI), a weighted scaling of blood particles experiencing low shear stress for a long period and high shear stress for a short period, is a metric previously developed to compare the risk of platelet activation, platelet aggregation and thrombogenicity between vascular devices [98, 272, 273]. Lower levels of PLI were seen with the VectorFlow (PLI = 0.019) and Palindrome (PLI = 0.015) catheters as well as the step tip design (PLI = 0.007) (Figure 14.2b). As reported previously [98], the highest PLI was associated with the concentric catheter tip design (PLI = 0.126), followed by the angled tip design (PLI = 0.045). Moderately high PLI was also present with the split tip design (0.036).

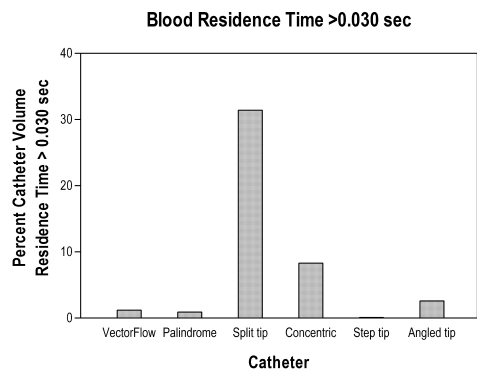
The percent volume of blood flowing through the catheter with a residence time (RT) exceeding 0.030 seconds was calculated. This showed that the VectorFlow catheter design produced a percent volume of RT > 0.030 s of 1.2%, compared to 0.9% for the Palindrome catheter and 8.3% for the concentric design. The highest residence time was present with the split tip



(a)



(b)



(c)

Figure 14.2: Comparison of mean shear stress [Pa] (a), of Platelet Lysis Index (b) and of blood Residence Time > 0.030 seconds (c) between the VectorFlow and Palindrome study catheters, and compared with the values of split-tip, concentric, step-tip, and angled-tip designs.

catheter, which was associated with a 31.4% percent volume of $RT > 0.030$ s (Figure 14.2c).

Recirculation was directly compared between the VectorFlow and Palindrome catheters using computational flow dynamics. The calculated percent of recirculation of the Palindrome catheter was 0.039%, compared to 13.6% for the step tip catheter in reversed position (with aspiration of blood through the venous lumen). However, recirculation of the VectorFlow catheter was calculated at $1.2 \cdot 10^{-4}\%$. Velocity streamlines entering and leaving the catheter and a detailed view of the flow inside the arterial lumen are shown in Figure 14.3.

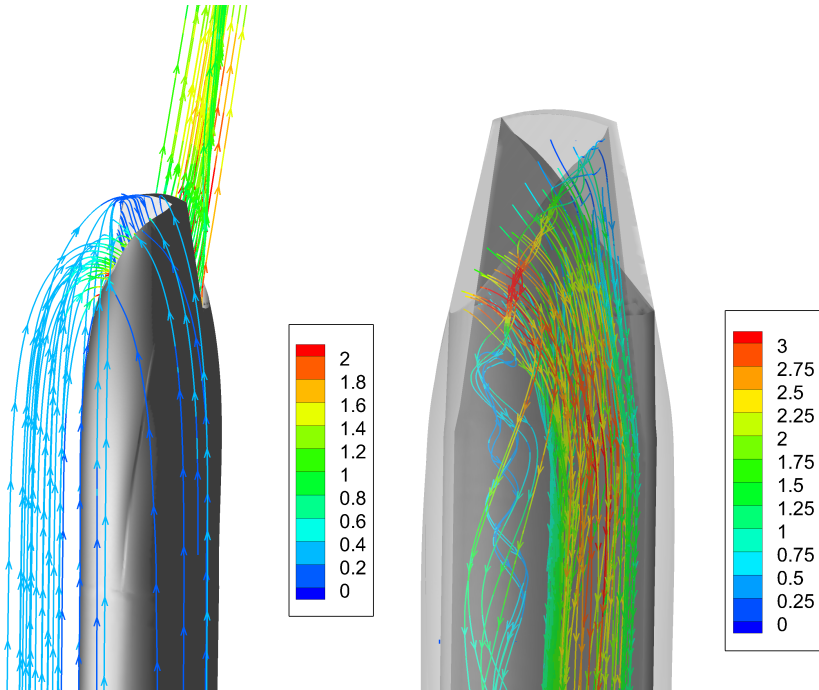


Figure 14.3: VectorFlow velocity streamlines, colored by velocity magnitude (m/s). Left: Pathlines of flow entering the arterial lumen and leaving the venous lumen. Note lack of streamtraces leaving the venous lumen entering the arterial lumen of the catheter (the recirculation was calculated at $1.2 \cdot 10^{-4}\%$). Right: Streamtraces inside the arterial lumen.

14.3.2 Bench model

The results of recirculation measurements at varying flows within the bench model are summarized in Figure 14.4. Among each of the studied catheters, with the exception of the VectorFlow and Palindrome catheters, higher rates of catheter flow resulted in higher percentages of catheter recirculation. In reversed positions, recirculation was highest with the Ash split catheter with a mean of 29.3% at a flow rate of 600 ml/min. Among the step tip catheter designs, the DuraMax catheter was associated with the highest percentage of mean recirculation (20.8%) at 600 ml/min. The Palindrome catheter had the lowest rate of recirculation among the remaining catheters, ranging from means of 7.3 - 9.5%. The VectorFlow catheter had no detectable recirculation (0%) at any flow rate. As the catheter has a symmetrical lumen design, reversal of lines did not influence this result.

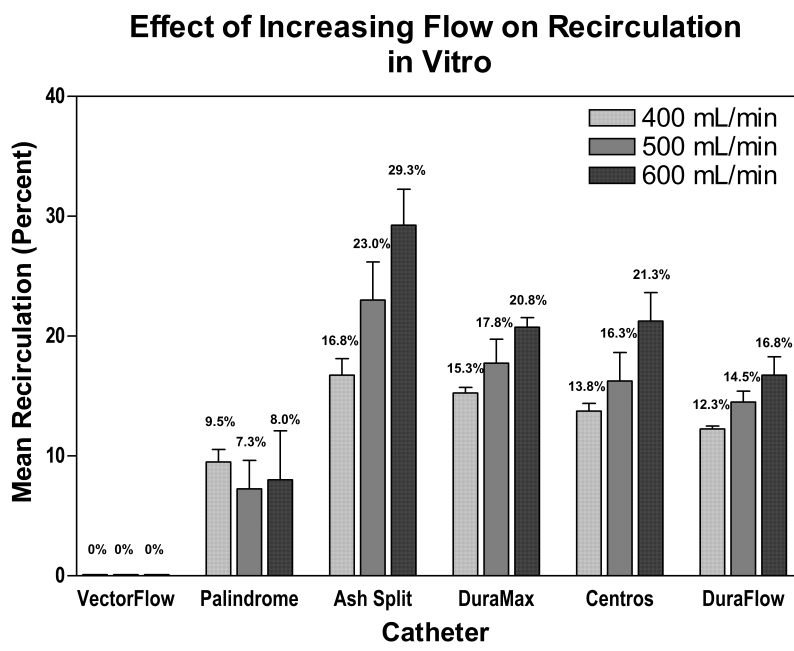


Figure 14.4: Comparison of catheter recirculation calculated from bench model of hemodialysis. The Ash Split, DuraMax, Centros, and DuraFlow catheters were run in reversed line position (aspirating through venous lumens). The VectorFlow and Palindrome catheters have symmetrical lumens so that line reversal did not affect recirculation.

14.3.3 *In vivo* model

For each catheter, recirculation was measured at each flow (with lines reversed to maximize the effects of recirculation). Triplicate recirculation measurements were performed at each flow rate; mean recirculation percentages are shown in Figure 14.5. The VectorFlow catheter, concordant with the findings of computational flow dynamics and bench model measurements, was associated with absence of measurable recirculation (0%). Moreover, significant reductions in recirculation were observed with a split tip catheter modified with VectorFlow lumens. With lines reversed, the VectorFlow-Split Tip design was associated with a 44% decrease in recirculation at 500 ml/min flow compared to the Palindrome catheter, and a 59% reduction in recirculation at 500 ml/min compared to the Ash split catheter.

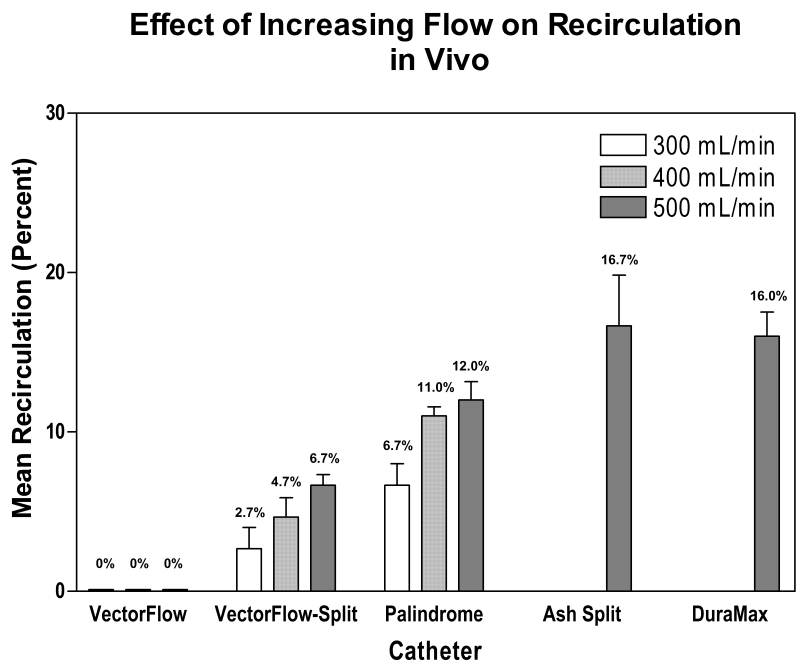


Figure 14.5: Comparison of catheter recirculation measured in an animal model of hemodialysis. VectorFlow-Split, Ash Split and DuraMax catheters were run in reversed line positions to produce maximal recirculation. (VectorFlow-Split = split-tip catheter with arterial and venous lumens modified to resemble the VectorFlow symmetrical tip catheter.)

14.4 DISCUSSION

Chronic dialysis catheters are the least optimal form of hemodialysis access due to higher rates of infection and dysfunction [280, 281]. However, catheters remain widely utilized as a bridge to permanent access placement or maturation, or when other access options have been depleted. Following the introduction of the K/DOQI guidelines by the National Kidney Foundation and the Fistula First initiative by the Centers for Medicare Services (CMS), the prevalence of fistulas among hemodialysis patients increased from 28% in 1998 to 55% in 2007 in the US. However, catheter utilization has been relatively constant at 17-18% since 2003, in part from the increased placement of arterio-venous fistulas resulting in longer periods of catheter use during access maturation [17].

There remains an ongoing need to improve catheter performance and decrease catheter-related morbidity. Current strategies to extend catheter longevity include surface coatings with antithrombotic [282] and/or antimicrobial agents [283, 284], antimicrobial lock solutions [285, 286] and modifications in catheter tip design to improve flow characteristics and decrease recirculation [99, 101].

Flow inside dialysis catheter lumens is three-dimensional. Whereas flow within straight segments of catheter lumens is aligned, the flow at the inlet and outlet of a catheter is more complex and greatly influenced by catheter tip design [98, 276]. Variation in shear stress has been identified as a risk factor for thrombogenicity through platelet activation. Clearance of blood from the catheter tip is also considered a critical component in catheter design; catheters with higher levels of blood residence times (exceeding 0.030 seconds) in computational flow models have been considered susceptible to thrombus formation through platelet activation and delayed washout of blood near the wall of the catheter lumens [98, 276].

A threshold of 10 Pa of shear stress for platelet activation has been identified as being within the range of shear stress resulting in platelet activation and aggregation, which occurs between 0.1 and 20 Pa [287]. In addition to high shear stress, areas of flow stagnation or recirculation can induce platelet aggregation. Strony et al. [288] observed in a model of coronary artery stenosis that platelet activation and aggregation was found to correlate with elevated regions of shear stress of 46 Pa and prolonged blood transit times.

An ideal dialysis catheter, from a flow dynamics perspective, is one which produces low shear stress, a low percentage of prolonged blood residence time, and a low Platelet Lysis Index. The Platelet Lysis Index is a weighted

scaling of blood particles experiencing low shear stress for a long exposure period within a vascular device and high shear stress for a short period within a vascular device. The PLI was initially developed by measuring lactic dehydrogenase (LDH) release *in vitro* from injured platelets and has been used in the comparison of platelet lysis among mechanical heart valves [273, 274] and dialysis catheters [98].

Minimal recirculation is another desirable attribute of a dialysis catheter [19]. Recirculation might decrease the efficiency of solute clearance. In this current era of available devices for vascular access, many dialysis catheters are capable of achieving rates of flow exceeding 500 ml/min, and some dialysis units (mostly in the US) may utilize catheter flow rates approaching these levels with the intent of producing a more efficient dialysis session. Depending on the catheter design, however, this can result in decreased efficiency and dialysis adequacy through an increase in recirculation [273, 274, 289–291]. A recent study found that 24% of patients with tunneled hemodialysis catheters had recirculation levels exceeding 10% [292]. Dialysis providers will often reverse lines of dialysis catheters to achieve higher rates of flow when ‘arterial’ lumen function is compromised; this line reversal will result in higher recirculation. Therefore, the ability to reverse lines when required without compromising through higher recirculation would be an additional desirable attribute of a dialysis catheter.

Using computational flow dynamics we evaluated the flow characteristics of a novel hemodialysis catheter, designated the VectorFlow catheter. The inlet and outlet of the catheter tip are designed to optimize the transition of blood flow vectors into and out of the catheter lumens through a helical, three-dimensional pattern of blood flow (Figure 14.3). Spiral flow is a normal phenomenon in the vascular system which reduces near wall kinetic energy and has been observed in healthy subjects within a variety of vascular territories including the aorta and the carotid artery [293, 294]. The spiral pattern of blood flow within the VectorFlow catheter was associated with a low level of shear stress. Compared to the Palindrome catheter, an 18% reduction in mean shear stress was observed. Blood cell residence times and the Platelet Lysis Index between the VectorFlow and Palindrome catheters were similar.

From the computational flow field, a negligible value of recirculation was found (0.00012%). Within the bench model of hemodialysis, the VectorFlow catheter was absent of any measurable recirculation as well. Since recirculation increases with higher rates of flow, we deliberately evaluated catheter recirculation at higher rates of flow than would be used clinically (up to 600 ml/min) to evaluate whether the VectorFlow catheter produced

any measurable recirculation. Concordant results were seen in an animal model of recirculation which also demonstrated absence of recirculation between different rates of flow within the catheter.

These findings concerning the recirculation can be attributed to the three-dimensional pattern of flow which occurs at the tip of the catheter (Figure 14.3). At the arterial lumen inlet, where blood experiences the greatest change in blood cell velocity and direction, a smoother transition of blood cells can account for the reduction in mean shear stress. Absence of measurable recirculation can be attributed to the opposing vectors of blood entering and leaving the catheter lumens (Figure 14.3). In contrast, the Palindrome catheter was associated with recirculation in the *in vitro* and *in vivo* models. We attribute this difference to the Palindrome catheter not having a flow-diverting interface at the catheter tip to impart a helical, three-dimensional pattern of blood flow with opposing vectors between the arterial and venous lumens. However, in the computational model, an almost negligible recirculation (0.39%) was found for the Palindrome, as in the VectorFlow.

Because the Palindrome and VectorFlow catheter tips are symmetrical, it is possible that clinical use of this device might be associated with a greater degree of flexibility among dialysis personnel since either lumen could be designated as the arterial lumen. However, we also observed a significant reduction in recirculation when the helical shape of the catheter tip was incorporated into a split-tip catheter design suggesting that the benefit of this design is applicable to other catheter configurations.

Our study has multiple limitations. Although in clinical practice dialysis catheters are preferentially placed in the right atrium, we utilized a straight tube of an SVC model to enable uniform conditions in which to compare catheter performance. Mareels et al. [276] studied the validity of the simplified model of a SVC (straight tube) compared to a model of a right atrium, three-dimensionally reconstructed from digital cryosection images from The Visible Human Project (National Library of Medicine, National Institutes of Health, Bethesda, MD, US). They found a discrepancy between both models, in that within the realistic model of the right atrium catheter recirculation seems to decrease in peak flow conditions, but was expected to increase the moment the tricuspid valve closes and blood flow stagnates. To achieve more comparable results, we chose the simplified model and believe that this choice does not compromise our global findings. Next, our *in vitro* model was larger in diameter (35 mm) than a typical human superior vena cava. Furthermore, *in vivo* measurements were obtained in only a single animal. Although our study received IACUC¹ approval to include

¹Institutional Animal Care and Use Committee

additional animals if necessary, given that the recirculation measurements were completely concordant with the CFD and bench model results we felt it unethical to repeat the same experiments on additional animals. It is possible that this decision represented a Type II error and additional differences in catheter recirculation would have emerged with a larger sample size of animals. However, our animal study enabled a sufficient number of repeated measurements in a single animal to detect statistically significant differences between recirculation rates between the study catheters.

We also recognize that the additional hemodynamic advantages of this catheter design (reduced catheter shear stress, blood cell residence time and Platelet Lysis Index), in terms of lower thrombogenicity, remain to be established with additional pre-clinical data over a longer implantation time.

14.5 CONCLUSION

We report a novel dialysis catheter with a symmetrical tip design and helically contoured lumens which optimize the vectors of blood entering and leaving the catheter. These features result in favorable levels of shear stress, blood cell residence time and Platelet Lysis Index. Although other catheter designs were associated with comparatively low levels of recirculation at modest rates of blood flow, the novel catheter we describe was associated with a complete absence of detectable recirculation. When these catheter tip features are incorporated into a split tip catheter design, a significant reduction in recirculation was also observed.

Dialysis providers are under increasing pressure to achieve optimal dialysis adequacy and minimize access-related morbidity; these results serve as encouraging pre-clinical assessment of this dialysis catheter design.

Computational study on malfunctioning CVCs

W. Van Biesen, J. Vanmassenhove, K. Van Canneyt, R. Vanholder, S. Eloot.
Influence of switching connection ports of double-lumen permanent tunnelled catheters on total solute removal during dialysis.
Journal of Nephrology. vol.24. 2011:338-344.

K. Van Canneyt, W. Van Biesen, R. Vanholder, P. Segers, P. Verdonck and S. Eloot.
Evaluation of alternatives for dysfunctional double lumen central venous catheters using a two compartmental mathematical model for different solutes.
The International Journal of Artificial Organs. In press.

K. Van Canneyt¹, S. Eloot¹, R. Vanholder, P. Segers, P. Verdonck and W. Van Biesen.
Slow extended nocturnal home hemodialysis shows superior adequacy compared to in-center dialysis: a mathematical analysis.
Blood Purification. In press.

¹Both authors equally contributed.

15.1 REVERSING LINES: *IN VIVO* AND 1-COMPARTMENT KINETIC MODELING**15.1.1 Introduction**

The use of central venous catheters (CVCs) as permanent access is discouraged in hemodialysis (HD) patients [22]. However, they are a life-saving option in the growing group of HD patients who ran out of native vascular access possibilities [295, 296]. Although the major reason to avoid CVCs is the risk for infection, other drawbacks are the risk for thrombosis, and inadequate blood flows (< 300 ml/min) [297]. A commonly used double lumen catheter is the so-called ‘shotgun’ type where the venous port (i.e. the lumen through which the blood is returned to the patient) is positioned more distally than the arterial port (i.e. the lumen through which the blood is pumped to the dialyzer). The flow of these large bore double lumen catheters can still be inadequate because of formation of a thrombus inside or a fibrinous sheet around the catheter. These problems can often successfully be solved by reversing the connection of the lines. This approach of reversing lines is criticized, as it is presumed to increase recirculation, reported to be between 5 and 28% [298]. Carson et al. indicated that reversing lines indeed enhanced recirculation in dysfunctional catheters, but that instantaneous clearance improved if blood flow increased after reversing the lines, balancing out the loss induced by recirculation [298]. Instantaneous clearance does however not equal total solute removal (TSR), which also depends upon the duration of the dialysis session and the compartmental behavior of different solutes. There are so far no data on how reversing catheter lines impacts on TSR during a dialysis session.

This study compares TSR and reduction ratios of different classes of uremic toxins in patients (*in vivo*) dialyzed with a double lumen catheter connected in the correct line (CL) position vs the reversed line (RL) position.

Next, we used a mathematical model to calculate how much increase in blood flow is necessary to compensate for different degrees of recirculation and obtain the same TSR with RL as compared to CL.

15.1.2 Patients and methods*In vivo study*

The study was approved by the local ethics committee and written informed consent was obtained. Each patient was dialyzed on two different occasions using the Genius system with high-flux Fresenius FX80 dialyzers using a double lumen central venous catheter: Bard Hemoglide ($n=14$), Optiflow ($n=3$), Medcomp Split Stream ($n=2$), Pourchez Retro ($n=2$), and Arrow ($n=1$). Patients were dialyzed during two consecutive midweek sessions of

equal duration, once with CL and once with RL connection, in random order. For each test session, blood flow (Q_b) was set at the maximum speed tolerated by the system, i.e. 350 ml/min. Each patient served as his/her own control.

Blood was sampled pre and post dialysis and a dialysate sample was taken post dialysis from the ultrafiltrate collector, representative for the total spent dialysate. As such, this allows calculation of the total solute removal obtained during the dialysis session. Urea, creatinine, phosphorus and β_2 M (β_2 -microglobulin) concentrations were determined from both the blood samples as the dialysate.

The reduction ratio (RR) [%] of urea, creatinine, phosphorus, and β_2 M was calculated from pre-dialysis (C_{pre}) and post-dialysis concentration (C_{post}) in blood samples from the dialyzer blood inlet line:

$$RR = \frac{(C_{pre} - C_{post})}{C_{pre}} \cdot 100 \quad (15.1)$$

Based on the total spent dialysate concentration at the end of dialysis ($C_{d,end}$) and the total waste dialysate volume ($V_{d,end}$), total solute removal (TSR) [mg] was calculated as:

$$TSR = C_{d,end} \cdot V_{d,end} \quad (15.2)$$

Mathematical study

A urea single-pool kinetic model was coupled with a dialyzer model to simulate solute removal in the patient and the dialyzer in different situations of catheter connection and degrees of access recirculation (Figure 15.1). Ultrafiltration and generation rate were assumed to be zero during the dialysis session. Urea extraction ratio, ER, in the dialyzer was taken at 80%. The extraction ratio, ER, and dialyzer clearance, K, are defined as:

$$ER = \frac{C_{bi} - C_{bo}}{C_{bi}} \quad (15.3a)$$

$$K = ER \cdot Q_b \quad (15.3b)$$

with C_{bi} and C_{bo} the blood dialyzer inlet and outlet concentrations and Q_b the blood flow rate.

The time variation of the compartmental concentrations, C, can, for a particular solute, be determined by solving the mass balance equation for the single compartment:

$$\frac{d(VC)}{dt} = -Q_b \cdot (C_{bi} - C_{bo}) = -K \cdot C_{bi} \quad (15.4)$$

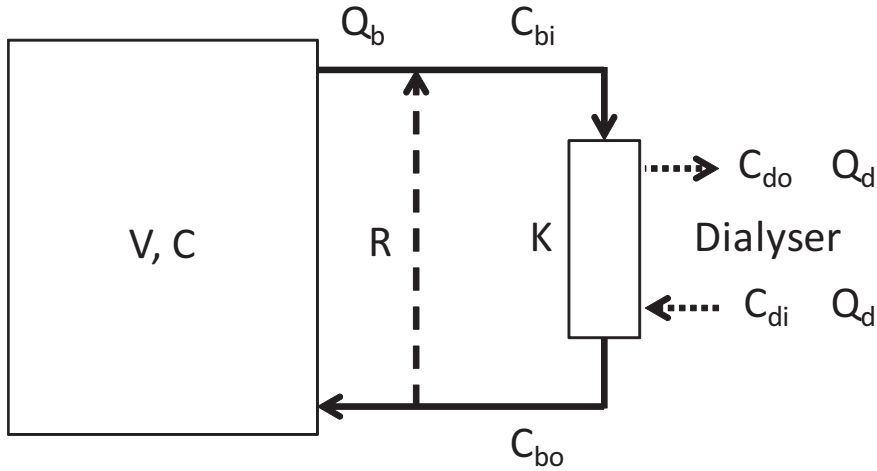


Figure 15.1: Mathematical model for urea removal, consisting of a single-pool kinetic model of the patient coupled with a dialyzer model. Kinetic model with V the single-pool volume [l] and C the single-pool concentration [mmol/l] corresponding to the patient's blood concentration. Dialyzer model with Q_b the blood flow [ml/min], Q_d the dialysate flow [ml/min], K the dialyzer clearance [ml/min], C_{bi} and C_{bo} the blood inlet and outlet concentration [mmol/l], and C_{di} and C_{do} the dialysate inlet and outlet concentration [mmol/l].

Simulations with coupled models rendered concentration profiles during dialysis: patient's blood concentration, blood dialyzer inlet and outlet concentrations (C_{bi} and C_{bo}), and dialysate inlet and outlet urea concentrations ($C_{di}=0$ and C_{do}). Herewith, C_{bi} was derived from the patient's concentration, C , based on Equation 15.4 and accounting for the percentage access recirculation (R - see Figure 15.1). C_{bo} was calculated by:

$$C_{bo} = C_{bi} \cdot (1 - ER) \quad (15.5)$$

and C_{do} was calculated for each time point during dialysis from the mass balance in the dialyzer:

$$C_{do} = \frac{Q_b \cdot C_{bi} - (Q_b - Q_{uf}) \cdot C_{bo}}{Q_d + Q_{uf}} \quad (15.6)$$

which can be simplified due to our assumption of a zero ultrafiltration flow ($Q_{uf}=0$).

From the patient's concentration decline during dialysis, the reduction ratio (RR) was calculated using Equation 15.1. Total solute removal (TSR)

was calculated according to:

$$TSR = \int_{begin}^{end} C_{do} \cdot Q_d dt = V_{d,end} \cdot \int_{begin}^{end} C_{do} dt \quad (15.7)$$

with $V_{d,end}$, the total waste dialysate volume, multiplied by the area under the dialysate outlet curve C_{do} , as derived with Equation 15.6.

For the parameter study, RR and TSR were calculated for a normal catheter connection with zero recirculation, and for a reversed catheter connection with a recirculation in the range 5 to 25% and a blood flow rate in the range 150-350ml/min.

Statistical analysis

Data were analyzed using SigmaStat software (Jandel Scientific, San Rafael, CA, USA). Data are expressed as mean \pm SD. The paired t-test was used for normally distributed samples. A p-value of <0.05 was taken the limit of significant difference.

15.1.3 Results

In vivo study

Twenty-two stable hemodialysis patients (18 women and 4 men) of 75.3 ± 10.0 years old and 67.3 ± 12.0 kg were included in the study. Sixteen patients had a dialysis session with CL and RL catheter connection, while 5 and 1 patients could not be dialyzed with CL connection and RL connection respectively. Furthermore, 1 patient was omitted from analysis because of technical problems. Thirteen patients were dialyzed with a blood flow of 350 ml/min in both conditions. Two other patients had a lower Q_b in reversed connection (250 ml/min and 300 ml/min, respectively).

Reduction Ratio (RR) and Total Solute Removal (TSR) for urea, creatinine, phosphorus, and β_2 M are given in Table 15.1.

Mathematical model

Figure 15.2 shows the patient's blood concentration, blood dialyzer inlet and outlet concentration, and dialysate outlet concentration during dialysis with a blood flow rate of 300 ml/min for a CL connection with zero recirculation (upper panel) and RL connection with 15% access recirculation (lower panel).

Table 15.2 gives the RR and TSR for different parameter settings of blood flow (range 150-350 ml/min) and access recirculation (range 5-25%) for the CL and RL catheter connection.

	RR [%]			TSR		
	Correct	Reversed	p-Value	Correct	Reversed	p-Value
Urea	73 ± 5	71 ± 4	0.14	301 ± 112 mmol	293 ± 104 mmol	0.35
Creatinine	65 ± 4	63 ± 3	0.06	483 ± 426 mg	465 ± 371 mg	0.41
Phosphorus	53 ± 11	51 ± 11	0.25	498 ± 98 mg	526 ± 108 mg	0.56
β_2 M	52 ± 10	51 ± 7	0.78	72.2 ± 53.6 mg	65.7 ± 39.3 mg	0.95

Table 15.1: Reduction ratio (RR) and total solute removal (TSR) for urea, creatinine, phosphorus, and β_2 M for correct and reversed catheter line connection in clinical conditions.

Figure 15.3 shows a nomogram of the blood flow that is needed with RL connection (y-axis) for different degrees of recirculation (range 5-25%), in order to obtain the same amount of urea TSR as with CL connection and zero recirculation (x-axis).

15.1.4 Discussion

This study demonstrates that connecting patients to double lumen dialysis catheters in a reverse (RL) mode does not impair total solute removal (TSR) of different types of uremic retention solutes in clinical practice. In the mathematical model, TSR in the RL mode was dependent upon the obtained blood flow in the CL connection mode, and the presumed degree of recirculation in the RL connection mode. Reversing lines is thus not problematic in well functioning catheters. In conditions of a dysfunctional catheter, the improvement in solute removal obtained by reversing connections depends upon the percentage of increase in flow obtained and the degree of recirculation.

Clearance in double lumen catheters might be hampered by presence of recirculation. Carson et al. found recirculation in the correct connection mode in well functioning catheters was 0% [298], whereas Trerotola et al. found that it was depending upon design of the catheter, being below 5% in the split tip vs below 10% in the shotgun design [274]. Canaud et al. used two separate single lumen catheters, with the tips at different depths along the vena cava superior, and under these conditions, recirculation was around 10% [299].

Catheter flow can be impaired by intraluminal thrombus formation, formation of fibrinous sheaths around the catheter, or kinking [101]. Many centers have a policy to reverse the connection of the lines to increase blood flow, a procedure that allows continuation of the dialysis session. There is however concern that recirculation may occur in this setting. Carson et al.

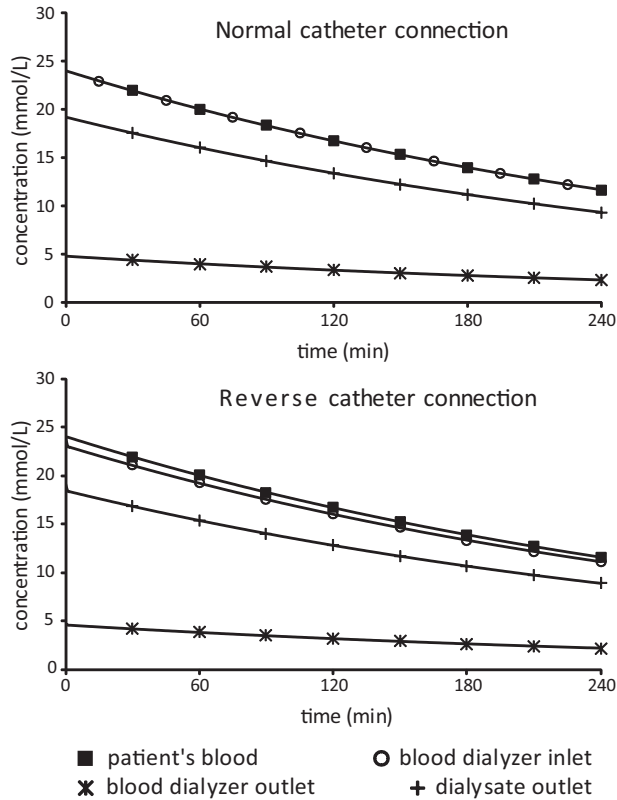


Figure 15.2: Concentration profiles during 240 min dialysis with blood flow 300 ml/min for a correct catheter connection with zero recirculation (upper panel) and for a reversed catheter connection with 15% access recirculation (lower panel). For the correct catheter connection the patient's blood concentration is equal to the blood dialyzer inlet concentration.

observed recirculation rates in RL mode ranging up to 25%, using a catheter where the two tips were separated by 2.5 cm. Reversing the lines significantly increased recirculation from 2.9 ± 5 to $12 \pm 9\%$, in a study, where catheter tips were separated with 3-5 cm [300]. However, when considering the individual data points, for the majority of patients, recirculation remains equal in the correct and reversed mode, and some outliers cause the overall difference, just as in the study by Carson et al. [298]. Recirculation in reversed mode connection can thus be a problem in some, but not in all patients.

However, recirculation is only of relevance as far as it hampers solute clearance and removal, the ultimate aim of dialysis. In addition, in catheters with impaired blood flows in the correct mode, blood flows are often higher

Line connection	R [%]	RR [%]	TSR [mmol]	TSR % decrease
$Q_b = 150 \text{ ml/min}$				
Correct	0	51	494	reference
Reversed	5	52	473	4.3
	10	52	451	8.7
	15	52	429	13.2
	20	53	407	17.6
	25	53	384	22.3
$Q_b = 250 \text{ ml/min}$				
Correct	0	70	672	reference
Reversed	5	70	641	4.6
	10	71	611	9.1
	15	71	580	13.7
	20	71	549	18.3
	25	72	518	23.3
$Q_b = 350 \text{ ml/min}$				
Correct	0	81	782	reference
Reversed	5	82	747	4.5
	10	82	710	9.2
	15	82	674	13.8
	20	83	637	18.5
	25	83	600	23.3

Table 15.2: Urea reduction ratio (RR) and total solute removal of urea (TSR) for correct and reversed catheter connection as calculated in the mathematical model. For the reversed connection, the results are calculated for different percentages of recirculation. It is presumed that in the correct connection, no recirculation will occur, so as a consequence, in real practice, the percentages recirculation are actually the difference between the recirculation in the reversed and in the correct connection mode. While no differences were found for RR, the last column indicates the percentage decrease in TSR when changing the correct connection to reversed connection for the same blood flow Q_b .

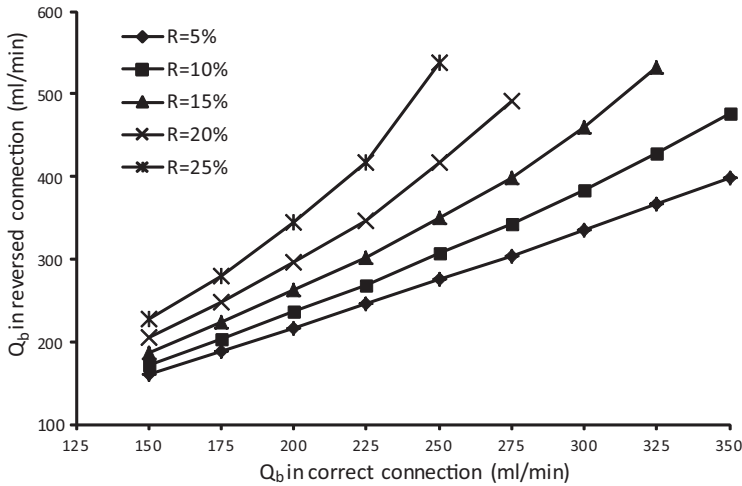


Figure 15.3: Nomogram relating blood flows in the correct connection mode (X-axis) to the blood flow needed in the reversed mode (Y-axis) to obtain comparable total solute removal, and this for different degrees of recirculation in reversed mode (5 to 25%). It is presumed that there is no recirculation in the correct connection mode, so in clinical practice, one should calculate the difference between recirculation in the reversed and the correct mode, and use that value as reference recirculation.

in the reversed mode, thus compensating for decreased clearance caused by the enhanced recirculation [298]. In the latter study, adequacy of dialysis was calculated as instantaneous clearance of urea, which might not be a relevant parameter, as different total solute removals can be obtained during a dialysis session, despite equal Kt/V 's or instantaneous clearances [301]. In the current study, reduction ratios were not different for different rates of recirculation in the reversed mode, and total solute removal in clinical practice was not different in the reversed or in the correct connection mode for urea, creatinine, phosphorus or β_2 M. It is possible that the difference in degree of recirculation in the reversed versus correct mode was not important in our patients, as all catheters were functioning properly.

We used a mathematical model to calculate total solute removals in different settings, with variable blood flow rates and degrees of recirculation in a nomogram (Figure 15.3). At a recirculation of 15%, the blood flow should increase from 200 and 250 (in CL) to 270 and 340 ml/min (in RL), respectively, values comparable to those obtained by Carson et al. [298]. However, our nomogram allows calculation of necessary blood flow increase for different degrees of recirculation, which gives it a better clinical applicability

and accuracy. Of note, as we assumed that in the correct mode, recirculation is zero, one should actually use the difference between recirculation in the reversed and correct mode as reference. If the difference in recirculation remains below 10%, small gains in blood flow after reversing the lines already result in improved solute removal; however, if the difference in recirculation is above 20%, substantial increases in blood flow are needed to achieve comparable solute removals. In cases where patients are dialyzed on reversed mode connections for a longer time, it might thus be wise to check recirculation to determine future access policy.

15.1.5 Conclusion

In conclusion, in well functioning catheters, solute removal is equal in reversed and in correct connection mode. As long as the difference in recirculation is below 10-15%, reversing the lines is a defensible practice to increase blood flow, without the need to replace the catheter. If the difference in recirculation is above 15-20%, then it would be better to replace the malfunctioning catheter to avoid suboptimal dialysis.

15.2 SINGLE VS. DOUBLE LUMEN CVC: 2-COMPARTMENT KINETIC MODELING

15.2.1 Introduction

As explained in the previous section (15.1), the use of central venous catheters (CVCs) as permanent vascular access for hemodialysis is strongly discouraged, mainly due to the risk of infection and thrombosis, and the occurrence of inadequate blood flows. The latter problem can, for double lumen catheters, often be solved successfully by reversing the catheter connection, an approach that is criticized since this might enhance access recirculation, lowering the efficiency of dialysis treatment [298]. By increasing blood flows after reversing the catheter connection, instantaneous dialyzer clearances can be improved, restoring the loss of adequacy which is due to recirculation [298]. In the previous section, it was found *in vivo* that solute removal of urea, creatinine, phosphate, and beta-2-microglobulin was only slightly influenced during hemodialysis by reversing the catheter connection. Furthermore, from single pool urea kinetics, coupled with a mathematical hemodialysis model, it was calculated to what extent blood flow must increase after reversing the lines to compensate for recirculation and to obtain equal total solute removal as with the correctly connected lines.

Once the degree of access recirculation has been quantified in a direct or indirect way (i.e. by measuring ionic dialysance with normal and reversed catheter connection) at the patient's bedside [302–308], the resulting nomograms (Figure 15.3) can help the clinician to make bedside decisions on optimal catheter application. These findings however do not count for the compartmental behavior in the patient. Furthermore, such nomogram information is still not available for single lumen (SL) catheters. When SL CVCs are used, solute removal is hampered due to the inherent recirculation and the lower effective blood flows that are reached due to the alternating functioning of the two blood pumps.

Furthermore, solute removal during hemodialysis is retarded if a solute is distributed over more than one compartment throughout the patient's body. Hence, even when the degree of recirculation is quantified by measurements, it is not possible to simply predict the impact on dialysis adequacy caused by the access recirculation. Even the previous findings, using a one compartmental model in Section 15.1, might have overestimated the impact of dialyzer clearance and/or recirculation on solute removal, by not counting for the retarded kinetics in the patient. This retardation is important for difficult to remove solutes, like middle molecules [144, 309, 310], but is known to be prominent as well with small and water soluble solutes [145, 146].

Therefore, we developed a calibrated mathematical model combining the two-compartmental kinetic behavior of different uremic toxins with a hemodialysis model, including the type of vascular access. Based on this approach, we compared total solute removal and reduction ratios with dialyses using a double lumen CVC either with or without reversed connection lines, and a single lumen CVC.

15.2.2 Material and methods

In order to compare hemodialysis (HD) adequacy in case of different types and modes of application of catheters, a 2-compartmental kinetic model, simulating the solute transfer in a patient, was coupled with a dialysis model, simulating the solute transfer in a hemodialyzer. Parameters, such as reduction ratios and total solute removals, were calculated for different solutes and different catheter scenarios.

The calibrated mathematical patient/dialyzer model

The coupled mathematical patient/dialyzer model in the setting of a double lumen (DL) catheter is shown in Figure 15.4, while that of a single lumen (SL) catheter is shown in Figure 15.5. Solute transfer in the patient was simulated according to two-compartmental kinetics, distinguishing between a perfused volume V_1 and a non-perfused volume V_2 . Both volumes are characterized by a homogeneous concentration and different inputs and outputs such as solute generation rate G_1 (in V_1) and/or G_2 (in V_2). Furthermore, solute is removed from V_1 by hemodialysis with a dialyzer clearance K (Equation 15.3), and solute is transported in between both compartments, driven by a concentration gradient, and proportional to the intercompartmental clearance K_{12} . Ultrafiltration (Q_{uf}) was assumed to occur in both compartments, keeping the ratio between both volumes constant.

The time variation of the compartmental concentrations C_1 and C_2 was, for a particular solute, determined by solving the mass balance equations for both compartments (similar to the simplified formulation in Equation 15.4):

$$\frac{d(V_1 C_1)}{dt} = G_1 + K_{12} \cdot (C_2 - C_1) - K \cdot C_{bi} \quad (15.8a)$$

$$\frac{d(V_2 C_2)}{dt} = G_2 - K_{12} \cdot (C_2 - C_1) \quad (15.8b)$$

Blood concentration variation over the dialyzer was, for a particular solute, determined by solving the mass balance equation in the dialyzer:

$$C_{bi} \cdot Q_{bi} + C_{di} \cdot Q_{di} = C_{bo} \cdot Q_{bo} + C_{do} \cdot Q_{do} \quad (15.9)$$

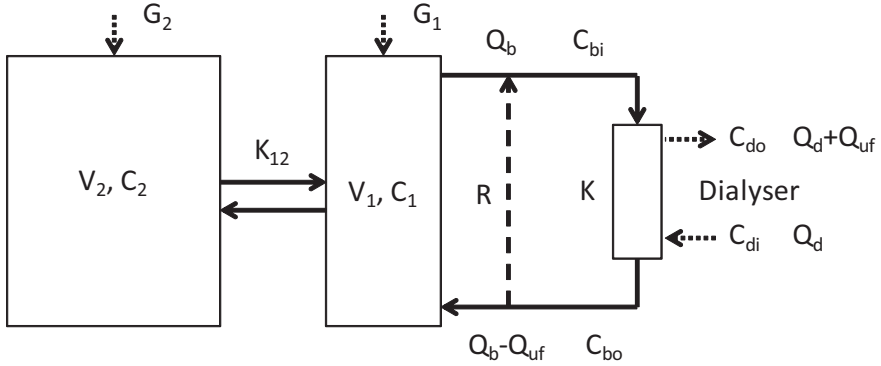


Figure 15.4: Extended mathematical model combining a kinetic model and a dialysis model using a double lumen central venous catheter, with or without access recirculation.

V_1 : perfused volume; V_2 : non-perfused volume; C_1 and C_2 : concentration in V_1 and V_2 ; K_{12} : intercompartmental clearance; G_1 and G_2 : generation rate in V_1 and V_2 ; Q_b : blood flow; Q_d : dialysate flow; Q_{uf} : ultrafiltration flow; K : dialyzer clearance; C_{bi} and C_{bo} : blood inlet and outlet concentration; C_{di} and C_{do} : dialysate inlet and outlet concentration; R : access recirculation.

C_{bi} and C_{bo} are the blood inlet and outlet concentrations, and C_{di} and C_{do} the dialysate inlet and outlet concentrations with respect to the dialyzer. C_{di} is zero in the normal dialysis setting.

Double lumen catheter

For a correctly connected DL catheter in which no recirculation occurs ($R=0$ in Figure 15.4), the blood inlet concentration C_{bi} is equal to the concentration in the perfused compartment C_1 . In case of switching the catheter connection, inducing access recirculation R [%], the blood inlet concentration C_{bi} is diluted by cleansed blood C_{bo} coming from the dialyzer outlet. Dealing with the time it takes for the blood to flow through the dialysis circuit, we accounted for this time delay, TD , to calculate blood inlet concentration C_{bi} at time t from the blood outlet concentration C_{bo} at time point $(t-TD)$ and the degree of recirculation R :

$$C_{bi}(t) = (1 - R) \cdot C_1(t) + R \cdot C_{bo}(t - T) \quad (15.10)$$

Single lumen catheter

In case of a single lumen double pump dialysis treatment (Figure 15.5), one cycle can be subdivided in two phases: an arterial phase (subscript ap) during which blood is pumped from the patient's perfused compartment into

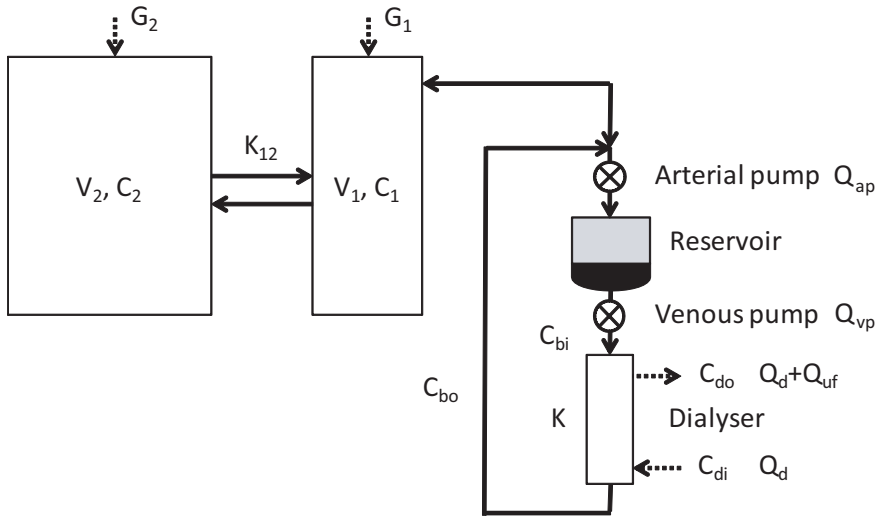


Figure 15.5: V_1 : perfused volume; V_2 : non-perfused volume; C_1 and C_2 : concentration in V_1 and V_2 ; K_{12} : intercompartmental clearance; G_1 and G_2 : generation rate in V_1 and V_2 ; Q_b : blood flow; Q_d : dialysate flow; Q_{uf} : ultrafiltration flow; K : dialyzer clearance; C_{bi} and C_{bo} : blood inlet and outlet concentration; C_{di} and C_{do} : dialysate inlet and outlet concentration; Q_{ap} : blood flow during arterial phase; Q_{vp} : blood flow during venous phase.

the buffer reservoir at a flow rate Q_{ap} , and a venous phase (subscript vp) during which the blood is pumped, at a flow rate Q_{vp} from the buffer reservoir through the dialyzer and back towards the patient. Herewith, Q_{vp} might be set higher than Q_{ap} according to a pump ratio larger than 1 and, hence, an effective blood flow rate of more than $Q_{ap}/2$ can be obtained. Within each cycle, the blood volume in the buffer reservoir (V_{res}) is strictly controlled in between a minimum and maximum level, corresponding respectively to a minimum and maximum buffer blood volume, V_{min} and V_{max} . This implies that blood entering the buffer reservoir during an arterial phase is mixed with V_{min} blood that was still in the buffer reservoir after the previous venous phase. Equation 15.8a should in this case be changed into Equation 15.11a for the arterial phase (with $Q_{bi} = Q_{ap}$) and Equation 15.11b for the venous phase (with $Q_{bo} = Q_{vp} - Q_{uf}$):

$$\frac{d(V_1 C_1)}{dt} = G_1 + K_{12} \cdot (C_2 - C_1) - Q_{ap} \cdot C_{bi} \quad (15.11a)$$

$$\frac{d(V_1 C_1)}{dt} = G_1 + K_{12} \cdot (C_2 - C_1) + (Q_{vp} - Q_{uf}) \cdot C_{bo} \quad (15.11b)$$

Furthermore, the concentrations C_{bi} and C_{bo} are not constant within one phase, since the arterial and venous phase can each be split into two extra phases. During the arterial phase, the cleansed blood (from the previous venous phase) in the catheter volume (V_c), is first entering the buffer reservoir, followed by uncleansed blood from the patient's perfused compartment. During the venous phase, the uncleansed blood in V_c (from the previous arterial phase) is first flowing back to the patient's perfused compartment, followed by cleansed blood. During all phases, we accounted for the number of cycles, TD, it takes for the blood to flow through the dialysis circuit, comparable to the modeling of the DL catheter in reversed connection mode.

Studied solutes

To see the impact of the kinetic behavior on the dialysis adequacy, four solutes were studied, each with a different kinetics during dialysis. The data of two-compartmental calibrated kinetic models were taken from literature for urea and methylguanidine (MG) [146], beta-2-microglobulin (β_2M) [144], and phosphate [145]. Table 15.3 shows the molecular weight and the kinetic parameters: pre-dialysis V_1 , V_2 , C_1 , and C_2 , generation rate G_1 and G_2 , inter-compartmental clearance K_{12} , and the dialyzer extraction ratio ER, which is defined as the relative concentration variation over the dialyzer length.

	Urea	MG	β_2M	P
Reference	Eloot et al.[146]	Eloot et al.[146]	Stiller et al.[144]	Spalding et al.[145]
MW	60Da	73Da	11,800Da	31Da
V_{1-pre}	6.4 L	8.0 L	2.56 L	13 L
V_{2-pre}	36.3 L	94.6 L	7.44 L	27 L
$C_{1-pre} = C_{2-pre}$	24.0 mmol/l	3.7 μ mol/l	33 mg/l	1.7 mmol/l
K_{12}	822 ml/min	1025 ml/min	56.3 ml/min	300 ml/min
G_1	310 mmol/24h	46 μ mol/24h	0	0
G_2	0	0	218 mg/24h	0
ER	0.84	0.79	0.19	0.57

Table 15.3: Kinetic parameters for urea, MG, β_2M , and P.

MG: methylguanidine; β_2M : beta-2-microglobulin; P: phosphate; MW: molecular weight; V_{1-pre} : predialysis perfused volume; V_{2-pre} : predialysis non-perfused volume; C_{1-pre} and C_{2-pre} : predialysis concentration in V_1 and V_2 ; K_{12} : inter-compartmental clearance; G_1 and G_2 : generation rate in V_1 and V_2 ; and ER: dialyzer extraction ratio, defined as the relative concentration variation over the dialyzer length.

Studied vascular access and dialysis strategies

For the four solutes, four different scenarios were studied. Three are based on the double lumen catheter: one for the normal 4 h dialysis treatment without any recirculation at a blood flow rate of 350 ml/min (DL-normal) and one at a reduced flow rate of 250 ml/min (mimicking an impaired catheter function) (DL-low flow), and a case mimicking dialysis with reversed connections at 350 ml/min (introducing e.g. 10% recirculation and a time delay TD_{DL} of 35s) (DL-reversed). The fourth scenario is based on single lumen catheter dialysis treatment (SL) with an effective blood flow rate of 273 ml/min and a time delay (TD_{SL}) of 5 cycles. All treatment parameters can be found in Table 15.4.

Next to these scenarios, extra calculations were performed on the adequacy of the DL-reversed dialysis for circulations in a range of 0-50%.

	DL-normal	DL-reversed	DL-low flow	SL
Session duration [min]	240	240	240	240
Post dialysis rebound [min]	60	60	60	60
Q_b [ml/min]	350	350	250	273
Q_{uf} [L/h]	1	1	1	1
R [%]	0	10	0	inherent
Q_{ap} [ml/min]	n/a	n/a	n/a	500
Pump ratio (Q_{vp}/Q_{ap})	n/a	n/a	n/a	1.2
V_c (12Fr) [ml]	n/a	n/a	n/a	2.9
V_{min} [ml]	n/a	n/a	n/a	10
V_{max} [ml]	n/a	n/a	n/a	55
TD	n/a	35 s	n/a	5 cycles

Table 15.4: Operating parameters dialyzing with a double lumen (DL) and single lumen (SL) catheter.

DL: double lumen; SL: single lumen; Q_b : blood flow; Q_{uf} : ultrafiltration flow; R: access recirculation; Q_{vp} : blood flow during venous phase; Q_{ap} : blood flow during arterial phase; V_c : catheter volume; V_{min} : minimum buffer volume; V_{max} : maximum buffer volume.

Simulations and adequacy parameters

The coupled mathematical patient/dialyzer model, was written in Matlab (R2010b, The MathWorks inc., MA, US), and iteratively solved the mass balance equations for a complete dialysis session of 240 minutes. The calculations were performed with a time step of 1 second for the continuous DL catheter simulations, while this was 0.01s for the periodical SL catheter simulations in order to include all four phases during a single cycle. In order to

be able to compare the impact of the different vascular access modalities on the dialysis adequacy for different solutes, each with their specific kinetics, different parameters were calculated.

We calculated a reduction ratio RR [%] for all studied solutes in the perfused ($RR-C_1$) as well as in the non-perfused compartment ($RR-C_2$), according to Equation 15.1.

Due to a redistribution in the body caused by the two-compartmental kinetic behavior of the studied solutes, a rebound effect will occur following dialysis. To have an idea about the percentage rebound (%rebound), the concentration in the perfused compartment was calculated 60 minutes after the dialysis end ($C_{1-post60}$), by compartmental modeling and setting dialyzer clearance K equal to zero:

$$\%rebound = \frac{(C_{1-post60} - C_{1-post})}{C_{pre} - C_{1-post}} \cdot 100 \quad (15.12)$$

Furthermore, total solute removal (TSR) was calculated during an entire dialysis session as the amount of solute found in the spent dialysate. From the mass balance equation in the dialyzer, TSR at time point T can be calculated, in accordance with Equation 15.7 as:

$$TSR = \int_0^T C_{bi} \cdot (ER \cdot Q_{bi} + (1 - ER) \cdot Q_{uf}) dt \quad (15.13)$$

For the vascular access modalities deviating from the well functioning DL catheter, the dialysis time was calculated which is additionally needed in order to obtain the same amount of TSR as with the well functioning DL catheter.

Finally, nomograms were derived indicating dialysis adequacy, expressed as TSR, as a function of blood flow for different degrees of recirculation. Herewith, TSR for a well functioning DL CVC (350 ml/min blood flow and no recirculation) was taken as reference and equal to 1.

Sensitivity study

Since our calculations are based on literature data and since we performed the analyses for a fixed number of kinetic and dialysis parameters, we performed a sensitivity analysis to check the impact of our parameter choice on the dialysis adequacy. For this purpose, we took the TSR as calculated for DL-normal as comparator, while introducing changing values for intercompartmental clearance (K_{12} : $\pm 10\%$), extraction ratio (ER : $\pm 10\%$), and the ratio

of compartmental volumes (V_1/V_2 : $\pm 10\%$) was calculated in a DL-normal CVC. In the DL-reversed CVC, TSR was determined for a range of time delay (TD_{DL} : 0-70 s) values, and in the SL CVC, TSR was calculated for a varying catheter volume (V_c : 2.5-3.5 ml), buffer reservoir volume (V_{res}), minimum volume in the buffer reservoir (V_{min} : 5-15 ml), venous versus arterial pump ratio (Pump ratio: 1.1-1.3), and time delay (TD_{SL} : 0-10 cycles).

15.2.3 Results

The urea concentration decrease during 4 h dialysis and 1 h rebound in the perfused (C_1) (for all studied scenarios) and the non-perfused compartment (C_2) (for the DL-normal) is illustrated in Figure 15.6A, while the cumulative TSR is shown in Figure 15.6B. The post dialysis urea reduction ratios are $RR-C_1=73.6\%$ and $RR-C_2=66.8\%$ with the DL-normal (Table 15.5). As observed in Table 15.6, the DL-reversed CVC only showed minor deviations (range 3.5-4.2%) of RRs compared to the well functioning DL CVC, while deviations are much more pronounced with the DL-low flow CVC and the SL CVC (range 13.0-17.5%). A similar trend is followed by the %rebound and TSR.

The concentration decrease of β_2M in the perfused (C_1) (for all studied scenarios) and non-perfused compartment (C_2) (for the DL-normal) is shown in Figure 15.7A, while the cumulative β_2M TSR is shown in Figure 15.7B. The large intercompartmental clearance K_{12} for β_2M , compared to that of urea (Table 15.3), causes a 4-fold larger %rebound (Table 15.5).

While an analogous trend for RR, %rebound and TSR is present for urea, MG and P (Table 15.5), β_2M is behaving differently. With the latter, RRs are comparable for DL-normal, DL-reversed, and SL CVC, with high deviations for the DL-low flow CVC (range 21.1-43.9%)(Table 15.6). Despite the

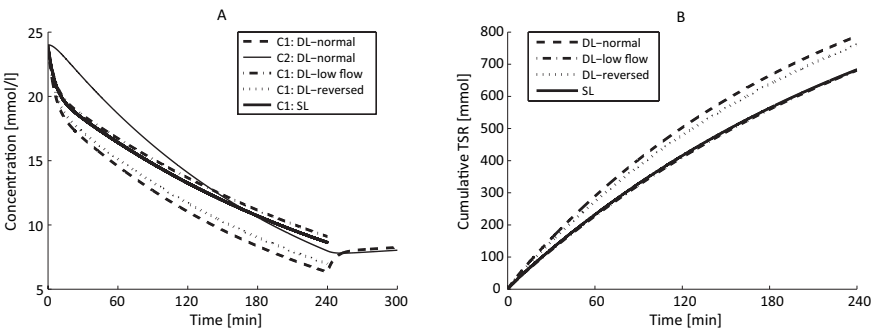


Figure 15.6: Urea concentration profile (panel A) and cumulative TSR (panel B) for different dialysis strategies.

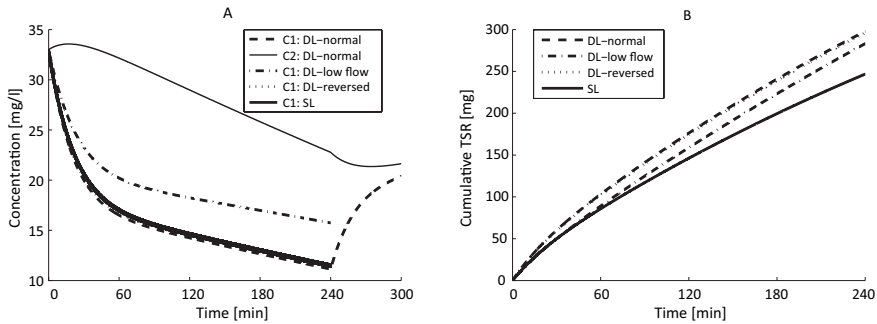


Figure 15.7: β_2 M concentration profile (panel A) and cumulative TSR (panel B) for different dialysis strategies.

low RRs for the DL-low flow CVC, TSR was found comparable to TSR with DL-normal and DL-reversed CVC, while TSR for the SL CVC shows large deviations (17.2%).

Table 15.6 also indicates the extra time needed to reach the same amount of TSR as with the 4 h dialysis with a DL-normal CVC. With the DL-reversed, the least extra time is needed for all studied solutes (2-17 min), while this is also minimum with the DL-low flow for β_2 M (16 min).

Figure 15.8 shows the impact on TSR of the degree of recirculation (0-50%) with a DL-reversed catheter. Adequacy is decreased by 10% for a recirculation degree of 17% (MG), 26% (urea), and 30% (phosphate). Even for a recirculation of 50%, the removal of β_2 M is only decreased by 5% compared to the scenario with the DL-normal catheter.

	RR-C ₁	RR-C ₂	%rebound	TSR	Time
	[%]	[%]	[%]	[mmol ^a]	min
Urea	73.6	66.8	10.9	787	240
MG	51.0	38.6	24.8	0.17	240
β_2 M	66.3	31.0	42.2	298	240
P	68.6	52.8	14	44	240

^a mg for β_2 M

Table 15.5: Adequacy parameters for DL-normal dialysis for different solutes, different types of vascular access.

RR: reduction ratio; TSR: total solute removal; MG: methylguanidine; β_2 M: beta-2-microglobulin; P: phosphate.

	RR-C ₁	RR-C ₂	%rebound	TSR	Time
	% reduction	% reduction	% reduction	% reduction	min
Urea					
DL-low flow	15.6	17.5	-20.2	13.5	65
DL-reversed	3.5	4.2	-4.6	3.3	15
SL	13.0	14.7	-16.5	13.2	65
MG					
DL-low flow	20.6	22.5	-9.7	19.1	73
DL-reversed	5.5	6.2	-2.4	5.3	17
SL	17.8	19.7	-8.5	17.9	70
β_2M					
DL-low flow	21.1	43.9	-25.6	4.9	16
DL-reversed	1.2	2.6	-1.4	0.6	2
SL	1.5	4.2	-2.4	17.2	75
P					
DL-low flow	16.3	19.5	-12.9	14.2	63
DL-reversed	2.8	3.4	-2.1	2.7	11
SL	11.5	13.8	-8.6	14.4	67

Table 15.6: Adequacy parameters for different solutes, different types of vascular access: % decrease and extra time versus DL-normal.

DL: double lumen; SL: single lumen; RR: reduction ratio; TSR: total solute removal; MG: methylguanidine; β_2M : beta-2-microglobulin; P: phosphate.

Figure 15.9 shows nomograms for urea (panel A), MG (B), β_2M (C), and P (D).

The results of the sensitivity study indicate that a 10% change in extraction ratio gives the largest variation in TSR (range 1-6%), whereas for all other parameters under study, TSR variations remain below 3% (see Table 15.7).

15.2.4 Discussion

We demonstrated that, as far as this procedure results in better blood flows, reversing the lines of double lumen-reversed central venous catheters (DL-CVC) is the best alternative in case of dysfunctional flow in normal connection mode (as in the study of Section 15.1). This is because rather similar total solute removals (TSR) were found with the DL-reversed as with the DL-normal CVC, and this for all solutes under study. Also, recirculation degrees of around 20% result in an adequacy decrease of merely 10%, which was found to be even more adequate than with a double lumen catheter with

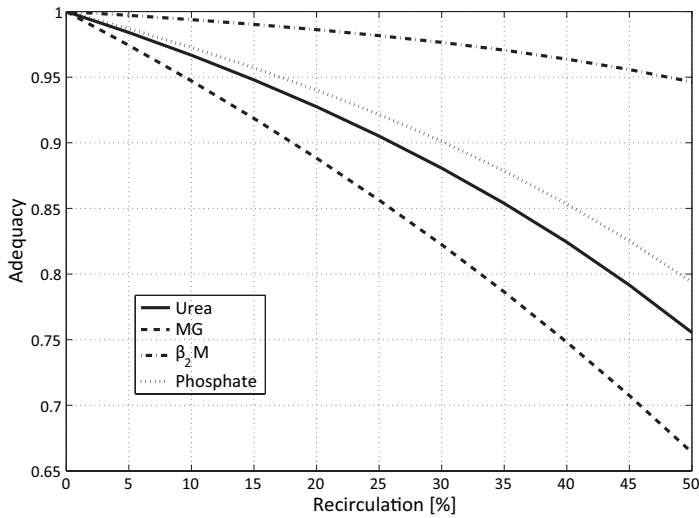


Figure 15.8: Dialysis adequacy (in terms of Total Solute Removal) for different solutes as a function of the degree of recirculation.

Parameter	Reference value	Reference treatment	Range	Urea	MG	β_2M	Phosphor
K_{12}	See Table 15.3	DL-normal	$\pm 10\%$	$<1\%$	$<2\%$	$<3\%$	$<2\%$
Er	See Table 15.3	DL-normal	$\pm 10\%$	$<4\%$	$<6\%$	$<1\%$	$<4\%$
V_1/V_2	See Table 15.3	DL-normal	$\pm 10\%$	$<0.01\%$	$<0.01\%$	$<0.2\%$	$<0.01\%$
T_{DL}	35 s	DL-reversed	0-70 s	$<1\%$	$<2\%$	$<3\%$	$<3\%$
V_{lumen}	2.9 ml	SL	2.5-3.5 ml	$<1\%$	$<1\%$	$<0.5\%$	$<1\%$
V_{over}	10 ml	SL	5-15 ml	$<0.5\%$	$<0.5\%$	$<0.5\%$	$<0.5\%$
V_{res}	55 ml	SL	50-60 ml	$<1\%$	$<1\%$	$<1\%$	$<1\%$
Pump ratio	1.2	SL	1.1-1.3	$<2\%$	$<3\%$	$<1\%$	$<3\%$
T_{SL}	5 cycles	SL	0-10 cycles	$<2\%$	$<2\%$	$<1\%$	$<2\%$

Table 15.7: 4-hour dialysis session: Parametric study on changes in TSR

reduced flow of 250 ml/min. Besides, the adequacy of a single lumen (SL) CVC is comparable to that obtained with a dysfunctional DL CVC (DL-low flow), except for β_2M for which reduction ratio (RR) is much better while TSR is much smaller for the SL CVC.

Although CVCs are strongly discouraged as permanent access for HD, as they are associated with higher mortality and infection rates, their use has become unavoidable in a growing number of patients. Beside the risk of infection, use of CVCs is also hampered by presence of impaired flow, frequently leading to interruption of the dialysis session. Different strategies, such as reversing the lines, continuing dialysis at lower blood flows, or even catheter replacement, can be applied to tackle this problem. However, clear

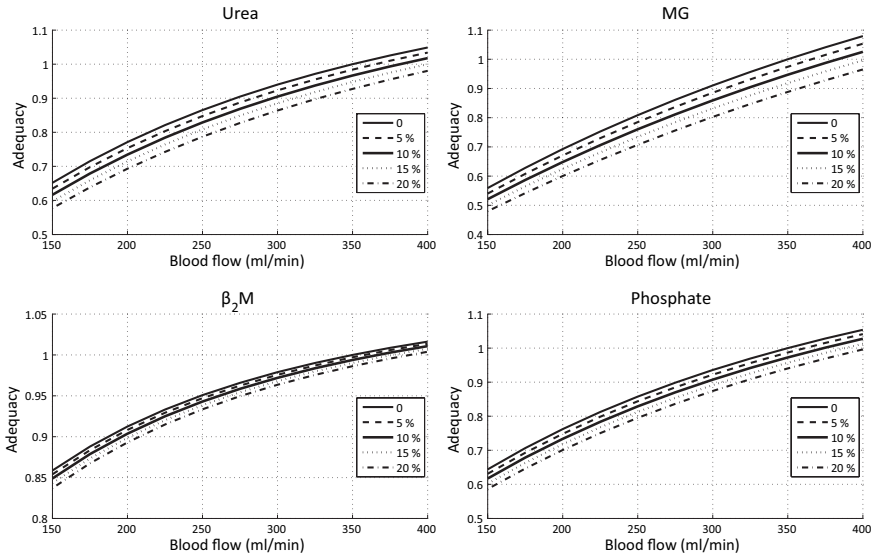


Figure 15.9: Nomograms for urea (panel A), MG (B), β_2M (C), and P (D), relating dialysis adequacy (TSR) for different blood flows and different degrees of access recirculation (0-20%). The DL-normal CVC with $R=0\%$ and with $Q_b=350$ ml/min is taken as reference with adequacy equal to 1.

evidence to support either of these options is lacking. More specifically, it is unclear in how far solute removal is hampered by access recirculation or lower blood flows. Solute kinetics play an important role in the solute removal during dialysis. From that point of view, it could be assumed that the presence of access recirculation, induced by reversing the catheter connection or by using a SL CVC, has minor impact on the removal of solutes like β_2M , with a hampered transport inside the patient, as confirmed in our study.

We derived nomograms from the obtained TSR results, illustrating the loss of adequacy (as defined by TSR) when using DL CVCs at different (lower) blood flows and/or the presence of access recirculation. These nomograms can be used in clinical practice to guide catheter management in individual patients in case access recirculation is quantified [302–308]. From the adequacy perspective, these graphs clearly illustrate that there is no straightforward relation between the degree of access recirculation and the loss of adequacy, and that the presence of access recirculation should not be necessarily considered as unacceptable. They illustrate as well that the type of vascular access has the least influence on the removal of the middle molecule

β_2M , due to the much slower kinetic transport in the patient compared to that of the small and water soluble solutes urea, MG, and phosphate.

Solute kinetics is also one of the reasons for the, at first sight, contradictory finding that β_2M reduction ratio is much better for SL CVCs compared to the dysfunctional DL CVCs, while total solute removal is much lower using SL CVCs (Figure 15.7 and Table 15.6). During hemodialysis with a SL CVC, plasma concentrations (concentrations in the perfused compartment C_1) are decreasing at the same degree as with the DL-normal and the DL-reversed, resulting in a high RR. This phenomenon is due to adequate β_2M removal in the hemodialyzer and the inherent access recirculation diluting the blood dialyzer inlet concentration, in combination with the slow β_2M transport from the non-perfused towards the perfused compartment (low intercompartmental clearance K_{12}). However, the lower blood dialyzer inlet concentrations lead to lower spent dialysate concentrations and, combined with the lower average flow rate, lower TSR. With respect to the middle molecule β_2M , the SL CVC is thus a worse alternative for a dysfunctional DL CVC when considering the difference in TSR, a more reliable adequacy parameter than RR [301].

Somewhat less expected, our study reveals that adequacy is not much different between the DL-normal and DL-reversed CVC (with $R=10\%$ or less) for all studied small and water soluble solutes, while adequacy was significantly lower with the DL-low flow and SL CVC. As long as recirculation, when reversing the connection lines, is limited to around 20%, and blood flow can be restored, the adequacy decrease will be limited to less than 10%. This is an important take home message, since the use of lower blood flows (250 ml/min) results already in an adequacy decrease in the range 14-20% for urea, MG, and phosphate.

One could think that our study is suffering from a major drawback, being purely based on mathematics. Validation is herewith rather difficult, not to say impossible, since the kinetic parameters, such as distribution volume and intercompartmental clearance, are not known in a particular patient. We should stress however that the models used here were based on kinetic models that were previously calibrated on patients data. Hence, our mathematical model can be considered as an 'average patient on dialysis'. It also allows us to compare different scenarios, i.e. double lumen, either with reversed connection lines or not, and single lumen CVCs in an 'average patient', something that is not possible to study *in vivo* in the same patient.

Some other weaknesses of the modeling approach can be highlighted. First, the solute extraction ratio was considered constant for all scenarios due to a lack of knowledge of how ER exactly changes with blood and/or

dialysate flows. Hence, since ER should be increased for lower blood flows, RR and TSR for low flow dialyses (i.e. DL-low flow and SL) might be slightly higher in vivo. Second, per studied solute, the calibrated kinetic models were taken from literature, being serial mathematical models. However, despite any physiological meaning, in contrast with the physiologically based parallel models [311–313], the applied models are based on patient data, describing solute kinetics in a correct way. And third, although of limited impact when dealing with our cross-over simulations, some other factors might play a (rather minor) role as well in the overall recirculation, such as tubing compliance, and the presence of a pre-arterial-pump flow chamber in the dialysis circuit [314].

Furthermore, our mathematical study has some important strengths. First, the removal of different types of solutes with a totally different kinetic behavior in the patient was modeled. The solutes mainly differ in distribution volume and intercompartmental clearance, both representing the retardation of transport from the deeper tissues towards the patients plasma (Table 15.3). Second, the different solutes were modeled with a two-compartmental model that was calibrated with clinical data, including urea that was previously studied using single-pool kinetics (Section 15.1). Third, our mathematical model is up till now the only available tool that allows direct comparison between solute removal with double and single lumen catheters on the one hand, and correct and reversed connected catheter lines on the other hand. And fourth, the single lumen catheter model is designed in such detail that dialysis modeling is possible with different stroke volumes, as determined by the arterial-venous pump ratio and the buffer volumes.

15.2.5 Conclusion

In case of a dysfunctioning double lumen catheter during 4 h standard hemodialysis, reversing the lines should be preferred above lowering the blood flow in correct connection mode, if this practice results in higher blood flows. Single lumen catheters are a suboptimal long term option in terms of adequacy for patients on regular dialysis (3 times a week for 4 hours).

15.3 SLOW EXTENDED DIALYSIS: 2-COMPARTMENT KINETIC MODELING

15.3.1 Introduction

Extended dialysis is gaining renewed interest over the last decade, especially since it has been associated with better outcome in observational studies [315, 316], and with more solute removal, even with low blood flows [301]. In dialysis centers, mainly short dialysis (4 h) is performed, while extended nocturnal hemodialysis (NHD) is more feasible in the homecare setting. There is however still uncertainty on the optimal blood and dialysate flows for this extended form of dialysis. High flows induce more frequent alarms, higher costs of water, and higher consumption of dialysate concentrates, with the need to change containers during the night. The question under study is whether the loss of adequacy due to lower flows in nocturnal home hemodialysis (NHHD) versus high flows in short in-center dialysis, is compensated by the longer dialysis duration.

Furthermore, in case of a graft or fistula, double needle puncturing in home dialysis is often unpractical if patients are dialyzing without assistance, and is substantially more dangerous in case of accidental needle dislodgement with subsequent blood loss out of the venous needle.

Since no data are available on solute removal for single versus double needle/lumen dialysis or for high versus low blood flows in extended dialysis, we developed a mathematical model combining a two-compartment kinetic model for different uremic toxins with a hemodialysis model. Here-with, we compared total solute removal and reduction ratios in different settings of extended NHHD versus short dialysis.

15.3.2 Material and methods

For this study, the same calibrated mathematical patient/dialyzer model was used as in Section 15.2 and shown in Figure 15.4 (omitting the recirculation R) and Figure 15.5. The same four solutes were studied (urea and methylguanidine (MG), beta-2-microglobulin (β_2M) and phosphate), with molecular weight and kinetic parameters as shown in Table 15.3.

For each of the four solutes, four different scenarios were studied: the standard double needle (lumen) 4 h dialysis at high flow Q_b 350 ml/min (DL-HF-4h), and three extended 8 h dialysis sessions: two double lumen with either high flow Q_b 350 ml/min (DL-HF-8h) or low flow Q_b 175 ml/min (DL-LF-8h), and one single lumen (SL-8h). All treatment parameters can be found in Table 15.8. For the SL approach, next to 12 Fr central venous catheter, the single needle approach ($V_c = 0.5$ ml) was considered.

	DL-HF-4h	DL-HF-8h	DL-LF-8h	SL-8h
Session duration [min]	240	480	480	480
Post dialysis rebound [min]	60	60	60	60
Q_b [ml/min]	350	350	175	273
Q_{uf} [L/h]	1	0.5	0.5	0.5
Q_{ap} [ml/min]	n/a	n/a	n/a	500
Pump ratio (Q_{vp}/Q_{ap})	n/a	n/a	n/a	1.2
V_c (12Fr) [ml]	n/a	n/a	n/a	2.9
V_{min} [ml]	n/a	n/a	n/a	10
V_{max} [ml]	n/a	n/a	n/a	55

Table 15.8: Operating parameters in the different dialysis settings.

DL: double lumen; SL: single lumen; HF: high flow; LF: low flow; Q_b : blood flow; Q_{uf} : ultrafiltration flow; R: access recirculation; Q_{vp} : blood flow during venous phase; Q_{ap} : blood flow during arterial phase; V_c : catheter volume; V_{min} : minimum buffer volume; V_{max} : maximum buffer volume.

15.3.3 Results

Reduction ratio (RR) and total solute removal (TSR) are presented in Table 15.9 for the four scenarios and the four solutes under study. Compared to the 4 h hemodialysis, RR's are equal in DL-LF-8h, higher in SL-8h, and even more increased in DL-HF-8h mode, and this for all studied solutes.

For the DL-LF-8h and the SL-8h approach, TSR was for all solutes higher compared to 4 h hemodialysis (range 6-18% and 13-35%, respectively). TSR with the SL-8h approach was even larger compared to the DL-LF-8h, except for β_2M .

By further increasing the flow during extended dialysis (from low flow DL-LF-8h to high flow DL-HF-8h), TSR increases but is not doubled compared to 4 h hemodialysis: only 7-30% higher compared to DL-LF-8h, and even only 7-15% higher compared to SL-8h hemodialysis. For β_2M , differences in TSR with DL-HF-8h are limited to only 7% (DL-LF-8h) and 11% (SL-8h).

Finally, with the single needle approach, RR and TSR, respectively, were only 1 and 2% higher compared to the values found with the SL CVC (data not shown).

	RR-C ₁ [%]				RR-C ₂ [%]				TSR [mmol ^a]			
	4 h	8 h			4 h	8 h			4 h	8 h		
	DL-HF	DL-HF	DL-LF	SL	DL-HF	DL-HF	DL-LF	SL	DL-HF	DL-HF	DL-LF	SL
Urea	73.6	90.5 (23)	71.8 (-2)	84.1 (14)	66.8	88.5 (32)	68.6 (3)	81.6 (22)	787	1031 (31)	851 (8)	957 (22)
MG	51.0	70.8 (39)	47.3 (-7)	61.0 (20)	38.6	63.7 (65)	41.1 (6)	54.0 (40)	0.17	0.27 (59)	0.18 (6)	0.23 (35)
β_2 M	66.3	83.8 (26)	60.2 (-9)	80.6 (22)	31.0	66.3 (114)	39.6 (28)	62.2 (101)	298	380 (28)	353 (18)	338 (13)
P	68.6	87.8 (28)	68.0 (-1)	81.5 (19)	52.8	81.6 (55)	60.3 (14)	74.5 (41)	44	59 (34)	47 (7)	54 (23)

^a mg for β_2 M

Table 15.9: Adequacy parameters for different solutes, and different dialysis settings.

RR: reduction ratio; TSR: total solute removal; DL: double lumen; SL: single lumen; HF: high flow; LF: low flow; MG: methylguanidine; β_2 M: beta-2-microglobulin; P: phosphate. The value between brackets is the percentage increase of the adequacy parameter, compared to 4h DL-HF.

15.3.4 Discussion

We demonstrated that total solute removal (TSR) during extended HD is higher when compared to 4 h HD for all studied solutes, even with low flow or using a single lumen approach. Although there was more solute removal with DL-HF-8h HD as compared to DL-LF-8h HD, these differences were rather limited, especially for solutes which are difficult to remove, such as β_2 M. Even in the 8 h single lumen HD approach, TSR was higher than with 4 h standard HD. Hence, our data demonstrate that vascular access has only a limited impact on total solute removal during extended dialysis regimens, especially for solutes with retarded multi-compartment behavior.

In extended slow dialysis (i.e. low blood and/or dialysate flow with DL-LF-8h HD), the lower solute clearance is counterbalanced by a financial benefit and better patient quality of life. Especially in the home dialysis setting, the use of low dialysate and/or blood flows is of relevance, as this reduces the frequency of alarms, and avoids the necessity to wake up during the night to exchange dialysate concentrate bags. All this substantially adds to the quality of sleep and thus quality of life of the patient. Furthermore, lower dialysate flows also reduce costs related to the water consumption, again of high relevance in the home dialysis setting, where these extra expenses in many countries are directly on the patient's costs.

A single needle access can be of importance for patients who dialyze without assistance, as double needle puncturing is cumbersome under these conditions. A single puncture also results in slower deterioration of vascular access and less access-related problems [317]. In addition, single needle dialysis enhances safety in case of disconnection of lines. Even for patients dialyzing with a central venous catheter as access, our findings are relevant, as several observational studies reported a lower incidence of complications in single vs double lumen catheters [85, 318, 319]. Our results indicate that these low blood and dialysate flows, even in a single needle setting (i.e. SL-8h), can be used without jeopardizing solute removal.

It can be remarked from the present results that increasing dialysis duration has most impact on TSR, with none or only limited impact on RR. A similar trend was found previously in an *in vivo* cross-over study of 4, 6 and 8 hours HD [301]. This seemingly discrepancy can be explained by the fact that during (slow) 8 h dialysis, more solute can be transported from the non-perfused into the perfused compartment where it can be removed by dialysis. Hence, this higher TSR results in a smaller post-dialysis rebound with 8 h dialysis, which is not necessarily reflected in a higher RR.

The fact that our study is purely based on mathematics should not be regarded as a drawback. Our simulations can be considered as being per-

formed in an ‘average patient on dialysis’ since we used kinetic models that were previously calibrated on patient’s data [144–146]. However, some weaknesses of the modeling approach should be highlighted.

First, for all scenarios, we started, per solute, from the same conditions as indicated in Table 15.3, although several parameters could be different between 4 h and 8 h dialysis, and between the first, second, and third dialysis session of the week (i.e. pre-dialysis concentrations and compartment volumes). In steady state, for instance, pre-dialysis concentrations will be lower with 8 h dialysis, while total solute removal, which is equal to generation rate, will become equal again to that during 4 h dialysis. Over a longer period, time averaged concentrations will be lower with extended dialysis. The aim of our study, however, was to compare the adequacy of different scenarios for a single session, such that a mathematical model based on an ‘average patient’ with same pre-dialysis conditions is a useful tool.

And second, per studied solute, the calibrated kinetic models were taken from literature. Herewith, phosphate modeling was performed using the calibrated two-compartment model, although it cannot accurately describe plasma concentrations as compared to the three- and four-compartment models [145], i.e. the modeled concentrations decrease slower during the first and faster during the second half of dialysis. Since the use of more complex models would need too many additional assumptions, and since we are mainly interested in pair wise comparisons of RR and TSR between different scenarios, our method seems quite defensible.

Beside these weaknesses, our mathematical study has some important strengths as well. Different types of solutes were modeled with a totally different kinetic behavior in the patient. Furthermore, the mathematical modeling of SL dialysis included several details like stroke volumes, arterial-venous pump ratio, buffer volumes and recirculation.

Although the present findings might not all be very surprising to each clinician [319], it is worthy to see the conclusions based on mathematical modeling, independent from the variability present in the general patient population, and from the variability present in the starting conditions of different dialysis strategies. Our data clearly shows that the loss of adequacy due to lower flows in nocturnal home hemodialysis can be compensated by longer dialysis duration, compared to short in-center dialysis.

15.3.5 Conclusion

Although high blood and dialysate flows still result in higher total solute removal during extended 8 hour dialysis as compared to lower flows, the

gain is limited, especially for solutes with more complex compartment behavior, such as β_2 M. Even when using a single lumen approach, total solute removal is superior in extended 8 h dialysis compared to standard 4 h dialysis. In view of the practical constraints of the home dialysis setting, low flow dialysis, even with single lumen approach, is a defensible option.

Six

General conclusions

Conclusions

This is it. After 6 years of swimming, diving, floating and sometimes even drowning in the biofluid site of vascular accesses (VA), you can find my final conclusions hereafter. Since my PhD-work was built around the three types of VA [arterio-venous fistula (AVF), arterio-venous graft (AVG) and central venous catheter (CVC)], not one general but several research statements will be discussed in the following section. While the different studies in this dissertation were grouped per VA type, the statements will be discussed per study method.

16.1 CFD ANALYSIS

The main pressure drop in the AVF circuit should be over the anastomosis.

In general, there is a huge absence of interest in the geometry of the created arterio-venous anastomosis. This can be noticed by the virtual total absence of studies regarding this topic, as well as by the lack of interest in the geometry of the anastomosis in clinical studies dealing with AVF outcome. Creating a too small anastomosis reduces the chance of proper fistula maturation. But avoiding the non-maturation by creating a (too) large anastomosis should not result in an increased prevalence of venous hypertension, cardiac overload, distal hypoperfusion or ischemia. We showed in our study on the impact of the anastomosis size (i.e. length and width) and

angle, that slightly changing the AVF anastomosis geometry has a large impact on the blood flow and local pressure distribution, with a quadratic and case-/patient-specific relation between flow rate and pressure drop.

During surgical creation of an AVF, as well as during complication solving interventions, should the anastomosis geometry be chosen with care, keeping in mind the impact of the geometry on pressure drop and flow distribution. Therefore, it can be stated that the main pressure drop in the arterio-venous circuit should be over the anastomosis to avoid complications such as high pressure in the venous system, cardiac overload and distal ischemia.

Using a helical pattern in the design of an AVG introduces a more complex flow field and reduces, but does not delete, zones with unfavorable hemodynamic conditions.

To investigate the influence of helicity in the graft design, a straight conventional graft was compared to five different helical designed grafts. We analyzed the flow field using different wall shear stress descriptors as well as the kinetic helicity in the bulk flow and the pressure drop over the graft section. The investigated wall parameters (time-averaged wall shear stress, oscillatory shear index and relative residence time) can be linked to an increasing risk of intimal hyperplasia formation, thus stenosis formation.

It is clear from our study, that introducing helicity in the design of an AVG changes the downstream hemodynamics and introduces a more complex flow field. There is however no trivial relationship between the number of helical turns and the investigated wall shear parameters. Only the very ‘swirling’ design, a pitch smaller than 6 times the graft diameter, significantly reduces the area with unfavorable hemodynamic conditions at the venous anastomosis. However, in clinical practice, inserting this design under the skin of a patient will not be obvious. So, a design with a more modest helicity pattern can be used to achieve more athero-protective conditions, but the unfavorable hemodynamics will not be vanished. Furthermore, because every graft is, irrespective of the graft design itself, subject to torsion and bending while connected in a loop configuration between an artery and a vein, grafts should be studied case-by-case to qualify their ability to reduce unfavorable hemodynamics.

The VectorFlow CVC outperforms standard catheters due to the negligible recirculation.

We showed, based on kinetic modeling, that reversing the lines is a defensible practice to increase blood flow in malfunctioning catheters. The VectorFlow catheter, a double-D design with symmetrical tip, showed in a CFD analysis, as well in an *in vitro* and *in vivo* investigation, a negligible recirculation. Note that correct and reverse line connection are equal due to the symmetrical design of the catheter tip. So from this point of view, the VectorFlow is a reliable option.

The CFD analysis had the advantage that not only a global factor as recirculation could be assessed, but a more in depth analysis could be performed as well. An ideal dialysis catheter, from a fluid-dynamic perspective, produces low shear stresses on the fluid, has a low percentage of prolonged blood residence time (cf. clotting) and maintains a low platelet lysis index (cf. hemolysis). The mean shear stress and platelet lysis index were only slightly elevated (8% maximum) compared to reference case of a ‘shotgun’ design, even with a significant higher Reynolds number (18%) in the arterial and venous lumen. The blood residence time was only modestly elevated.

The symmetrical-tip design of the VectorFlow catheter introduces a negligible recirculation and keeps the blood (flow) parameters in a very acceptable range. However, additional pre-clinical data are required to confirm the increased catheter patency during long-term implantation.

16.2 EXPERIMENTAL ASSESSMENT

The pulse wave propagation model and the high flow CFD solver, developed in the ARCH-project, are experimentally validated and can be used for further clinical implementation.

For 1D-modeling, one cannot merely rely on patient data to determine whether the physical descriptions in the model are complete. Conducting an experimental validation on an *in vitro* setup, with controllable and measurable boundary conditions (e.g. no vessel adaption), is probably the best option. For example, due to the inter-day variability of the patient’s blood pressure (i.e. by room temperature or the tranquility of the patient), an *in vitro* setup seems more ‘reliable’ when it comes to investigate the model’s fundamental principles and the underlying physics. More over, compared to *in vivo* validation, *in vitro* validation is not hampered by the search for non-invasive measurement methods and by a limited number of accessible locations in the circuit.

The experimental validation of the pulse wave propagation model showed that mean values of flow and pressure can be predicted adequately, but that viscoelasticity should be introduced in the model to match the diastole or systole values.

The pulse wave propagation model validation showed that calculating the pressure and flow waves (with correct attenuation) is very challenging. This knowledge makes it clear that studies relying on sensitive detection of the reduction or magnification of the pulse pressure, cannot just rely on computational modeling.

For new CFD-codes, one can rely, in first instance, on the comparison of the code against known benchmark results. However, to ensure that flow vs. pressure drop simulations, in challenging cases, give reliable results, *in vitro* assessment seems still needed. Herewith, the overall flow field is well described by the solver and the pressure drop values are reliable up to a Reynolds numbers of 2000. Hence, introducing a non-linear pressure loss coefficient in the pulse wave propagation model, calculated by the CFD code seems a good option to replace the pressure loss coefficients based on e.g. T-shaped fittings.

The experimental validation of the models' fundamental principles opens the way for further clinical implementation and *in vivo* validation.

Experimental lab work needs experienced researchers.

During the experiments in the context of *in vitro* validation, concerning the pulse pressure analysis stenosis detection method and in the field of neurosurgery [320, 321], much knowhow is gained on how *in vitro* fluid-mechanical experiments should be executed.

As computers get faster and computational power increases (in 2006 the Hydraulics lab had 3 single calculation computers, at present, a cluster of over 200 cpus is available for the bioMMeda research group), the time consuming experimental validation seems to vanish. But, still, *in vitro* validation of numerical models is very valuable.

In contrast to numerical investigations, constructing a large set of experimental models and setups is not possible, while keeping cost, both money and time, within 'budget'. One should, either investigate time to build up in-house knowledge on model construction or invest money in purchasing a state-of-the-art model.

It was found in large multicenter PIV-studies that fluctuations in the flow conditions and fluid properties need to be well controlled to increase accuracy and reproducibility. We had the same experience when analyzing the results of the preliminary PIV-study on a model of a kinked blood vessel

[322, 323]. Herewith, we minimized, in our final PIV study, fluctuations on the flow conditions by installing a 1 m long stiff tube proximal to the model to obtain a symmetric inflow and even checked the correctness of the assumed velocity profile. Furthermore, we closely monitored the fluid temperature and consequently adapted and measured the viscosity, to minimize fluid property fluctuations.

To conclude, I want to point out that experimental work needs an experienced investigator. During the first construction of models and setups, a lack of skills may lead to leakages on multiple (unexpected) locations, air bubbles in the circuit, and inflating and/or bursting silicon models (by misjudgment of clamps or valves), such that pressure and flow data will make crazy antics. However, after obtained the necessary experience, collecting data from a well controllable setup (as a validation for example), provides most certainly a great sense of accomplishment.

16.3 DIAGNOSTIC TOOLS

Pulse pressure analysis at the arterial needle can be used to detect stenoses in early stage.

The disadvantage of current stenoses detection methods, based on pressure drop or flow reduction, is the fact that they can only ‘trace’ stenoses with a diameter reduction of about 70% ($\approx 90\%$ area reduction).

Our developed pulse pressure analysis (PPA) method, however, can detect stenoses with a 50% and even a 25% diameter reduction. This detection in early stage can help the clinicians in the patient-specific fistula patency management. The PPA method is even independent of the flow and heart rate.

For use in clinical practice, the full pressure profile should be acquired and analyzed. This technique is feasible since most of the dialysis machines nowadays have arterial line pressure sensors reporting mean pressures. However, a longitudinal study should reveal whether stenoses can be detected in early stage only by, for example, weekly registration of the arterial needle pulse pressure.

Standard pulsed wave Doppler ultrasound measurements cannot provide reliable blood flow rates.

We performed a theoretical study based on patient-specific data, both pre and post arterio-venous fistula creation, integrating computational fluid dynamics calculations with an ultrasound simulator. We found that, when analyzing the simulated pulsed wave Doppler (PWD) spectrum in the brachial

and radial artery, the velocity component in the direction of the ultrasound (US) beam, in a centered, small, sample volume, can be captured accurately provided that the velocity is derived using the mean of the pulsed wave Doppler spectrum rather than the outer envelope contour. However, when deriving the final blood flow rate based on these measurements, a high degree of inaccuracy occurs. We found that two factors induce this inaccuracy.

First, the angle-correction of the velocity in the direction of the US-beam towards the velocity in the longitudinal direction is largely influenced by the radial velocity components in the complex flow field.

Second, the largest error is introduced when the velocity in one point (e.g. in the center of the vessel, 0D) has to be transferred to the cross-sectional mean velocity (2D) without any knowledge on the flow profile: i.e. is the profile symmetrical, with its maximum velocity in the center and is the shape of the profile parabolic, flat or something in between like Womersley flow? It cannot be predicted in advance, even not for the low flow pre-operative cases.

In our study case, flow at the brachial artery (pre- and postoperative) and pre-operatively at the radial artery was best estimated assuming a parabolic flow profile. For the post-operative radial artery acquisition, the most complex flow pattern occurred and assuming a plug flow profile resulted in the lowest bias.

One might expect that the use of the larger sample volume (e.g. over the full diameter of the vessel, 1D) should provide the most accurate estimate of the volume flow (2D). Interestingly, our data indicated that this was not systematically the case, probably because this method is challenged by the fact that velocities near the vessel wall are difficult to measure, even in straight vessel segments.

16.4 KINETIC MODELING

Reversing connection lines is the best alternative for dysfunctional double lumen CVCs during standard (4 h) dialysis.

In case of a dysfunctional double lumen CVC, two options can be taken: i.e. lowering blood flow, or reversing the lines simultaneously and thereby increasing blood flow. First, we found during an *in vivo* study, including 22 patients, that reversing the lines in a well-functioning double lumen CVC did not influence the solute removal of four generally studied solutes. Since reversing the catheter lines might increase recirculation (suction of cleansed blood back to the dialyzer) in a standard 'shotgun'-type CVC, a mathematical study, combining single pool modeling with a dialyzer model, was performed to determine dialysis adequacy based on urea removal. The study

revealed that the total solute removal (TSR) of urea was only reduced by 9.2% (at blood flow rate, Q_b , of 350 ml/min) when the recirculation was below 10%.

To better describe the retarded solute transport in the patient's body, a more complex 2-compartment kinetic model was combined with a dialyzer model. Dialysis adequacy was checked for 4 different solutes in 4 different access types. We found a reduction of urea-TSR of only 3.3% when introducing 10% recirculation (Q_b 350 ml/min). For a solute with a hampered transport within the patient (like β_2M), an enormous recirculation of 47% only reduces solute removal with 5%.

Through the 2-compartment kinetic modeling, we revealed that double lumen reversed connection (introducing recirculation) with a high blood flow rate, should be preferred above the correct line connection (negligible recirculation) with a lowered flow. Single lumen CVC dialysis seemed a suboptimal option in regular 4 h dialysis.

Low-flow dialysis with double lumen CVC, or dialysis with single lumen CVC or single needle with an AVF, are considerable alternatives during extended (8 h) dialysis.

Due to the available time during 8 h dialysis, solute kinetics in the patient play an important role as compared to the dialyzer clearance. Therefore, 2-compartment kinetic modeling was performed for 4 solutes and 4 different cases.

We found the obvious fact that solute removal was higher when, for the full length of the dialysis, a high flow (as in regular dialysis) was maintained. However, solute removal with 8 h was not doubled compared to the 4 h dialysis (increase of 28-51%).

One should keep in mind that when searching for the optimal parameters for extended (nocturnal) dialysis, especially in the homecare setting, extra boundary conditions play a role compared to a regular dialysis treatment (4 h in dialysis center). First, the quality of life is influenced by the patient's quality of sleep. Therefore avoiding the necessity of waking up during the night to change concentrate bags, by reducing the blood and dialysate flow rate, is preferable. This reduction in flow rates also reduces the costs of water, which is in home-dialysis mostly covered by the patients themselves. Since solute removal in low flow (175 instead of 350 ml/min) dialysis is comparable with that in regular daytime dialysis, low-flow dialysis is a worth considering alternative.

With a single lumen catheter, an increase in solute removal with 8 h dialysis (13-35%) was present compared to the regular 4 h dialysis. Finally, with

a single needle punctured in an AVE, solute removal even increases a few percentages compared to the results for the single lumen CVC dialysis. This last option was studied because in the homecare setting, patients often dialyze (relying on their arterio-venous fistula as preferable vascular access) without assistance and a single needle puncturing might be preferable. This because double needle puncturing is cumbersome and single needle puncturing increases safety, due to a decreased frequency of line disconnection. Thus, single needle/lumen hemodialysis seems to be the best option in the home setting, keeping a good balance between dialysis adequacy, practical use, quality of life, and financial burden.

Bibliography

- [1] E.N. Marieb and K. Hoehn. *Anatomy & Physiology*. Pearson Benjamin Cumming, third edition, 2008.
- [2] K. Van Canneyt and P. Verdonck. *Comprehensive Biomedical Physics, Physical Medicine and Rehabilitation: Principles and Applications*, chapter Mechanics of biofluids in living body, pages -. Elsevier inc., 2013.
- [3] D.E. Mohrman and L.J. Heller. *Cardiovascular physiology*. McGraw-Hill Professional, 2003.
- [4] S. Eloot and P. Verdonck. *Wiley Encyclopedia of Biomedical Engineering*, volume 6, chapter Modeling of transport phenomena in an artificial kidney, pages AK1–AK24. John Wiley & Sons, Inc., 2006.
- [5] A.S. Levey, K.-U. Eckardt, Y. Tsukamoto, A. Levin, J. Coresh, J. Rossert, D. De Zeeuw, T.H. Hostetter, N. Lameire, and G. Eknoyan. *Definition and classification of chronic kidney disease: a position statement from Kidney Disease: Improving Global Outcomes (KDIGO)*. *Kidney Int*, 67(6):2089–2100, 2005.
- [6] R.A. Hamer and A.M. El Nahas. *The burden of chronic kidney disease*. *BMJ*, 332(7541):563–564, 2006.
- [7] *NKF-K/DOQI Clinical guidelines for chronic kidney disease: Evaluation, classification, and stratification*. *Am J Kidney Dis*, 39(1 Suppl 1):S1–S266, 2002.
- [8] M.K. Peck, N. Dusserre, K. Zagalski, S.A. Garrido, W. Wystrychowski, M.H. Glickman, N.A.F. Chronos, L. Cierpka, N. L'heureux, and T.N. McAllister. *New biological solutions for hemodialysis access*. *J Vasc Access*, 12(3):185–192, 2011.

- [9] N. Lameire, K. Jager, W. Van Biesen, D. de Bacquer, and R. Vanholder. *Chronic kidney disease: A European perspective*. *Kidney Int*, S99:S30–S38, 2005.
- [10] A. Grassmann, S. Gioberge, S. Moeller, and G. Brown. *ESRD Patients in 2004: Global Overview of Patients Number, Treatment Modalities and Associated Trends*. *Nephrol Dial Transplant*, 20:2587–2593, 2005.
- [11] A. Grassmann, S. Gioberge, S. Moeller, and G. Brown. *End-stage renal disease: global demographics in 2005 and observed trends*. *Artif Organs*, 30(12):895–897, 2006.
- [12] *ERA-EDTA Registry Annual Report 2009*. Technical report, ERA-EDTA Registry, Academic Medical Center, Department of Medical Informatics, Amsterdam, The Netherlands, 2011.
- [13] *Eurotransplant International Foundation Annual Report 2010*. Technical report, Eurotransplant International Foundation, 2011.
- [14] *Organ Procurement and Transplantation Network (OPTN) and Scientific Registry of Transplant Recipients (SRTR) 2010 Annual Data Report*. Technical report, Department of Health and Human Services, Health Resources and Services Administration, Healthcare Systems Bureau, Division of Transplantation, Rockville, MD, US, 2011.
- [15] K.S. Rabindranath, J. Adams, T.Z. Ali, A.M. MacLeod, L. Vale, J. Cody, S.A. Wallace, and C. Daly. *Continuous ambulatory peritoneal dialysis versus automated peritoneal dialysis for end-stage renal disease*. *Cochrane Database Syst Rev*, (2):CD006515, 2007.
- [16] S. Eloot, W. Van Biesen, and R. Vanholder. *Does the higher number of dwells with APD result in better solute removal compared to CAPD*. *Int J Artif Organs*, 33(7):484, 2010.
- [17] *USRDS 2010 Annual Data Report: Atlas of Chronic Kidney Disease and End-Stage Renal Disease in the United States*. Technical report, National Institutes of Health, National Institute of Diabetes and Digestive and Kidney Diseases, 2010.
- [18] J. Feehally, J. Floege, and R.J. Jonson. *Comprehensive Clinical Nephrology*. Mosby Elsevier, 2007.
- [19] *NKF-K/DOQI Clinical Practice Guidelines for Vascular Access: update 2006*. *Am J Kidney Dis*, 48(1 Suppl 1):S177–S322, 2006.

- [20] J.J. Sands. *Vascular access: the past, present and future*. Blood Purif, 27(1):22–27, 2009.
- [21] M. Allon and M.L. Robbin. *Increasing arteriovenous fistulas in hemodialysis patients: problems and solutions*. Kidney Int, 62(4):1109–1124, 2002.
- [22] J. Tordoir, B. Canaud, P. Haage, K. Konner, A. Basci, D. Fouque, J. Kooman, A. Martin-Malo, L. Pedrini, F. Pizzarelli, J. Tattersall, M. Vennegoor, C. Wanner, P. ter Wee, and R. Vanholder. *EBPG on Vascular Access*. Nephrol Dial Transplant, 22 Suppl 2:ii88–ii117, 2007.
- [23] C.M. Kjellstrand. *The Achilles’ heel of the hemodialysis patient*. Arch Intern Med, 138(7):1063–1064, 1978.
- [24] A. Santoro, C. Canova, A. Freyrie, and E. Mancini. *Vascular access for hemodialysis*. J Nephrol, 19(3):259–264, 2006.
- [25] J.H.M. Tordoir and V. Mickley. *European Guidelines for Vascular Access: Clinical Algorithms on Vascular Access for Hemodialysis*. EDTNA ERCA J, 29:131–136, 2003.
- [26] J.H.M. Tordoir, P. Rooyens, R. Dammers, F.M. van der Sande, M. de Haan, and T.I. Yo. *Prospective evaluation of failure modes in autogenous radiocephalic wrist access for hemodialysis*. Nephrol Dial Transplant 2003; 18:, .18:378–383, 2003.
- [27] B.S. Dixon. *Why don’t fistulas mature?* Kidney Int, 70(8):1413–1422, 2006.
- [28] M.J. Brescia, J.E. Cimino, K. Appel, and B.F. Hurwich. *Chronic Hemodialysis Using Venipuncture and a Surgically Created Arteriovenous Shunt*. N Engl J Med, 275:1089–1092, 1966.
- [29] J.E. Cimino. *Historical Perspective on More Than 60 Years of Hemodialysis Access*. Semin Vasc Surg, 20:136–140, 2007.
- [30] M. Allon. *Current management of vascular access*. Clin J Am Soc Nephrol, 2(4):786–800, 2007.
- [31] W.D. Paulson, Ram. S.J., and G.B. Zibari. *Vascular Access: Anatomy, Examination, Managment*. Sem Nephrol, 22(3):183–194, 2002.

- [32] V. Wong, R. Ward, J. Taylor, S. Selvakumar, T. V. How, and A. Bakran. *Factors associated with early failure of arteriovenous fistulae for haemodialysis access*. Eur J Vasc Endovasc Surg, 12(2):207–213, 1996.
- [33] J. Tordoir. *Commentary. Factors associated with early failure of arteriovenous fistulae for haemodialysis access*. Eur J Vasc Endovasc Surg, 42 Suppl 1:S55–S56, 2011.
- [34] K. Van Canneyt, T. Pourchez, S. Eloit, C. Guilleme, A. Bonnet, P. Segers, and P. Verdonck. *Hemodynamic impact of anastomosis size and angle in side-to-end arteriovenous fistulae: a computer analysis*. J Vasc Access, 11(1):52–58, 2010.
- [35] R.N. Planken. *Hemodialysis vascular access imaging: Duplex ultrasound and contrast-enhanced magnetic resonance angiography*. PhD thesis, Universiteit Maastricht, 2007.
- [36] T.C. Hodges, M.F. Fillinger, R.M. Zwolak, D.B. Walsh, F. Bech, and J.L. Cronenwett. *Longitudinal comparison of dialysis access methods: risk factors for failure*. J Vasc Surg, 26(6):1009–1019, 1997.
- [37] A. Falk. *Maintenance and salvage of arteriovenous fistulas*. J Vasc Interv Radiol, 17(5):807–813, 2006.
- [38] K.M. Rigg. *Dialysis access: Current Practice*, chapter Complications of Vascular Access, pages 211–238. Imperial College Press, 2001.
- [39] S.E. Wilson. *Vascular Access Principles and Practice*, chapter Autologous Arteriovenous Fistulas: Direct Anastomosis for Hemodialysis Access, pages 82–100. Mosby, 2002.
- [40] A. Asif. *Vascular Access*, chapter How can we make fistulae mature?, pages 29–34. Edizioni Minerva Medica, Turin, 2009.
- [41] P. Roy-Chaudhury. *Vascular Access*, chapter Biological aspects of vascular access failure, pages 1–13. Edizioni Minerva Medica, Turin, 2009.
- [42] B. Ene-Iordache, L. Mosconi, L. Antiga, S. Bruno, A. Anghileri, G. Remuzzi, and A. Remuzzi. *Radial artery remodeling in response to shear stress increase within arteriovenous fistula for hemodialysis access*. Endothelium, 10(2):95–102, 2003.

-
- [43] R. Baer, S. McDonald, R. Wu, and M. Mantha. *Reversible advanced ischemic hand atrophy due to arteriovenous fistula steal*. *Kidney Int*, 73(10):1203–1204, 2008.
- [44] J.H. Tordoir, R. Dammers, and F.M. van der Sande. *Upper extremity ischemia and hemodialysis vascular access*. *Eur J Vasc Endovasc Surg*, 27(1):1–5, 2004.
- [45] M. De Haan. *Vascular Access*, chapter Endovascular Treatment of Angio-access induced upper extremity ischemia, pages 151–153. Edizioni Minerva Medica, Turin, 2009.
- [46] H. Schanzer, M. Schwartz, E. Harrington, and M. Haimov. *Treatment of ischemia due to "steal" by arteriovenous fistula with distal artery ligation and revascularization*. *J Vasc Surg*, 7(6):770–773, 1988.
- [47] R.C. Knox, S.S. Berman, J.D. Hughes, A.T. Gentile, and J.L. Mills. *Distal revascularization-interval ligation: a durable and effective treatment for ischemic steal syndrome after hemodialysis access*. *J Vasc Surg*, 36(2):250–5; discussion 256, 2002.
- [48] C. Sessa, A. De Lambert, E. Cochet, O. Pichot, P. Palacin, and J.L. Magne. *Vascular Access*, chapter Ischemia and drill procedure, pages 161–178. Edizioni Minerva Medica, Turin, 2009.
- [49] J. Zanow, U. Kruger, and H. Scholz. *Proximalization of the arterial inflow: a new technique to treat access-related ischemia*. *J Vasc Surg*, 43(6):1216–21; discussion 1221, 2006.
- [50] D.J. Minion, E. Moore, and E. Endean. *Revision using distal inflow: A novel approach to dialysis-associated steal syndrome*. *Ann Vasc Surg*, 19(5):625–628, 2005.
- [51] J. Zanow, K. Petzold, M. Petzold, U. Krueger, and H. Scholz. *Flow reduction in high-flow arteriovenous access using intraoperative flow monitoring*. *J Vasc Surg*, 44(6):1273–8, 2006.
- [52] P.N. Suding and S.E. Wilson. *Strategies for Management of Ischemic Steal Syndrome*. *Semin Vasc Surg*, 20:184–188, 2007.
- [53] M. Sheltinga and F. Van Hoek. *Vascular Access*, chapter Banding for high flow hemodialysis access, pages 141–150. Edizioni Minerva Medica, Turin, 2009.

- [54] J.G. White, A. Kim, L.G. Josephs, and J.O. Menzoian. *The Hemodynamics of Steal Syndrome and Its Treatment*. Ann Vasc Surg, 13(3):308–312, 1999.
- [55] V. Gambillara, G. Montorzi, C. Haziza-Pigeon, N. Stergiopulos, and P. Silacci. *Arterial wall response to ex vivo exposure to oscillatory shear stress*. J Vasc Res, 42(6):535–544, 2005.
- [56] Bogdan Ene-Iordache and Andrea Remuzzi. *Disturbed flow in radial-cephalic arteriovenous fistulae for haemodialysis: low and oscillating shear stress locates the sites of stenosis*. Nephrol Dial Transplant, 27(1):358–368, 2012.
- [57] S. Sivanesan, T. How, and A. Bakran. *Sites of Stenosis in AV Fistulae for Haemodialysis access*. Nephrol Dial Transplant, 14:118–120, 1999.
- [58] L. Matyas, I. Mogan, A. Ebner, M. Lazarides, M. Mantell, R. Manson, E. Chemla, S. Mitra, M. Nikam, A. Tavakoli, and P. Roy-Chaudhury. *Arteriovenous Anastomosis Creation using the Optiflow Anastomotic Connector*. J Vasc Access, 12(2):527–528, 2011.
- [59] B.H. Scribner, R. Buri, J.E. Caner, R. Hegstrom, and J.M. Burnell. *The treatment of chronic uremia by means of intermittent hemodialysis: a preliminary report*. Trans Am Soc Artif Intern Organs, 6:114–122, 1960.
- [60] I. Van Tricht, D. De Wachter, J. Tordoir, and P. Verdonck. *Comparison of the hemodynamics in 6mm and 4-7 mm hemodialysis grafts by means of CFD*. J Biomech, 39(2):226–236, 2006.
- [61] R. Dammers, R.N. Planken, K.P.M. Pouls, R.J. Van Det, H. Burger, F.M. Van Der Sande, and J.H.M. Tordoir. *Evaluation of 4-mm to 7-mm versus 6-mm prosthetic brachial-antecubital forearm loop access for hemodialysis: results of a randomized multicenter clinical trial*. J Vasc Surg, 37(1):143–148, 2003.
- [62] D.E. Finlay, D.G. Longley, M.C. Foshager, and J.G. Letourneau. *Duplex and color Doppler sonography of hemodialysis arteriovenous fistulas and grafts*. Radiographics, 13(5):983–989, 1993.
- [63] C.J. Chang, P.J. Ko, L.A. Hsu, Y.S. Ko, Y.L. Ko, C.F. Chen, C.C. Huang, T.S. Hsu, Y.S. Lee, and J.H.S. Pang. *Highly increased cell proliferation activity in the restenotic hemodialysis vascular access after percutaneous transluminal angioplasty: implication in prevention of restenosis*. Am J Kidney Dis, 43(1):74–84, 2004.

- [64] F.P. Christidou, V.I. Kalpakidis, K.D. Iatrou, I.A. Zervidis, G.I. Bamichas, L.C. Gionanlis, T.A. Natse, and K.J. Sombolos. *Per-cutaneous transluminal angioplasty (PTA) and venous stenting in hemodialysis patients with vascular access-related venous stenosis or occlusion*. Radiographiy, 12:127–133, 2006.
- [65] L. Soletti, Y. Hong, J. Guan, J.J. Stankus, M.S. El-Kurdi, W.R. Wagner, and D.A. Vorp. *A bilayered elastomeric scaffold for tissue engineering of small diameter vascular grafts*. Acta Biomater, 6(1):110–122, 2010.
- [66] O. Sakai, K. Kanda, H. Ishibashi-Ueda, K. Takamizawa, A. Ametani, H. Yaku, and Y. Nakayama. *Development of the wing-attached rod for acceleration of "Biotube" vascular grafts fabrication in vivo*. J Biomed Mater Res B Appl Biomater, 83(1):240–247, 2007.
- [67] M. Lei, J. P. Archie, and C. Kleinstreuer. *Computational design of a bypass graft that minimizes wall shear stress gradients in the region of the distal anastomosis*. J Vasc Surg, 25(4):637–646, 1997.
- [68] A.J. Sorom, Christopher B. Hughes, J.T. McCarthy, B.M. Jenson, M. Prieto, J.M. Panneton, S. Sterioff, M.D. Stegall, and S.L. Nyberg. *Prospective, randomized evaluation of a cuffed expanded polytetrafluoroethylene graft for hemodialysis vascular access*. Surgery, 132(2):135–140, 2002.
- [69] Y.-H. Liu, Y.-N. Hung, H.-C. Hsieh, and P.-J. Ko. *Impact of cuffed, expanded polytetrafluoroethylene dialysis grafts on graft outlet stenosis*. World J Surg, 30(12):2290–2294, 2006.
- [70] C.G. Caro, N.V. Watkins, and S.J. Sherwin. *Helical graft*. Patent. US 2007/0021707 A1, 2007.
- [71] S.J. Sherwin, O. Shah, D.J. Doorly, J. Peir  s, Y. Papaharilaou, N. Watkins, C.G. Caro, and C.L. Dumoulin. *The influence of out-of-plane geometry on the flow within a distal end-to-side anastomosis*. J Biomech Eng, 122(1):86–95, 2000.
- [72] Y. Papaharilaou, D. J. Doorly, and S. J. Sherwin. *The influence of out-of-plane geometry on pulsatile flow within a distal end-to-side anastomosis*. J Biomech, 35(9):1225–1239, 2002.
- [73] G. Coppola and C. Caro. *Arterial geometry, flow pattern, wall shear and mass transport: potential physiological significance*. J R Soc Interface, 6(35):519–528, 2009.

- [74] C.G. Caro, N.J. Cheshire, and N. Watkins. *Preliminary comparative study of small amplitude helical and conventional ePTFE arteriovenous shunts in pigs*. J R Soc Interface, 2(3):261–266, 2005.
- [75] F. Loth, P.F. Fischer, and H.S. Bassiouny. *Blood flow in end-to-side anastomoses*. Annu Rev Fluid Mech, 40:367–393, 2008.
- [76] H.J.T.A.M. Huijbregts, P.J. Blankestijn, C.G. Caro, N.J.W. Cheshire, M.T.C. Hoedt, R.P. Tutein Nolthenius, and F.L. Moll. *A helical PTFE arteriovenous access graft to swirl flow across the distal anastomosis: results of a preliminary clinical study*. Eur J Vasc Endovasc Surg, 33(4):472–475, 2007.
- [77] M. Glickman. *Vascular Access*, chapter New Advancements in prosthetic grafts for hemodialysis, pages 95–98. Edizioni Minerva Medica, 2009.
- [78] A. Krueger, U. and Huhle, K. Krysz, and H. Scholz. *Effect of tapered grafts on hemodynamics and flow rate in dialysis access grafts*. Artif Organs, 28(7):623–628, 2004.
- [79] S. Shaldon, L. Chiandussi, and B. Higgs. *Haemodialysis by percutaneous catheterization of the femoral artery and vein with regional heparinization*. Lancet, II:857–859, 1961.
- [80] L. Kamper and M. Hofer. *The Chest X-Ray: A Systematic Teaching Atlas*, chapter Foreign Bodies, pages 157–182. Georg Thieme Verlag, 2007.
- [81] K. Konner. *History of vascular access for haemodialysis*. Nephrol Dial Transplant, 20(12):2629–2635, 2005.
- [82] J. Erben, J. Kvasnicaka, J. Bastecky, and V. Vortel. *Experience with routine use of subclavian vein cannulation in haemodialysis*. Proc EDTA, 6:59–64, 1969.
- [83] F. Schillinger, D. Schillinger, R. Montagnac, and T. Milcent. *Post catheterisation vein stenosis in haemodialysis: comparative angiographic study of 50 subclavian and 50 internal jugular accesses*. Nephrol Dial Transplant, 6(10):722–724, 1991.
- [84] Z.J. Twardowski. *Advantages and limits of the jugular catheter approach*. Nephrol Dial Transplant, 10(12):2178–2182, 1995.

- [85] W. Develter, A. De Cubber, W. Van Biesen, R. Vanholder, and N. Lameire. *Survival and complications of indwelling venous catheters for permanent use in hemodialysis patients*. *Artif Organs*, 29(5):399–405, 2005.
- [86] R. Schindler. *Vascular Access*, chapter Catheter implantation and complications, pages 71–74. Edizioni Minerva Medica, Turin, 2009.
- [87] Rhode Island Vascular Institute (RIVI). <http://www.rivascularinstitute.com/images/da2.jpg>, 2012.
- [88] J.A. Akoh. *Dialysis access: Current Practice*, chapter Central venous catheters, pages 257–302. Imperial College Press, 2001.
- [89] M.G. Tal, A.J. Peixoto, S.T. Crowley, N. Denbow, D. Eliseo, and J. Pollak. *Comparison of side hole versus non side hole high flow hemodialysis catheters*. *Hemodial Int*, 10(1):63–67, 2006.
- [90] H.-D. Polaschegg and C. Shah. *Overspill of catheter locking solution: safety and efficacy aspects*. *ASAIO J*, 49(6):713–715, 2003.
- [91] M. Vorweg, E. Monaca, M. Doehn, and F. Wappler. *The 'heparin lock': cause for iatrogenic coagulopathy*. *Eur J Anaesthesiol*, 23(1):50–53, 2006.
- [92] M. Agharazii, I. Plamondon, M. Lebel, P. Douville, and S. Desmeules. *Estimation of heparin leak into the systemic circulation after central venous catheter heparin lock*. *Nephrol Dial Transplant*, 20(6):1238–1240, 2005.
- [93] S. Ruesch, B. Walder, and M.R. Tram  r. *Complications of central venous catheters: internal jugular versus subclavian access—a systematic review*. *Crit Care Med*, 30(2):454–460, 2002.
- [94] S.R. Ash. *Fluid mechanics and clinical success of central venous catheters for dialysis—answers to simple but persisting problems*. *Semin Dial*, 20(3):237–256, 2007.
- [95] H.L. Moore. *Side holes at the tip of chronic hemodialysis catheters are harmful*. *J Vasc Access*, 2(1):8–16, 2001.
- [96] F. Tesio, H. De Baz, G. Panarello, G. Calianno, P. Quaia, A. Raimondi, and D. Schinella. *Double catheterization of the internal jugular vein for hemodialysis: indications, techniques, and clinical results*. *Artif Organs*, 18(4):301–304, 1994.

- [97] B. Canaud, H. Leray-Moragues, V. Garrigues, and C. Mion. *Permanent twin catheter: a vascular access option of choice for haemodialysis in elderly patients*. Nephrol Dial Transplant, 13 Suppl 7:82–88, 1998.
- [98] G. Mareels, R. Kaminsky, S. Eloot, and P.R. Verdonck. *Particle image velocimetry-validated, computational fluid dynamics-based design to reduce shear stress and residence time in central venous hemodialysis catheters*. ASAIO J, 53(4):438–446, 2007.
- [99] M.G. Tal. *Comparison of recirculation percentage of the palindrome catheter and standard hemodialysis catheters in a swine model*. J Vasc Interv Radiol, 16(9):1237–1240, 2005.
- [100] R.A. Mankus, S.R. Ash, and J.M. Sutton. *Comparison of blood flow rates and hydraulic resistance between the Mahurkar catheter, the Tesio twin catheter, and the Ash Split Cath*. ASAIO J, 44(5):M532–M534, 1998.
- [101] S.R. Ash. *Advances in tunneled central venous catheters for dialysis: design and performance*. Semin Dial, 21(6):504–515, 2008.
- [102] H.E. Katzman, R.B. McLafferty, J.R. Ross, M.H. Glickman, E.K. Peden, and J.H. Lawson. *Initial experience and outcome of a new hemodialysis access device for catheter-dependent patients*. J Vasc Surg, 50(3):600–7, 607.e1, 2009.
- [103] R.L. Pisoni, E.W. Young, D.M. Dykstra, R.N. Greenwood, E. Hecking, B. Gillespie, R.A. Wolfe, D.A. Goodkin, and P.J. Held. *Vascular access use and outcomes: results from the DOPPS*. Kidney Int, 137:305–316, 2002.
- [104] National Vascular Access Improvement Initiative: Fistula First Breakthrough Initiative FFBI. <http://www.fistulafirst.org/>, 2012.
- [105] A.N. Sidawy, R. Gray, A. Besarab, M. Henry, E. Ascher, M. Silva Jr, A. Miller, L. Scher, S. Trerotola, R.T. Gregory, R.B. Rutherford, and K.C. Kent. *Recommended standards for reports dealing with arteriovenous hemodialysis accesses*. J Vasc Surg, 35(3):603–610, 2002.
- [106] H.J.T. Huijbregts, M.L. Bots, C.H.A. Wittens, Y.C. Schrama, F.L. Moll, P.J. Blankestijn, and C.I.M.I.N.O study group. *Hemodialysis arteriovenous fistula patency revisited: results of a prospective, multicenter initiative*. Clin J Am Soc Nephrol, 3(3):714–719, 2008.

- [107] M.J. Oliver, R.L. McCann, O.S. Indridason, D.W. Butterly, and S.J. Schwab. *Comparison of transposed brachiobasilic fistulas to upper arm grafts and brachiocephalic fistulas*. *Kidney Int*, 60(4):1532–1539, 2001.
- [108] K. McLaughlin, B. Jones, R. Mactier, and C. Porteus. *Long-term vascular access for hemodialysis using silicon dual-lumen catheters with guidewire replacement of catheters for technique salvage*. *Am J Kidney Dis*, 29(4):553–559, 1997.
- [109] J.L. Xue, D. Dahl, J. P. Ebben, and A.J. Collins. *The association of initial hemodialysis access type with mortality outcomes in elderly Medicare ESRD patients*. *Am J Kidney Dis*, 42(5):1013–1019, 2003.
- [110] S. Pastan, J.M. Soucie, and W.M. McClellan. *Vascular access and increased risk of death among hemodialysis patients*. *Kidney Int*, 62(2):620–626, 2002.
- [111] M. Allon, J. Daugirdas, T.A. Depner, T. Greene, D. Ornt, and S.J. Schwab. *Effect of change in vascular access on patient mortality in hemodialysis patients*. *Am J Kidney Dis*, 47(3):469–477, 2006.
- [112] H.C. Rayner, R.L. Pisoni, B.W. Gillespie, D.A. Goodkin, T. Akiba, T. Akizawa, A. Saito, E.W. Young, F.K. Port, Dialysis Outcomes , and Practice Patterns Study. *Creation, cannulation and survival of arteriovenous fistulae: data from the Dialysis Outcomes and Practice Patterns Study*. *Kidney Int*, 63(1):323–330, 2003.
- [113] R.L. Anel, A.S. Yevzlin, and P. Ivanovich. *Vascular access and patient outcomes in hemodialysis: questions answered in recent literature*. *Artif Organs*, 27(3):237–241, 2003.
- [114] A. Bode, A. Caroli, W. Huberts, N. Planken, L. Antiga, M. Bosboom, A. Remuzzi, J. Tordoir, and ARCH project consortium . *Clinical study protocol for the ARCH project - computational modeling for improvement of outcome after vascular access creation*. *J Vasc Access*, 12(4):369–376, 2011.
- [115] W. Huberts. *Personalized computational modeling of vascular access creation*. PhD thesis, Universiteit Maastricht, 2012.
- [116] A.C. Guyton. *Textbook of Medical Physiology*. Saunders, Philadelphia, 2nd edition, 1961.

- [117] L.F. Mockros and R. Leonard. *Compact cross-flow tubular oxygenators*. Trans Am Soc Artif Intern Organs, 31:628–33, 1985.
- [118] D. Quemada. *A rheological model for studying the hematocrit dependence of red cell-red cell and red cell-protein interactions in blood*. Biorheology, 18(3-6):501–516, 1981.
- [119] G. Cockett. *Handbook of Bioengineering*, chapter The rheology and tube flow of blood, pages 14.11–14.17. McGraw-Hill Book Company, 1986.
- [120] R. Berguer and N.H.C. Hwang. *Critical Arterial Stenosis: A Theoretical and Experimental Solution*. Ann. Surg., 180:39–50, 1974.
- [121] L. Antiga and D.A. Steinman. *Rethinking turbulence in blood*. Biorheology, 46(2):77–81, 2009.
- [122] A.M. Malek, S.L. Alper, and S. Izumo. *Hemodynamic shear stress and its role in atherosclerosis*. JAMA, 282(21):2035–2042, 1999.
- [123] D.N. Ku, D.P. Giddens, C.K. Zarins, and S. Glagov. *Pulsatile flow and atherosclerosis in the human carotid bifurcation. Positive correlation between plaque location and low oscillating shear stress*. Arteriosclerosis, 5(3):293–302, 1985.
- [124] H.A. Himburg, D.M. Grzybowski, A.L. Hazel, J.A. LaMack, X.M. Li, and M.H. Friedman. *Spatial comparison between wall shear stress measures and porcine arterial endothelial permeability*. Am J Physiol Heart Circ Physiol, 286(5):H1916–H1922, 2004.
- [125] S.-W. Lee, L. Antiga, and D.A. Steinman. *Correlations among indicators of disturbed flow at the normal carotid bifurcation*. J Biomech Eng, 131(6):061013, 2009.
- [126] A. Belian, O. Chkhetiani, E. Golbraikh, and S. Moiseev. *Helical turbulence: turbulent viscosity and instability of the second moments*. Physica A, 258(1-2):55–68, 1998.
- [127] M. Grigioni, C. Daniele, U. Morbiducci, C. Del Gaudio, G. D’Avenio, A. Balducci, and V. Barbaro. *Proposal for a quantitative description of blood spiral flow in medical devices*. Int J Artif Organs, 27(3):231–242, 2004.

-
- [128] M. Grigioni, C. Daniele, U. Morbiducci, C. Del Gaudio, G. D'Avenio, A. Balducci, and V. Barbaro. *A mathematical description of blood spiral flow in vessels: application to a numerical study of flow in arterial bending*. J Biomech, 38(7):1375–1386, 2005.
- [129] R. Kaminsky. *Particle Image Velocimetry Analysis of the Blood Flow in Cardiovascular Devices*. PhD thesis, Ghent University, 2007.
- [130] I. Khodarahmi, M. Shakeri, M. Sharp, and A.A. Amini. *Using PIV to determine relative pressures in a stenotic phantom under steady flow based on the pressure-poisson equation*. Conf Proc IEEE Eng Med Biol Soc, 2010:2594–2597, 2010.
- [131] Y. Hoi, S.H. Woodward, M. Kim, D.B. Taulbee, and H. Meng. *Validation of CFD simulations of cerebral aneurysms with implication of geometric variations*. J Biomech Eng, 128(6):844–851, 2006.
- [132] S.W. Day and J.C. McDaniel. *PIV measurements of flow in a centrifugal blood pump: time-varying flow*. J Biomech Eng, 127(2):254–263, 2005.
- [133] S.W. Day and J.C. McDaniel. *PIV measurements of flow in a centrifugal blood pump: steady flow*. J Biomech Eng, 127(2):244–253, 2005.
- [134] R.B. Medvitz, V. Reddy, S. Deutsch, K.B. Manning, and E.G. Patterson. *Validation of a CFD methodology for positive displacement LVAD analysis using PIV data*. J Biomech Eng, 131(11):111009, 2009.
- [135] G.A. Giridharan, C. Lederer, A. Berthe, L. Goubergrits, J. Hutzenlaub, M.S. Slaughter, R.D. Dowling, P.A. Spence, and S.C. Koenig. *Flow dynamics of a novel counterpulsation device characterized by CFD and PIV modeling*. Med Eng Phys, 33(10):1193–1202, 2011.
- [136] J. Charonko, S. Karri, J. Schmieg, S. Prabhu, and P. Vlachos. *In vitro, time-resolved PIV comparison of the effect of stent design on wall shear stress*. Ann Biomed Eng, 37(7):1310–1321, 2009.
- [137] R. Kaminsky, K. Dumont, H. Weber, M. Schroll, and P. Verdonck. *PIV validation of blood-heart valve leaflet interaction modelling*. Int J Artif Organs, 30(7):640–648, 2007.
- [138] R. Kaminsky, U. Morbiducci, M. Rossi, L. Scalise, P. Verdonck, and M. Grigioni. *Time-resolved PIV technique for high temporal resolution measurement of mechanical prosthetic aortic valve fluid dynamics*. Int J Artif Organs, 30(2):153–162, 2007.

- [139] K.B. Manning, V. Kini, A.A. Fontaine, S. Deutsch, and J.M. Tarbell. *Regurgitant flow field characteristics of the St. Jude bileaflet mechanical heart valve under physiologic pulsatile flow using particle image velocimetry*. *Artif Organs*, 27(9):840–846, 2003.
- [140] M.D. Ford, H.N. Nikolov, J.S. Milner, S.P. Lownie, E.M. Demont, W. Kalata, F. Loth, D.W. Holdsworth, and D.A. Steinman. *PIV-measured versus CFD-predicted flow dynamics in anatomically realistic cerebral aneurysm models*. *J Biomech Eng*, 130(2):021015, 2008.
- [141] S.C.P. Cheung, K.K.L. Wong, G.H. Yeoh, W. Yang, R. Tu, J. and Beare, and T. Phan. *Experimental and numerical study on the hemodynamics of stenosed carotid bifurcation*. *Australas Phys Eng Sci Med*, 33(4):319–328, 2010.
- [142] K. Stanislas, K. Okamoto, C.J. Kahler, J. Westerweel, and F. Scarano. *Main Results of the Third International Challenge*. *Exp. Fluids*, 45:27–71, 2008.
- [143] P. Hariharan, M. Giarra, V. Reddy, S.W. Day, K.B. Manning, S. Deutsch, S.F.C. Stewart, M.R. Myers, M.R. Berman, G.W. Burgreen, E.G. Paterson, and R.A. Malinauskas. *Multilaboratory particle image velocimetry analysis of the FDA benchmark nozzle model to support validation of computational fluid dynamics simulations*. *J Biomech Eng*, 133(4):041002, 2011.
- [144] S. Stiller, X. Q. Xu, N. Gruner, J. Vienken, and H. Mann. *Validation of a two-pool model for the kinetics of beta2-microglobulin*. *Int J Artif Organs*, 25(5):411–420, 2002.
- [145] E.M. Spalding, P.W. Chamney, and K. Farrington. *Phosphate kinetics during hemodialysis: Evidence for biphasic regulation*. *Kidney Int*, 61(2):655–667, 2002.
- [146] S. Eloot, A. Torremans, R. De Smet, B. Marescau, D. De Wachter, P.P. De Deyn, N. Lameire, P. Verdonck, and R. Vanholder. *Kinetic behavior of urea is different from that of other water-soluble compounds: the case of the guanidino compounds*. *Kidney Int*, 67(4):1566–1575, 2005.
- [147] U. Krueger, J. Zanolow, and H. Scholz. *Computational Fluid Mechanics and Vascular Access*. *Art Org*, 26(7):571–575, 2002.

- [148] Z. Kharboutly, M. Fenech, J.M. Treutenaere, I. Claude, and C. Legal-lais. *Investigations into the relationship between hemodynamics and vascular alterations in an established arteriovenous fistula*. Med Eng Phys, 29:999–1007, 2007.
- [149] S. Sivanesan, T.V. How, R.A. Black, and A. Bakran. *Flow patterns in the radiocephalic arteriovenous fistula: an in vitro study*. J Biomech, 32:915–925, 1999.
- [150] J.R. Welty, C.E. Wicks, S.E. Wilson, and G. Rorrer. *Fundamentals of Momentum, Heat and Mass Transfer*. John Wiley & Sons Inc., New York, 4th edition, 2001.
- [151] A.E. Hendriksson and D. Bergqvist. *Steal syndrome of the hemodialysis vascular access: Diagnosis and treatment*. J Vasc Access, 5:62–68, 2004.
- [152] P. Bachleda, P. Utikal, Z. Kojecy, P. Drac, M. Káčáňcher, M. Cerna, and J. Zadrazil. *Autogenous Arteriovenous Elbow Fistula For Haemodialysis and Upper Extremity Ischemia*. Biomed Pap Med Fac Univ Palacky Olomouc Czech Repub, 151(1):129–132, 2007.
- [153] R.W. Barnes. *Hemodynamics for the Vascular Surgeon*. Arch Surg, 115:216–223, 1980.
- [154] C.L. Wixon, J.D. Hughes, and J.L. Mills. *Understanding Strategies for the Treatment of Ischemic Steal Syndrome after Hemodialysis Access*. J Am Coll Surg, 191(3):301–310, 2000.
- [155] C.B. Anderson, E.E. Etheredge, H.R. Harter, R.J. Graff, J.E. Codd, and W.T. Newton. *Local Blood Flow Characteristics of Arteriovenous Fistulas in the Forearm for Dialysis*. Surg Gynec Obst, 144(4):531–533, 1977.
- [156] Y. Pousset, P. Lermusiaux, G. Berton, J. Le Gouez, and R. Leroy. *Flow dynamics through end-to-side anastomosis*. Ann Vasc Surg, 20(6):774–779, 2006.
- [157] L.P. Chua, W. Ji, and T. Zhou. *In vitro study on the steady flow characteristics of proximal anastomotic models*. Int Commun Heat Mass, 32:464–472, 2005.

- [158] N.H. Staalsen, M. Ulrich, J. Winther, E.M. Pederson, T. How, and H. Nygaard. *The anastomosis angle does change the flow fields at vascular end-to-side anastomoses in vivo*. J Vasc Surg, 21(3):460–471, 1995.
- [159] C. Leon and A. Asif. *Arteriovenous access and hand pain: the distal hypoperfusion ischemic syndrome*. Clin J Am Soc Nephrol, 2(1):175–83, 2007.
- [160] J. Malik, V. Tuka, Z. Kasalova, E. Chytilova, M. Slavikova, P. Clagett, I. Davidson, B. Dolmatch, D. Nichols, and M. Gallieni. *Understanding the dialysis access steal syndrome. A review of the etiologies, diagnosis, prevention and treatment strategies*. J Vasc Access, 9(3):155–66, 2008.
- [161] H. Schanzer and D. Eisenberg. *Management of steal syndrome resulting from dialysis access*. Semin Vasc Surg, 17(1):45–9, 2004.
- [162] K. Konner. *A primer on the AV fistula - Achilles' heel, but also Cinderella of haemodialysis*. Nephrol Dial Transplant, 14(9):2094–2098, 1999.
- [163] R. Dammers. *Non-invasive Assessment of Arterial Remodeling in Arteriovenous Fistulas for Hemodialysis*. PhD thesis, University of Maastricht, The Netherlands, 2003.
- [164] E. Wijnen, X.H.A. Keuter, R.N. Planken, F.M. van der Sande, Tordoir J.H.M., K.M. Leunissen, and J.P. Kooman. *The relation between vascular access flow and different types of vascular access with systemic hemodynamics in hemodialysis patients*. Artificial Organs, 29(12):960–964, 2005.
- [165] M.L. Robbin, N.E. Chamberlain, M.E. Lockhart, M.H. Gallichio, C.J. Young, M.H. Deierhoi, and M. Allon. *Hemodialysis arteriovenous fistula maturity: US evaluation*. Radiology, 225:59–64, 2002.
- [166] A. Bakran, V. Mickley, and J. Passlick-Deetjen, editors. *Management of the Renal Patient: Clinical Algorithms on Vascular Access for Haemodialysis*. Pabst Science Publishers, D-49525 Lengerich, Deutschland, 2003. ISBN 978-3-936142-86-0.
- [167] D. Shemesh, I. Goldin, D. Berelowitz, I. Zaghal, C. Zigelman, and O. Olsha. *Blood Flow Volume Changes in the Maturing Arteriovenous Fistula for Hemodialysis*. Ultrasound in Med Biol, 33(5):727–733, 2007.

- [168] W. Huberts, A.S. Bode, W. Kroon, R.N. Planken, J.H.M. Tordoir, F.N. van de Vosse, and E.M.H. Bosboom. *A pulse wave propagation model to support decision-making in vascular access planning in the clinic*. Med Eng Phys, 34(2):233–248, 2012.
- [169] P. Reymond, Y. Bohraus, F. Perren, F. Lazeyras, and N. Stergiopulos. *Validation of a patient-specific one-dimensional model of the systemic arterial tree*. Am J Physiol Heart Circ Physiol, 301(3):H1173–H1182, 2011.
- [170] K.S. Matthys, J. Alastrueya, J. Peiro, A.W. Khir, P. Segers, P.R. Verdonck, K.M. Parker, and S.J. Sherwin. *Pulse wave propagation in a model human arterial network: Assessment of 1-D numerical simulations against in vitro measurements*. Journal of Biomechanics, 40:3476–3486, 2007.
- [171] P. Reymond, F. Merenda, F. Perren, D. Rüfenacht, and N. Stergiopulos. *Validation of a one-dimensional model of the systemic arterial tree*. Am J Physiol Heart Circ Physiol, 297:208–222, 2009.
- [172] D. Bessems, C.G. Giannopapa, M.C.M. Rutten, and van de Vosse F.N. *Experimental Validation of a Time-domain-based Wave Propagation Model of Blood Flow in Viscoelastic Vessels*. J Biomech, 41:284–91, 2008.
- [173] A. Swillens, L. Lanoye, J. De Backer, N. Stergiopulos, P.R. Verdonck, F. Vermassen, and S. Segers. *Effect of an Abdominal Aortic Aneurysm on Wave Reflection in the Aorta*. IEEE Transactions on biomedical engineering, 55(5):1602–1611, 2008.
- [174] D. Xiu and S.J. Sherwin. *Parametric uncertainty analysis of pulse wave propagation in a model of a human arterial network*. J Comp Phys, 226:1385–1407, 2007.
- [175] C.P. Robert and G.C. Casella. *Monte Carlo statistical methods*. Springer, New York, 2000.
- [176] K. Van Canneyt, R.N. Planken, S. Eloot, P. Segers, and P. Verdonck. *Experimental study of a new method for early detection of vascular access stenoses: pulse pressure analysis at hemodialysis needle*. Artif Organs, 34(2):113–117, 2010.

- [177] M. in 't Veer, M.C.F. Geven, M.C.M. Rutten, A. van der Horst, W.H. Aarnoudse, N.H.J. Pijls, and F.N. van de Vosse. *Continuous infusion thermodilution for assessment of coronary flow: theoretical background and in vitro validation*. Med Eng Phys, 31(6):688–694, 2009.
- [178] B.W.A.M.M. Beulen, N. Bijmens, G.G. Koutsouridis, P.J. Brands, M.C.M. Rutten, and F.N. van de Vosse. *Toward noninvasive blood pressure assessment in arteries by using ultrasound*. Ultrasound in Med Biol, 37(5):788–797, 2011.
- [179] A.C. Guyton and J.E. Hall. *Textbook of medical physiology*. W.B. Saunders Company, 1996.
- [180] A. Gardel. *Pressure Drops in Flows Through T-shaped Fittings*. Bulletin Technique de la Suisse Romande, 9:123–130, 1957.
- [181] A. Gardel. *Pressure Drops Through T-shaped Fittings*. Bulletin Technique De La Suisse Romande, 10:143–148, 1957.
- [182] N. Westerhof, G. Elzinga, and P. Sipkema. *An Artificial Arterial System for Pumping Hearts*. J Appl Phys, 31(5):776–781, 1971.
- [183] N. Stergiopoulos, J.J. Meister, and N. Westerhof. *Evaluation of Methods for Estimation of Total Arterial Compliance*. Am J Physiol, 268:H1540–H1548, 1995.
- [184] M.D. McKay, R.J. Beckman, and W.J. Conover. *A comparison of three methods for selecting values of input variables in the analysis of output from a computer code*. Technometrics, 21:239–245, 1979.
- [185] W. Huberts, C. de Jonge, W.P.M. van der Linden, M.A. Inda, J.H.M. Tordoir, F.N. van de Vosse, and E.M.H. Bosboom. *A sensitivity analysis to improve the measurement protocol to assess parameters for a personalized wave propagation model: application to AVF surgery*. Submitted to Med Eng Phys, 2011.
- [186] J. Alastruey, A.W. Khir, K.S. Matthys, P. Segers, S.J. Sherwin, P.R. Verdonck, K.H. Parker, and J. Peiró. *Pulse wave propagation in a model human arterial network: Assessment of 1-D visco-elastic simulations against in vitro measurements*. J Biomech, 44:2250–2258, 2011.
- [187] D.E. Strandness and D.S. Sumner. *Hemodynamics for surgeons*. Grune and Stratton, New York, 1975.

- [188] W.W. Nichols and M.F. O'Rourke. *McDonalds's blood flow in arteries : theoretical, experimental and clinical principles*. Edward Arnold, London, 1998.
- [189] R. Raghu, I. E. Vignon-Clementel, C. A. Figueroa, and C.A. Taylor. *Comparative study of viscoelastic arterial wall models in nonlinear one-dimensional finite element simulations of blood flow*. J Biomech Eng, 133(8):081003, 2011.
- [190] B.N. Steele, D. Valdez-Jasso, M.A. Haider, and M.S. Olufsen. *Predicting arterial flow and pressure dynamics using a 1D fluid dynamics model with a viscoelastic wall*. Siam J Appl Math, 71 (4):1123–1143, 2011.
- [191] B. Learoyd and M. Taylor. *Alterations with age in the viscoelastic properties of human arterial walls*. Clinical Research, 18:278–292, 1966.
- [192] T. Imura, K. Yamamoto, T. Satoh, K. Kanamori, T. Mikami, and H. Yasuda. *In vivo viscoelastic behavior in the human aorta*. Circulation Research, 66:1413–1419, 1990.
- [193] L. Botti and D.A. Di Pietro. *A pressure-correction scheme for convection-dominated incompressible flows with discontinuous velocity and continuous pressure*. J. Comput. Phys., 230:572–585, 2011.
- [194] Z. Kharboutly, V. Deplano, E. Bertrand, and C. Legallais. *Numerical and experimental study of blood flow through a patient-specific arteriovenous fistula used for hemodialysis*. Med Eng Phys, 32(2):111–118, 2010.
- [195] F. Loth, P.F. Fischer, N. Arslan, C.D. Bertram, S.E. Lee, T.J. Royston, W.E. Shaalan, and H.S. Bassiouny. *Transitional flow at the venous anastomosis of an arteriovenous graft: potential activation of the ERK1/2 mechanotransduction pathway*. Journal of biomechanical engineering, 125(1), 2003.
- [196] L. Antiga, M. Piccinelli, L. Botti, B. Ene-Iordache, A. Remuzzi, and D.A. Steinman. *An image-based modeling framework for patient-specific computational hemodynamics*. Medical and Biological Engineering and Computing, 46(11):1097–1112, 2008.
- [197] A.H. Morsy, M. Kulbaski, C. Chen, H. Isiklar, and A.B. Lumsden. *Incidence and characteristics of patients with hand ischemia after a hemodialysis access procedure*. J Surg Res, 74(1):8–10, 1998.

- [198] A. Asif, C. Leon, D. Merrill, B. Bhimani, R. Ellis, M. Ladino, and F.N. Gadalean. *Arterial steal syndrome: a modest proposal for an old paradigm*. Am J Kidney Dis, 48(1):88–97, 2006.
- [199] NKF-K/DOQI clinical practice guidelines for vascular access. National Kidney Foundation-Dialysis Outcomes Quality Initiative. Am J Kidney Dis, 30(4 Suppl 3):S150–S191, 1997.
- [200] D. Bouchouareb, A. Saveanu, J.M. Bartoli, and M. Olmer. *A new approach to evaluate vascular access in hemodialysis patients*. Artif Organs, 22(7):591–5, 1998.
- [201] G.J. Murphy, S.A. White, and M.L. Nicholson. *Vascular access for haemodialysis*. Brit J Surg, 87(10):1300–15, 2000.
- [202] A. Besarab, S. Frinak, R.A. Sherman, J. Goldman, F. Dumbler, M.V. Devita, T. Kapoian, F. Al-Saghir, and T. Lubkowski. *Simplified Measurement of Intra-Access Pressure*. J Am Soc Nephrol, 9(2):284–289, 1998.
- [203] A. Besarab. *Access Monitoring Methods*. Blood Purif, 18:255–259, 2000.
- [204] A. Asif, F.N. Gadalean, D. Merrill, G. Cherla, C.D. Cipleu, D.L. Epstein, and D. Roth. *Inflow stenosis in arteriovenous fistulas and grafts: a multicenter, prospective study*. Kidney Int, 67(5):1986–92, 2005.
- [205] A. Besarab, A. Asif, P. Roy-Chaudhury, L.M. Spergel, and P. Ravani. *The Native Arteriovenous Fistula in 2007, Surveillance and Monitoring*. J Nephrol, 20:656–667, 2007.
- [206] M. Tonelli, M. James, N. Wiebe, K. Jindal, and B. Hemmelgarn. *Ultra-sound Monitoring to Detect Access Stenosis in Hemodialysis Patients: A Systemic Review*. Am J Kidney Dis, 51(4):630–640, 2008.
- [207] W.D. Paulson, S.J. Ram, C.G. Birk, and J. Work. *Does blood flow accurately predict thrombosis or failure of hemodialysis synthetic grafts? A meta-analysis*. Am J Kidney Dis, 34(3):478–85, 1999.
- [208] S.J. Schwab, J.R. Raymond, M. Saeed, G.E. Newman, P.A. Dennis, and R.R. Bollinger. *Prevention of hemodialysis fistula thrombosis. Early detection of venous stenoses*. Kidney Int, 36(4):707–711, 1989.

- [209] N. Stergiopoulos, D.F. Young, and T.R. Rogge. *Computer simulation of arterial flow with applications to arterial and aortic stenoses*. J Biomech, 25(12):1477–88, 1992.
- [210] C.J. Konings, R. Dammers, P.L. Rensma, J.P. Kooman, A.P. Hoeks, L. Kornet, U. Gladziwa, F.M. van der Sande, and K.M. Leunissen. *Arterial wall properties in patients with renal failure*. Am J Kidney Dis, 39(6):1206–12, 2002.
- [211] H.-D. Polaschegg. *Verfahren und Vorrichtung zur Erkennung von Stenoses bei der extrakorporalen Blutbehandlung*. Patent. EP 1 829 570 A1, 2000.
- [212] H.-D. Polaschegg. *Method and device for the detection of stenosis in extra-corporeal blood treatment*. Patent. US 6,623,443 B1, 2003.
- [213] T. Yzet, R. Bouzerar, J.D. Allart, F. Demuynck, C. Legallais, B. Robert, H. Deramond, M.E. Meyer, and O. Baledent. *Hepatic Vascular Flow Measurements by Phase Contrast MRI and Doppler Echography: A Comparative and Reproducibility Study*. Journal of Magnetic Resonance Imaging, 31(3):579–588, 2010.
- [214] P.R. Hoskins. *Accuracy of maximum velocity estimates made using Doppler ultrasound systems*. British Journal of Radiology, 69(818):172–177, 1996.
- [215] R. Steel, K.V. Ramnarine, A. Criton, F. Davidson, P.L. Allan, N. Humphries, H.F. Routh, P.J. Fish, and P.R. Hoskins. *Angle-dependence and reproducibility of dual-beam vector Doppler ultrasound in the common carotid arteries of normal volunteers*. Ultrasound in Medicine and Biology, 30(2):271–276, 2004.
- [216] A. Denys and Y. Menu. *Portal and splanchnic blood flow measurements in vivo: US Doppler or MR angiography?* Journal of Hepatology, 26(2):437–438, 1997.
- [217] G.J.L.A. Nijeholt, K. Burggraaf, M.N.J.M. Wasser, L.J.S. Kool, R.C. Schoemaker, A.F. Cohen, and A. deRoos. *Variability of splanchnic blood flow measurements using MR velocity mapping under fasting and post-prandial conditions - Comparison with echo-Doppler*. Journal of Hepatology, 26(2):298–304, 1997.

- [218] A. Swillens, T. De Schryver, L. Lovstakken, H. Torp, and P. Segers. *Assessment of Numerical Simulation Strategies for Ultrasonic Color Blood Flow Imaging, Based on a Computer and Experimental Model of the Carotid Artery*. Annals of Biomedical Engineering, 37(11):2188–2199, 2009.
- [219] A. Swillens, L. Lovstakken, J. Kips, H. Torp, and P. Segers. *Ultrasound Simulation of Complex Flow Velocity Fields Based on Computational Fluid Dynamics*. Ieee Transactions on Ultrasonics Ferroelectrics and Frequency Control, 56(3):546–556, 2009.
- [220] G. De Santis, M. De Beule, P. Segers, P. Verdonck, and B. Verheghe. *Patient-specific computational haemodynamics: generation of structured and conformal hexahedral meshes from triangulated surfaces of vascular bifurcations*. Computer Methods in Biomechanics and Biomedical Engineering, 14(9):797–802, 2011.
- [221] G. De Santis, M. De Beule, K. Van Canneyt, P. Segers, P. Verdonck, and B. Verheghe. *Full-hexahedral structured meshing for image-based computational vascular modeling*. Med Eng Phys, 33(10):1318–1325, 2011.
- [222] J.A. Jensen. *FIELD: a program for simulating ultrasound systems*. Medical & biological engineering & computing, 34:351–352, 1996.
- [223] J.A. Jensen and N.B. Svendsen. *Calculation of Pressure Fields from Arbitrarily Shaped, Apodized, and Excited Ultrasound Transducers*. Ieee Transactions on Ultrasonics Ferroelectrics and Frequency Control, 39(2):262–267, 1992.
- [224] G.E. Tupholme. *Generation of Acoustic Pulses by Baffled Plane Pistons*. Mathematika, 16(32P2):209–&, 1969.
- [225] P.R. Stepanishen. *Transient Radiation from Pistons in an Infinite Planar Baffle*. Journal of the Acoustical Society of America, 49(5):1629–&, 1971.
- [226] D.H. Evans and W.N. McDicken. *Doppler Ultrasound: Physics, Instrumentation and Signal processing*. John Wiley & Sons Ltd., West Sussex, UK, second edition, 2000.
- [227] M. Napoli. *Echo color Doppler & Vascular accessess for hemodialysis*. Wichtig Editore Srl, Milano, Italy, 2011.

- [228] A.P. Hoeks, M. Hennerici, and R.S. Reneman. *Spectral composition of Doppler signals*. Ultrasound in medicine & biology, 17(8):751–60, 1991.
- [229] C.A. Leguy, E.M. Bosboom, A.P. Hoeks, and F.N. van de Vosse. *Assessment of blood volume flow in slightly curved arteries from a single velocity profile*. Journal of biomechanics, 42(11):1664–72, 2009.
- [230] C.A. Leguy, E.M. Bosboom, A.P. Hoeks, and F.N. van de Vosse. *Model-based assessment of dynamic arterial blood volume flow from ultrasound measurements*. Medical & biological engineering & computing, 47(6):641–8, 2009.
- [231] L.A. Ledoux, P.J. Brands, and A.P. Hoeks. *Reduction of the clutter component in Doppler ultrasound signals based on singular value decomposition: a simulation study*. Ultrasonic imaging, 19(1):1–18, 1997.
- [232] A. Swillens, J. Degroote, J. Vierendeels, L. Lovstakken, and P. Segers. *A simulation environment for validating ultrasonic blood flow and vessel wall imaging based on fluid-structure interaction simulations: ultrasonic assessment of arterial distension and wall shear rate*. Medical physics, 37(8):4318–30, 2010.
- [233] B. Beulen, N. Bijmens, M. Rutten, P. Brands, and F. van de Vosse. *Perpendicular ultrasound velocity measurement by 2D cross correlation of RF data. Part A: validation in a straight tube*. Experiments in Fluids, 49(5):1177–1186, 2010.
- [234] B. Beulen, A. C. Verkaik, N. Bijmens, M. Rutten, and F. van de Vosse. *Perpendicular ultrasound velocity measurement by 2D cross correlation of RF data. Part B: volume flow estimation in curved vessels*. Experiments in Fluids, 49(6):1219–1229, 2010.
- [235] L.N. Bohs, B.H. Friemel, B.A. Mcdermott, and G.E. Trahey. *A Real-Time System for Quantifying and Displaying 2-Dimensional Velocities Using Ultrasound*. Ultrasound in Medicine and Biology, 19(9):751–761, 1993.
- [236] B. Dunmire, K.W. Beach, K.H. Labs, M. Plett, and D.E. Strandness. *Cross-beam vector Doppler ultrasound for angle-independent velocity measurements*. Ultrasound in Medicine and Biology, 26(8):1213–1235, 2000.

- [237] M.D. Fox. *Multiple Crossed-Beam Ultrasound Doppler Velocimetry*. Ieee Transactions on Sonics and Ultrasonics, 25(5):281–286, 1978.
- [238] H.B. Kim, J.R. Hertzberg, and R. Shandas. *Development and validation of echo PIV*. Experiments in Fluids, 36(3):455–462, 2004.
- [239] M.M. Pedersen, M.J. Pihl, P. Haugaard, J.M. Hansen, K.L. Hansen, M.B. Nielsen, and J.A. Jensen. *Comparison of Real-Time in Vivo Spectral and Vector Velocity Estimation*. Ultrasound in Medicine and Biology, 38(1):145–151, 2012.
- [240] A. Swillens, P. Segers, and L. Lovstakken. *Two-Dimensional Flow Imaging in the Carotid Bifurcation Using a Combined Speckle Tracking and Phase-Shift Estimator: A Study Based on Ultrasound Simulations and in Vivo Analysis*. Ultrasound in Medicine and Biology, 36(10):1722–1735, 2010.
- [241] A. Swillens, P. Segers, H. Torp, and L. Lovstakken. *Two-Dimensional Blood Velocity Estimation With Ultrasound: Speckle Tracking Versus Crossed-Beam Vector Doppler Based on Flow Simulations in a Carotid Bifurcation Model*. Ieee Transactions on Ultrasonics Ferroelectrics and Frequency Control, 57(2):327–339, 2010.
- [242] G.E. Trahey, J.W. Allison, and O.T. Vonramm. *Angle Independent Ultrasonic-Detection of Blood-Flow*. Ieee Transactions on Biomedical Engineering, 34(12):965–967, 1987.
- [243] J. Udesen, M.B. Nielsen, K.R. Nielsen, and J.A. Jensen. *Examples of in vivo blood vector velocity estimation*. Ultrasound in Medicine and Biology, 33(4):541–548, 2007.
- [244] P. Tortoli, F. Andreuccetti, G. Manes, and C. Atzeni. *Blood-Flow Images by a Saw-Based Multigate Doppler System*. Ieee Transactions on Ultrasonics Ferroelectrics and Frequency Control, 35(5):545–551, 1988.
- [245] E.C. Scott and M.H. Glickman. *Conduits for hemodialysis access*. Semin Vasc Surg, 20(3):158–163, 2007.
- [246] P. Roy-Chaudhury, V.P. Sukhatme, and A.K. Cheung. *Hemodialysis vascular access dysfunction: a cellular and molecular viewpoint*. J Am Soc Nephrol, 17(4):1112–1127, 2006.

- [247] S.E. Rittgers, P.E. Karayannacos, J.F. Guy, R.M. Nerem, G.M. Shaw, J.R. Hostetler, and J.S. Vasko. *Velocity distribution and intimal proliferation in autologous vein grafts in dogs*. *Circ Res*, 42(6):792–801, 1978.
- [248] P. Roy-Chaudhury, L.M. Spergel, A. Besarab, A. Asif, and P. Ravani. *Biology of arteriovenous fistula failure*. *J Nephrol*, 20(2):150–163, 2007.
- [249] Y.J. Zhuang, T.M. Singh, C.K. Zarins, and H. Masuda. *Sequential increases and decreases in blood flow stimulates progressive intimal thickening*. *Eur J Vasc Endovasc Surg*, 16(4):301–310, 1998.
- [250] S.J. Sherwin, O. Shah, D.J. Doorly, Y.J. Zhuang, T.M. Singh, C.K. Zarins, and H. Masuda. *Sequential increases and decreases in blood flow stimulates progressive intimal thickening*. *Eur J Vasc Endovasc Surg*, 16(4):301–310, 1998.
- [251] C.G. Caro, D.J. Doorly, M. Tarnawski, K.T. Scott, Q. Long, and C.L. Dumoulin. *Non-planar curvature and branching of arteries and non-planar-type flow*. *Proceedings of the Royal Society of London Series a-Mathematical Physical and Engineering Sciences*, 452(1944):185–197, 1996.
- [252] U. Morbiducci, D. Gallo, R. Ponzini, D. Massai, L. Antiga, F.M. Montevvecchi, and A. Redaelli. *Quantitative analysis of bulk flow in image-based hemodynamic models of the carotid bifurcation: the influence of outflow conditions as test case*. *Ann Biomed Eng*, 38(12):3688–3705, 2010.
- [253] U. Morbiducci, R. Ponzini, M. Grigioni, and A. Redaelli. *Helical flow as fluid dynamic signature for atherogenesis risk in aortocoronary bypass. A numeric study*. *J Biomech*, 40(3):519–534, 2007.
- [254] F. Zhan, Y.B. Fan, and X.Y. Deng. *Swirling flow created in a glass tube suppressed platelet adhesion to the surface of the tube: Its implication in the design of small-caliber arterial grafts*. *Thrombosis Research*, 125(5):413–418, 2010.
- [255] U. Morbiducci, D. Gallo, D. Massai, R. Ponzini, M.A. Deriu, L. Antiga, A. Redaelli, and F.M. Montevvecchi. *On the importance of blood rheology for bulk flow in hemodynamic models of the carotid bifurcation*. *J Biomech*, 44(13):2427–2438, 2011.

- [256] A. Sun, Y. Fan, and X. Deng. *Numerical comparative study on the hemodynamic performance of a new helical graft with noncircular cross section and SwirlGraft*. *Artif Organs*, 34(1):22–27, 2010.
- [257] T. Zheng, Y. Fan, Y. Xiong, W. Jiang, and X. Deng. *Hemodynamic performance study on small diameter helical grafts*. *ASAIO J*, 55(3):192–199, 2009.
- [258] J. Wen, T. Zheng, W. Jiang, X. Deng, and Y. Fan. *A comparative study of helical-type and traditional-type artery bypass grafts: numerical simulation*. *ASAIO J*, 57(5):399–406, 2011.
- [259] A.N. Cookson, D.J. Doorly, and S.J. Sherwin. *Mixing through stirring of steady flow in small amplitude helical tubes*. *Ann Biomed Eng*, 37(4):710–721, 2009.
- [260] T.H. Zheng, W. Wang, W. Jiang, X. Deng, and Y. Fan. *Assessing Hemodynamic Performances of Small Siameter Helical Grafts: Transient Simulation*. *Journal of Mechanics in Medicine and Biology*, 12(1):1250008, 2012.
- [261] G. De Santis, P. Mortier, M. De Beule, P. Segers, P. Verdonck, and B. Verheghe. *Patient-specific computational fluid dynamics: structured mesh generation from coronary angiography*. *Medical & Biological Engineering & Computing*, 48(4):371–380, 2010.
- [262] S.-W. Lee, D.S. Smith, F. Loth, P.F. Fischer, and H.S. Bassiouny. *Importance of flow division on transition to turbulence within an arteriovenous graft*. *J Biomech*, 40(5):981–992, 2007.
- [263] U. Morbiducci, R. Ponzini, G. Rizzo, M. Cadioli, A. Esposito, F.M. Montevecchi, and A. Redaelli. *Mechanistic insight into the physiological relevance of helical blood flow in the human aorta: an in vivo study*. *Biomech Model Mechanobiol*, 10(3):339–355, 2011.
- [264] L. Shtilman, E. Levich, S.A. Orszag, R.B. Pelz, and A. Tsinober. *On the Role of Helicity in Complex Fluid-Flows*. *Physics Letters A*, 113(1):32–37, 1985.
- [265] H.K. Moffatt and A. Tsinober. *Helicity in Laminar and Turbulent-Flow*. *Annual Review of Fluid Mechanics*, 24:281–312, 1992.
- [266] W.R. Dean. *Note on the motion of fluid in a curved pipe*. *Phil. Mag. J. Sci*, 4:208–223, 1927.

- [267] M. Germano. *On the Effect of Torsion on a Helical Pipe-Flow*. Journal of Fluid Mechanics, 125(Dec):1–8, 1982.
- [268] S.J. Liu and J.H. Masliyah. *Axially Invariant Laminar-Flow in Helical Pipes with a Finite Pitch*. Journal of Fluid Mechanics, 251:315–353, 1993.
- [269] Z. Chen, Y. Fan, X. Deng, and Z. Xu. *A new way to reduce flow disturbance in endovascular stents: a numerical study*. Artif Organs, 35(4):392–397, 2011.
- [270] Z. Chen, Y. Fan, X. Deng, and Z. Xu. *Swirling flow can suppress flow disturbances in endovascular stents: a numerical study*. ASAIO J, 55(6):543–549, 2009.
- [271] S. O. Trerotola. *Hemodialysis catheter placement and management*. Radiology, 215(3):651–658, 2000.
- [272] T.A. Depner. *Catheter performance*. Semin Dial, 14(6):425–431, 2001.
- [273] R.A. Sherman and S.S. Levy. *Rate-related recirculation: the effect of altering blood flow on dialyzer recirculation*. Am J Kidney Dis, 17(2):170–173, 1991.
- [274] S.O. Trerotola, M. Kraus, H. Shah, J. Namyslawski, M.S. Johnson, M.S. Stecker, I. Ahmad, G. McLennan, N.H. Patel, E. O’Brien, K.A. Lane, and W.T. Ambrosius. *Randomized comparison of split tip versus step tip high-flow hemodialysis catheters*. Kidney Int, 62(1):282–289, 2002.
- [275] T.W.I. Clark, K. Van Canneyt, and P. Verdonck. *Computational Flow Dynamics and Preclinical Assessment of a Novel Hemodialysis Catheter*. Semin Dial, 2012.
- [276] G. Mareels, D.S. De Wachter, and P.R. Verdonck. *Computational fluid dynamics-analysis of the Niagara hemodialysis catheter in a right heart model*. Artif Organs, 28(7):639–648, 2004.
- [277] M.L. Cohen, B.S. Cohen, I. Kronzon, G.W. Lighty, and H.E. Winer. *Superior vena caval blood flow velocities in adults: a Doppler echocardiographic study*. J Appl Physiol, 61(1):215–219, 1986.
- [278] L. Goubergrits and K. Affeld. *Numerical estimation of blood damage in artificial organs*. Artif Organs, 28(5):499–507, 2004.

- [279] M. Giersiepen, L.J. Wurzinger, R. Opitz, and H. Reul. *Estimation of shear stress-related blood damage in heart valve prostheses—in vitro comparison of 25 aortic valves*. Int J Artif Organs, 13(5):300–306, 1990.
- [280] R.K. Dhingra, E.W. Young, T.E. Hulbert-Shearon, S.F. Leavey, and F.K. Port. *Type of vascular access and mortality in U.S. hemodialysis patients*. Kidney Int, 60(4):1443–1451, 2001.
- [281] K.R. Polkinghorne, S.P. McDonald, R.C. Atkins, and P.G. Kerr. *Vascular access and all-cause mortality: a propensity score analysis*. J Am Soc Nephrol, 15(2):477–486, 2004.
- [282] T.W.I. Clark, D. Jacobs, H.W. Charles, S. Kovacs, T. Aquino, J. Erinjeri, and J.A. Benstein. *Comparison of heparin-coated and conventional split-tip hemodialysis catheters*. Cardiovasc Intervent Radiol, 32(4):703–706, 2009.
- [283] S.O. Trerotola, M.S. Johnson, H. Shah, M.A. Kraus, M.A. McKusky, W.T. Ambrosius, V.J. Harris, and J.J. Snidow. *Tunneled hemodialysis catheters: use of a silver-coated catheter for prevention of infection—a randomized study*. Radiology, 207(2):491–496, 1998.
- [284] H. Hanna, R. Benjamin, I. Chatzinikolaou, B. Alakech, D. Richardson, P. Mansfield, T. Dvorak, M.F. Munsell, R. Darouiche, H. Kantarjian, and I. Raad. *Long-term silicone central venous catheters impregnated with minocycline and rifampin decrease rates of catheter-related bloodstream infection in cancer patients: a prospective randomized clinical trial*. J Clin Oncol, 22(15):3163–3171, 2004.
- [285] Y. Jaffer, N.M. Selby, M.W. Taal, R.J. Fluck, and C.W. McIntyre. *A meta-analysis of hemodialysis catheter locking solutions in the prevention of catheter-related infection*. Am J Kidney Dis, 51(2):233–241, 2008.
- [286] D. Yahav, B. Rozen-Zvi, A. Gafer-Gvili, L. Leibovici, U. Gafer, and M. Paul. *Antimicrobial lock solutions for the prevention of infections associated with intravascular catheters in patients undergoing hemodialysis: systematic review and meta-analysis of randomized, controlled trials*. Clin Infect Dis, 47(1):83–93, 2008.
- [287] M.H. Kroll, J.D. Hellums, L.V. McIntire, A.I. Schafer, and J.L. Moake. *Platelets and shear stress*. Blood, 88(5):1525–1541, 1996.

- [288] J. Strony, A. Beaudoin, D. Brands, and B. Adelman. *Analysis of shear stress and hemodynamic factors in a model of coronary artery stenosis and thrombosis*. Am J Physiol, 265(5 Pt 2):H1787–H1796, 1993.
- [289] J.A. Hasbargen and R.J. Bergstrom. *Variable blood pump flow rates and the effect on recirculation*. Clin Nephrol, 42(5):322–326, 1994.
- [290] Z.J. Twardowski, J.C. Van Stone, M.E. Jones, M.E. Klusmeyer, and J.D. Haynie. *Blood recirculation in intravenous catheters for hemodialysis*. J Am Soc Nephrol, 3(12):1978–1981, 1993.
- [291] L. Senecal, E. Saint-Sauveur, and M. Leblanc. *Blood flow and recirculation rates in tunneled hemodialysis catheters*. ASAIO J, 50(1):94–97, 2004.
- [292] S. Moossavi, T.J. Vachharajani, J. Jordan, G.B. Russell, T. Kaufman, and S. Moossavi. *Retrospective analysis of catheter recirculation in prevalent dialysis patients*. Semin Dial, 21(3):289–292, 2008.
- [293] P.J. Kilner, G.Z. Yang, R.H. Mohiaddin, D.N. Firmin, and D.B. Longmore. *Helical and retrograde secondary flow patterns in the aortic arch studied by three-directional magnetic resonance velocity mapping*. Circulation, 88(5 Pt 1):2235–2247, 1993.
- [294] J.G. Houston, S.J. Gandy, D.G. Sheppard, J.B. Dick, J.J.F. Belch, and P.A. Stonebridge. *Two-dimensional flow quantitative MRI of aortic arch blood flow patterns: Effect of age, sex, and presence of carotid atheromatous disease on prevalence of spiral blood flow*. J Magn Reson Imaging, 18(2):169–174, 2003.
- [295] R. Hayashi, E. Huang, and A.R. Nissenson. *Vascular access for hemodialysis*. Nat Clin Pract Nephrol, 2(9):504–513, 2006.
- [296] A. Di Benedetto, A. Basci, S. Cesare, D. Marcelli, P. Ponce, and N. Richards. *Increased use of catheters as vascular access: is it justified by patients' clinical conditions?* J Vasc Access, 8(1):21–27, 2007.
- [297] NKF-K/DOQI. *Clinical practice guidelines for vascular access: update 2006*. American journal of kidney diseases, 48 Suppl 1:S248–73, 2006.
- [298] R.C. Carson, M. Kiaii, and J.M. MacRae. *Urea clearance in dysfunctional catheters is improved by reversing the line position despite increased access recirculation*. Am J Kidney Dis, 45(5):883–890, 2005.

- [299] B. Canaud, H. Leray-Moragues, N. Kerkeni, J.-Y. Bosc, and K. Martin. *Effective flow performances and dialysis doses delivered with permanent catheters: a 24-month comparative study of permanent catheters versus arterio-venous vascular accesses*. Nephrol Dial Transplant, 17(7):1286–1292, 2002.
- [300] C. Level, C. Lasseur, P. Chauveau, H. Bonarek, L. Perrault, and C. Combe. *Performance of twin central venous catheters: influence of the inversion of inlet and outlet on recirculation*. Blood Purif, 20(2):182–188, 2002.
- [301] S. Eloot, W. Van Biesen, A. Dhondt, H. Van de Wynkele, G. Glorieux, P. Verdonck, and R. Vanholder. *Impact of hemodialysis duration on the removal of uremic retention solutes*. Kidney Int, 73(6):765–770, 2008.
- [302] T. Petitclerc, N. Goux, A.L. Reynier, and B. BălnĂl. *A model for non-invasive estimation of in vivo dialyzer performances and patient's conductivity during hemodialysis*. Int J Artif Organs, 16(8):585–591, 1993.
- [303] H.-D. Polaschegg. *Automatic, noninvasive intradialytic clearance measurement*. Int J Artif Organs, 16(4):185–191, 1993.
- [304] R.M. Lindsay, E. Bradfield, C. Rothera, C. Kianfar, P. Malek, and P.G. Blake. *A comparison of methods for the measurement of hemodialysis access recirculation and access blood flow rate*. ASAIO J, 44(1):62–67, 1998.
- [305] F.A. Gotch, R. Buyaki, F. Panlilio, and T. Folden. *Measurement of blood access flow rate during hemodialysis from conductivity dialysance*. ASAIO J, 45(3):139–146, 1999.
- [306] L. Mercadal, S.T. Du Montcel, M.C. Jaudon, A. Hamani, H. Izzedine, G. Deray, B. BălnĂl, and T. Petitclerc. *Ionic dialysance vs urea clearance in the absence of cardiopulmonary recirculation*. Nephrol Dial Transplant, 17(1):106–111, 2002.
- [307] S. Eloot, A. Dhondt, H. Hoeben, and R. Vanholder. *Comparison of different methods to assess fistula flow*. Blood Purif, 30(2):89–95, 2010.
- [308] S. Mohan, M. Madhrira, M. Mujtaba, R. Agarwala, V. Pogue, and J.-T. Cheng. *Effective ionic dialysance/blood flow rate ratio: an indicator of access recirculation in arteriovenous fistulae*. ASAIO J, 56(5):427–433, 2010.

- [309] J.K. Leypoldt, A.K. Cheung, and R.B. Deeter. *Rebound kinetics of beta2-microglobulin after hemodialysis*. *Kidney Int*, 56(4):1571–1577, 1999.
- [310] J.K. Leypoldt. *Kinetics of beta2-microglobulin and phosphate during hemodialysis: effects of treatment frequency and duration*. *Semin Dial*, 18(5):401–408, 2005.
- [311] D. Schneditz, J.C. Van Stone, and J.T. Daugirdas. *A regional blood circulation alternative to in-series two compartment urea kinetic modeling*. *ASAIO J*, 39(3):M573–M577, 1993.
- [312] D. Schneditz, D. Platzer, and J.T. Daugirdas. *A diffusion-adjusted regional blood flow model to predict solute kinetics during haemodialysis*. *Nephrol Dial Transplant*, 24(7):2218–2224, 2009.
- [313] A.M. Kaufman, D. Schneditz, S. Smye, H.D. Polaschegg, and N.W. Levin. *Solute disequilibrium and multicompartment modeling*. *Adv Ren Replace Ther*, 2(4):319–329, 1995.
- [314] H.D. Polaschegg. *Dialysis Therapy*, chapter Single-Needle Dialysis, in *Dialysis Therapy*, 3rd ed., edited by Nissenson AR, Fine RN, Philadelphia, HanleyBelfus, Inc, 2002, pp 65–68, pages 65–68. Hanley & Belfus, Inc, 2002.
- [315] R.P. Pauly, M. Copland, P. Komenda, A. Levin, A. Pierratos, and C.T. Chan. *Utility and limitations of a multicenter nocturnal home hemodialysis cohort*. *Clin J Am Soc Nephrol*, 3(6):1846–1851, 2008.
- [316] R.P. Pauly, K. Maximova, J. Coppens, R.A. Asad, A. Pierratos, P. Komenda, M. Copland, G.E. Nesrallah, A. Levin, A. Chery, C.T. Chan, and C.A.N-S.L.E.E.P Collaborative Group. *Patient and technique survival among a Canadian multicenter nocturnal home hemodialysis cohort*. *Clin J Am Soc Nephrol*, 5(10):1815–1820, 2010.
- [317] R.S. Suri, A.X. Garg, G.M. Chertow, N.W. Levin, M.V. Rocco, T. Greene, G.J. Beck, J.J. Gassman, P.W. Eggers, R.A. Star, D.B. Ornt, A.S. Klinger, and Frequent Hemodialysis Network Trial Group. *Frequent Hemodialysis Network (FHN) randomized trials: study design*. *Kidney Int*, 71(4):349–359, 2007.

- [318] N.D.C. Duncan, S. Singh, T.D.H. Cairns, M. Clark, A. El-Tayar, M. Griffith, N. Hakim, M. Hamady, A.G. McLean, V. Papalois, A. Palmer, and D. Taube. *Tesio-Caths provide effective and safe long-term vascular access*. *Nephrol Dial Transplant*, 19(11):2816–2822, 2004.
- [319] R. Ponikvar and J. Buturovic-Ponikvar. *Temporary hemodialysis catheters as a long-term vascular access in chronic hemodialysis patients*. *Ther Apher Dial*, 9(3):250–253, 2005.
- [320] K. Van Canneyt, J. Kips, G. Mareels, E. Baert, D. Van Roost, and P. Verdonck. *Experimental and numerical modelling of the ventriculosinus shunt (El-Shafei shunt)*. *Proc Inst Mech Eng H*, 222(4):455–464, 2008.
- [321] F. Dewaele, A.F. Kalmar, K. Van Canneyt, H. Vereecke, A. Absalom, J. Caemaert, M.M.R.F. Struys, and D. Van Roost. *Pressure monitoring during neuroendoscopy: new insights*. *Br J Anaesth*, 107(2):218–224, 2011.
- [322] K. Van Canneyt, R. Kaminsky, L. Botti, L. Antiga, J. Tordoir, P. Verdonck, and S. Eloot. *Can a kinked arterio-venous graft cause unstable flow? A patient-specific validated computational study*. *Journal of Biomechanics*, 41:S210, 2008.
- [323] L. Antiga, R.N. Planken, K. Van Canneyt, L. Botti, A. Caroli, B. Ene-Iordache, J. Tordoir, P. Verdonck, and A. Remuzzi. *Non-linear resistance associated to complex geometry at high flow rates in vascular access for hemodialysis*. In *World Congress on Medical Physics and Biomedical Engineering*, pages 543–546, 2009.

Abbreviations and symbols

Abbreviations

APD	Automatic peritoneal dialysis
ARCH	Patient-specific image-based computational modeling for improvement of short- and long-term outcome of vascular access in patients on hemodialysis therapy
ATP	Adenosine triphosphate
AVF	Arterio-venous fistula
AVG	Arterio-venous graft
CAPD	Continuous ambulatory peritoneal dialysis
CFD	Computational fluid dynamics
CKD	Chronic kidney disease
CSA	Cross-sectional area [m ²]
CT	Computed tomography
CVC	Central venous catheter
DA	Distal artery
DL	Double lumen
DOPPS	Dialysis outcomes and practice patterns study
DRIL	Distal revascularisation-interval ligation
EBPG	European best practice guidelines
EPO	Erythropoietin
ePTFE	Expanded PTFE
ER	Extraction ratio [%]
ESRD	End-stage renal disease
FDA	Food and drug administration
FSI	Fluid structure interaction
HD	Hemodialysis
NKF-K/DOQI	National kidney foundation - kidney disease outcomes quality initiative

LNH	Local normalized helicity	
LVH	Left ventricular hypertrophy	
MR	Magnetic resonance	
NHD	Nocturnal hemodialysis	
NHHD	Nocturnal home hemodialysis	
OSI	Oscillatory shear index	
PA	Proximal artery	
PAI	Proximalisation of the arterial inflow	
PD	Peritoneal dialysis	
PIV	Particle image velocimetry	
PLI	Platelet lysis index	
PRF	Pulse repetition frequency	
PTA	Percutaneous transluminal angioplasty	
PTFE	Polytetrafluoroethylene	
PV	Proximal vein	
PWD	Pulsed wave Doppler	
Qdp	Flow rate versus pressure drop	
RBC	Red blood cell	
RF	Radiofrequency	
ROI	Region of interest	
RR	Reduction ratio	[%]
RRT	Relative residence time	
RRT	Renal replacement therapy	
RT	Residence time	
RUDI	Revision using distal inflow	
SL	Single lumen	
SLF	Spiral laminar flow	
SMAHT	Small amplitude helical technology	
TAWSS	Time-averaged wall shear stress	
TD	Time delay	
TSR	Total solute removal	
Tx	Renal transplantation	
US	Ultrasound	
VA	Vascular access	
WSS	Wall shear stress	

Symbols

\overline{a}	Acceleration vector	[m/s ²]
A	Angle	[°]

C	Compliance	$[m^2/Pa]$
C_1/C_2	Concentration in the perfused / non-perfused compartment	$[g/l \text{ or } mol/l]$
C_{bi}/C_{bo}	Blood concentration at the dialyzer inlet / outlet	$[g/l \text{ or } mol/l]$
C_{di}/C_{do}	Dialysate concentration at the dialyzer inlet / outlet	$[g/l \text{ or } mol/l]$
C_{post}/C_{post60}	Blood concentration post dialysis / 60min after dialysis	$[g/l \text{ or } mol/l]$
C_{pre}	Blood concentration pre dialysis	$[g/l \text{ or } mol/l]$
D	Distensibility	$[Pa^{-1}]$
$\overline{e_x}, \overline{e_y} \text{ and } \overline{e_z}$	x,y and z-component of the unity vector \overline{e}	
Eu	Euler number	$[-]$
\overline{F}	Force vector	$[N]$
\overline{g}	Gravity vector	$[m/s^2]$
G_1/G_2	Solute generation rate in the perfused / non-perfused compartment	$[g/min \text{ or } mol/min]$
H	Hematocrit	$[\%]$
H	Helicity	$[m/s^2]$
H_k	Kinetic helicity density	$[1/(m^2 \cdot s^2)]$
K	Dialyzer clearance	$[ml/min]$
K_{12}	Intercompartmental clearance	$[ml/min]$
L	Length	$[m]$
μ	Dynamic viscosity	$[Pa \cdot s]$
μ_p	Plasma dynamic viscosity	$[Pa \cdot s]$
ν	Kinematic viscosity	$[m^2/s]$
\overline{n}	Normal vector on a surface	
ω	Vorticity	$[1/s]$
p	Pressure	$[Pa]$
Q	Flow rate	$[m^3/s \text{ or } ml/min]$
Q_{ap}/Q_{vp}	Blood pump flow rate during the arterial / venous phase	$[ml/min]$
Q_{bi}/Q_{bo}	Blood flow rate at the dialyzer inlet / outlet	$[ml/min]$
Q_{di}/Q_{do}	Dialysate flow rate at the dialyzer inlet / outlet	$[ml/min]$
Q_{uf}	Ultrafiltration flow rate	$[ml/min]$
ρ	Mass density	$[kg/m^3]$
R	Access recirculation	$[\%]$
R	Radius	$[m]$

R_p	Pheripheral resistance	[Pa·s/m ³]
Re	Reynolds number	[]
τ	Shear stress	[N/m ²]
τ_o	Critical shear stress	[N/m ²]
T	Time period	[s]
t	Time	[s, min or h]
u, v and w	x,y and z-component of the velocity vector \vec{v}	[m/s]
\vec{v}	Velocity vector	[m/s]
V_1/V_2	Perfused / non-perfused volume	[l]
V_c	Catheter volume	[ml]
V_{min}/V_{max}	Minimum / maximum volume in the buffer reservoir	[ml]
V_{res}	Volume of the buffer reservoir	[ml]
W	Width	[m]
Z_o	Characteristic impedance	[Pa·s/m ³]

Operators

Δ	Difference
δ	Partial derivative
D	Substantial derivative $\left(\frac{D}{Dt} = \frac{\delta}{\delta t} + u \frac{\delta}{\delta x} + v \frac{\delta}{\delta y} + w \frac{\delta}{\delta z} \right)$
d	Derivative
$\vec{\nabla}$	Nabla $\left(\vec{\nabla} = \vec{e}_x \frac{\delta}{\delta x} + \vec{e}_y \frac{\delta}{\delta y} + \vec{e}_z \frac{\delta}{\delta z} \right)$

Subscripts

o	At mean pressure
ai	Arterial inlet
ao	Arterial outlet
avg	Average
vo	Venous outlet
d	Distal
dia	Diastolic
DL	Double lumen
max	Maximal
p	Proximal
SL	Single lumen
v	Venous

Superscripts

Units

cm	Centimeter
Fr	French needle gauge
h	Hour
kg	Kilogram
l	Liter
μm	Micrometer
m	Meter
min	Minute
ml	Milliliter
mm	Millimeter
mmHg	Millimeters of mercury
N	Newton
Pa	Pascal
s	Second

List of figures

1.1	Cardiovascular system containing blood vessels and heart.	3
1.2	Schematic representation of the heart.	4
1.3	Deformation of red blood cells when exposed to an increasing shear force.	5
1.4	Arterial anatomy of the upper extremity.	7
1.5	Venous anatomy of the upper extremity.	8
2.1	Prevalence of ESRD-patients in Flanders on a RRT	10
2.2	Patients on a kidney transplant waiting list and transplant numbers registered by Eurotransplant.	11
2.3	Schematic representation of peritoneal dialysis treatment.	12
2.4	Schematic overview of hemodialysis treatment.	14
3.1	Cimino-Brescia shunt.	18
3.2	Three different AVF configurations.	19
3.3	Seven segment AVF circuit.	20
3.4	The ‘fistula hurdle’.	22
3.5	Ischemia.	23
3.6	Stenosis formation: from pathogenesis to pathology.	24
3.7	Stenosis locations.	24
3.8	Optiflow	25
4.1	Scribner-Quinton (external) shunt.	28
4.2	Brachial artery to cephalic vein loop graft.	28
4.3	Venaflo graft.	31
4.4	Flixene Trumpet Vascular Graft.	31
4.5	SwirlGraft.	32
4.6	Patency SwirlGraft compared to standart ePTFE graft.	32
4.7	Tayside Flow Spiral graft.	33
4.8	Tapered graft inlet.	34
4.9	Flixine IFG graft.	34

5.1	CVC in internal jugular vein.	36
5.2	Clothing of CVC.	37
5.3	Comparison double-D, oval-shape and concentric lumen.	39
5.4	Shotgun tip designs.	40
5.5	Palindrome catheter.	40
5.6	Split tip catheters (4).	41
5.7	Centros catheter.	42
5.8	HeRo graft-catheter.	42
6.1	AVF use in Europe versus US.	44
6.2	Visual explanation of patency rates.	45
6.3	Secondary patency rate at 1 year for AVF versus AVG.	45
6.4	Revision rate for AVF versus AVG.	46
7.1	ARCH concept.	50
8.1	Shear stress.	52
8.2	Rheological behavior of different fluids.	53
8.3	Dynamic viscosity calculated by the Quemada model.	55
8.4	Schematic representation of the velocity in a 3D-differential element.	57
8.5	Schematic representation of surface forces in the x-direction in a 3D-differential element.	58
8.6	Flow rate and pressure drop over a stenosis.	61
8.7	Womersley profiles for different Womersley parameters.	65
9.1	General PIV set-up.	70
9.2	Example of experimental setup.	71
9.3	Flowchart of CFD analysis.	73
9.4	Arterial and venous anastomosis of an AVG configuration.	74
9.5	General representation of a double pool kinetic model.	76
10.1	Seven segment AVF circuit	82
10.2	Reference arterio-venous fistula configuration.	84
10.3	Pressure drop for different anastomosis sizes and angles.	86
10.4	Flow rate for different anastomosis sizes and angles.	87
10.5	Velocity streamlines and WSS distribution	90
11.1	Network model mock loop scheme and computational domain.	97
11.2	Pump input step function.	98
11.3	Minor loss coefficients: experimental and computational.	100
11.4	Preoperative pressure and flow waveforms.	106

11.5	Postoperative pressure and flow waveforms: arteries.	107
11.6	Postoperative pressure and flow waveforms: veins.	108
11.7	<i>In vitro</i> anastomosis model.	115
11.8	Contours of velocity magnitude.	118
11.9	Iso-surfaces of the velocity magnitude.	119
11.10	CFD versus PIV.	120
11.11	Re vs. Eu and Δp vs. flow rate.	122
12.1	Vascular access model integrated in mock loop.	128
12.2	%-PP for varying arterial blood flow rates	130
12.3	Pre- and postoperative model.	135
12.4	PWD-spectra.	139
12.5	PWD-velocity and angle-corrected velocity.	140
12.6	Volume flows.	141
12.7	Angle-correction: unidirectional versus complex flow.	144
12.8	Angle-correction: unidirectional versus complex flow.	145
13.1	Summary of model, mesh, material properties and boundary conditions.	154
13.2	Overview of the studied designs.	155
13.3	Area with unfavorable shear stress-related parameters.	157
13.4	Average of shear stress-related parameters in patches.	157
13.5	Kinetic helicity and pressure drop.	158
13.6	Iso-surfaces of LNH.	160
13.7	Axial velocity contours and in-plane streamlines at early systole.	161
13.8	Axial velocity contours and in-plane streamlines at peak systole.	162
13.9	Axial velocity contours and in-plane streamlines at late systole.	163
14.1	VectorFlow and Palindrome catheter tips.	172
14.2	Comparison of mean shear stress, Platelet Lysis Index and blood Residence Time	176
14.3	VectorFlow velocity streamlines.	177
14.4	Comparison of catheter recirculation calculated: bench model.	178
14.5	Comparison of catheter recirculation: animal model.	179
15.1	Single compartment mathematical model scheme.	188
15.2	Concentration profiles correct vs reversed.	191
15.3	Nomogram correct vs reversed.	193
15.4	2-compartment mathematical model scheme: double lumen.	197
15.5	2-compartment mathematical model scheme: single lumen.	198
15.6	Urea concentration profile and cumulative TSR.	202

15.7 β_2 M concentration profile and cumulative TSR. 203

15.8 Dialysis adequacy as a function of the degree of recirculation. . . 205

15.9 Nomograms. 206

List of tables

1.1	Parameters of cell types in blood.	4
7.1	Members of the ARCH consortium.	50
11.1	Semi-empirical determined dimensionless constants.	101
11.2	Input data.	104
11.3	Preoperative mean pressures and flows.	105
11.4	Postoperative mean pressures and flows.	111
12.1	Bias for flow rate: small sample volume.	142
12.2	Bias for flow rate: large sample volume.	142
15.1	<i>In vivo</i> results.	190
15.2	Mathematical results.	192
15.3	Kinetic parameters for urea, MG, β_2 M, and P.	199
15.4	Operating parameters dialyzing with a double lumen and single lumen catheter.	200
15.5	Adequacy parameters for DL-normal dialysis.	203
15.6	Adequacy parameters compared to DL-normal.	204
15.7	Parametric study.	205
15.8	Operating parameters in the different dialysis settings.	210
15.9	Adequacy parameters.	211

